Special issue: Electronics and Biomedical Engineering, Computer Science and Informatics

Erik V. Cuevas-Jiménez Marco A. Pérez-Cisneros Daniel Zaldivar -Navarro

Special issue: Electronics and Biomedical Engineering, Computer Science and Informatics

Erik V. Cuevas-Jiméne Marco A. Pérez-Cisnero Daniel Zaldivar-Navarro Juan Humberto Sossa-Azuel Raúl Rojas (Eds.)

Vol. 35



ISSN: 1870-4069

Control, Robotics and Artificial Intelligence

·		

Special Issue in Electronics and Biomedical Engineering, Computer Science and Informatics

Research in Computing Science

Series Editorial Board

Comité Editorial de la Serie

Editors-in-Chief:

Editores en Jefe

Juan Humberto Sossa Azuela (Mexico) Gerhard Ritter (USA) Jean Serra (France) Ulises Cortés (Spain)

Associate Editors:

Editores Asociados

Jesús Angulo (France) Jihad El-Sana (Israel) Jesús Figueroa (Mexico) Alexander Gelbukh (Russia) Ioannis Kakadiaris (USA) Serguei Levachkine (Russia) Petros Maragos (Greece) Julian Padget (UK) Mateo Valero (Spain)

Editorial Coordination:

Coordinación Editorial Blanca Miranda Valencia Formatting: Formación

J. Humberto Sossa Azuela

Research in Computing Science es una publicación trimestral, de circulación internacional, editada por el Centro de Investigación en Computación del IPN, para dar a conocer los avances de investigación científica y desarrollo tecnológico de la comunidad científica internacional. Volumen 35, Mayo, 2008. Tiraje: 500 ejemplares. Certificado de Reserva de Derechos al Uso Exclusivo del Título No. 04-2004-062613250000-102, expedido por el Instituto Nacional de Derecho de Autor. Certificado de Licitud de Título No. 12897, Certificado de licitud de Contenido No. 10470, expedidos por la Comisión Calificadora de Publicaciones y Revistas Ilustradas. El contenido de los artículos es responsabilidad exclusiva de sus respectivos autores. Queda prohibida la reproducción total o parcial, por cualquier medio, sin el permiso expreso del editor, excepto para uso personal o de estudio haciendo cita explícita en la primera página de cada documento. Impreso en la Ciudad de México, en los Talleres Gráficos del IPN - Dirección de Publicaciones, Tres Guerras 27, Centro Histórico, México, D.F. Distribuida por el Centro de Investigación en Computación, Av. Juan de Dios Bátiz S/N, Esq. Av. Miguel Othón de Mendizábal, Col. Nueva Industrial Vallejo, C.P. 07738, México, D.F. Tel. 57 29 60 00, ext. 56571.

Editor Responsable: Juan Humberto Sossa Azuela, RFC SOAJ560723

Research in Computing Science is published by the Center for Computing Research of IPN. Volume 35, May, 2008. Printing 500. Authors are responsible for the contents of their papers. All rights reserved. No part of this publication may be reproduced, stored in a retrieval system, or transmitted, in any form or by any means, electronic, mechanical, photocopying, recording or otherwise, without prior permission of Centre for Computing Research. Printed in Mexico City, May, 2008, in the IPN Graphic Workshop - Publication Office.

Volume 35

Volumen 35

Special Issue in Electronics and Biomedical Engineering, Computer Science and Informatics

Volume Editors:

Editores del Volumen

Erik V. Cuevas-Jiménez Marco A. Pérez-Cisneros Daniel Zaldívar-Navarro Juan Humberto Sossa-Azuela Raúl Rojas

> Instituto Politécnico Nacional Centro de Investigación en Computación México 2008











ISSN: 1870-4069

Copyright © 2008 Instituto Politécnico Nacional Copyright © 2008 Instituto Politécnico Nacional

Instituto Politécnico Nacional (IPN) Centro de Investigación en Computación (CIC) Av. Juan de Dios Bátiz s/n esq. M. Othón de Mendizábal Unidad Profesional "Adolfo López Mateos", Zacatenco 07738, México D.F., México

http://www.ipn.mx http://www.cic.ipn.mx

Indexada en LATINDEX Indexed in LATINDEX

Printing: 500 Impresiones: 500

Printed in Mexico Impreso en México

Preface

The use of engineering related subjects to study the systems of nature is one of the most significant trends of the century. Driven by the need for more precise scientific understanding, several fields have shown a massive growth expanding their boundaries in a quest to solve new challenging problems, generating new scientific knowledge and technology applications.

This special issue presents original research papers on several engineering field of remarkable importance such as Electronics and Biomedical Engineering, Computer Science and Informatics. The volume is organized into four sections as follows:

Control, Robotics and Artificial Intelligence,

Signal and Image and Processing,

Computer Science and Embedded Architectures and Biomedical Engineering

The overall issue covers 21 papers carefully chosen from a peer-to-peer reviewing process on 47 contributions. Each submission was reviewed by at least three independent members of the Editorial Board and the final acceptation rate was 45.9%.

As we are deeply thankful to all people involve in the preparation of this volume, it is to all the authors and the excellence of their research work that the true value of this book is owed.

We also want to express our gratitude to all members of the editorial board of the volume and additional referees. The submission, reviewing and selection process was supported for free by the EasyChair[©] system.

Erik Cuevas Marco A. Perez Daniel Zaldívar Humberto Sossa Raul Rojas

May 2008

Table of Contents Indice

Page/Pág.

Control, Robotics and Artificial Intelligence

Hardware Implementation of an Optimal Pole Placement Controller for a Liquid Level System	3
Discrete Time Nonlinear Identification via Recurrent High Order Neural Networks	11
A Framework for Teleoperators Control Emmanuel Nuño, Adolfo Rodriguez, Leopoldo Palomo, and Luis Basañez	21
Using Reinforcement Learning in Chess Engines	3
Genetic Algorithm, a Multivariable and Multiobjective Approach	41

No Linear Haptic Rendering of Deformation and Cutting Based on Orthogonal Decomposition Gabriel Sepulveda, Vicente Parra, Omar Dominguez	51
Robust Synchronization of a Class of Robot Manipulators	63
Signal and Image and Processing	
Control of a Nurse Robot Using Voice Commands and Associative Memories. *Roberto A. Vazquez and Humberto Sossa*	77
Detecting Scale-Sensitivity in Image Hierarchies for Coding and Compression. J. Alejandro Butron Guillen and Richard Harvey	87
Smart Camera Desing Ivan Olaf Hernandez, Miguel Enrique Bravo Zanoguera, Guillermo Galaviz Yañes	97
Object Recognition Using Coupled Filters Jorge Hernandez Constante, Josue Alvarez Borrego, and Marco A. Cedano Olvera	107
Mixed Analog-Digital Implementation of the Semidiscrete Wavelet Transform	117
Computer Science and Embedded Architecture	
Improving Search and Publish of Knowledge by Means of Ontology in a Virtual Learning Environment. Hector Diez Rodriguez and Jose Oscar Olmedo Aguirre	127

Construction of an Optimal Solution for a Real World Routing Scheduling Loading Problem	137
Efficient Pattern Recalling Using Parallel Alpha-Beta Associative Memories	147
Synchronization of Complex Networks withNonidentical Nodes	157
Walle Rodriguez Hot Rolling Scheduling Optimization Problem Carlos A. Hernandez Carrion, Hector Fraire Huacuja Karla Espriella Fernandez, Guadalupe Castilla Valdez, and Juana Mancilla Tolama	165
Biomedical Engineering	
Analysis of 5 Source Separation Algorithms on Simulated EEG Signals	177
SISELS: A Mediation System for Giving Access to Biology Resources	187
Fuzzy Gain Scheduling of PI Controller for an Anaerobic Digester	199

Response of the Gravity-Inertial Mechanoreceptors	
During a Fall: Mathematical Model	209
Vladimir Aleksandrov, Tamara Aleksandrova,	
Rosario Vega, Gregorio Castillo, Maribel	
Reyes, Yaneri Aguilar Aida Ortega, Nelly	
Shulenina and Enrique Soto	

Hardware Implementation of a an Optimal Pole Placement Controller for a Liquid Level System

Basil M. Al-Hadithi¹, Juan Suardíaz Muro¹, Susana Ortega Cisneros²,

Juan J. Raygoza Panduro², Juan A. López Riquelme¹

División de Sistemas e Ingeniería Electrónica. Universidad Politécnica de Cartagena.

Campus Muralla del Mar. 30202 Cartagena (Murcia).

bmal@uax.es, {juan.suardiaz, jantonio.lopez}@upct.es http://www.dsie.upct.es

² Departamento de Electrónica y Computación CUCEI, Universidad de Guadalajara. Blvd. Marcelino Garcia Barragan 1421 Guadalajara, México

{susana.ortega, juan.raygoza}@cucei.udg.mx

(Paper received on February 14, 2008, accepted on April 15, 2008)

Abstract. This paper presents a hardware implementation of an optimal pole placement controller for a liquid level system. It is designed to control the level set point by adjusting the flow rate of a liquid entering the tank through a feed pump [1][4]. The control algorithm is used to achieve optimal performance using the Integral of Time Multiplied Absolute Error (ITAE) criterion, which is characterized by little overshoot in the transient response and well-damped oscillations. The performance of the proposed controller is verified using the Xilinx System Generator modelling tool. The results show that the response of this proposed hardware implementation was good and robust implementation.

1 Introduction

This paper presents a hardware implementation of a design method which extends the basic pole placement method to discrete time systems. This method is intuitive and simple to use and can be applied equally well to either continuous or discrete time systems.

Several authors have applied the pole placement technique [9] [3] [5]. In [6][7] [8] studies were carried out to show how the pole placement controller affects the robust stability of the resulting closed-loop system.

In this paper a hardware implementation is applied using the Xilinx System Generator [11] tool to examine the robustness of the proposed controller and also to check the accuracy of the results obtained using hardware tools against those obtained by simulation. The Xilinx System Generator is a tool that extends Simulink with software and blocks for bit and cycle-accurate modelling of digital logic and DSP functions. It also has a translator that converts a Simulink model into hardware for Xilinx eld programmable gate arrays (FPGAs). Models constructed from Xilinx blocks behave exactly in the same way in Simulink as they do in hardware. As part of the

© E. V. Cuevas, M. A. Perez, D. Zaldivar, H. Sossa, R. Rojas (Eds.) Special Issue in Electronics and Biomedical Informatics, Computer Science and Informatics
Research in Computing Science 35, 2008, pp. 3-10



Simulink environment, these models can readily be combined with non Xilinx blocks to model parts of a system not bound to the FPGA. Xilinx blocks, like most Simulink blocks, can be customized by setting parameters from the MATLAB work space. System Generator translates into hardware only the portion of a model built from Xilinx blocks. The behaviour of the non Xilinx portion of a System Generator model can be captured on HDL test bench using simulation vectors computed in Simulink.

2 Pole Assignment Method

Let us consider a completely controllable and observable multiple inputs multiple outputs (MIMO) dynamic process with 'm' inputs, 'n' states and 'm' outputs, described by the following linear discrete-time nominal model.

$$x(k+1) = G \cdot x(k) + H \cdot u(k)$$

$$y(k) = C \cdot x(k)$$
 (1)

where

x(k) = state vector.

u(k) = control signal.

y(k) = output signal.

The basic idea of the pole placement method is the design of state feedback such that all poles of the closed-loop system assume prescribed values. The control system is shown in Fig. 1a.

Applying the state feedback u(k)=-Kx(k) with K being the solution of the pole placement technique according to the Ackermann's formula [3] obtained once the desired closed-loop poles are specified as shown in Fig. 1b.

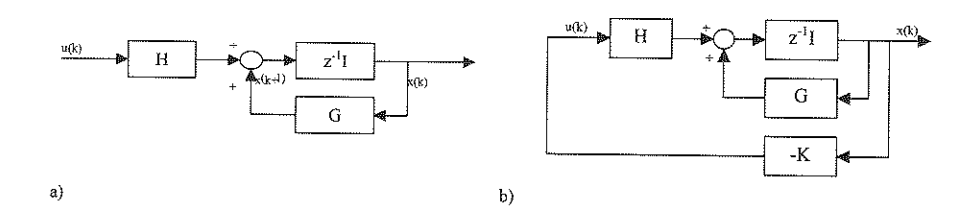


Fig. 1. (a) Control system scheme. (b) State Feedback Scheme.

Therefore the system becomes a closed loop one with the state equation as follows:

$$x(k+1) = (G - HK) \cdot x(k)$$
 (2)

In this paper, the ITAE criterion specified by [2] is characterized by little overshoot and well-damped oscillations. This criterion possesses good selectivity.

It is however difficult to evaluate analytically, although it can readily be measured experimentally. 4

Let us consider a control system whose desired output and actual output are x(t) and y(t) respectively. The error is defined as:

$$e(t) = x(t) - y(t) \tag{3}$$

The optimum response one that minimizes the following Performance index is:

$$\int_{0}^{\infty} t |e(t)| dt$$
 (4)

In applying the ITAE, a large initial error in a unit step is weighted lightly, while errors occurring late in the transient response are penalized heavily.

3 **Control System Design and Experiments**

The process consists of a pump, which is considered to be a 2nd linear system. It pumps the liquid into a tank with a uniform horizontal cross-section up to a predetermined level, and the liquid is discharged through a narrow outlet in the base as shown in Fig. 2

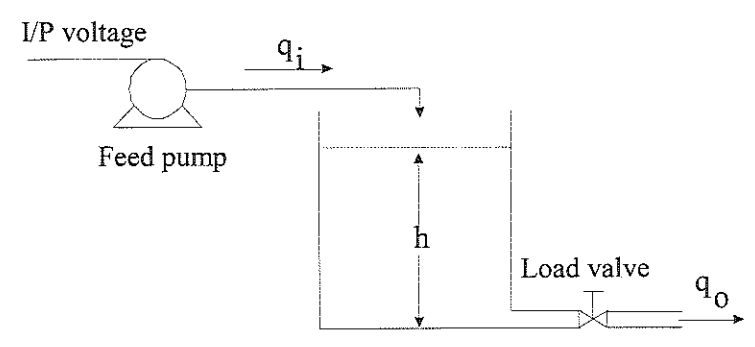


Fig. 2. Liquid Level System

The feed pump unit has been approximated to a second order linear system

$$\frac{Q_1(s)}{U(s)} = \frac{K_{p}}{(1+T_1s)(1+T_2s)} = \frac{1.3}{(1+0.36s)(1+0.71s)}$$
(5)

K_p represents the steady state gain and T₁ and T₂ represent the time constants of the pump. Their values are evaluated using the data obtained from the experimental tests. The tank is a non-linear system with the output flow rate proportional to the square root of the decreasing level. The differential equation is:

$$A \frac{dh}{dt} = q_i(t) - q_o(t)$$
 (6)

where A=10 cm² is the capacitance of the tank, which is defined as the change in the quantity of stored liquid necessary to cause a unit change in the potential (head). The capacitance of the tank is equal to its cross-sectional area. qi and qo represent the inflow rate and outflow rate. The relationship between q₀ and h can be represented as:

$$q_o(t) = k \cdot \sqrt{h(t)} \tag{7}$$

where k is related to the restriction of the valve at the tank output. Substituting (6) in (5) we obtain:

$$A \cdot \frac{dh}{dt} + k \cdot \sqrt{h(t)} = q_i(t)$$
 (8)

Linearizing the resulting non-linear system (8) and substituting in (5):

ting non-linear system (8) and substituting in (5):
$$\frac{d^{3}h}{dt^{3}} + \frac{\left[A(T_{1} + T_{2}) + \frac{kT_{1}T_{2}}{2\sqrt{h_{0}}}\right]}{AT_{1}T_{2}} \frac{d^{2}h}{dt^{2}} + \frac{\left[A + \frac{k}{2\sqrt{h_{0}}}(T_{1} + T_{2})\right]}{AT_{1}T_{2}} \frac{dh}{dt} + \frac{\left[\frac{k}{2\sqrt{h_{0}}}\right]}{AT_{1}T_{2}} h = \frac{\left[K_{p}u\right]}{AT_{1}T_{2}}$$
(9)

The tank was simulated on the basis of a number of experiments to find a suitable model that would coincide with the non-linear model given by (8). The area of the tank A is assumed to be 10 cm². By applying (9), which represents the mathematical model of the controlled process, we get:

$$\frac{Y(s)}{U(s)} = \frac{0.2}{s^3 + 6.5s^2 + 13.5s + 8.7}$$
 (10)

By choosing a sampling time of 0.1 seconds, the equivalent discrete process model is:

$$\frac{Y(z)}{U(z)} = \frac{0.0000205}{z^3 - 2.42z^2 + 1.949z - 0.522}$$
(11)

which can be described in state space form as follows:

$$G = \begin{bmatrix} 0 & 1 & 0 \\ 0 & 0 & 1 \\ 2.42 & -1.949 & 0.522 \end{bmatrix} \qquad H = \begin{bmatrix} 0 \\ 0 \\ 2.05.10^{-5} \end{bmatrix}$$
 (12)

Using the pole placement method, the desired closed loop poles are (0.2856±j0.52, 0.4938) and the feedback controller parameters are: [16985 -64112 66097].

Hardware Implementation

Firstly, a Simulink model of the system under control was developed as follows:

$$X1[n+1] = X2[n]$$

$$X2[n+1] = X3[n]$$

$$X3[n+1] = SX1 \cdot X1[n] + SX2 \cdot X2[n] + SX3 \cdot X3[n] + +KReg \cdot U[n]$$
(13)

with the previously deduced values: SX1 = 0.522, SX2 = -1.949, SX2 = 2.42 and 6

 $KReg = 2.05 \cdot 10^{-5}$.

The next design step is to compose a hardware description of the proposed controller using the Xilinx System Generator modelling tool. The response of the regulator has to obey the following rule:

$$U[n] = Vref - C1 \cdot X1[n] - C2 \cdot X2[n] - C3 \cdot X3[n]$$

$$(14)$$

This hardware model is depicted in Fig. 3. Note that special input units are needed to represent the A/D conversion. As we will discuss later, this is the critical point of the design, because the accuracy of the real response is dependent on the selected data format.

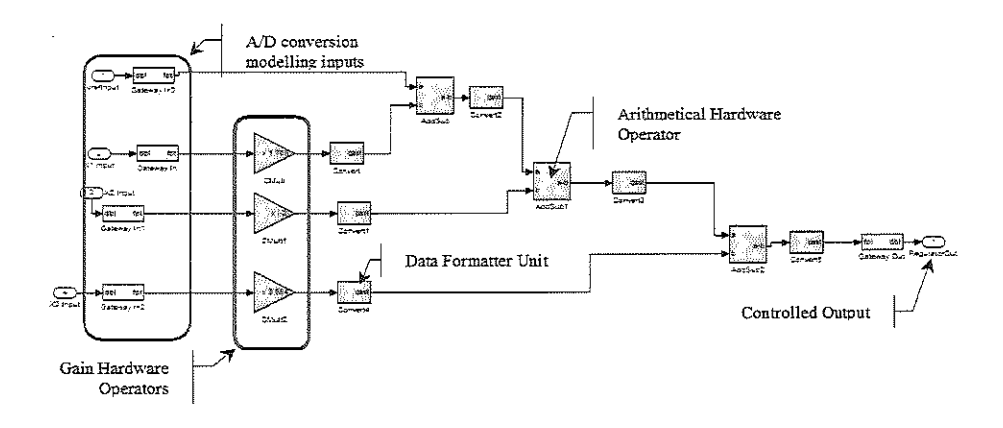


Fig. 3. Hardware model of the proposed controller.

In order to avoid data overflow when performing hardware computations, it has been assumed that there is a signal conditioner between the inputs and outputs of the hardware block and the real system, which changes the voltages levels to allow the minimization of the digital formats used by the hardware controller.

Once the hardware model is described, it can be connected to the previously defined system model and simulated in the Simulink environment.

Several simulations have been performed varying the data format to obtain the best ratio of FPGA occupancy versus response accuracy. Desired results and real results for the hardware controller diverge when a data format of 8 bits is used with 5 bits for the fractional part. If a 24-bit representation is used, with 12 bits allocated to the fractional part, both responses converge exactly. However the FPGA area consumption of inner resources is not optimized. Best results were obtained with a data format of 16 bits, using 8 for the fractional part. With this implementation, results are satisfactorily obtained and the inner resources of the FPGA are also optimized. The maximum error of this representation between the desired and real response is 0.0068, which is acceptable for the purposes of this controller.

5 Results

The performance of the proposed controller has been verified using the Xilinx System Generator modeling tool. The results show a good robust response for the proposed hardware implementation. It is shown that the precision of the results is highly influenced by the word-length. As expected, the greater the word-length, the higher was the precision. Also the resolution has been improved without the need of a large size by allocating the major length to the fractional part. The results suggest that the 16-bit fixed-point implementation, which allocates 8 bits to the fractional part achieves good performance (very similar to that offered by a 24/12 implementation) while optimizing the area consumption of the final design. Table 1 summarizes both, implementation results using a Virtex2 XC2V1000 device and the percentage of occupation for each implementation.

Table 1. Implementation results.

Resource	16_8	24_12	
External IOBs	80 (48%)	120 (72%)	
Slices	161 (1%)	319 (3%)	
Max Error value	0.0068	0.0004	

The first value, External IOBs, is a fixed value associated with the data format chosen. The controller has four inputs (X1, X2, X3 and Vref) and one output (Regulator Output). When a 16-bit format is selected, the resulting usage need is 5x16=80 pins. However, if the associated format is 24-bit, the new need is 5x24=120 pins. The second value, 'Slices' is normally used to measure the overall device usage in terms of processing elements [6]. It should be noted that the 16-bit solution takes up almost three times less area than the 24-bit solution with similar response accuracy. In any case, there is still enough area available to perform additional tasks inside the FPGA, which will be used at later to develop more dense controlling algorithms.

Finally the 'Max Error Value' measures the maxima deviation from the expected controller output. Although the 24-bit implementation presents a lower error, the 16-bit solution presents an acceptable associated error plus the advantage of optimized device occupation. Therefore, it still remains a lot of free space inside the FPGA for further improvements, or a smaller FPGA device could be used for such implementation.

The responses of the designed hardware controller are depicted in Fig.4 for a functional simulation and comparison between the continuous controller response and its associated hardware response. As it can be observed, both response superposes, as it was desired.

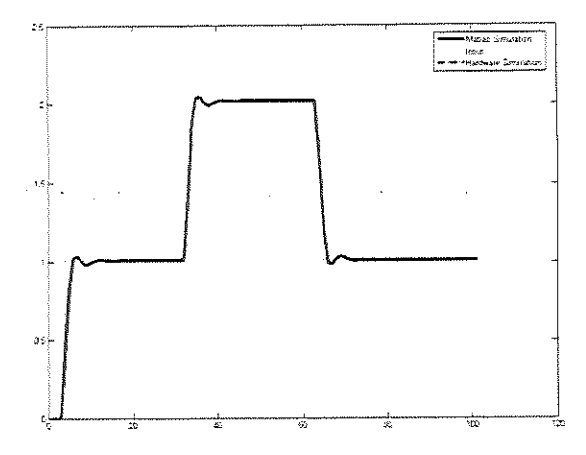


Fig. 4. Responses of the designed hardware controller to perturbations in the level input

Figure 5a shows the real response under a uncontrolled situation and Figure 5b shows the output when the FPGA based hardware controller is connected to the system. Note that the uncontrolled system presents a very slow dynamics, and when the FPGA based controlled is connected to the hardware system the closed loop dynamics is highly improved, according to the theoretical response described in section 4.

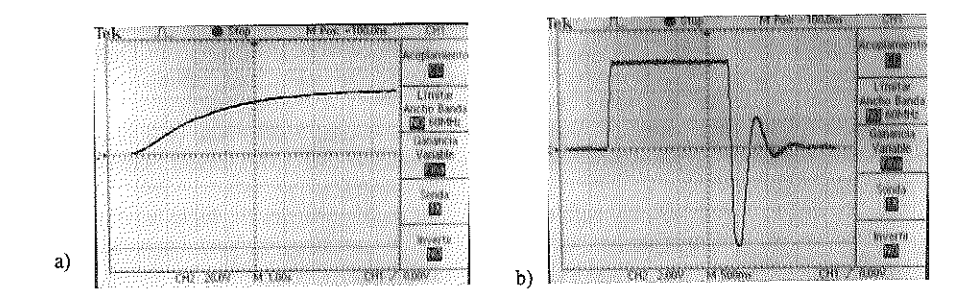


Fig. 5. Hardware responses to unitary step input. (a)No controlled (b) FPGA based control

6 Conclusions

In the hardware implementation of a pole placement control presented in this paper, the problem was to control level set point changes by adjusting the flow rate of liquid entering the tank through a feed pump. The results show a fast response with little overshoot in the transient response and well damped oscillations with zero steady state error.

The design process was optimized using the Xilinx System Generator toolbox, which allows an easy way to analyze and verify each proposed solution. And finally it was successfully implemented in a FPGA device using the ISE design environment. Optimal results were achieved using a 16 bits implementation for the proposed controller.

Acknowledgments. This work was partially supported by Seneca Program with reference ID-02998-PI-05.

References

- Al-Hadithi, B. M., F. Matía and A. Jiménez, "Fuzzy Control for Liquid Level System," EUSFLAT, International Con-ference in Fuzzy Logic and Technology, Zittau, Germany, September, 2003, pp. 355-360.
- Anderson, B. D. O. and J. B. Moore, "Optimal Control-Linear Quadratic Methods", Prentice Hall, Englewood Cliffs, NJ, (1990)
- Garcia, G., J. Daafouz and J. Bernussou Output feedback disk pole placement with positive real uncertainty. IEEE Transactions on Automatic Control AC-41, 1385–1391 (1996).
- Graham, B. P. and R. B. Newell, "Fuzzy identification and control of a liquid rig.," Fuzzy Sets and Systems, 1988, Vol. 26, pp. 255-273.
- Jiandong Zhu; Yu-Ping Tian. "Pole placement and stabilization of discrete systems with unknown equilibrium points" Control Conference, 2006. CCC 2006. Aug. 2006 pp.867 -872
- Kyoung Kwan Ahn; Ho Pham Huy Anh. "System Identification and Self-Tuning Pole Placement Control of the Two-Axes Pneumatic Artificial Muscle Manipulator Optimized by Genetic Algorithm". International Conference on Mechatronics and Automation, 2007. ICMA 2007. Aug. 2007 pp.2604 - 2609
- Michiels W., K. Engelborghs, P. Vansevenant and D. Roose, "Continuous pole placement for delay equations", Auto-matica, vol. 38, no. 5, pp. 747-761(15). Elsevier Science May (2002).
- Min Xu and F. J. Kurdahi, "Accurate prediction of quality metrics for logic level designs targeted toward lookup-table-based FPGA's", IEEE Transactions on Very Large Scale Integration (VLSI) Systems, 7(4):411–418, Decem-ber (1999).
- Sen M.D. "An Algebraic Method for Pole Placement in Multi-variable Systems with Internal and External Point Delays by Using Single Rate or Multirate Sampling", Dynamics and Control vol. 10, no. 1, pp. 5-31(27), Kluwer Academic Publishers, January (2000).
- Soylemez, M. T., "Pole Placement for Uncertain Systems. UMIST Control Systems Centre Series, Research Studies Press. Baldock, UK (1999).
- 11. Xilinx Inc.: http://www.xilinx.com

Discrete Time Nonlinear Identification via Recurrent High Order Neural Networks

Alma Y. Alanis ¹, Edgar N. Sanchez ², and Alexander G. Loukianov ²

¹Departamento de Ciencias Computacionales, CUCEI, Universidad de Guadalajara, Av. Revolucion 1500, Col. Olimpica, C.P. 44430, Guadalajara, Jalisco, Mexico. e-mail: almayalanis@gmail.com

² CINVESTAV, Unidad Guadalajara, Apartado Postal 31-438, Plaza La Luna, Guadalajara, Jalisco, C.P. 45091, Mexico, e-mail: sanchez@gdl.cinvestav.mx (Paper received on February 13, 2008, accepted on April 15, 2008)

Abstract. This paper deals with the problem of discrete-time nonlinear system identification via Recurrent High Order Neural Networks. It includes the respective stability analysis on the basis of the Lyapunov approach for the extended Kalman filter (EKF)-based NN training algorithm, which is applied for learning. Applicability of the scheme is illustrated via simulation for a discrete-time nonlinear model of an electric induction motor.

1 Introduction

Neural networks (NN) have become a well-established methodology as exemplified by their applications to identification and control of general nonlinear and complex systems. In particular, the use of recurrent high order neural networks (RHONN) has increased recently [7]. There are recent results which illustrate that the NN technique is highly effective in the identification of a broad category of complex discrete-time nonlinear systems without requiring complete model information ([12], [13]).

Lyapunov approach can be used directly to obtain robust training algorithms for countinuous-time recurrent neural networks ([7], [9]). For discrete-time systems, the problem is more complex due to the couplings among subsystems, inputs and outputs. Few results have been published in comparison with those for continuous-time domain ([12], [13]). By other hand discrete-time neural networks are more convenient for real-time applications.

For many nonlinear systems it is often difficult to obtain their accurate and faithful mathematical models, regarding their physically complex structures and hidden parameters as discussed in [1]. Therefore, system identification becomes important and even necessary before system control can be considered not only for understanding and predicting the behavior of the system, but also for obtaining an effective control law.

The identification problem consists of choosing an appropriate identification model and adjusting its parameters according to some adaptive law, such that the

© E. V. Cuevas, M. A. Perez, D. Zaldivar, H. Sossa, R. Rojas (Eds.) Special Issue in Electronics and Biomedical Informatics, Computer Science and Informatics

Pescarch in Committing Science 35, 2008, pp. 11-20



response of the model to an input signal (or class of input signals), approximates the response of the real system to the same input [9].

Several training methods for discrete-time recurrent networks have been proposed in the literature as a viable alternative. New training algorithms, e.g., those based on Kalman filtering, have appeared [3], [4], [10]. In this paper, we use an Extended Kalman Filter (EKF)-based training algorithm for the RHONN, in order to identify discrete-time nonlinear systems.

2 Mathematical preliminaries

Through this paper we use k as the step sampling, $k \in 0 \cup \mathbb{Z}^+$, $|\bullet|$ for the absolute value, $||\bullet||$ for the Euclidian norm for vectors and for any adequate norm for matrices. For more details related to this section see [2]. Consider a MIMO nonlinear system:

$$\chi(k+1) = F(\chi(k), u(k)) \tag{1}$$

where $\chi \in \mathbb{R}^n$, $u \in \mathbb{R}^m$ and $F \in \mathbb{R}^n \times \mathbb{R}^m \to \mathbb{R}^n$ is nonlinear function.

Definition 1. The solution of (1) is semiglobally uniformly ultimately bounded (SGUUB), if for any Ω , a compact subset of \Re^n and all $\chi(k_0) \in \Omega$, there exists an $\epsilon > 0$ and a number $N(\epsilon, \chi(k_0))$ such that $||\chi(k)|| < \epsilon$ for all $k \ge k_0 + N$. In other words, the solution of (1) is said to be SGUUB if, for any apriori given (arbitrarily large) bounded set Ω and any apriori given (arbitrarily small) set Ω_0 , which contains (0,0) as an interior point, there exists a control u, such that every trayectory of the closed loop system starting from Ω enters the set $\Omega_0 = {\chi(k) | ||\chi(k)|| < \epsilon}$, in a finite time and remains in it thereafter [2].

Theorem 1 [2] Let $V(\chi(k))$ be a Lyapunov function for the discrete-time system (1), which satisfies the following properties:

$$\gamma_{1}\left(\left\|\chi\left(k\right)\right\|\right) \leq V\left(\chi\left(k\right)\right) \leq \gamma_{2}\left(\left\|\chi\left(k\right)\right\|\right)$$

$$V\left(\chi\left(k+1\right)\right) - V\left(\chi\left(k\right)\right) = \Delta V\left(\chi\left(k\right)\right) \leq -\gamma_{3}\left(\left\|\chi\left(k\right)\right\|\right) + \gamma_{3}\left(\zeta\right)$$

where ζ is a positive constant, γ_1 (\bullet) and γ_2 (\bullet) are strictly increasing functions, and γ_3 (\bullet) is a continuous, nondecreasing function. Thus if

$$\Delta V(\chi) < 0$$
 for $\|\chi(k)\| > \zeta$

then $\chi\left(k\right)$ is uniformly ultimately bounded, i.e. there is a time instant k_{T} , such that $\|\chi\left(k\right)\|<\zeta,\forall\ k< k_{T}.$

3 Discrete-time Recurrent Neural Networks

Consider the following discrete-time recurrent high order neural network (RHONN):

$$x_i(k+1) = w_i^{\mathsf{T}} z_i(x(k), u(k)), \quad i = 1, \dots, n$$
 (2)

where x_i $(i = 1, 2, \dots, n)$ is the state of the *i*th neuron, L_i is the respective number of higer-order connections, $\{I_1, I_2, \dots, I_{L_i}\}$ is a collection of non-ordered subsets of $\{1, 2, \dots, n\}$, n is the state dimension, w_i $(i = 1, 2, \dots, n)$ is the respective on-line adapted weight vector, and $z_i(x(k), u(k))$ is given by

$$z_{i}(x(k), u(k)) = \begin{bmatrix} z_{i_{1}} \\ z_{i_{2}} \\ \vdots \\ z_{i_{L_{i}}} \end{bmatrix} = \begin{bmatrix} \Pi_{j \in I_{1}} y_{i_{d_{i_{j}}(2)}}^{d_{i_{j}}(1)} \\ \Pi_{j \in I_{2}} y_{i_{j}}^{d_{i_{j}}(2)} \\ \vdots \\ \Pi_{j \in I_{L_{i}}} y_{i_{j}}^{d_{i_{j}}(L_{i})} \end{bmatrix}$$
(3)

with $d_{j_i}(k)$ being a nonnegative integers, and y_i is defined as follows:

$$y_{i} = \begin{bmatrix} y_{i_{1}} \\ \vdots \\ y_{i_{n}} \\ y_{i_{n+1}} \\ \vdots \\ y_{i_{n+m}} \end{bmatrix} = \begin{bmatrix} S(x_{1}) \\ \vdots \\ S(x_{n}) \\ u_{1} \\ \vdots \\ u_{m} \end{bmatrix}$$

$$(4)$$

In (4), $u = [u_1, u_2, \dots, u_m]^{\top}$ is the input vector to the neural network, and $S(\bullet)$ is defined by

$$S(x) = \frac{1}{1 + \exp(-\beta x)} \tag{5}$$

Consider the problem to approximate the general discrete-time nonlinear system (1), by the following discrete-time RHONN serie-parallel representation [9]:

$$\chi_i(k+1) = w_i^{*\top} z_i(x(k), u(k)) + \epsilon_{z_i}$$
 (6)

where χ_i is the *i*th plant state, ϵ_{x_i} is a bounded approximation error, which can be reduced by increasing the number of the adjustable weights [9]. Assume that there exists ideal weights vector w_i^* such that $\|\epsilon_{z_i}\|$ can be minimized on a compact set $\Omega_{z_i} \subset \Re^{L_i}$ The ideal weight vector w_i^* is an artificial quantity required for analytical purpose [9]. In general it is assumed that this vector exists and is constant but unknown. Let us define its estimate as w_i and the estimation error as

$$\widetilde{w}_{i}(k) = w_{i}^{*} - w_{i}(k) \tag{7}$$

The estimate w_i is used for stability analysis which will be discussed later. Since w_i^* is constant, then $\widetilde{w}_i(k+1) - \widetilde{w}_i(k) = w_i(k+1) - w_i(k)$, $\forall k \in 0 \cup \mathbb{Z}^+$.

4 The EKF Training Algorithm

Kalman filtering (KF) estimates the state of a linear system with additive state and output white noises [1], [3]. For KF-based neural network training, the network weights become the states to be estimated, with the error between the

neural network output and the desired output being considered; this error considered as additive white noise. For identification, the desired output is information generated by the plant; in this paper, the respective state. Due the fact that the neural network mapping is nonlinear, an extended Kalman Filtering (EKF)-type is required.

The training goal is to find the optimal weight values that minimize the prediction errors (the differences between the desired outputs and the neural network outputs). The EKF-based NN training algorithm is described by

$$K_{i}(k) = P_{i}(k) H_{i}(k) M_{i}(k) \qquad i = 1, \dots, n$$

$$w_{i}(k+1) = w_{i}(k) + \eta_{i} K_{i}(k) e_{i}(k)$$

$$P_{i}(k+1) = P_{i}(k) - K_{i}(k) H_{i}^{\top}(k) P_{i}(k) + Q_{i}(k)$$
(8)

with

$$M_{i}(k) = \left[R_{i}(k) + H_{i}^{T}(k) P_{i}(k) H_{i}(k) \right]^{-1}$$

$$e_{i}(k) = \chi_{i}(k) - \chi_{i}(k)$$
(10)

where $e_i(k)$ is the respective identification error, $P_i(k) \in \Re^{L_i \times L_i}$ is the prediction error covariance matrix at step k, $w_i \in \Re^{L_i}$ is the weight (state) vector, L_i the respective number of neural network weights, χ_i is the ith plant state, x_i the ith neural network state, n is the number of states, $K_i \in \Re^{L_i}$ is the Kalman gain vector, $Q_i \in \Re^{L_i \times L_i}$ is the NN weight estimation noise covariance matrix, $R_i \in \Re$ is the error noise covariance; $H_i \in \Re^{L_i}$ is a vector, in which each entry $(H_{i,j})$ is the derivative of one of the neural network state, (x_i) , with respect to one neural network weight, $(w_{i,j})$, as follows

$$H_{i,j}(k) = \left[\frac{\partial x_{i,j}(k)}{\partial w_{i,j}(k)}\right]_{w_{i,j}(k) = w_{i,j}(k+1)}^{\mathsf{T}} \tag{11}$$

where i = 1, ..., n and $j = 1, ..., L_i$

Usually P_i and Q_i are initialized as diagonal matrices, with entries $P_i(0)$ and $Q_i(0)$, respectively. It is important to remark that $H_i(k)$, $K_i(k)$ and $P_i(k)$ for the EKF are bounded; for a detailed explanation of this fact see [11].

Then the dynamics of the identification error (10) can be expressed as

$$e_i(k+1) = \widetilde{w}_i(k) z_i(x(k), u(k)) + \epsilon_{z_i}$$
 (12)

By the other hand the dynamics of (7) is

$$\widetilde{w}_{i}(k+1) = \widetilde{w}_{i}(k) - \eta_{i}K_{i}(k)e(k)$$
(13)

Now, we establish the main result of this paper in the following theorem. Theorem 2: The RHONN (2) trained with the EKF-based algorithm (8) to identify the nonlinear plant (1), ensures that the identification error (10) is semiglobally uniformly ultimately bounded (SGUUB); moreover, the RHONN weights remain bounded.

Proof. Consider the Lyapunov function candidate

$$V_{i}(k) = \widetilde{w}_{i}^{T}(k) \, \widetilde{w}_{i}(k) + e_{i}^{2}(k)$$

$$\Delta V_{i}(k) = V(k+1) - V(k)$$

$$= \widetilde{w}_{i}^{T}(k+1) \, \widetilde{w}_{i}(k+1) + e_{i}^{2}(k+1) - \widetilde{w}_{i}^{T}(k) \, \widetilde{w}_{i}(k) - e_{i}^{2}(k)$$
(14)

Using (12) and (13) in (14)

$$\Delta V_{i}\left(k\right) = \left[\widetilde{w}_{i}\left(k\right) - \eta_{i}K_{i}\left(k\right)e_{i}\left(k\right)\right]^{T}\left[\widetilde{w}_{i}\left(k\right) - \eta_{i}K_{i}\left(k\right)e_{i}\left(k\right)\right] - \widetilde{w}_{i}\left(k\right)\widetilde{w}_{i}\left(k\right) + \left[\widetilde{w}_{i}\left(k\right)z_{i}\left(x(k),u(k)\right) + \epsilon_{z_{i}}\right]^{T}\left[\widetilde{w}_{i}\left(k\right)z_{i}\left(x(k),u(k)\right) + \epsilon_{z_{i}}\right] - e_{i}^{2}\left(k\right)$$

which can be expressed as

$$\begin{split} \Delta V_{i}\left(k\right) &= \widetilde{w}_{i}^{T}\left(k\right)\widetilde{w}_{i}\left(k\right) - \widetilde{w}_{i}^{T}\left(k\right)\widetilde{w}_{i}\left(k\right) + \eta^{2}e_{i}^{2}\left(k\right)K^{T}K_{i}\left(k\right) \\ &+ 2\epsilon_{z_{i}}\widetilde{w}_{i}\left(k\right)z_{i}\left(x(k),u(k)\right) + z_{i}^{T}\left(x(k),u(k)\right)\widetilde{w}_{i}^{T}\left(k\right)\widetilde{w}_{i}\left(k\right)z_{i}\left(x(k),u(k)\right) \\ &+ \epsilon_{z_{i}}^{2} - 2\eta_{i}e_{i}\left(k\right)\widetilde{w}_{i}^{T}\left(k\right)K_{i}\left(k\right) - e_{i}^{2}\left(k\right) \\ \Delta V_{i}\left(k\right) &\leq \left|e_{i}\left(k\right)\right|^{2}\left\|\eta K_{i}\right\|^{2} - \left|e_{i}\left(k\right)\right|^{2} - \left|2\eta_{i}\right|\left|e_{i}\left(k\right)\right|\left\|\widetilde{w}_{i}\left(k\right)\right\|\left\|K_{i}\left(k\right)\right\| + \left|\epsilon_{z_{i}}\right|^{2} \\ &+ \left|2\epsilon_{z_{i}}\right|\left\|\widetilde{w}_{i}\left(k\right)\right\|\left\|z_{i}\left(x(k),u(k)\right)\right\| + \left\|\widetilde{w}_{i}\left(k\right)\right\|^{2}\left\|z_{i}\left(x(k),u(k)\right)\right\|^{2} \end{split}$$

Then $\Delta V_i(k) < 0$ when

$$\left|e_{i}\left(k\right)\right| > \frac{\left|\epsilon_{z_{i}}\right|^{2}}{1-\left\|\eta K_{i}\right\|^{2}} \equiv \kappa_{1}$$

and

$$\left\|\widetilde{w}_{i}\left(k\right)\right\| > \frac{\left|2\eta_{i}e_{i\max}\right|\left\|K_{i}\left(k\right)\right\|}{\left\|z_{i}\left(x(k),u(k)\right)\right\|^{2}} - \frac{\left|2\epsilon_{z_{i}}\right|}{\left\|z_{i}\left(x(k),u(k)\right)\right\|} \equiv \kappa_{2}$$

Therefore the solution of (12) and (13) is stable, hence the identification error and the RHONN weights are SGUUB [5].

5 Application

In this section we apply the above developed scheme to a three-phase induction motor model

5.1 Motor model

The six-order discrete-time induction motor model in the stator fixed reference frame (α, β) under the assumptions of equal mutual inductances and linear mag-

netic circuit is given by [6]

$$\omega(k+1) = \omega(k) + \frac{\mu}{\alpha} (1-\alpha) M \left(i^{\beta}(k) \psi^{\alpha}(k) - i^{\alpha}(k) \psi^{\beta}(k) \right) - {T \choose J} T_L(k)$$

$$\psi^{\alpha}(k+1) = \cos(n_p \theta(k+1)) \rho_1(k) - \sin(n_p \theta(k+1)) \rho_2(k)$$

$$\psi^{\beta}(k+1) = \sin(n_p \theta(k+1)) \rho_1(k) + \cos(n_p \theta(k+1)) \rho_2(k)$$

$$i^{\alpha}(k+1) = \varphi^{\alpha}(k) + \frac{T}{\sigma} u^{\alpha}(k)$$

$$i^{\beta}(k+1) = \varphi^{\beta}(k) + \frac{T}{\sigma} u^{\beta}(k)$$

$$\theta(k+1) = \theta(k) + \omega(k) T + \frac{\mu}{\alpha} \left[T - \frac{(1-a)}{\alpha} \right]$$

$$\times M \left(i^{\beta}(k) \psi^{\alpha}(k) - i^{\alpha}(k) \psi^{\beta}(k) \right) - \frac{T_L(k)}{J} T^2$$
(15)

with

$$\rho_{1}(k) = a \left(\cos \left(\phi(k) \right) \psi^{\alpha}(k) + \sin \left(n_{p} \phi(k) \right) \psi^{\beta}(k) \right)
+ b \left(\cos \left(\phi(k) \right) i^{\alpha}(k) + \sin \left(\phi(k) \right) i^{\beta}(k) \right)
\rho_{2}(k) = a \left(\cos \left(\phi(k) \right) \psi^{\alpha}(k) - \sin \left(\phi(k) \right) \psi^{\beta}(k) \right)
+ b \left(\cos \left(\phi(k) \right) i^{\alpha}(k) - \sin \left(\phi(k) \right) i^{\beta}(k) \right)
\varphi^{\alpha}(k) = i^{\alpha}(k) + \alpha \beta T \psi^{\alpha}(k) + n_{p} \beta T \omega(k) \psi^{\alpha}(k) - \gamma T i^{\alpha}(k)
\varphi^{\beta}(k) = i^{\beta}(k) + \alpha \beta T \psi^{\beta}(k) + n_{p} \beta T \omega(k) \psi^{\beta}(k) - \gamma T i^{\beta}(k)
\phi(k) = n_{p} \theta(k)$$
(16)

with $b=(1-a)\,M$, $\alpha=\frac{R_r}{L_r}$, $\gamma=\frac{M^2R_r}{\sigma L_r^2}+\frac{R_s}{\sigma}$, $\sigma=L_s-\frac{M^2}{L_r}$, $\beta=\frac{M}{\sigma L_r}$, $a=e^{-\alpha T}$ and $\mu=\frac{Mn_p}{JL_r}$, besides Ls, L_r and M are the stator, rotor and mutual inductance respectively; R_s and R_r are the stator and rotor resistances respectively; n_p is the number of pole pairs; i^α and i^β represents the currents in the α and β phases, respectively; ψ^α and ψ^β represents the fluxes in the α and β phases, respectively and θ is the rotor angular displacement. Simulations are performed for the system (15), using the following parameters: $R_s=14\Omega$; $L_s=400mH$; M=377mH; $R_r=10.1\Omega$; $L_r=412.8mH$; $n_p=2$; $J=0.01Kgm^2$; T=0.001s.

5.2 Neural network identification

The RHONN proposed for this application is as follows:

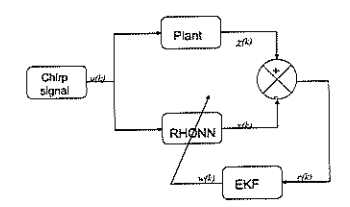


Fig. 1. Identification scheme

$$\begin{split} x_{1}\left(k+1\right) &= w_{11}\left(k\right)S\left(\omega\left(k\right)\right) + w_{12}\left(k\right)S\left(\omega\right)S\left(\psi^{\beta}\left(k\right)\right)i^{\alpha}\left(k\right) \\ &+ w_{13}\left(k\right)S\left(\omega\right)S\left(\psi^{\alpha}\left(k\right)\right)i^{\beta}\left(k\right) \\ x_{2}\left(k+1\right) &= w_{21}\left(k\right)S\left(\omega\left(k\right)\right)S\left(\psi^{\beta}\left(k\right)\right) + w_{22}\left(k\right)i^{\beta}\left(k\right) \\ x_{3}\left(k+1\right) &= w_{31}\left(k\right)S\left(\omega\left(k\right)\right)S\left(\psi^{\alpha}\left(k\right)\right) + w_{32}\left(k\right)i^{\alpha}\left(k\right) \\ x_{4}\left(k+1\right) &= w_{41}\left(k\right)S\left(\psi^{\alpha}\left(k\right)\right) + w_{42}\left(k\right)S\left(\psi^{\beta}\left(k\right)\right) \\ &+ w_{43}\left(k\right)S\left(i^{\alpha}\left(k\right)\right) + w_{44}\left(k\right)u^{\alpha}\left(k\right) \\ x_{5}\left(k+1\right) &= w_{51}\left(k\right)S\left(\psi^{\alpha}\left(k\right)\right) + w_{52}\left(k\right)S\left(\psi^{\beta}\left(k\right)\right) \\ &+ w_{53}\left(k\right)S\left(i^{\beta}\left(k\right)\right) + w_{54}\left(k\right)u^{\beta}\left(k\right) \end{split}$$

The training is performed on-line, using a series-parallel configuration as illustrated in Fig. 1. During the identification process the plant and the NN operates in open-loop. Both of them (plant and NN) have the same input vector $\begin{bmatrix} u_{\alpha} \ u_{\beta} \end{bmatrix}^{\mathsf{T}}$; u_{α} and u_{β} are chirps functions with 170volts of maximal amplitude and incremental frecuencies from 0Hz to 250Hz and 0Hz to 200Hz respectively. All the NN states are initialized in a random way as well as the weights vectors. It is important remark that the initial conditions of the plant are completely different from the initial conditions for the NN. The identification is performed using (8) with $i=1,2,\cdots,n$ with n the dimension of plant states (n=6).

5.3 Simulation results

The results of the simulation are presented in Figs. 2-8. Fig. 2 shows the identification of rotor angular displacement; Fig. 3 displays the identification performance for the speed rotor; Fig. 4 and Fig. 5 present the identification performance for the fluxes in phase α and β , respectively. Figs 6 and 7 portray the identification performance for currents in phase α and β , respectively. Finally, the weights evolution are presented in Fig. 8.

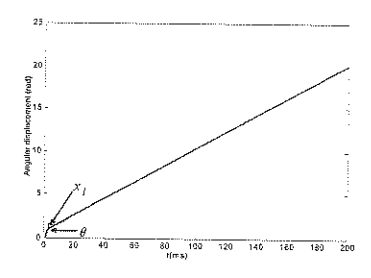


Fig. 2. Angular displacement identification

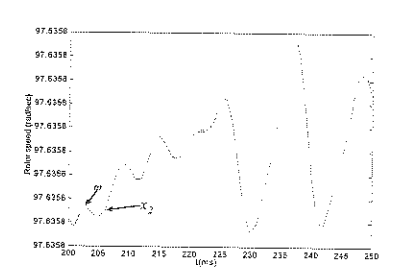


Fig. 3. Rotor speed identification

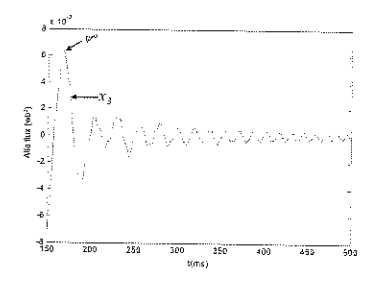


Fig. 4. ψ^{α} identification

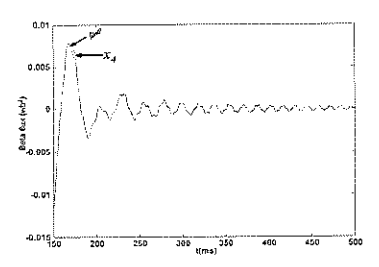


Fig. 5. ψ^{β} identification

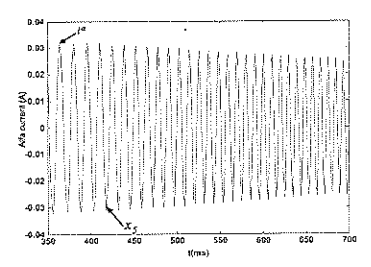


Fig. 6. i^{α} identification

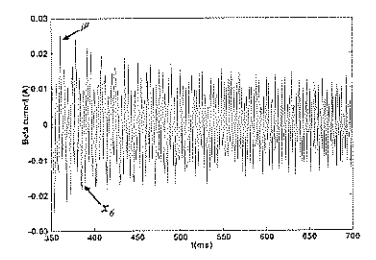


Fig. 7. i^{β} identification

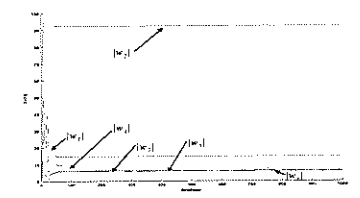


Fig. 8. Weights evolution

6 Conclusions

This paper has presented the application of recurrent high order neural networks to identification of discrete-time nonlinear systems. The training of the neural networks was performed on-line using an extended Kalman filter. The boundness of the identification error was established on the basis of the Lyapunov approach. Simulation results illustrate the applicability of the proposed identification methodology. Researches are being pursued to develop new discrete-time nonlinear adaptive control based on the discussed identification scheme.

Acknowledgement: The authors thank the support of CONACYT Mexico, through Projects 46069Y and 57801Y. The first author also thanks the support of "CONACYT Fondo Institucional".

References

- C. K. Chui and G. Chen, Kalman Filtering with Real-Time Applications, 3rd ed., Springer-Verlag, New York, USA, 1998.
- S. S. Ge, J. Zhang and T.H. Lee, "Adaptive neural network control for a class of MIMO nonlinear systems with disturbances in discrete-time", *IEEE Transactions* on Systems, Man and Cybernetics, Part B, Vol. 34, No. 4, August, 2004.
- R. Grover and P. Y. C. Hwang, Introduction to Random Signals and Applied Kalman Filtering, 2nd ed., John Wiley and Sons, New York, USA, 1992.
- S. Haykin, Neural Networks. A comprehensive foundation, 2nd ed., Prentice Hall, New Jersey, USA, 1999.
- Y. H. Kim and F. L. Lewis, High-Level Feedback Control with Neural Networks, World Scientific, Singapore, 1998.
- A. G. Loukianov, J. Rivera and J. M. Cañedo, "Discrete-time sliding mode control of an induction motor", Proceedings IFAC'02, Barcelone, Spain, July, 2002.
- E. N. Sanchez and J. L. Ricalde, "Trajectory tracking via adaptive recurrent neural control with input saturation", Proceedings of International Joint Conference on Neural Networks'03, Portland, Oregon, USA, July, 2003.
- E. N. Sanchez, A. Y. Alanis and G. Chen, "Recurrent neural networks trained with Kalman filtering for discrete chaos reconstruction", Proceedings of Asian-Pacific Workshop on Chaos Control and Synchronization'04, Melbourne, Australia, July, 2004.
- 9. G. A. Rovithakis and M. A. Chistodoulou, Adaptive Control with Recurrent High -Order Neural Networks, Springer Verlag, New York, USA, 2000.
- S. Singhal and L. Wu, Training multilayer perceptrons with the extended Kalman algorithm, in D. S. Touretzky (ed), Advances in Neural Information Processing Systems 1, pp. 133-140, Morgan Kaufmann, San Mateo, CA, USA, 1989.
- 11. Y. Song and J. W. Grizzle, *The extended Kalman Filter as Local Asymptotic Observer for Discrete-Time Nonlinear Systems*, Journal of Mathematical systems, Estimation and Control, Vol. 5, No. 1, pp. 59-78, Birkhauser-Boston, 1995.
- W. Yu and X. Li, "Discrete-time neuro identification without robust modification", IEE Proc-Control Theory Appl., Vol. 150, No. 3, May, 2003.
- W. Yu and X. Li, "Nonlinear system identification using discrete-time recurrent neural networks with stable learning algorithms", *Information Sciences*, Vol. 158, pp. 131-147, 2004.

A Framework for Teleoperators Control

Emmanuel Nuño, Adolfo Rodríguez, Leopold Palomo, and Luis Basañez

Institute of Industrial and Control Engineering (IOC)
Technical University of Catalonia (UPC)
Barcelona, Spain.

{emmanuel.nuno;adolfo.rodriguez;leopold.palomo;luis.basanez}@upc.edu

(Paper received on February 29, 2008, accepted on April 15, 2008)

Abstract. This work presents a framework for teleoperators control which is composed of a local and a remote station connected through a communication channel. This framework makes use of novel tools and techniques, such as robust controllers and geometric guidance. The controllers render asymptotic zero-convergence of velocities and position error despite variable time-delays. Experimental evidence is presented to validate this framework.

1 Introduction

A teleoperator is commonly referred as the interconnection of five elements: a human operator that exerts force on a local manipulator connected through a communication channel to a remote manipulator that interacts with an environment. The application of such a system spans multiple fields, the most illustrative being space, underwater, medicine, and, in general, tasks with hazardous environments.

One of the main control objectives in such system is force reflection, which is a means to provide the operator with a sense of immersion on the remote station. However, this objective is compromised by instabilities caused by time-delays. In 1989, Anderson and Spong [1] presented the basis of delay independent teleoperation control. Their approach was to render the communications passive by using scattering theory and the analogy of a lossless transmission line. They showed that the scattering transformation ensures passivity of the communications regardless any constant time-delay. Following the previous approach, Niemeyer and Slotine [2] introduced wave variables (scattering transformation), and proved that by matching the impedance of the local and remote manipulator controllers with the impedance of the virtual transmission line, reflections are avoided. Since then, the scattering transformation has dominated the field of teleoperation control.

On the other hand, an ever-growing number of devices connected to the Internet are now accessible to a multitude of users. Being an ubiquitous communication means, the Internet enables users to reach and command any device connected to the network. However, Internet imposes variable time-delays, and the aforementioned schemes cannot guarantee a stable behavior under such conditions. Several works have tackled the issue of providing position tracking under

© E. V. Cuevas, M. A. Perez, D. Zaldivar, H. Sossa, R. Rojas (Eds.) Special Issue in Electronics and Biomedical Informatics, Computer Science and Informatics
Research in Computing Science 35, 2008, pp. 21-30



variable time-delays. Chopra et al. [3], with an adaptation of Lozano et al. [4], have proposed a position-drift free scheme in which the remote manipulator has a control term that depends on the position error between the local and remote manipulators. Hirche and Buss [5] extended these results analyzing the effects of packet loss in packet switched communication networks, like the Internet. Munir and Book [6] used a Kalman filter and a position-drift compensator to provide position tracking, and Nuño et. al. [7,8] have proved that simple PD controllers can also achieve position tracking despite variable time-delays, without the use of the scattering variables. The reader is invited to see [9] and [10] for two interesting survey articles focused on control of teleoperators.

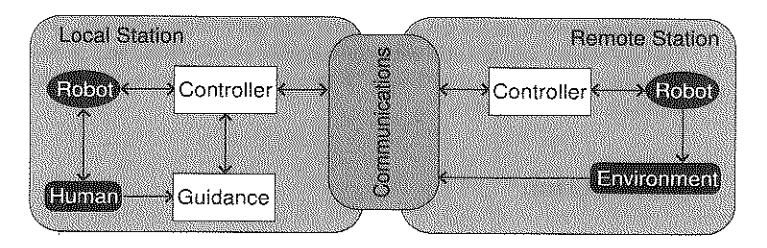


Fig. 1. Framework's overall structure

This work presents a framework for teleoperators control composed of three parts: 1) local station; 2) communications, and; 3) remote station. Fig. 1 shows the overall structure of this framework and, Fig. 2 for its main physical components. The framework copes with variable time-delays, position-drift, operator uncertainty and safety at the remote station. Moreover, it gathers two important tools: geometric guidance and the possibility to use Internet2 and Quality of Service (QoS). The main contribution of this work is the framework as a whole, incorporating various advanced tools, some of them developed by the authors, for rendering bilateral robotic teleoperation secure and reliable, like robust controllers and geometric guidance. Experimental evidence supports the advantages of the presented framework.

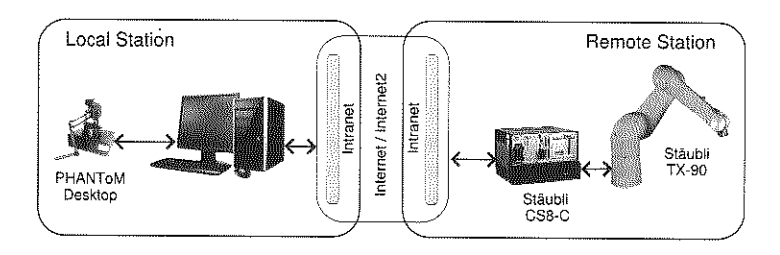


Fig. 2. Physical components of the system

2 Local Station

The human operator is the main component of the local station, it interacts with the local robot manipulator and the Guidance module (Fig. 1). The human selects which controller will be used, sets the geometric restriction—if any—that will be haptically displayed, exerts forces on the local manipulator, and 'feels' what the remote manipulator is touching. The user is also provided with a 3D video stream form the remote station. However, this aspect is not covered in the present article. The following Sections explain how the interactions between the physical system and the software take place.

2.1 Physical System

As can be seen in Fig. 2, the physical elements in the local station are a PC and a robot manipulator, which in this case is a haptic device. Also, communications require an IPv4/IPv6 switch (cf. Section 5.2). The haptic device is a PHANTOM 1.5TM from Sensable Technologies, connected through a parallel port to the PC. The device provides position and velocity sensing on 6 Degrees of Freedom (DOF), and most importantly, 6 DOF force reflection. The human interacts directly with this device.

2.2 Software Structure

All software is written in C++. The interaction with the haptic device is done using the educational version of Sensable's OpenHapticsTM library. The Graphic User Interface (GUI) has been developed using Trolltech's Qt 4. The left side of Fig. 3 shows the GUI, in which the human operator can: choose different control schemes (cf. Section 4.2); enable or disable different geometric restrictions (cf. Section 5.1); and modify the controller's gains. The software structure is composed by seven POSIX threads that run in parallel with equal priority, and whose interaction is regulated by semaphores and mutex locks.

The Guidance thread is responsible for applying geometric restrictions to the workspace of the haptic device. It does so by generating forces locally on the device that restrict operator movements to a submanifold of free space that is meaningful for the task at hand. The Controller thread contains the implementation of different control laws (Table 1), and the operator can select one of them through the GUI. The Haptic Rendering thread maps the incoming forces and torques from the Guidance and Controller threads into the haptic device frame.

The Haptic ServoLoop thread directly interacts with the PHANToM device at a frequency of 1 kHz. The Guidance and Controller threads receive position and velocity signals from the Haptic ServoLoop and send force and torque signals to the Haptic Rendering thread. While the Server thread receives all incoming data from the remote station, the Client thread returns position and velocity signals. Both threads use UDP sockets with either IPv4 or IPv6. The right side of Fig. 3 depicts the threads and the flow of information between them.

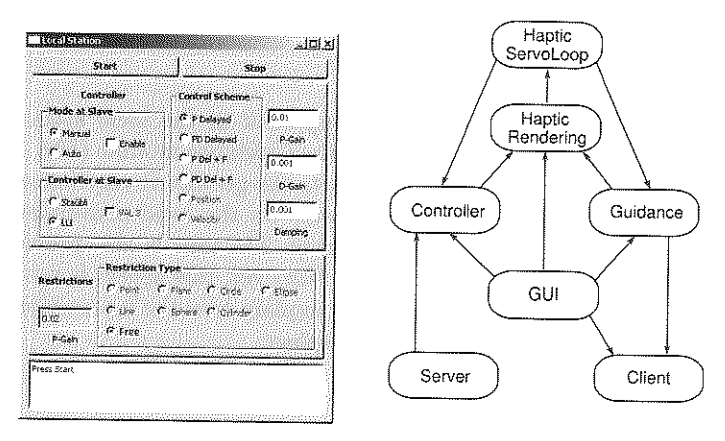


Fig. 3. Graphic User Interface (GUI) and program threads at local station

3 Remote Station

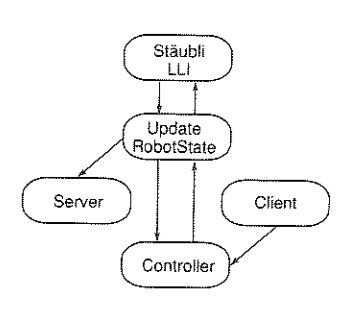


Fig. 4. Program threads on the remote station

The physical system on the remote station consists of a TX-90TM Stäubli robot and a CS8-CTM Stäubli controller, four cameras with actuated pan, tilt and zoom, and a high speed switch connected to Internet and Internet2. Fig. 2 shows these physical components. The software program runs under Wind River's VxWorksTM, a Real-Time Operating System (RTOS). The programs are compiled with the cross platform TornadoTM environment and are written in C++. Fig. 4 depicts the threads running on the RTOS.

The $St\ddot{a}ubli\ LLI$ is a thread that runs the Low Level Interface library provided by St\ddot{a}ubli, and runs at 250 Hz. In each interrup-

tion it updates all state variables, that is, position, velocity and motor torques. The $Update\ RobotState$ thread contains a zero order hold for the state variables, and all the information needed for the Controller, Client and Server threads. The Client and Server threads are UDP sockets. Semaphores and Mutex locks are used to synchronize the program threads. As in the local station, the Controller thread can use different control laws that provide the torques τ_r to be applied to the joints of the remote manipulator (Table 1). The clocks of both sites are synchronized each time the program starts using a Network Time Protocol (NTP) Server.

The LLI library provided by Stäubli allows direct access to motor torques on the remote manipulator, but unfortunately it is a black–box, thus limiting manipulation capabilities on the Controller thread. Moreover, VxWorksTM, al-

though suitable for real-time control, makes difficult to implement new software. One approach to overcome these difficulties consists on wrapping the LLI and the VxWorksTM on a higher-level layer and connect it to an external PC with an open operating system through a deterministic dedicated communication channel. Thus, Controller, Client, Server and other possible threads could be implemented with less difficulties. This approach can open new horizons for the presented framework, ranging from cooperative control to multi-arm teleoperation.

Controlling the Teleoperator

The statements about the control schemes in this Section are presented without proof. The interested reader can find them in [7,8].

In the following, $\mathbb R$ stands for the real number set, $\mathbb R^+$ for the positive real number set, \mathbb{R}^+_0 for the set containing \mathbb{R}^+ and zero, $|\cdot|$ for the Euclidean norm and $\|\cdot\|_{\infty}$ for the \mathcal{L}_{∞} norm.

Table 1. Control Laws for the local and remote robot manipulators. Where $\{K_i, B_i, K_d, K_{di}, K\} \in \mathbb{R}^+$ are the control gains

Type	Control Laws
	$\begin{vmatrix} \tau_l = K_l[\mathbf{q}_r(t - T_r(t)) - \mathbf{q}_l] - B_l\dot{\mathbf{q}}_l \\ \tau_r = K_r[\mathbf{q}_r - \mathbf{q}_l(t - T_l(t))] + B_r\dot{\mathbf{q}}_r \end{vmatrix}$
PD	$\begin{vmatrix} \boldsymbol{\tau}_l = K_d[\gamma_r \dot{\mathbf{q}}_r(t - T_r(t)) - \dot{\mathbf{q}}_l] + K_l[\mathbf{q}_r(t - T_r(t)) - \mathbf{q}_l] - B_l \dot{\mathbf{q}}_l \\ \boldsymbol{\tau}_r = K_d[\dot{\mathbf{q}}_r - \gamma_l \dot{\mathbf{q}}_l(t - T_l(t))] + K_r[\mathbf{q}_r - \mathbf{q}_l(t - T_l(t))] + B_r \dot{\mathbf{q}}_r \end{vmatrix}$
Scattbased	$\begin{aligned} \boldsymbol{\tau}_{l} &= \boldsymbol{\tau}_{ld} + K[\mathbf{q}_{r}(t - T_{r}(t)) - \mathbf{q}_{l}] - B_{l}\dot{\mathbf{q}}_{l}; & \boldsymbol{\tau}_{ld} &= -K_{dl}[\dot{\mathbf{q}}_{l} - \dot{\mathbf{q}}_{ld}] \\ \boldsymbol{\tau}_{r} &= \boldsymbol{\tau}_{rd} + K[\mathbf{q}_{r} - \mathbf{q}_{l}(t - T_{l}(t))] + B_{r}\dot{\mathbf{q}}_{r}; & \boldsymbol{\tau}_{rd} &= K_{dr}[\dot{\mathbf{q}}_{r} - \dot{\mathbf{q}}_{rd}] \end{aligned}$

Mathematical Model 4.1

The local and remote manipulators together with the human and environment interactions, that conform the teleoperator, are modeled as a pair of n-DOF serial links with revolute joints. Their corresponding nonlinear dynamics are

$$\begin{aligned} \mathbf{M}_{l}(\mathbf{q}_{l})\ddot{\mathbf{q}}_{l} + \mathbf{C}_{l}(\mathbf{q}_{l},\dot{\mathbf{q}}_{l})\dot{\mathbf{q}}_{l} + \mathbf{g}_{l}(\mathbf{q}_{l}) &= \boldsymbol{\tau}_{l}^{*} - \boldsymbol{\tau}_{h} \\ \mathbf{M}_{r}(\mathbf{q}_{r})\ddot{\mathbf{q}}_{r} + \mathbf{C}_{r}(\mathbf{q}_{r},\dot{\mathbf{q}}_{r})\dot{\mathbf{q}}_{r} + \mathbf{g}_{r}(\mathbf{q}_{r}) &= \boldsymbol{\tau}_{e} - \boldsymbol{\tau}_{r}^{*}, \end{aligned} \tag{1}$$

where: $\ddot{\mathbf{q}}_i, \dot{\mathbf{q}}_i, \mathbf{q}_i \in \mathbb{R}^n$ are the joint acceleration, velocity and position; $\mathbf{M}_i(\mathbf{q}_i) \in$ $\mathbb{R}^{n \times n}$ the inertia matrices; $\mathbf{C}_i(\mathbf{q}_i, \dot{\mathbf{q}}_i) \in \mathbb{R}^{n \times n}$ the Coriolis and centrifugal effects; $\mathbf{g}_i(\mathbf{q}_i) \in \mathbb{R}^n$ the gravitational forces; $\boldsymbol{\tau}_i^* \in \mathbb{R}^n$ the controllers; and $\boldsymbol{\tau}_h \in \mathbb{R}^n$, $\boldsymbol{\tau}_e \in \mathbb{R}^n$ the forces exerted by the human and the environment. The subscript i stands for both l and r, local and remote manipulators, respectively.

4.2 Control Schemes

There are three control schemes that can be used in this framework: P, PD and Scattering-based, which are summarized in Table 1. These schemes have been developed in the context of this framework.

Using standard Lyapunov arguments it can be shown that using P or PD controllers with the teleoperator dynamics (1), the closed-loop positions and velocities are bounded. *i.e.*, $\{\dot{\mathbf{q}}_i, \mathbf{q}_i - \mathbf{q}_r\} \in \mathcal{L}_{\infty}$, if the gains are set according to

$$4B_l B_r > [*T_l^2 + *T_r^2] K_l K_r, \tag{2}$$

under the assumptions that

a) the human operator and the environment define passive maps. i.e., $\exists \kappa_i \in \mathbb{R}_0^+$ s.t. $\forall t \geq 0$,

 $\int_{0}^{t} \dot{\mathbf{q}}_{l}^{\top} \boldsymbol{\tau}_{h} d\sigma \geq -\kappa_{l}, \quad -\int_{0}^{\tilde{\tau}} \dot{\mathbf{q}}_{r}^{\top} \boldsymbol{\tau}_{e} d\sigma \geq -\kappa_{r}; \tag{3}$

- b) the gravitational forces are pre-compensated by the controllers τ_i^* . That is $\tau_l^* = \tau_l + \mathbf{g}_l(\mathbf{q}_l)$ and $\tau_r^* = \tau_r \mathbf{g}_r(\mathbf{q}_r)$;
- c) the variable time-delay has a known upper bound T_i . i.e. $T_i(t) \leq T_i < \infty$, and its time derivative does not grow or decrease faster than time itself, thus, $|T_i(t)| \leq 1$.

Moreover, if the human does not move the local manipulator and the remote manipulator does not touch anything (i.e. $\tau_h = \tau_e = 0$), then the teleoperator's velocities asymptotically converge to zero and position tracking is achieved:

$$|\dot{\mathbf{q}}_i| \to 0 \quad |\mathbf{q}_l - \mathbf{q}_r(t - T_r(t))| \to 0 \quad t \to \infty.$$

If the P or PD controller is replaced by the scattering-based one, with gains satisfying (2), then boundedness of position error and velocities together with position tracking can be also established for variable time-delays. For this case the desired velocities are encoded using the classic scattering transformation given by

$$\mathbf{u}_{l} = \frac{1}{\sqrt{2b}} [\boldsymbol{\tau}_{ld} - b\dot{\mathbf{q}}_{ld}] \quad \mathbf{u}_{r} = \frac{1}{\sqrt{2b}} [\boldsymbol{\tau}_{rd} - b\dot{\mathbf{q}}_{rd}]$$

$$\mathbf{v}_{l} = \frac{1}{\sqrt{2b}} [\boldsymbol{\tau}_{ld} + b\dot{\mathbf{q}}_{ld}] \quad \mathbf{v}_{r} = \frac{1}{\sqrt{2b}} [\boldsymbol{\tau}_{rd} + b\dot{\mathbf{q}}_{rd}]$$
(4)

where b is the virtual impedance of the communications, $\gamma_i^2 = 1 - \dot{T}_i(t)$ and $\mathbf{u}_r = \gamma_l \mathbf{u}_l(t - T_l(t)), \ \mathbf{v}_l = \gamma_r \mathbf{v}_r(t - T_r(t)).$

Note that the key feature for the stability of the teleoperator is condition (2), it clearly states that if time-delay increases then damping injection has to be increased in order to maintain stability and position tracking. This condition may seem somewhat restrictive, however, on-earth time-delays are in the order of magnitude of hundreds of milliseconds, thus over-damped behaviors can be avoided.

Besides the use of robust controllers, the framework enhances its capabilities with the employment of geometric guidance and the QoS of Internet2.

5.1 Geometric Guidance

Teleoperated tasks can often be decomposed into a sequence of simple movements that do not require using the six DOF an object has in free space. For example, the insertion of a cylindrical peg in a hole only requires two DOFs, translations and rotations around the hole's axis, provided that the axis of the two objects are aligned. Haptic feedback can be used to assist the operator by restricting his/her movements to a region of interest, lowering the mental burden needed to execute the task [11, 12]. Geometric restrictions can be explicitly created by means of the user interface shown in Fig. 3, or with the aid of a geometric constraint solver like PMF [13, 14], in order to define a submanifold of allowed movements.

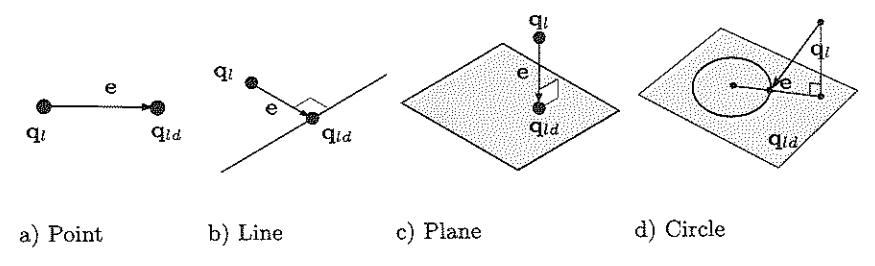


Fig. 5. Geometric restrictions

Guidance forces are generated in the constrained directions based on the difference (e) between the actual (\mathbf{q}_l) and desired (\mathbf{q}_{ld}) positions of the end-effector, where \mathbf{q}_{ld} is computed as the projection of \mathbf{q}_l on the restriction submanifold. Currently, the position of the haptic end-effector can be translationally restricted to points, lines, planes, spheres, cylinders, and ellipses. Fig. 5 shows four examples of geometric restrictions.

Depending on the task, two different reference motion commands for the remote manipulator can be used. One of these is given by \mathbf{q}_{ld} and then the remote manipulator movements are strictly along the restriction submanifold. The other option is to use \mathbf{q}_l as commands, in this case, the remote manipulator reproduces the operator's movements, which are locally constrained by the haptic device to the restriction submanifold. Both operation modes are possible and switching between them can be done online.

5.2 Internet and Internet2 Communications

The UDP sockets on the local and remote stations are implemented using either the version 4 or 6 of the Internet Protocol. The 'classic' Internet runs over IPv4,

while the Internet2 uses both IPv4 and IPv6. Amongst the several differences that exist between the two, the most relevant from a teleoperation point of view are:

- IPv4 has 2^{32} assignable addresses while IPv6 has 2^{128} [15, 16].
- IPv6 incorporates the Quality of Service (QoS) paradigm, in which packets can be sent using different priorities. Its predecessor, IPv4 did not have it, and in its place other protocols, namely RSVP, had to be used [17].

Internet is far from being a deterministic communication channel. However, by using the QoS paradigm, priorities can be imposed on control packages, thus providing more reliable communications by lowering the probability of instability caused by highly time-varying communications.

6 Experimental Validation

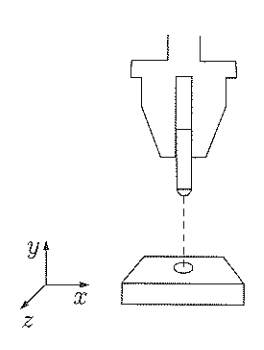


Fig. 6. Peg-in-hole scheme

In order to provide experimental evidence of the presented framework, several teleoperated tasks have been designed. One of these is a peg-in-hole task that has been remotely performed using the proposed architecture. The peg-in-hole insertion has the following characteristics:

- Motion of the peg is restricted to the hole's centerline, providing a natural guide towards the task goal.
- The input to the remote manipulator controller are positions of the human operator, namely \mathbf{q}_l .
- Packets have been transmitted using UDP/IPv6 sockets.

For the experiments, the P controller was used with control gains set such that (2) holds. The gains are: for the local manipulator, $K_l = 20$ and $B_l = 5$, and for the remote manipulator $K_r = 750$ and $B_r = 200$. The experiments have been performed using only 3 DOF of each manipulator. Fig. 7 plots the time evolution of positions along the x, y, and z directions of the remote manipulator end-effector. The force plots show the components of the two forces acting on the haptic device: the restriction force \mathbf{f}_r , and the force provided by the controller \mathbf{f}_l . The insertion direction is along the y axis. From 0s to 1.5s no restriction has been set and the manipulator moves freely in space, thus $\mathbf{f}_r = \mathbf{0}$. Once the restriction is set, at 1.5s, the corresponding restriction forces appear on the x and z directions. No restriction force is exerted in the y axis since it corresponds to the unconstrained direction. The position plot in the y direction shows the approach and insertion processes, that take place until the 9s time mark, and from that moment on, the peg is removed from the hole.



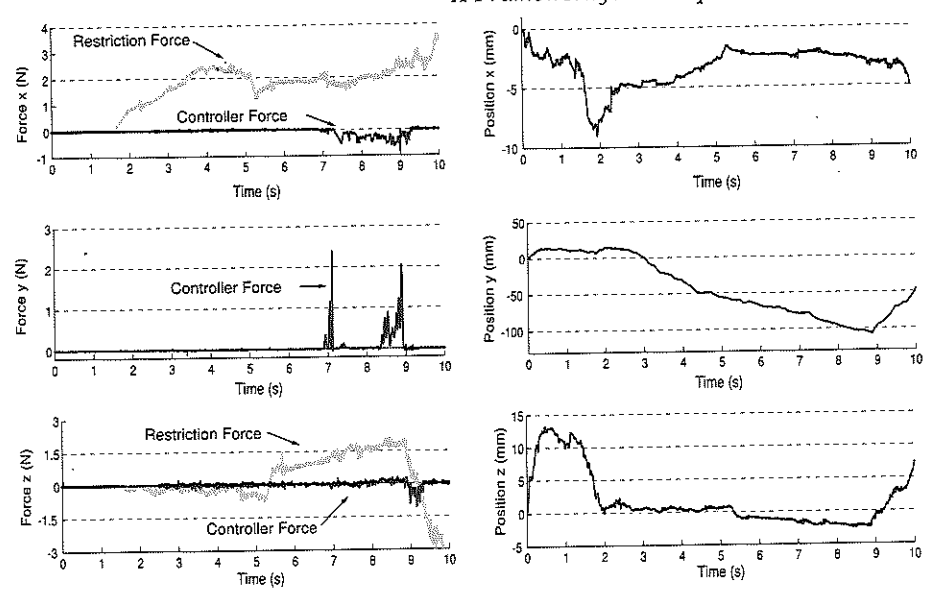


Fig. 7. Force and position in the x, y, z directions

7 Conclusions

This work has presented a framework for teleoperators control. The human operator can decide which controller to use in the local and remote manipulators, he can easily set and remove geometric motion restrictions such as points, lines, planes, spheres, cylinders, and ellipses. The framework makes use of robust controllers that provide position tracking despite variable time-delays. Thus, they allow to use the Internet as communication channel. The framework also gives the option to use the Internet2, with the IPv6 protocol, hence providing QoS over network traffic. Real experiments have demonstrated the effectiveness of the proposed framework. Future research include the study of an active human interaction.

Acknowledgement. The authors would like to thank the members of the robotics division of the IOC for their valuable help in this work. This work has been partially supported by the Spanish CICYT projects: DPI2005-00112 and DPI2007-63665, the FPI program with reference BES-2006-13393, and also by the Mexican CONACyT grant-169003.

References

1. Anderson, R.J., Spong, M.W.: Bilateral control of teleoperators with time delay. IEEE Transactions on Automatic Control, 34(5):494-501, May (1989)

- Niemeyer, G., Slotine, J.J. E.: Stable adaptive teleoperation. IEEE Journal of Oceanic Engineering, 16(1):152–162, Jan. (1991)
- 3. Chopra, N., Spong, M.W., Hirche, S., Buss, M.: Bilateral teleoperation over the internet: the time varying delay problem. In: Proc. American Control Conference, 1(4):155 160, June (2003)
- 4. Lozano, R., Chopra, N., Spong, M.W.: Passivation of force reflecting bilateral teleoperators with time varying delay. In: Proc. Mechatronics, June (2002)
- Hirche, S., Buss, M.: Packet loss effects in passive telepresence systems. In: Proc. IEEE Conference on Decision and Control, pp.4010-4015, Dec. (2004)
- Munir, S., Book, W.J.: Control techniques and programming issues for time delayed internet based teleoperation. Journal of Dynamic Systems, Measurement and Control, 125(2):205-214, June (2004)
- Nuño, E., Ortega, R., Barabanov, N., Basañez, L.: A globally stable PD controller for bilateral teleoperators. IEEE Transactions on Robotics (in Press), Feb. (2008)
- 8. Nuño, E., Basañez, L., Ortega, R., Spong, M.W.: On position tracking for nonlinear teleoperators with variable time-delay. Int. Journal of Robotics Research (Submitted), Nov. (2007)
- Arcara, P., Melchiorri, C.: Control schemes for teleoperation with time delay: A comparative study. Robotics and Autonomous Systems, 38(1):49-64, Jan. (2002)
- Hokayem, P.F., Spong, M.W.: Bilateral teleoperation: An historical survey. Automatica, 42:2035–2057 (2006)
- Nuño, E., Basañez, L., Ortega, R.: Passive bilateral teleoperation framework for assisted robotic tasks. In: Proc. IEEE Conference on Robotics and Automation, pp.1645-1650, April (2007)
- Nuño, E., Rodríguez, A., Basañez L.: Force Reflecting Teleoperation via IPv6 Protocol with Geometric Constraints Haptic Guidance. In: Advances in Telerobotics, Chapter 26. STAR series. pp.445-458. Springer-Verlag. (2007)
- Rodríguez, A., Basañez, L., Celaya, E.: Robot Task Specification and Execution Through Relational Positioning. IFAC Workshop on Intelligent Manufacturing Systems, May 23-25, (2007)
- Rodríguez, A., Basañez, L., Celaya, E.: A Relational Positioning Methodology for Robot Task Specification and Execution. IEEE Transactions on Robototics (Conditionally accepted), Feb. (2008)
- 15. Waddington, D.G., Chang, F.: Realizing the Transition to IPv6. IEEE Communications Magazine, 40(6):138-147, June (2002)
- Geer, D.: In brief: IPv6 and distributed applications. IEEE Distributed Systems Online, 6(12):1–4 Dec. (2005)
- 17. Lee, D.C., Lough, D.L., Midkiff, S.F., Davis, N.J., Benchoff, P.E.: The next generation of the Internet: aspects of the IPv6. IEEE Network, 12(1):28-33, Feb. (1998)

Using Reinforcement Learning in Chess Engines

Marco Block, Maro Bader, Ernesto Tapia, Marte Ramírez, Ketill Gunnarsson, Erik Cuevas², Daniel Zaldivar², and Raúl Rojas

Free University of Berlin, Institut of Computer Science
 Takustr. 9, 14195 Berlin, Germany
 [block, bader, tapia, marte, ketill, rojas]@inf.fu-berlin.de
 Universidad de Guadalajara, Depto. Electrónica y Computación
 Av. Revolución 1500, 44430 Guadalajara, Jalisco, México
 [erik.cuevas, daniel.zaldivar]@cucei.udg.mx

(Paper received on February 29, 2008, accepted on April 15, 2008)

Abstract. Up until recently, the use of reinforcement learning (RL) in chess programming has been problematic and failed to yield the expected results. The breakthrough was finally achieved through Gerald's Tesauros work on backgammon, which resulted in a program that could beat the world champion of backgammon in the majority of the matches they played. Our chess engine proved that reinforcement learning in combination with the classification of board state leads to a notable improvement, when compared with other engines that only use reinforcement learning, such as KnightCap. We extended KnightCap's learning algorithm by using a bigger and more complete board state database, and adjusting and optimizing the coefficients for each position class individually. A clear enhancement of our engine's learning and playing skills is reached after only a few trained games.

1 Introduction

The complexity of chess makes it impossible for computers to explore every possible move throughout the whole space of possible variants and pick the best one. Most chess engines therefore focus on a brute force strategy to search in the space of the next possible moves up to a certain depth only. Many pruning-processes are used, as well as linear position evaluation which incorporates knowledge based approaches in order to evaluate a special position. However, the main problem still lies in the correct tuning of the coefficients used in these functions. The method presented in this paper optimizes the evaluation functions and its coefficients by automating the use of temporal differences [2,3] and thereby increasing it's own understanding of chess after each game.

1.1 Related Work

Temporal difference was first tested in the program SAL by Michael Gherrity [5]. The structure of SAL allows the realisation of a move generation for different games and the determination of the best next move using a search-tree based algorithm. SAL learns good and bad moves from the played games. The evaluation

© E. V. Cuevas, M. A. Perez, D. Zaldivar, H. Sossa, R. Rojas (Eds.)
Special Issue in Electronics and Biomedical Informatics,
Computer Science and Informatics
Research in Computing Science 35, 2008, pp. 31-40



of individual moves is performed using an artificial neuronal network. TD was used for the optimization of the networks parameters by comparing the evaluation values for the root nodes of the search tree. In a test against the prominent chess program GNUChess [18], where SAL was using 1031 position evaluation factors, 8 remis could be achieved in 4200 games (while the rest was lost).

The chess program NeuroChess, developed by Sebastian Thrun, also uses a neuronal network as position evaluation and a TD-method based on the root nodes to modify the coefficients. In contrast to SAL, NeuroChess only learns from itself. Games from a grand master database have mostly been used as entry points of the learning process (90%), while only 10% of the training games where played from the initial positioning. Later experiments with other programs showed that a learning strategy based on playing against oneself, does not yield satisfying results. In an experiment against GNUChess, where both programs where calculating a move depth of 2 and using the same evaluation, 316 out of 2400 games could be won by NeuroChess and the learned coefficients. Thrun, the main developer of NeuroChess admitted two fundamental problems of his approach: the large training time and the incompleteness of the evaluation coefficients. Thrun concludes that it is unclear whether TD-based solutions will ever find usage in chess programming.

Tesauro describes a better application of TD for the adjustment of the evaluation coefficients [8]. By using the open source chess program SCP he demonstrate that TD with a search depth of 1 will never yield good results. SCP works with an alpha-beta-algorithm with fixed search depth and the evaluation of 165 factors. The clear separation of the search and the evaluation procedure in SCP allows a stronger focus on the learning of evaluation factors by keeping a fixed search solution. A version of this algorithm has also been used at Deep Blue [12] to improve the king security in the game (1).

Tridgell implemented the chess program KnightCap [9,10], which has a parallel nature. The main idea was not to work on the root nodes, but rather applying the learning procedure on the best forced move-path of the search-tree. Small changes had to be made, e.g. storing all evaluation factors in a vector. Even the first experiment was a major success: in only three days and 308 games played on the Internet Chess Server(ICC) the rating of KnightCap increased from 1650 to 2150. The usage of ToPiecesBoard as an internal board representation allows an evaluation that can quickly identify complex patterns. The move selection algorithm MTD(f) [11] was chosen. A naive classification of the game situation into four different categories was made by the evaluation function: opening, midgame, endgame and mate positions. For each position class 1468 different evaluation factors were defined, so that KnightCap could evaluate a total of 5872 different coefficients. The version using a opening book reaches an ELO rating around 2400-2500 and beats international masters (2400-2600) ELO points on a regular basis.

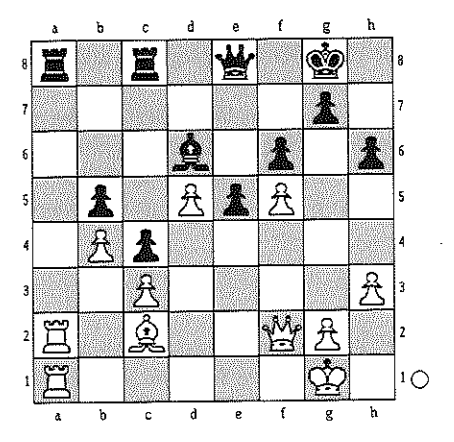


Fig. 1. Deep Blue versus Garry Kasparov, game 2 in 1997. At this position Deep Blue, using the normal coefficients, would have played the typical computer move Qb6 in order to win a pawn. Kasparov and the viewers were quit surprised by Deep Blues move Be4. This positionally strong move almost chokes every counter play and makes the threatening move Qb6 now even stronger. Kasparov eventually lost this game.

Reinforcement Learning and Temporal Difference 2

In this section we introduce a reinforcement learning method known as Temporal Difference (TD) and the learning algorithm $TD(\lambda)$. This methodology was first introduced by Samuel in 1959 [13], but our discussion adopts notation and concepts first introduced by Sutton in 1988 [14]. Even though we explain the learning algorithm in the context of chess, it can easily be regarded as a general discussion about the methodology.

Let us denote with S the set of all possible states (chess positions) and with $x_t \in S$ the state at time t. The index t also means that x_t was obtained after t played "actions". For simplicity, we also assume that each game has a fix length of N moves. Each state x_t defines a set A_{x_t} of possible actions (legal moves). An agent selects one action $a \in A_{x_t}$ that produces a new state x_{t+1} from x_t to x_{t+1} with probability $p(x_t, x_{t+1}, a)$. The next state x_{t+1} denotes the position when both own and opponent moves have been performed. Hence only these positions will be examined, at which the agent can perform an action.

The agent will receive after each finished game a reward for the final move $r(x_N)$, which in chess takes the values 0 for remis, 1 for victory and -1 for a defeat. The expected value of the reward with an ideal evaluation function $J^*(x)$ is $J^* := E_{x_N|x} r(x_N)$. The main goal of the learning process is to approximate the unknown and (probably non-linear) evaluation function with a linear function $J': S \times \mathbb{R}^k \to \mathbb{R}$:

$$J'(x,\omega) = \sum_{i=1}^{k} \omega_i J_i(x),$$

where $\omega = (\omega_1, ..., \omega_k)^T$ is the parameter vector. This assumption reduces the problem to find ω the for the corresponding $J'(\cdot, \omega)$ that best approximates the function $J^*(\cdot)$.

The learning algorithm $\mathrm{TD}(\lambda)$ consist of an iterative update of the coefficients ω . Each iteration consist of playing a complete game with a fixed parameter ω to obtain a state sequence x_1,\ldots,x_N . Thus, the $\mathrm{TD}(\lambda)$ -algorithm computes the temporal difference d_t between the evaluations of consecutive positions x_t and x_{t+1} in the game:

$$d_t := J'(x_{t+1}, \omega) - J'(x_t, \omega)$$

Since the function $J'(x_N,\omega)$ for the last state x_N can be set to $r(x_N)$, we can compute the temporal difference for the predecessor state using $d_{N-1} = r(x_N) - J'(x_{N-1},\omega)$. It is expected for any ideal evaluation function that if the evaluation of the state x_t at any time t is positive, then the outcome of the complete game will also be positive (that is, a victory). If the temporal difference is positive, then the actions of the agent improved. Since the player and the opponent played during the transition from x_t to x_{t+1} , it is possible that the opponent made an error. Therefore positive temporal differences are not taken into account, because they can degrade the approximation. Playing errors of opponent are not forced and should not be learned. If the temporal difference was negative, then the state x_t was not correctly evaluated. This evaluation needs to be degraded, since the chosen move turned out to be worse than expected. We therefore search the smallest change to the set of parameters holding the biggest effect towards this goal. The direction of the correction is obtained by computing the gradient $\nabla J'(\cdot,\omega)$. The strength of the correction Δt is defined as:

$$\Delta t := \sum_{j=t}^{N-1} \lambda^{j-t} d_j$$

The update of ω is performed is

$$\omega := \omega + \alpha \sum_{t=1}^{N-1} \nabla J'(x_t, \omega) \left[\sum_{j=t}^{N-1} \lambda^{j-t} d_j \right].$$

The value Δt is the weighted sum of the differences in the rest of the game. A value $\Delta t > 0$ means that the position x_t was probably undervalued. Therefore a positive multiplier of the gradient is added to the vector ω , which will result in a better evaluation with the updated parameters. If $\Delta t < 0$ holds, then the position x_t was overestimated and therefore w will be updated with a negative multiplier of the gradient. The positive parameter α is the learning rate and will slowly converge stepwise after each learned game to 0. The parameter λ controls the contribution of the temporal difference from a position x_t until the end of a game. With $\lambda = 0$ no succeeding positions will be taken into account, and with $\lambda = 1$ the complete state sequence influences the learning update. It has been shown that $\lambda = 0.7$ gives the most satisfying results [10].

In 1995 Tesauro published an article on the use of TD in his backgammon program. His solution trained the coefficients of the very complex evaluation function with the $\mathrm{TD}(\lambda)$ -algorithm. The performance of the program was astonishing. In its first appearance at the backgammon world championship in 1992 a version participated that had been trained with 800.000 games. From a total of 38 tournaments encounters, only seven were lost. The succeeding version which had been trained with 1.5 million games, lost only one of 40 games against one of the world strongest players, Bill Robertie.

Combining the Min-Max-Algorithm with Temporal Differences 2.1

Even though some learning approaches have successfully been applied to backgammon, they can not be applied to chess directly. There are fundamental differences between the two games. For example, small changes in the position of a backgammon game will result in only small changes of position evaluation. This represents a big difference in chess, where the main focus of the search lies in the chosen future tactic. More computational effort should therefore be spent in order to quickly analyze the search tree and make a prediction about the probable course of the game. Thus, a fast evaluation of the position is required, which makes the application of neuronal networks inadvisable.

A neuronal network seems suitable to correctly classify and cluster a current position into position types. Unfortunately, a small change in the position can result in a strong difference of the evaluation. This becomes obvious in chess programming, where two position differing in only one figures location, may need to be evaluated totally different. Hence a combination of forward computation in a search tree and the usage of a temporal difference algorithm $TD(\lambda)$ seems to be logical solution.

The strategy used in the backgammon engine consists on the selection of the action a out of a position x, which minimizes the chances of the opponent to increase its evaluation:

$$a(x) := \arg\min_{a \in A_x} J'(x'_a, \omega),$$

where x_a denotes the position reached after the action α has been performed on x. Since the approach only to look forward a single move is not yet satisfying in chess, some modifications had to be made, in order to use a search procedure taking into note all future possible game situation until a specific depth. It seems reasonable that modified algorithm TD-Leaf(λ) will work on the best forced leaf nodes of the search tree rather then just working on the root node like $TD(\lambda)$.

Let $J_d'(x,\omega)$ denote the evaluation value of the position x, when forward looking d steps starting at x. The modified temporal algorithm is now using a new temporal difference definition:

$$d_t := J_d'(x_{t+1}, \omega) - J_d'(x_t, \omega)$$

and a new the update step for ω

$$\omega := \omega + \alpha \sum_{t=1}^{N-1} \nabla J_d'(x_t,\omega) \left[\sum_{j=t}^{N-1} \lambda^{j-t} d_j \right]$$

In an experiment made by KnightCap, all evaluation coefficients but the material values (pawn 1, bishop and knight 4, rook 6, queen 12) were set to 0. Playing on the Internet chess server FICS the initial elo rating of 1650 of the program was computed in 25 non learning played games using this coefficient vector. In the fallowing three days and 308 played games with the usage of TD the rating could be raised to 2150.

3 State Classification

During a typical opening phase the figures bishops and knights should advance, the king castle, and the pawns assume control of the center. The midgame is most difficult to learn, since it can contain many different advantageous patterns such as the opening of lines, defense of open line with rooks, and attack possibilities on the opponent king. In other words, many typical constellations and short term goals are possible. In the endgame the king becomes a more important and active figure. It holds the opponent away from his own pawns, which are crucial due to their ability to transform into higher figures by reaching the endline. Most beginners are thought to correctly differentiate between these three position types, in order to avoid bringing the queen or king too early into the game. With further experience and game practice one quickly learns further criteria to distinguish between more position types in order to improve one's game evaluation. For example, opposing castle direction (large castle vs small castle) are most often followed by a tactical attack, which should result in a different evaluation of the position. Closed positions require a more strategical and long termed based plan. In chess programming these observations are often not taken into account. Chess-specific knowledge is not reflected enough in the implementation of a evaluation function. A main goal of the FUSc# development was to include the Plan im Schach (the chess plan) and give the chess engine the ability to search for its decision according to the current position type. Smaller, short termed plans exist, such as the exchange of a strong opponent bishop, the control of key fields, strong figure patterns and long termed plans such as a coordinated attack on the king side wind.

3.1 Chess Programming: Opening, Middle Game and End Game

Only a few open-source chess programs can be found that differ between position types beyond opening, mid, and end-game. A popular approach is to stress the importance of king security in the opening phase and evaluate it highly, while assigning a poor evaluation to the use of the center fields as target fields. This is done in order to prevent the king from going forward and instead bring him to safety on one side to allow the mid-game to start. In the endgame however, the king is a key figure which should be brought to the center fields. The same

applies to the other figures. In the beginning development is important, and in the mid-game the control of the center and attacks on the opponent king.

In contrast, a method using TD-Leaf(λ) to optimize coefficients, succeeded in maintaining each position type represented in one game. On the other hand, shortcomings include the fact that on average the mid-game is over-represented, which results in very well learned mid-game coefficients, but others, like the endgame coefficients get left out.

The planed future approach of FUSc# is to use a grandmaster database to classify position types with the use of few important position properties, and evaluate these position types with their own coefficients. It is not possible to use TD-Leaf(λ)to achieve this, since some position types occur more often than others. This would mean, that for example, after 1000 games the position type x was optimized 400 times, but the position type y only 5 times.

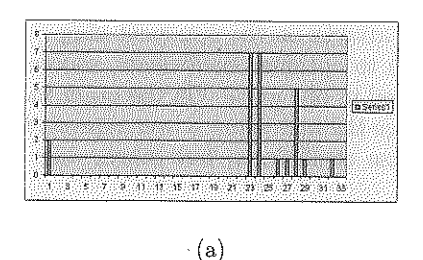
Classification Types of the Chess Engine FUSc#

FUSc# extends the basis set of position classes with the 32 combinations of these boolean rules: both queens on the board (yes/no), kings position (left, middle, right). Additionally a position vector for the endgame is added, which applies when no more queen is on the board and the sum of bishops, knights, and rooks is smaller then six or this sum is smaller then 3, when queens are still on the board.

Only a few basic operations are required to decide which evaluation vector is chosen for its detected position type. For each of the 33 position types a respective vector containing 1706 coefficients is stored, to a total of 56298 adaptable position criteria. KnightCap used 4 different position classes throughout the training phase which each had1468 position criteria, differentiating 5872 coefficients.

TD-Leaf with Complex Evaluation

When using a very complex evaluation function, based on the differentiation of various position classes and therefore differentiating the evaluation coefficients of each class, a global learning rate α for the TD learning method would falsify the learning process. This is due to the fact, that the distribution of the position classes may not be normal and hence some classes will learn stronger than others, depending on their detection frequency in the best move search routine. Like many other chess programs, KnightCap only used three different position classes, so that the learning difference between these classes grew negligibly small, since most trained games had positions in each position class. The chess engine FUSc# deals with a wider set of position classes, so that it is likely to happen, that some classes will be detected significantly less often then others. A local learning rate solves this problem: for each position coefficient vector $s_1, s_2, ..., s_k$ a local learning rate $\alpha_1, \alpha_2, \dots \alpha_k$ is defined, that is individually adjusted depending on its detection accuracy.



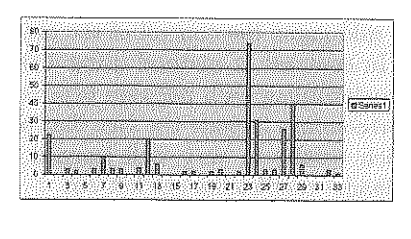


Fig. 2. Distribution of the position classes. (a) The learning rate of the 33 position types after 7 played games. Initially the learning rate was set to 1.0. After each learning step the rate was decreased for each detected position type. The classes 23 and 24 have detected most often. (b) The distribution of the 33 position types detected in the 72 learned games. Position class 23 represents the opening phase.

The update function for the coefficient vector ω , containing all 56298 values of all partial position vectors $\omega_1, \omega_2, ..., \omega_{33}$ has to be adapted, so that the $\alpha_1, \alpha_2, ..., \alpha_{33}$ local learning rates are assigned to the position vectors:

$$\omega_k := \omega_k + \alpha_k \sum_{t=1}^{N-1} \nabla J_d'(x_t, \omega_k) \left[\sum_{j=t}^{N-1} \lambda^{j-t} d_j \right],$$

where k=1,2,...,33 denotes the position class to the employed position x_t . The difference to TD-Lear(λ)-algorithm used by KnightCap therefore lies in the usage of the data gained during a game and by the independent optimization of each position class detected in a trained game. Further improvements can be achieved by using information gathered during a game, for example the main variant and its computed position class values, and to use them in the learning process.

5 Conclusion and Experimental Results

To determine FUSc#'s performance, it was tested on human players in 50 games with different time settings (1-5 minutes time consideration). The evaluation on the chess server resulted in a strength around 1800 ± 50 . A manually created vector was assigned to each position type. FUSc# thus did not. The initial values for the learning rates $\alpha_1, \alpha_2, ..., \alpha_{33}$ were 1.0 and λ set to 0.7. After a few games a small increase in performance was observable, since FUSc# was making first adaptions to the evaluation of the figure position and their effects on the game. One problem was that some position classes were not detected at all and therefore could not be learned, while others were found and learned regularly. The distribution of the 33 position classes after 7 played games is shown in Fig. 2.

At the end of the experiment FUSc# had played 119 games and increased its performance from 1800 to 2016 (see 3). The position classes 23 and 24 were found most often. The position type 23 represents an opening position, with both kings on their ground lines. Position type 24 is detected when the black player

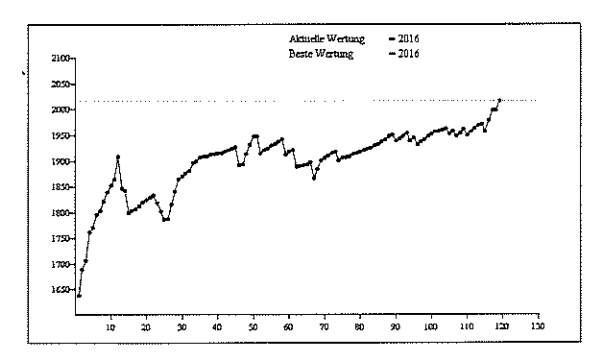


Fig. 3. Evaluation in the chess server after 119 games.

has made a short castle, 28 means that both players have made a short castle. From the 119 played games 72 have been used to adapt the coefficients and learn from the outcome of the game. The distribution of all detected position types is shown in Fig. 2b.

Improved performance was notably after playing only few games. It is crucial that all position types receive enough information for a correct adjustment of the coefficients. We estimate that FUSc# requires more then 50000 training games to correctly adapt all 56000 of the 33 position types and correctly learn them. This has not been verified yet. Looking at the results, it is clear that the optimization of the manually set values (all class types were set to the same initial values) increased the game quality remarkable. After 72 trained games the elo rating raised up to more then 2000. A main factor here was the king's security, which was correctly learned by FUSc#, activating the king in some of the position types and bringing him to the center of the board.

The successful usage of TD-Leaf(λ) in the chess engine KnighCap could be confirmed with FUSc#. Since the evaluation function of FUSc# takes into account many more position types, it needs a much greater sum of games to train with in order to achieve results comparable to KnightCap. Not even human players can become grand masters over night. It remains difficult to compare the learning progress of both programs, since KnightCap calculates its moves deeper then FUSc# and therefore has more success in finding tactical moves. Often, FUSc# appeared to be in a superior position and could have developed its strategy pretty good, but oversaw tactical implications and for this reason lost the respective games. To extend the automatization of the learning process the UCI-protocol needs to be changed. The chess engine should e.g. be informed about the outcome of a game and be allowed to perform a thinking phase, where learning parameters can be updated and allowing for learning to take place. Tests on the chess servers showed that the choice of the 33 different position types was a little unfortunate. e.g no differentiation was made whether both or just one queen was on the board or not. FUSc# classification does not take this information into account. Also some of the classifications occurred seldom or not at all. The opening phase needs some rethinking. At the moment only one vector is used to train it, but it seams that more diversified features are needed.

References

- 1. Zipproth S.: "Suchet, so werdet ihr finden.", CSS, p.15, 3/2003
- Luger G.F.: "Künstliche Intelligenz . Strategien zur Lösung komplexer Probleme", 2001
- 3. Zhang B.-T.: "Lernen durch Genetisch-Neuronale Evolution: Aktive Anpassung an unbekannte Umgebungen mit selbstentwicklenden parallelen Netzwerken.", Doktorarbeit, Infix 1992
- Thong B.T., Anwer S.B., Nikhil D.: "Temporal Difference Learning in Chinese Chess.", IEA/AIE (Vol. 2), 612-618, 1998
- Gherrity M.: "A Game-Learning Machine", Dissertation, University of California, San Diego, 1993
- Thrun S.: "Learning To Play the Game of Chess", Advances in Neural Information Processing Systems (NIPS) 7, Cambridge, MIT Press, 1995
- Baxter J., Triddgell A., Weaver L.: "Experiments in Parameter Learning Using Temporal Differences", ICCA JOURNAL ,ISSN 0920-234X, Vol. 21 No. 2, pages 84-99, 1998
- 8. Tesauro G.: "Comparison Training of Chess Evaluation Functions", Advances In Computation: Theory And Practice archive, Machines that learn to play games, pages: 117 130, 2001
- Tridgell A.: "KnightCap a parallel chess program on the AP1000+", Technical Report, Australian National University, 1997
- Baxter J., Tridgell A., Weaver L.: "KnightCap:A chess program that learns by combining TD(lambda) with minimax search", In MACHINE LEARNING Proceedings of the Fifteenth International Conference (ICML '98), ISBN 1-55860-556-8, ISSN 1049-1910, Madison WISCONSIN, pages 28-36, 1998
- 11. Plaat A.: "RESEARCH, RE:SEARCH & RE-SEARCH", Doktorarbeit, Tinbergen Institute, 1996
- 12. King D.: "KASPAROW gegen DEEP BLUE", Beyer Verlag 1997
- Samuel A.L.: "Some Studies in Machine Learning Using the Game of Checkers".
 IBM Journal of Research and Development, 3:210-229, 1959
- Sutton R.S.: "Learning to Predict by the Methods of Temporal Differences". Machine Learning, 3:9-44, 1988
- Tesauro G.: "Temporal Difference Learning and TD-Gammon", Communications of the ACM, Vol. 38, No. 3, 1995
- 16. Rojas R.: Theorie der Neuronalen Netze, Springer-Verlag, 1993
- 17. T-Rex Webseite: http://membres.lycos.fr/refigny63/nf3.htm
- 18. GNUChess Webseite: http://www.gnu.org/software/chess/
- NeuroChess Webseite: http://satirist.org/learn-game/systems/neurochess.html

Genetic algorithms in PD Control Systems, a multivariable and multiobjective approach

Edgar Chavolla, Erik Cuevas, Daniel Zaldivar, Marco Perez and Alberto De La Mora chavolla@gmail.com Universidad de Guadalajara, CUCEI, Av. Revolución 1500, 44430 Guadalajara, Jalisco, México.

(Paper received on February 29, 2008, accepted on April 15, 2008)

Abstract.

The design of a PID controller is a multiobjective problem. The designer has to adjust the controller parameters such that the feedback interconnection of the plant and the controller satisfies a set of specifications. The specifications are usually competitive and any acceptable solution requires a trade-off among them. In this work an approach for adjusting the parameters of a PD controller based on multiobjective optimization and genetic algorithms is presented. This approach was proven successfully to find the parameters of a PD controller on a level plant

1 Introduction

In recent years the development of controllers on the base of genetic algorithms has been paid much attention. The PID is the most accepted controller in the industry. In fact, most of them are PD controllers because the integral action has been switched off. Although the number of parameters to adjust in a PID controller is very small and a great deal of tuning rules can be found in the literature [1]. In a recent study, it has been experimentally checked that more than 30% of the installed controllers are operating in manual mode and 65% of the loops operating in automatic mode are poorly tuned [2]. This justifies the search for new approaches to adjust industrial controllers.

During the past decades great attention has been paid to optimization methods for controller design. The control design problem is a multiobjective problem. An effective design method should allow one to deal with several objectives that could possibly be expressed using various types of norms.

The fixed structure of the PID controllers creates serious problems for applying the modern optimal design methods that deal with unstructured controllers. Moreover, the resultant optimization problem is not convex and local optimization methods can be stuck in a local minimum. This has motivated the use of genetic algorithms GA's for adjusting PID controllers [3-5].

© E. V. Cuevas, M. A. Perez, D. Zaldivar, H. Sossa, R. Rojas (Eds.) Special Issue in Electronics and Biomedical Informatics, Computer Science and Informatics
Research in Computing Science 35, 2008, pp. 41-50



The genetic algorithm is a method for solving both constrained and unconstrained optimization problems that is based on natural selection. The genetic algorithm repeatedly modifies a population of individual solutions. At each step, the genetic algorithm selects individuals at random from the current population to be parents and uses them to produce the children for the next generation. Over successive generations, the population "evolves" toward an optimal solution. Genetic algorithm can be applied to solve a variety of optimization problems that are not well suited for standard optimization algorithms, including problems in which the objective function is discontinuous, multiple, nondifferentiable, stochastic, or highly nonlinear.

In this work an approach for adjusting the parameters of a PD controller based on multiobjective optimization and genetic algorithms is presented. This approach was proven successfully to find the parameters of a PD controller on a level plant

The document is organized as follows: in section 2 the plant is described, in section 3 the optimization approach is explained, in 4 the results are presented and finally in section 5 the conclusions are established.

2. System description

The plant in this work is a water level system. This system is controlled by a PD Fuzzy system [6]. The PD Controller has three gain parameters to adjust the behavior of the control. Every parameter has an effect over the system behavior. In the water level System there are three objectives identified to be considered in the output level: Maximum Peak level (MP), Time to reach the desired level (TC), Time for Stabilization (TSS). These objectives are shown in the figure 1.

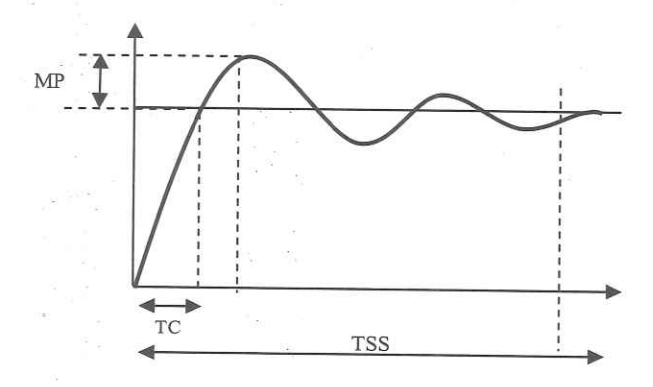


Fig. 1. System response objectives.

Our whole system has the following configuration: The reference level block, the error signal and error rate block, the PD Fuzzy Block, the output signal block and the plant. Figure 2 shows the system configuration.

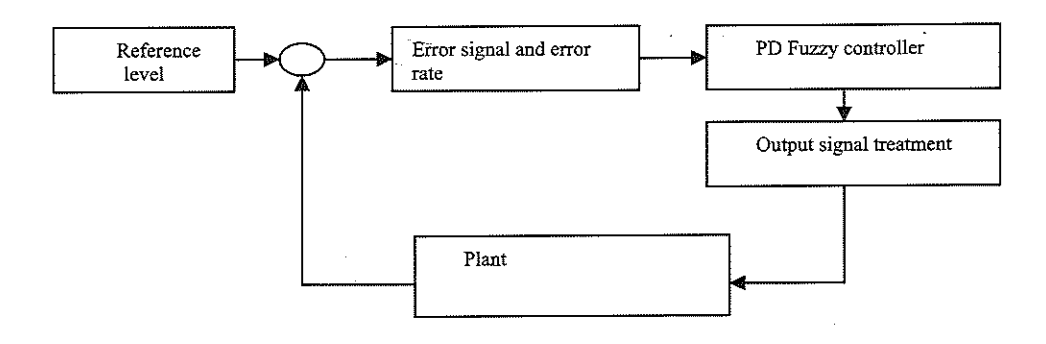


Fig. 2. System configuration

There are inside the "error signal, error rate" and the "output signal" blocks three gains that affect lineally the system. The gains are for the input: Error Gain (Ge) and Rate Gain (Gr), and Output Gain (Gu) [7] for the output.

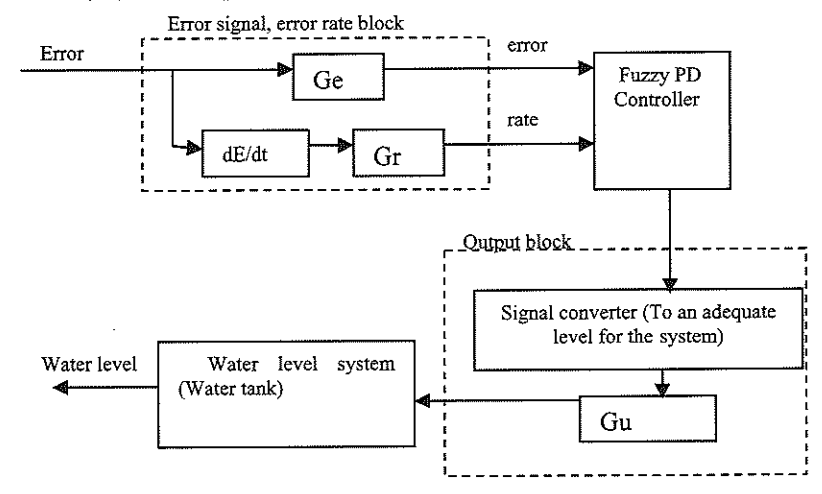


Fig. 3. A closer look into the target system. Here the gains can be located (Ge, Gr and Gu).

Ge, Gr and Gu will be the input variables for the GA, while TC, MP and TSS will be the objectives to achieve.

3 GA procedure

Multi Objective Problems (MOP) is a field where in the latest years has been many advances and new algorithms have been developed and proposed. The general field where all these algorithms have been classified is named Multi-Objective Evolutionary Algorithm (MOEA) [8].

In the process to solve the multi-variable algorithm and the MOP, some techniques that allow improving the effectiveness of the algorithm will be used. These techniques converge in a faster way to a convenient solution.

The problem can be divided in three main sections: A general GA implementation, the Multi-Objective Algorithm (MOA), and the Multi-Variable Algorithm (MVA)

The general implementation procedure contains the following operations:

- 1. Set parameters
- 2. Create randomly a population
- 3. loop until condition
- 4. mix population
- 5. crossover
- 6. mutation
- 7. evaluate fitness
- natural selection
- 9. end loop
- 10. Show results

MOA will act in the fitness evaluation process (step 7), and MVA will act in the crossover process (step 5). The rest of the steps can be created as any normal GA.

3.1 General GA implementation

This process is almost the same as any other GA; however is needed to add some specific parameters that help to the MOA and MVA procedures. The crossover step will not take place in the general GA implementation, it will be done in the MVA procedure, and the fitness evaluation will be completed by the MOA procedure.

For the MVA, three random seeds will be created (one for every variable), so it can have independent values to create or mutate each gene. Also for the MOA a dominance factor is needed; this will tell the crossover algorithm (the MVA) how to mix the genes. In MOA the parameters are set to the desired values for the objectives, and the weight of them.

3.2 MVA implementation (Crossover)

In this part the inheritance theory from Gregor Johann Mendel is used. The Mendel's Theory states a set of primary tenets relating to the transmission of hereditary characteristics from parent organisms to their children

This theory basically tells the way the parent's genes are affecting genes in the offspring. There are two types of genes in the parents, the dominant genes and the recessive genes. The dominant genes will affect mostly in the offspring, while the recessive gene will have little effect. Enumerating some cases from the gene combination based on the dominant factor (Table 1).

Parent 1 gene	Parent 2 gene	Offspring gene
+X	-Y	X(Y) Mainly affect by X
-X	+Y	Y(X) Mainly affect by Y
+X	+Y	XY Equally affected by X and Y
-X	-Y	XY Equally affected by X and Y
++X	Y	X Only affected by X
X	++Y	Y Only affected by Y

Table 1. The possible combinations from the genes considering the dominance factor. + means a dominant gene, ++ means a superior gene, while - means a recessive gene, and -- a gene that is likely to disappear.

Table 1 shows that there are 5 different kinds of breed from the parents. This table applies for every gene in the chromosome. It is needed to consider all the possible combination, because it cannot be decided a priori what would be the dominant gene. This is due to the Multi-objective problem; cannot be assured if giving more weight to a gene will improve or will degrade one or some of the objectives.

Based on table 1, the total number of the new breed for each pair of individuals can calculate as:

$$offspring _number = number _of _combinations^{number _of _genes}$$
 (1)

In the system there are 3 genes and using 5 combinations, this will give using equation (1), 125 new offsprings in every generation for every parent pair. This is a big breed, but eliminating some the possible combinations can reduce it.

For the combination of the genes, it will be used Eq. (2), so the general definition of the crossover is an arithmetic operation. The values for gain_1 and gain_2 correspond to the dominance factor defined for the gene.

$$new_gene = (gene_1*gain_1 + gene_2*gain_2)/2$$
 (2)

The dominant factor will be multiplied by gene_ 1 or gene_2, depending on the combination and the way the algorithm needs to converge (table 2).

Parent gene 1	Parent gene 2	Formula for the offspring gene	
+X	-Y	(X * (Dominant factor) + Y) /2	
-X	+Y	(Y * (Dominant factor) + X) / 2	
+X	+Y	(X+Y)/2	
-X	-Y	(X + Y)/2	
++X	Y	X	
X	++Y	Y	

Table 2. This table shows the formulas used depending on the gene combination.

Considering the previous tables and equations, the MVA can be described as:

- 1. Take pairs of individuals (parents) from the population
- 2. Create the number of children according to the combination formula (1)
- 3. Assign values to the genes depending on the combinations done base on Table 1 using the formulas given by Table 2

3.3 MOA implementation (Evaluate fitness)

This process operates with each individual that has not been yet evaluated. In the water level plant, the objective functions are measures from the output response. As the controller affects the system, it is relatively easy to define equations that evaluate the objectives of the system dynamics.

The solution is to accomplish an implementation of the whole system, and set the gain values using the data contained in the genes of each individual. So for each individual it will be run a simulation of the whole process in order to obtain the objective values.

After evaluating the objective values with the data from the individual, the output values are compared against the desired values, and the error rate is obtained. The equation (3) can be used if the desired value is not zero. If the desired value is zero, the error rate can be approximated by equation (3a). The correction value in equation (3a) should be set by testing; the value should be set between 0 and 1. This correction value prevents big values in the error rate.

$$error_rate = (|desired_value - obtained_value|)/desired_value$$
 (3)

$$error_rate = |obtained_value| * correction_value$$
 (3a)

Equations (3) and (3a) produce three error values (one for each objective). Now the error values are combined in a fitness value, so this fitness value ranks the individual behavior obtained.

The next step involves the weight values set for every objective. These weigh values define how strong is the objectives in the algorithm. Thus, a stronger objective will affect more the fitness values than one with a low weight.

In MOP the fitness value is calculated from the three objectives using (4), this expression calculates the weight mean depending on the weights values and error rates of every objective (lower fitness values are considered to be better).

$$fitness = \frac{(error_1*weight_1 + error_2*weight_2 + error_3*weight_3)}{(weight_1 + weight_2 + weight_3)}$$
(4)

The process is summarized as:

- 1. Evaluate the system for every individual in the population
- 2. Get the objective values for each individual
- 3. Calculate the error rate for every objective
- 4. Calculate the fitness values

4 Results

The implementation of the GA was made in Matlab and Java. Java was chosen due to the nature of the problem that can be mapped directly to OOP; and also because it is supported by Matlab.

In the water level plant, MP parameter is defined as the absolute difference between the maximum real value and the desired value. This is a little different from the original definition. This change makes possible support the case, when the output is under the desired level.

Considering the importance of the parameters, the weights must be selected. MP is the most important parameter as well as the TC parameter, while the TSS parameter is not considered as critical in the application. In order to set TC and TSS to the desired values, the minimum filling time for the water plant should be considered. This is around to 162 seconds, so TC an TSS can not be less then this value.

Parameter	Value	
Weight for MP	1	
Weight for TC	1	
Weight for TSS	0.1	

4	S

Population size	10
Dominance factor	0.2
Mutation factor	50%
Desired level	60
Seed for Ge	140
Seed for Gr	2
Seed for Gu	3
Desired MP	.01
Desired TC	170
Desired TSS	180

Table 3. The parameter used in the GA implementation.

After running the GA 30 generations, acceptable results were found (Table 4). TSS is exactly the required value and a better Mp value was found (closer to the desired level), only TC was higher than expected. This can be considered a good solution to the plant (only 0.0886 in the fitness value).

Parameter	Desired values	Obtained values
MP (weight 1)	.01	.0085
TC (weight 1)	170	174
TSS (weight .1)	180	180

Table 4. The result from the tuned up parameters after 30 generations

An optimal result was found after only 18 generations, which can be considered a fast way to get the gain values for the PD controller (Fig.4). The gain values were Gu: 1.674270492132032, Gr. 83.5564484964882, and Ge. 75.69871513072385.

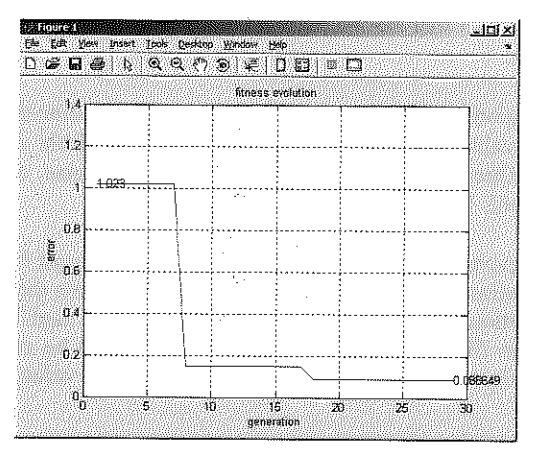


Fig.4. The fitness function shows how an optimal result was found after 30 generations.

5 Conclusions

In this work an approach for adjusting the parameters of a PD controller based on multiobjective optimization and genetic algorithms was presented. This approach was proven successfully to find the parameters of a PD controller on a level plant

PD and PID controller systems can be greatly improved using the techniques described in this paper. The controller can be set to operate in a desired operation range with a minimum of error.

Moreover, the technique used in the controller finds an optimal set of gain values faster than manual procedure or other techniques. This is true most of the time, due to the randomness in the nature of the technique itself. Some times the GA would find a local solution, so the algorithm should be stop and started again. Doing this restating process will allow the GA to find a better place to converge to a good solution.

To find a good solution the dominance factor was set to a level that let the GA to change in fast way without losing precision (a high value make the GA converge faster, and low values make the GA get more precise values). It was found that this value can be between 0.1 and 1 to find optimal precision-speed performance.

The seeds for Gr, Ge and Gu were chosen using previous experiences in the system, so the random values were generated close to some values that give a stable behavior. These seeds guaranty that the GA will start around a value that can be closer the desired. The mutation factor was chosen to 50% to let the GA have plenty of new points to search without being a random search with not a tendency.

The problem using GA-MVA-MOA, is the amount of resources needed to make it run. The memory and the computer speed affects greatly in the GA performance. As a consequence a really careful setting in the initial parameters in the GA should be done in order to get good results and have a good performance in the GA.

The population was set to 10, this was due to limitations of resource in the computer, also 10 is wide enough to let the GA have a good number of combinations without overwhelming the algorithm.

The incorporation of MVA and MOA in GA allows to find optimal gain values faster than other methods and to reach the global minimum.

References

[1] O'Dwyer, A.: PI and PID Controller Tuning Rules for Time Delay Processes: a Summary. Tech. Rep. AOD-00-01 Ver. 1, Dublin Institute of Technology, Ireland (2000)

- [2] Ender, D. B.: Process control performance: Not as good as you think. Control. Eng. 40 -10, 180-190 (1993)
- [3] Jones, A. and De Moura Oliveira, P.: Genetic autotuning of PID controller. In Proceedings of the First International Conference on Genetic Algorithms in Engineering Systems: Innovations and Applications, Sheffield, UK, IEE, (1995) pp. 141–530.
- [4] Salami, M. and Cain, G., An adaptive PID controller based on genetic algorithm processor. In Proceedings of the First International Conference on Genetic Algorithms in Engineering Systems: Innovations and Applications, Sheffield, UK, IEE, (1995), pp. 88–94.
- [5] Chen, B. and Cheng, Y., A structure-specified H optimal control design for practical applications: A genetic approach. IEEE Trans. Control Syst. Technol, (1998) pp. 707–718.
- [6] Sanchez E., Nuno L.A., Hsu Y.C., and Guanrong C, Real Time Fuzzy Swing-up Control for an Underactuated Robot, *JCIS '98 Proceedings, Vol 1*, N.C., USA, (1998)
- [7] Cuevas E. V., Zaldívar D., and R. Rojas.: Incremental fuzzy control for a biped robot balance. IASTED International Conference on ROBOTICS AND APPLICATIONS ~RA 2005, Cambridge, USA (2005) pp.7-12.
- [8] Carlos A. Coello Coello, Gary B. Lamont and David A. Van Veldhuizen, Evolutionary Algorithms for Solving Multi-Objective Problems (Second edition), Springer, (2007)

Nonlinear Haptic Rendering of Deformation and Cutting Based on Orthogonal Decomposition

Gabriel Sepúlveda¹, Vicente Parra², Omar Domínguez³

- Departamento de Ingeniería Eléctrica, CINVESTAV, México DF gsepulveda@cinvestav.mx
- ² Grupo de Robótica y Manufactura Avanzada, CINVESTAV, Saltillo vparra@cinvestav.mx
- ³ Centro de Investigación en Tecnologías de Información y Sistemas, UAEH, Pachuca, México omar_arturo@uaeh.edu.mx

(Paper received on February 29, 2008, accepted on April 15, 2008)

Abstract. This document presents a new method for the induction of nonlinear dynamics for deforming and cutting virtual objects using haptic devices. The properties of the virtual objects are obtained of bio-mechanical characterization reported in the literature. The dynamics are generated over differentiable manifolds defined by implicit functions and using the orthogonal decomposition of the haptic device dynamic. An exponential bio-mechanic model of liver tissue during deformation is implemented along with an energetic model of cutting based on fracture mechanical approach. The experimental results are presented within a platform running with a 3DOF haptic device and a 3D environment showing a stable interaction.

1 Introduction

Modeling the dynamic properties of different kind of tissues during deformation and cutting is an essential task for developing a surgery simulator that pretends to approximate the perception of the user to the reality. The more realistic the model programmed is, the more accurate the force feedback is computed during the simulation using a haptic device. The bio-mechanical properties of tissues during deformation and cutting are generally nonlinear mathematic models. A haptic engine that allows the recreation of this kind of dynamic models is needed to accomplish the task.

An approach using mass-spring-damper(MSD) model system are shown in [1]. An approach based on the bookkeeping of force deflections curves stored at the nodes of a triangulated body surface is presented in [2] and [3]. An energetic model of interaction during cutting of samples of potato and real pig's liver tissue is presented in [4]. A nonlinear dynamic model due to friction, deformation and cut during needle insertion is presented in \cite{aguja2}. A cutting model approach using Local Element Method (LEM) is presented in [5]. An exponential model of deformation, of in-vivo and ex-vivo pig tissues, is obtained in \cite{In-vivo} using specific devices to measure tissue properties under extension and indentation, as well as to record instrument-tissue interaction forces. To produce realistic behavior in virtual environment simula-

© E. V. Cuevas, M. A. Perez, D. Zaldivar, H. Sossa, R. Rojas (Eds.) Special Issue in Electronics and Biomedical Informatics, Computer Science and Informatics
Research in Computing Science 35, 2008, pp. 51-61



tions for surgical training, it is important to have a haptic engine that allows the recreation of this models and characterization using a haptic device.

1.1 Contributions

Arimoto [8] presented a method for orthogonal decomposition of the forces during the interaction between a robot manipulator and an infinitely rigid object. We propose a new methodology based on this orthogonal decomposition applied over a haptic device's dynamics, enabling the implementation of a control law that generates different kinds of dynamic models for haptic rendering virtual object's dynamics, this new method permits the simultaneous generation of contact forces like deformation and cutting and surfaces properties like tangent friction. In this paper a nonlinear deformation model and tissue cutting characterization model are presented along with simple surface properties for virtual objects. The models presented in [7] and [4] are implemented using Phantom Premium haptic device [9]. The human-in-the-loop experimental interaction results are presented with a discussions an future work.

2 Dynamic induction using orthogonal decomposition

A methodology that allows the orthogonal decomposition of the dynamic of a haptic device is presented in [10], and the most important issues are dicussed here.

The dynamic of a haptic device is modeled as chained linked robot:

$$H(q)\ddot{q} + C(q, \dot{q})\dot{q} + q(q) = \tau + \tau_h \tag{1}$$

$$\tau_h = J^T F \tag{2}$$

where $q,q\in\Re^n$ are vectors that represents the articular position and velocities, n is the number of degrees of freedom (DOF), $H(q)\in\Re^{n\times n}$ is a matrix representing the inertial forces of the haptic device with $H(q)=H(q)^T$ positive defined, $H(q)\in\Re^{n\times n}$ is the Coriolis forces matrix with H(q)-2C(q,q) an antisymmetric matrix, $g(q)\in\Re^n$ is the gravitational force vector, $\tau\in\Re^n$ is the input torques vector, $J\in\Re^n$ is the haptic device's analytic Jacobian, $F_h\in\Re^3$ is the human input force, $\tau_h\in\Re^n$ represents the input torques due to F_h .

The virtual object's dynamic properties are generated by two manifolds defined as an implicit functions of the articular variables q as follows:

$$V_0 = \{ q \in \mathfrak{R}^n \mid \varphi(q) = 0 \}$$
 (3)

$$V_{psi} = \{ q \in \Re^n \mid \psi(q) = 0 \}$$
 (4)

with $\varphi(q):V_o\to\Re$ called object manifold and $\psi(q):V_o\to\Re^n$ called *psi* manifold.

The orthogonal decomposition of the haptic device's dynamic is achieved applying the following control law:

$$\tau_1 = C(q, q)q + g(q) - PH(q)J_{\varphi^*}J_{\varphi}q - QH(q)Qq - J_{\varphi}^T\lambda_d - Q\zeta_d$$
 (5)

$$P = \frac{J_{\varphi}^{T} J_{\varphi}}{J_{\varphi} J_{\varphi}^{T}} \tag{6}$$

where J_{φ} and Q are the jacobian matrices of functions $\varphi(q)$ and $\psi(q)$ respectively, J_{φ^*} is the pseudo inverse of J_{φ} . The variables λ_d and ζ_d are used to induce the dynamics and surface properties of the virtual object as is presented later in this document.

Substituting (5) in (1) and using the analysis presented in [10] the close loop equation that is to be analyzed is:

$$\varphi(q) = M_{\varphi}(\lambda - \lambda_d) \tag{7}$$

$$\psi(q) = M_{\psi}(\zeta - \zeta_d) \tag{8}$$

with

$$M_{\varphi} = J_{\varphi} H(q)^{-1} J_{\varphi}^{T} \tag{9}$$

$$M_{\scriptscriptstyle W} = QH(q)^{-1}Q \tag{10}$$

3 Exponential deformation model

For recreating the correct force feedback during interaction with nonlinear dynamic object like organic tissue, it is important to implement mathematic models that represents the properties of the real tissue. One form to accomplish this task is to implement the bio-mechanical models obtained form direct experiments.

A mathematical model of pig's abdominal tissues is presented in [7], the biomechanical characterization is done using surgery tools coupled with sensors during deformation. The mathematic model is:

$$F = \alpha e^{\beta \sigma} \tag{11}$$

where F is the reaction force, α and β are specific constants for each kind of tissue, σ represents the stretch ratio during deformation. For pig intestine sample the values reported in [7] are $\alpha=3.7\times10^{-9}$ and $\beta=9.4$ for ex-vivo experiments and $\alpha=4.3\times10^{-7}$ and $\beta=13$ for in-vivo experiments. To induce this behavior the variable λ_d is defined as follows:

$$\lambda_{d1} = -M_{\varphi}^{-1} B_0 \phi(q) + M_{\varphi}^{-1} \alpha e^{-\beta \frac{\phi(q)}{L_0}}$$
(12)

where α, β are the constants reported in [7] and L_0 represents the sample's thickness in the direction of the compression force, B_0 is a defined positive constant that represents the virtual object's viscosity coefficient, used to induce stability to the whole system. The sign within the exponential is because the value of $\varphi(q)$ is negative inside the virtual object. Substituting (12) in (7) we obtain the following dynamic system:

$$\varphi(q) + B_0 \varphi - \alpha e^{-\beta \frac{\varphi(q)}{L_0}} = M_{\varphi} \lambda$$
 (13)

The implementation of tangent friction is achieved through the variable ζ_d as follows:

$$\zeta_d = B_1 \psi(q) \tag{14}$$

where B_1 is a diagonal matrix with all positive values b_1 . Substituting (14) in (8) the following system is obtained:

$$\psi(q) = M_{\psi} \zeta - M_{\psi} B_1 \psi(q) \tag{15}$$

4 Cutting model using a fracture mechanics approach

One of the principal task during the interaction with tissue is cutting. An approach of this task is presented in [4] based on fracture mechanical approach, this model presents an energetic interchange between three states: deformation, fracture and cutting.

The analysis in [4] is done considering a rectangular sharp tool as is shown in Fig. 1. The energetic interchange is represented by the following equation:

$$\Delta W_e = \Delta U + \Delta W_s \tag{16}$$

where ΔW_e represents the extern energy applied, ¢U is the change in the elastic potential energy and ΔU is the irreversible work of fracture. During deformation the external energy applied is stored as elastic potential energy, one example of this behavior is the deformation of a linear spring ($E = \frac{1}{2}kx^2$) where the energy applied to the spring is stored and recover when the spring is released, this behavior is presented in the following equation:

$$\Delta W_e = \Delta U \tag{17}$$

If the interaction during deformation reaches a stored energy limit the behavior changes from deformation to fracture interaction, this limit is called the material's yield point. During fracture the elastic potential energy stored instantaneously creates a crack in the object:

$$\Delta W_{\rm s} = \Delta U \tag{18}$$

During cutting interaction the energy applied increases the depth of the crack done during fracture interaction.

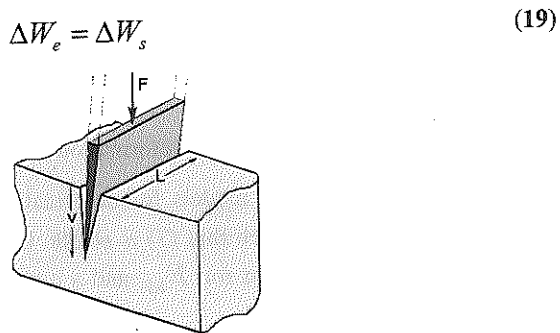


Fig. 1. Tool-body interaction model presented in [4], F represents the force applied, ν represents the penetration depth, and L represents the length of the tool.

The transition between the interaction modes is as follows:

- 1. Without contact the state is considered as free movement.
- Once the virtual tool is in contact with the virtual object the deformation state is present.
- The external force applied stores elastic energy accordingly with the elastic deformation model used.
- The deformation interaction continues until the yield point is reached at this
 point the interaction changes to fracture.

5. The elastic potential energy stored at this point is released creating the crack. If the tool keeps going inside the object the cutting interaction is reached otherwise the state returns to free movement with the new contact surface at the end of the crack.

The procedure is shown in the Fig. 2, where v represents the penetration speed.

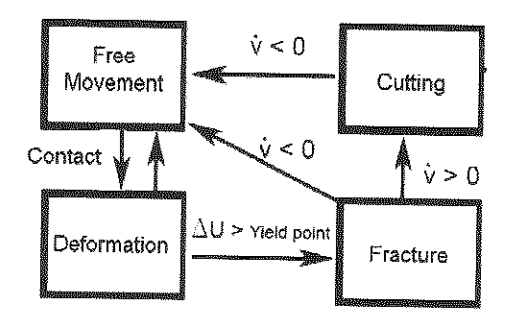


Fig. 2. Interaction modes sequence presented in [4].

To induce this behavior the variable λ_d from (5) is dened for the deformation and cutting interaction modes as follows:

$$\lambda_{d2} = F_{def}(\varphi, \dot{\varphi}) \tag{20}$$

$$\lambda_{d3} = F_c(\varphi, \phi) \tag{21}$$

where λ_{d2} and λ_{d3} are used for deformation and cutting respectively, F_{def} and F_c represents the interaction models for deformation and cutting interactions, this models have to be chosen such that (7) is stable. One example could be the spring-damper model for deformation for F_{def} and a constant force F_c as is presented in [4].

5 Experimental platform

The models presented in this paper are implemented in a computer to simulate nonlinear deformation and cutting interaction. The PC is running at 2.4GHz with AMD Athlon processor, 1Gb RAM, 64Mb NVIDIA Ge Force 4 MX and RedHat Linux 9.0 with real time patch. The user application was developed using Qt [11] for graphical tools and OpenGL and GLU for 3D graphics, the programming language was C++.

Fig. 3. Experimental platform. Left: PC, monitor and haptic device. Right: GUI using a wired virtual hand used as proxy during the interaction with a virtual sphere, the buttons, sliders and text boxes for changing the experimental parameters in-line.

The haptic device used is Phantom Premium [12], the dynamic model is obtained in [13]. The Fig. 3 shows the GUI during the interaction with a virtual sphere along with the tools used to change in line the parameters during the simulation. The graphics of the most important process variables are shown, also a wired hand used as proxy is presented.

6 Experimental results

The experimental results of two interaction models are presented, the first using the exponential deformation and the second using the cutting model both with tangent friction and using a plane as the virtual object. The virtual plane is defined as de XZ plane at the coordinates origin as it is shown in Fig. 4.

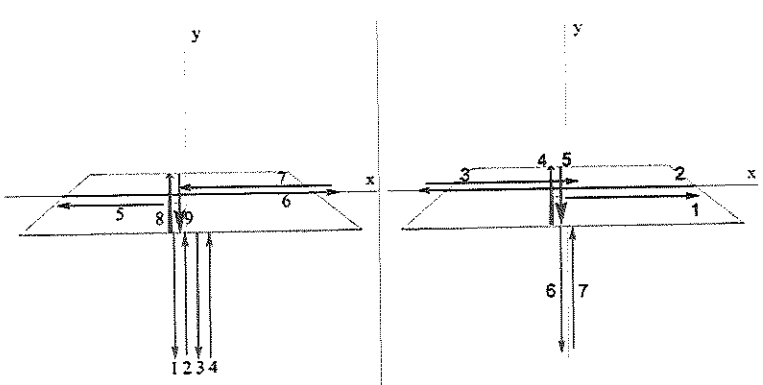


Fig. 4. Displacements during interaction with a virtual plane. Left: displacements order during experiment 1. Right: displacements order during experiment 2. The z axis is considered in direction outside the sheet.

Experiment 1: the experiment starts with the proxy at the origin of cartesian coordinates (x = 0; y = 0; z = 0), the displacements are done using straight lines in the following directions: -y, y, -y, y, -x, x, -x, -z, z. This is shown in Fig. 4 left, where the numbers 1-9 represents the order of the displacements.

Experiment 2: the experiment starts also at the origin of cartesian coordinates, the displacements are done using also straight lines in the following directions: x, -x, x, -z, z, -y until reaching the cutting mode then and finally y. This is shown in Fig. 4 right.

The implementation of the exponential deformation model the equation used was (12) and for the cutting model the following variables were defined:

$$\lambda_{d2} = -M_{\varphi}B_0\phi + M_{\varphi}^T\alpha e^{-\beta\frac{\varphi}{L_0}}$$
 (22)

$$\lambda_{d3} = -2.0 \tag{23}$$

Both experiments use the following parameters: $B_0=20$, $\alpha=4.3\times 10^{-7}$, $\beta=13$, $L_0=0.1$ the tangent friction is induced using (14) con $b_1=0.06$ for experiment 1 and $b_1=0$ for experiment 2.

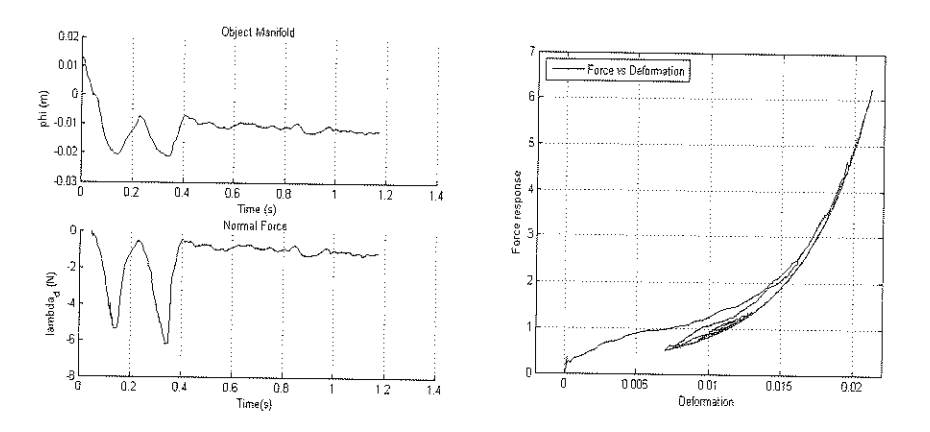


Fig. 5. Experiment 1, interaction with a virtual plane using the exponential deformation model with tangent friction. Left: Object manifold and normal force vs *t*. Right: Deformation vs Force response

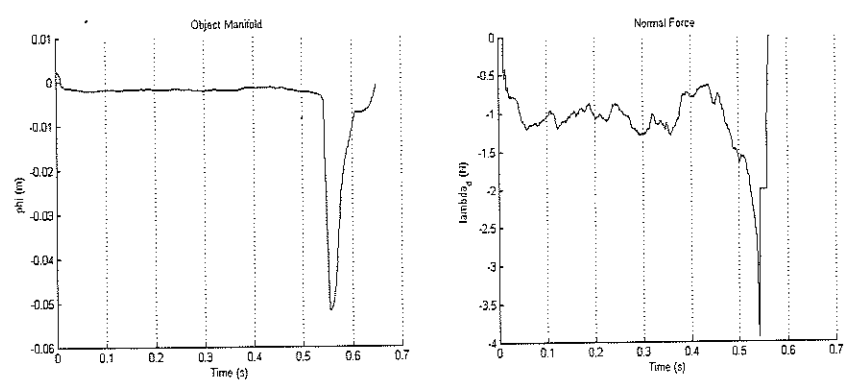


Fig. 6. Experiment 2, interaction with a virtual plane using the exponential deformation and cutting model without tangent friction. Left: Object manifold vs t. Right Normal force vs t.

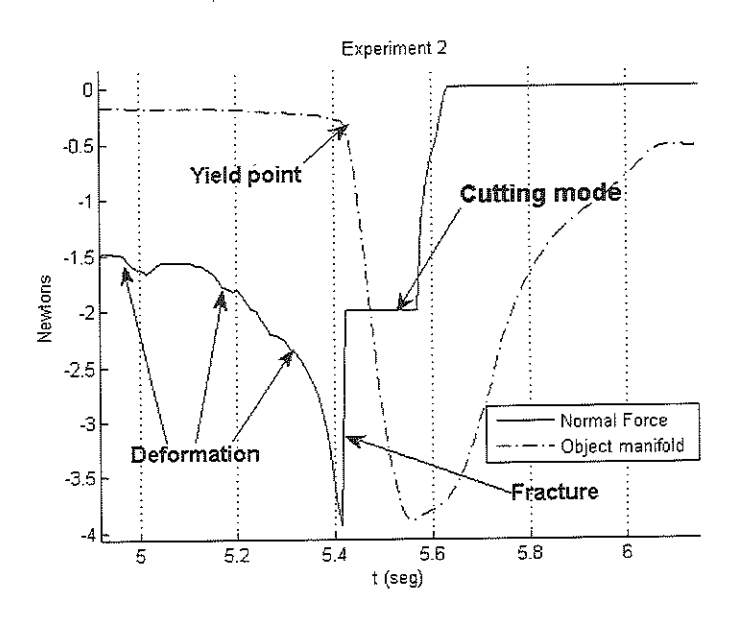


Fig. 7. Transition between the different modes in the cutting algorithm, the reaction force is presented with a filled line and the object manifold with dotted line. The deformation mode is presented until t=5.4128 seconds, then the yield point is reached and the interaction switches to rupture mode for 1 millisecond this is due to the platform's sampling period, then the interaction switches to cutting for 156 milliseconds, in this mode a constant force of -2 Newton is presented, at last the tool moves outside the virtual object and the reaction force is zero.

7 Conclusions

A new methodology for the implementation of bio-mechanical characterization for the interaction with a virtual object simultaneously with surface properties, using a haptic device has been tested presenting a high performance on a low end computer. The experimental results using two different interaction models, exponential deformation Fig. 5 and cutting interaction Fig. 6, presented in the literature is shown. An extended explanation of the interaction during cutting is explained in Fig. 7, where it could be seen the four interaction models presented in [4]: Free motion, deformation, fracture creation and cutting.

The methodology could be implemented to any nonlinear bio-mechanical model as long as it could be expressed in terms of the depth penetration and penetration speed. Complex surfaces properties could also be implemented. The extension to any arbitrary object form could be implemented as long as it could be expressed with a set of implicit equations. The experiments were done during a human-in-the-loop interaction showing a stable behavior in a low end experimental platform.

8 Future work

The future work will be to implement complex surface properties like textures and advanced friction models for making more realistic the interaction. Also the implementation of complex objects defined by a set of implicit equations is the next step. The implementation of the methodology using different haptic devices is at hand.

9 Acknowledgment

The authors thank to CONACYT, CINVESTAV Cd. de México, CINVESTAV Saltillo and CITIS UAEH, Hidalgo México.

References

- Cagatay Basdogan et al. Simulation of tissue cutting and bleeding for laparascopic surgery using auxiliary surfaces. Technical report, Cambridge, MIT, USA.
- Nicholas Ayache Stéphane Cotin, Hervé Delingette. A hybrid elastic model allowing real-time cutting, deformation and force feedback for surgery training and simulation. INRIA, 2004.
- Mohsen Mahvash & Vincent Hayward. High-fidelity passive force-reflecting virtual environments. IEEE Transactions on Robotics, pages 38-46, 2005.
- Mohsen Mahvash & Vincent Hayward. Haptic rendering of cutting: A fracture mechanics aproach. Technical report, McGill University, Quebec, Canada, 2001.

- 5. Allison M. Okamura. Force modeling for needle insertion into soft tissue. IEEE TRANSACTIONS ON BIOMEDICAL ENGINEERING, 51(10), October 2004.
- 6. Teeranoot Chanthasopeephan Jaydev P. Desai and Alan C. W. Lau. 3d and 2d finite element analysis in soft tissue cutting for haptic display. ICAR, pages 360-
- 7. Iman Brouwer et al. Measuring in vivo animal soft tissue properties for haptic modeling in surgical simulation. Technical report, University of California, USA,
- 8. Suguru Arimoto. Control Theory of Non-linear Mechanical Systems. Oxford Science Publications, 1 edition, 1996.
- SensAble Technologies Inc. Phantom premium 1.0/1.5a, 3d touch components: Hardware installation and technical manual, ver 6.5, August 2000.
- 10. Gabriel Sepúlveda Vicente Parra and Omar Domínguez. A high performance haptic rendering method based on orhogonal decomposition of haptic device's dynamics. Subminited to IEEE Transaction on Haptics, 2008.
- 11. http://trolltech.com/products/qt.
- 12. SensAble Technologies Inc. Specifications for the phantom ® omni haptic device, March 2004.
- 13. Omar Arturo Domínguez Ramírez. Design and integration of a Realistic Haptic Interface. Phd thesis, CINVESTAV, Mechatronic Section, México,

Robust Synchronization of a Class of Robot Manipulators

Manfred Gilium and Gualberto Solís-Perales *

Faculty of Mechanical Engineering, University of Stuttgart, 70550 Stuttgart, Germany
Departamento de Electrónica, CUCEI, U. de G.,
Av. Revolución 1500, Guadalajara Jalisco, México

(Paper received on February 29, 2008, accepted on April 15, 2008)

Abstract. In this work, an adaptive control strategy for the synchronization of robotic manipulators is presented and verified with numerical results. The idea of synchronization is that various systems, that may have completely different dynamics, behave in a way that there exist no residual difference of their outputs. Here we present an approach for the synchronization of robot manipulators in spite of unmodeled dynamics and parametric uncertainties, external disturbances as well as parametric and structural differences of the robots. It is achieved with the help of a nonlinear controller with robust characteristics that only requires the measurement of the angular positions. The uncertain functions are grouped into a new state that is, together with the other states of the system, estimated by a high-gain observer. With the estimated states a feedback is implemented that is based on the idea of linearization. Finally the proposed methodology is demonstrated for a two degree of freedom (DOF) robot manipulator and numerical results are presented. Keywords: Robot synchronization, Synchronization, Robust synchronization.

1 Introduction

Synchronization is a phenomenon that has many examples in natural processes, such as the perfectly coincided oscillation of two pendulum clocks hanging from the same base [1], the synchronous firing of neurons [2],[3] or the symmetry of animal gaits [4]. As in these examples the synchronization is achieved by interconnections in the systems without any external interference, we speak of self-synchronization. Additionally we find numerous examples in different mechanical and electrical structures, such as transmitter receiver systems, quadruped robot movements [5] etc. where the synchronization is achieved by external inputs and couplings, because of which we speak of controlled synchronization. This article focuses on the controlled synchronization of robot manipulators. We find many applications in production processes, where the synchronous behavior of robotic systems is necessary for the production of parts with equal quality. In surgery,

© E. V. Cuevas, M. A. Perez, D. Zaldivar, H. Sossa, R. Rojas (Eds.) Special Issue in Electronics and Biomedical Informatics, Computer Science and Informatics
Research in Computing Science 35, 2008, pp. 63-73



^{*} Corresponding Author, e-mail: gualberto.solis@cucei.udg.mx

new minimal invasive robotic systems have been developed [6] that require the synchronization of the robot with the trajectory that is generated by the operating surgeon.

While the control of robot manipulators is a classical control problem, the problem of synchronization of robots has not received much attention. We can find some approaches in [7] where the parameters of the system are estimated by an observer using only angular positions. Using those estimates an adaptive control strategy is realized. However, this technique requires the exact knowledge of the dynamics of the system, which results in a non robust approach. Therefore, in a realistic case, there are no knowledge of the frictions terms, parameter variations, etc.

In this article we assume that the parameters and the dynamics of the robot system are uncertain and that only the angular positions can be measured. Departing from the ideas presented in [8] we use the proposed robust nonlinear control scheme for the Multiple Input Multiple Output (MIMO) case. The methodology achieves the synchronization of an arbitrary number of robots in spite of structural and parametric differences of the robots and it is robust against external perturbations, friction and parameter variations. After a transformation of the system into a linearizable canonical form, the uncertain dynamics and parameters are lumped into an new state. This new state is, as well as the angular velocities, unknow and because of which it is estimated by a high-gain observer. With the estimated states a stabilizing controller is implemented that bases on the idea of linearization. Finally the robots are connected in a mutual pattern that achieves the synchronization between the robots and with respect to a trajectory that is given by the user.

2 Problem Statement

Let us consider a robotic manipulator that consist of w links and has m rotatory degrees of freedom that create the generalized angular positions $q_i, i = 1...m$. We assume that it is possible to generate m torques τ_i , i = 1...m in the link connections, for example with the help of electrical motors, hydraulic systems etc. It was presumed that it is possible to measure the angular positions of links at each point in time while the availability of the angular velocity was not postulated. The links of the robot were modeled as perfectly stiff, i.e. bending and vibration effects were neglected. With the help of the Lagrange or similar equations we can derive the following model of a robot with m rotatory degrees of freedom:

$$\ddot{q} = M(q)^{-1} \left(\tau - C(q, \dot{q}) \dot{q} - g(q) - p(\dot{q}) \right) \tag{1}$$

 $M(q) \in R^{m \times m}$ is the symmetric, positive definite inertia matrix while $C(q,\dot{q})\dot{q} \in R^m$ represent the Coriolis and centrifugal forces. $g(q) = \frac{\partial}{\partial q} E_{pot} \in R^m$ denotes the gravity forces and the friction in the element connections is represented by

$$p_i(\dot{q}_i) = B_{v_i}\dot{q}_i + B_{f_{i,1}}\left(1 - \frac{2}{1 + e^{2\omega_{i,1}q_i}}\right) + B_{f_{i,2}}\left(1 - \frac{2}{1 + e^{2\omega_{i,2}q_i}}\right) \quad i = 1...m \quad (2)$$

Where B_v is used to model the viscous friction while the remaining terms approximate the Coulomb and Stribeck friction effects. We carry out the following transformation:

$$\begin{bmatrix} x_1 \\ \vdots \\ x_m \end{bmatrix} = \begin{bmatrix} q_1 \\ \vdots \\ q_m \end{bmatrix} and \begin{bmatrix} x_{m+1} \\ \vdots \\ x_{2m} \end{bmatrix} = \begin{bmatrix} \dot{q}_1 \\ \vdots \\ \dot{q}_m \end{bmatrix}$$
(3)

Now (1) becomes a nonlinear $m \times m$ MIMO system, that is characterized by n=2m first order differential equations:

$$\dot{x} = f(x) + g_1(x)\tau_1 + \dots + g_m(x)\tau_m
y = [x_1...x_m]^T$$
(4)

With the states $x \in \mathbb{R}^n$, the system input $\tau \in \mathbb{R}^m$ and the system output $y \in \mathbb{R}^m$. The system is characterized by the function $f(x) \in \mathbb{R}^n$ and the matrix $g(x) \in \mathbb{R}^{n \times n}$:

$$f(x) = \begin{bmatrix} x_{m+1} \\ \vdots \\ x_{2m} \\ M(x)^{-1} \left(-C(x, \dot{x}) \dot{x} - g(x) - p(\dot{x}) \right) \end{bmatrix}; g(x) = \begin{bmatrix} 0_{m \times m} & 0_{m \times m} \\ 0_{m \times m} & M(x)^{-1} \end{bmatrix}$$
(5)

For the synchronization of two or various robotic manipulators, we will presume that every system fulfills the following assumptions:

A.1: Only the angular positions $[q_1...q_m]$ can be measured at each point in time, i.e. not all the states x_i , i = 1...n of the system are available.

A.2: There is no exact knowledge of the structure and the coefficients of M(q), $C(q, \dot{q})$, g(q) and $p(\dot{q})$.

A.3: The robotic manipulators may be strictly different, but they all have the same degrees of freedom and the same inputs.

There are numerous synchronization designs, such as serial or parallel master-slave models etc. [7]. However, in this work we will discuss the mutual synchronization pattern, where synchronous behavior is achieved with the interaction between the robots. The robots are arranged in a network and every robot could be connected to all the other robots. Let us suppose we have a number of l robots. For mutual synchronization the trajectories of reference $y_{ref_{i,k}}$ with

 $i=1...l,\ k=1...m$ of the robot i for the degree of freedom k are calculated as follows:

$$y_{ref_{i,k}} = y_{d_k} - \sum_{j=1, j \neq i}^{l} K_{cp_{i,j}}(y_{i,k} - y_{j,k})$$
 (6)

Where $y_d \in R^m$ is the desired trajectory that is given by the user, which is equal for all the robots and has to be smooth. $K_{cp_{i,j}}$ are the so called coupling factors. They define how strong the robot i will interact with the robot j. High values of the coupling factors will lead to a fast synchronization between the robots, low values will lead to a fast synchronization of the robots with the desired trajectory y_d . The synchronization of all robot manipulators is achieved if $\lim_{t\to\infty} \|y_{ref_{i,k}}(t)-y_{i,k}(t)\|\to 0$ for i=1...l and k=1...m. It is straightforward that this is only possible if also $\lim_{t\to\infty} \|y_{d_k}(t)-y_{i,k}(t)\|\to 0$ for i=1...l and k=1...m. The synchronization problem can be formulated as the design of the interconnections between the robots and the creation of control feedbacks for the robots. In the next chapter we will propose a robust control feedback strategy that is well suited for the mutual synchronization of robots.

3 The robust synchronization scheme

For the implementation of the proposed feedback scheme the system has to be transformed on *Burnes Isidori Normal Form*. Because this transformation requires the knowledge of the relative degree vector, we will use the following definition [11]:

Definition 2: (Relative Degree) The relative degree vector $[r_1...r_m]$ of an affine MIMO system as in (4) is defined by:

- 1. $L_{g_j}L_f^kh_i(x)=0$ for all x close to x_0 and $1\leq i,\,j\leq m,\,0\leq k\leq r_i-2$
- 2. The matrix $A(x_0)$ is nonsingular

$$A(x_0) = \begin{bmatrix} L_{g_1} L_f^{r_1 - 1} h_1(x_0) & \dots & L_{g_m} L_f^{r_1 - 1} h_1(x_0) \\ \vdots & \ddots & \vdots \\ L_{g_1} L_f^{r_m - 1} h_m(x_0) & \dots & L_{g_m} L_f^{r_m - 1} h_m(x_0) \end{bmatrix}$$

With this definition we can find that, for the robot manipulators $A(x) = M(x)^{-1}$ and that the relative degree of every input is $r_i = 2$. As $\zeta = r_1 + ... + r_m = n$ the system has full order and therefore it has no internal dynamics. Now we can carry out the transformation $z = \phi(x), \phi: \mathbb{R}^n \to \mathbb{R}^n$, with:

$$\phi(x) = \begin{bmatrix} z_{1,1} \\ z_{2,1} \\ z_{1,2} \\ \vdots \\ z_{2,m} \end{bmatrix} = \begin{bmatrix} h_1(x) \\ L_f h_1(x) \\ h_2(x) \\ \vdots \\ L_f h_m(x) \end{bmatrix} = \begin{bmatrix} x_1 \\ x_{m+1} \\ x_2 \\ \vdots \\ x_{2m} \end{bmatrix}$$
(7)

With this transformation the system (4) is linearizable and becomes:

$$\dot{z} = \begin{bmatrix} \dot{z}_{1,1} \\ \dot{z}_{2,1} \\ \dot{z}_{1,2} \\ \vdots \\ \dot{z}_{2,m} \end{bmatrix} = \begin{bmatrix} z_{2,1} \\ \alpha_1(z) + \sum_{j=1}^m \beta_{j,1}(z)\tau_j \\ z_{2,2} \\ \vdots \\ \alpha_m(z) + \sum_{j=1}^m \beta_{j,m}(z)\tau_j \end{bmatrix}
y = \begin{bmatrix} y_1 & \dots & y_m \end{bmatrix}^T = \begin{bmatrix} z_{1,1} & \dots & z_{1,m} \end{bmatrix}^T$$
(8)

In the case of robot manipulators the transformation $z = \phi(x), \phi: \mathbb{R}^n \to \mathbb{R}^n$ is always a diffeomorphism and thereby $z=\phi(x)$ is an invertible transformation. This means, that if we can control (8) we can also control (4). The vector $\alpha(z): \mathbb{R}^{2m} \to \mathbb{R}^m$ is defined by $\alpha_i(z) = L_f^2 h_i(\phi^{-1}(z))$ and the matrix $\beta(z): R^{2m} \to R^{m \times m}$ by $\beta_{j,i}(z) = L_{g_j} L_f h_i(\phi^{-1}(z))$. We find that $\alpha(z) = [f_{m+1}(\phi^{-1}(z))...f_{2m}(\phi^{-1}(z))]^T$ and $\beta(z) = M(\phi^{-1}(z))^{-1}$. Thus the linearizing controller $\tau = \beta(z)^{-1}(v - \alpha(z))$ is called the perfect control. If we choose v_i for i = 1...m as follows

$$v_{i} = \dot{z}_{2,i} = \ddot{y}_{i} = \ddot{y}_{ref_{i}} - \rho_{1,i}(\dot{y}_{i} - \dot{y}_{ref_{i}}) - \rho_{2,i}(y_{i} - y_{ref_{i}})$$
(9)

the outputs of the system can follow any affine vector of trajectories of reference $y_{ref} \in C^2$ without any permanent error.

Remark 1: The controller $\tau = \beta(z)^{-1}(v - \alpha(z))$ requires the exact knowledge of all the states z_i as well as the knowledge of $\alpha_i(z) = L_f^2 h_i(x)$ and $\hat{\beta_{j,i}}(z) = L_{g_j} L_f h_i(x)$ for i = 1...m, j = 1...m at each point in time.

However, as we have assumed in assumption A.2, in the case of the robot manipulators we have no exact knowledge of the structure and the coefficients of $M(q),~C(q,\dot{q}),~g(q)$ and $p(\dot{q})$ which means that also $\alpha(z)$ and $\beta(z)$ are uncertain. Besides, according to assumption A.1, only the angular positions y = $[z_{1,1}...z_{1,m}]^T=[q_1...q_m]^T$ can be measured while the angular velocities $\dot{y}=[z_{2,1}...z_{2,m}]^T=[\dot{q}_1...\dot{q}_m]^T$ are unknown.

Following the ideas that presented in [8], [9] and [10] where the controller requires only least prior knowledge about the system (8) and can stabilize the system at the origin or make it follow any affine trajectory. The control scheme does not require the knowledge of $\alpha(z)$ and $\beta(z)$. The idea is to lump these uncertain terms into a new observable state that can be reconstructed from the available angular positions $[q_1...q_m]$. We introduce the new variable vector $\Theta \in \mathbb{R}^m$, which contains the uncertain functions $\alpha(z)$ and $\beta(z)$ for i=1...m:

$$\Theta_i(z,\tau) = \alpha_i(z) + \sum_{j=1}^m \left(\beta_{j,i}(z) - \beta_{e_{j,i}}(z)\right) \tau_j \tag{10}$$

 $\beta_e(z) \in R^{m \times m}$ is an user-defined approximation of $\beta(z)$ that has to fulfill $sign(\beta_e(z)) = sign(\beta(z))$. With this we can rewrite the system (8), for i = 1...m:

$$\dot{z}_{1,i} = z_{2,i}
\dot{z}_{2,i} = \Theta_i(z,\tau) + \sum_{j=1}^m \beta_{e_{j,i}}(z)\tau_j$$
(11)

Now we augment our system by m additional states $\eta_i(t) = \Theta_i(z,\tau)$ with i=1...m. In this way (11) becomes:

$$\dot{z}_{1,i} = z_{2,i}
\dot{z}_{2,i} = \eta_i(t) + \sum_{j=1}^m \beta_{e_{j,i}}(z)\tau_j
\dot{\eta}_i(t) = \Xi_i(z, \eta, \tau)$$
(12)

Where $\Xi_i(z,\eta,\tau)=\frac{\partial\Theta_i}{\partial z}\frac{dz}{dt}+\frac{\partial\Theta_i}{\partial\tau}\frac{d\tau}{dt}$, in assumption A.1 we have supposed that we have no exact knowledge about all the states x_i . Consequently the new state vector $\eta(t)\in R^m$ is also unknown. To solve this problem, we construct the following high-gain observer that is based on the available states $y=[z_{1,1}...z_{1,m}]$.

$$\dot{\hat{z}}_{1,i} = \hat{z}_{2,i} + L\kappa_{1,i}(z_{1,i} - \hat{z}_{1,i})
\dot{\hat{z}}_{2,i} = \hat{\eta}_i + \sum_{j=1}^m \beta_{e_{j,i}}(z)\tau_j + L^2\kappa_{2,i}(z_{1,i} - \hat{z}_{1,i})
\dot{\hat{\eta}}_i = L^3\kappa_{3,i}(z_{1,i} - \hat{z}_{1,i}), \quad i = 1...m$$
(13)

Now we have to choose the coefficients $\kappa_{i,j}$ in such a way that the polynomials $s^3 + \kappa_{1,i} s^2 + \kappa_{2,i} s + \kappa_{3,i}$, i=1...m have poles with negative real parts. L is a tuning parameter that has a strong influence on the error dynamics. Based on the estimates of the uncertainties $\eta(t)$ and the estimates of $[z_{2,1}...z_{2,m}]^T$ we can construct the following linearizing-like feedback controller

$$\tau = \beta_e(z)^{-1}(v - \hat{\eta}) \tag{14}$$

With the input vector $v \in \mathbb{R}^m$ that is defined as:

$$v_i = \ddot{y}_{ref_i} - \rho_{1,i}(\hat{z}_{2,i} - \dot{y}_{ref_i}) - \rho_{2,i}(z_{1,i} - y_{ref_i}),$$

$$i = 1...m$$
(15)

Proposition 1: The robust feedback method consists of the dynamic estimator (13) and the linearizing controller (15), that was constructed using the estimates of Θ (i.e. $\eta(t)$) and z that are provided by the high-gain observer.

Proof The proof of stability is equal for all the m degrees of freedom. Because of this, we will carry out a parallel proof for all the degrees of freedom and i=1...m will be valid. The stability of the observer, we define an estimation error $e_i \in R^3$ in the following way: $e_{j,i} = L^{r-j+1}(z_{j,i} - \hat{z}_{j,i}), \ j=1,2$ and $e_{3,i} = \eta_i - \hat{\eta}_i$. Now, using (12) and (13) we can write the error dynamics \dot{e}_i as:

$$\dot{e}_{1,i} = L(-\kappa_{1,i}e_{1,i} + e_{2,i})
\dot{e}_{2,i} = L(-\kappa_{2,i}e_{1,i} + e_{3,i})
\dot{e}_{3,i} = -L\kappa_{r+1,i}e_{1,i} + \Xi_{i}$$
(16)

Or written in Matrix form:

$$\dot{e}_{i} = L \underbrace{\begin{bmatrix} -\kappa_{1,i} & 1 & 0 \\ -\kappa_{2,i} & 0 & 1 \\ -\kappa_{3,i} & 0 & 0 \end{bmatrix}}_{A_{i}(\kappa)} e_{i} + \underbrace{\begin{bmatrix} 0 \\ 0 \\ \Xi_{i} \end{bmatrix}}_{\Gamma_{i}}$$

$$= LA_{i}(\kappa)e_{i} + \Gamma_{i} \tag{17}$$

The matrix $A_i(\kappa)$ is Hurwitz if the poles of the polynomial $s^3 + \kappa_{1,i}s^2 + \kappa_{2,i}s + \kappa_{3,i}$ are in the left pane of the complex plane. If this is the case, then, according to Lyapunov, there exists a positive definite and symmetric matrix P_i such that $P_iA_i + A_i^TP_i = -I_n$ where I_n is the identity matrix of dimension n. Now we choose $V_i(e_i) = e_i^TP_ie_i$ as Lyapunov function and get:

$$\dot{V}_{i}(e_{i}) = \frac{\partial V_{i}(e_{i})}{\partial e_{i}} \dot{e}_{i} = -L \|e_{i}\|^{2} + 2e_{i}^{T} P_{i} \Gamma_{i}
\leq -L \|e_{i}\|^{2} + 2 \|P_{i}\| \|e_{i}\| \|\Gamma_{i}\|$$
(18)

If Γ_i satisfies $\|\Gamma_i\| < r_1$ and $\|e_i\| < r_2$ for some $r_1 > 0$ and $r_2 > 0$ then $||P_i|| ||e_i|| ||\Gamma_i||$ is a bounded function. Let $\mu_i > 0$ be some positive constant and $2\|P_i\|\|e_i\|\|\Gamma_i\|<\mu_i$. We can write $V_i(e_i)\leq -L\|e_i\|^2+\mu_i$ for the stability of the observer $||e_i|| \leq \sqrt{\frac{\mu_i}{L}}$ has to be fulfilled for all i. We can see, that the estimation error e_i depends directly on L. As L increases, e_i will decrease and thereby also the estimation error bound. Because of this, L should be chosen as big as possible. We conclude: As all Γ_i are bounded, if $L>L^*>0$ then $e(t)\to 0$ for $t\to \infty$ and $(\hat{z}, \hat{\eta}) \to (z, \eta)$. With this we conclude, that (13) and (14) yield asymptotical stabilization of the system (8).□

To illustrate the proposed control scheme we will now apply the methodology to the case of a robot manipulator with m=2 rotatory degrees of freedom. With the help of the Lagrange or similar equations we can calculate $M(q), C(q,\dot{q}), g(q)$ of (1) as follwos

$$\begin{split} M_{11} &= m_1 l_{c1}^2 + m_2 l_1^2 + m_2 l_{c2}^2 + I_1 + I_2 + 2 m_2 l_1 l_{c2} cos(q_2) \\ &\cdot M_{12} = m_2 l_{c2}^2 + m_2 l_1 l_{c2} cos(q_2) + I_2 \\ M_{21} &= m_2 l_{c2}^2 + m_2 l_1 l_{c2} cos(q_2) + I_2 \\ M_{22} &= m_2 l_{c2}^2 + I_2 \\ C_{11} &= -m_2 l_1 l_{c2} sin(q_2) \dot{q}_2 \\ C_{12} &= -m_2 l_1 l_{c2} sin(q_2) (\dot{q}_1 + \dot{q}_2) \\ C_{21} &= m_2 l_1 l_{c2} \dot{q}_1 sin(q_2) \\ C_{22} &= 0 \\ g_1(q) &= g sin(q_1(m_1 l_{c1} + m_2 l_1) + m_2 g sin(q_1 + q_2) l_{c2} \\ g_2(q) &= m_2 g l_{c2} sin(q_1 + q_2) \end{split}$$

We will use the same friction term $p(\dot{q}) \in \mathbb{R}^2$ as in (2). Again $q \in \mathbb{R}^2$ are the angular positions of the links while $\dot{q} \in R^2$ are the angular velocities and $\tau \in R^2$ are the torques that are applied to the links. l_1, l_2 are the lengths of the links and l_{c1}, l_{c2} are the distances to their centers of mass. m_1, m_2 are the masses of the two elements, I_1, I_2 are their moments of inertia (including the motors, joints etc.) and g is the acceleration of gravity. After replacing $[x_1, x_2]^T = [q_1, q_2]^T$, $[x_3, x_4]^T = [\dot{q}_1, \dot{q}_2]^T$ and $M^*(x) = M^{-1}(x)$ we can rewrite our system (1):

$$\begin{bmatrix} \dot{x}_1 \\ \dot{x}_2 \\ \dot{x}_3 \\ \dot{x}_4 \end{bmatrix} = \begin{bmatrix} x_3 \\ x_4 \\ f_3(x) + M_{1,1}^* \tau_1 + M_{1,2}^* \tau_2 \\ f_4(x) + M_{2,1}^* \tau_1 + M_{2,2}^* \tau_2 \end{bmatrix}$$
(19)

Where $[f_3(x), f_4(x)]^T = M(x)^* (-C(x, \dot{x})\dot{x} - g(x) - p(\dot{x}))$. Using Definition 2 we find that the relative degree is r = 2. Now we introduce the augmented state vector $\eta(t) = [\eta_1(t), \eta_2(t)]^T$ and the user-defined approximation of $\beta_e(z)$ of $\beta(z) = M(\phi^{-1}(z))^{-1}$ and get:

$$\dot{z}_{1,1} = z_{2,1}
\dot{z}_{2,1} = \eta_1(t) + \beta_{e_{1,1}}(z)\tau_1 + \beta_{e_{2,1}}(z)\tau_2
\dot{\eta}_1(t) = \Xi_1(z, \eta, \tau)
\dot{z}_{1,2} = z_{2,2}
\dot{z}_{2,2} = \eta_2(t) + \beta_{e_{1,2}}(z)\tau_1 + \beta_{e_{2,2}}(z)\tau_2
\dot{\eta}_2(t) = \Xi_2(z, \eta, \tau)$$
(20)

For the reconstruction of the angular velocities $[z_{2,1},z_{2,2}]^T$ and the extended state $\eta(t)$ we construct the high-gain observer:

$$\dot{\hat{z}}_{1,1} = \hat{z}_{2,1} + L\kappa_{1,1}(z_{1,1} - \hat{z}_{1,1})
\dot{\hat{z}}_{2,1} = \hat{\eta}_1 + \sum_{j=1}^2 \beta_{e_{j,1}}(z)\tau_j + L^2\kappa_{2,1}(z_{1,1} - \hat{z}_{1,1})
\dot{\hat{\eta}}_1 = L^3\kappa_{3,1}(z_{1,1} - \hat{z}_{1,1})
\dot{\hat{z}}_{1,2} = \hat{z}_{2,2} + L\kappa_{1,2}(z_{1,2} - \hat{z}_{1,2})
\dot{\hat{z}}_{2,2} = \hat{\eta}_2 + \sum_{j=1}^2 \beta_{e_{j,2}}(z)\tau_j + L^2\kappa_{2,m}(z_{1,2} - \hat{z}_{1,2})
\dot{\hat{\eta}}_2 = L^3\kappa_{3,2}(z_{1,2} - \hat{z}_{1,2})$$
(21)

With the estimates of (21) we can implement the following controller:

$$\begin{bmatrix} \tau_1 \\ \tau_2 \end{bmatrix} = \begin{bmatrix} \beta_{e_{1,1}}(z) \ \beta_{e_{1,2}}(z) \\ \beta_{e_{2,1}}(z) \ \beta_{e_{2,2}}(z) \end{bmatrix}^{-1} \begin{bmatrix} v_1 - \hat{\eta}_1 \\ v_2 - \hat{\eta}_2 \end{bmatrix}$$
(22)

In order to follow the smooth trajectory of reference $y_{ref} = [y_{ref_1}, y_{ref_2}]^T$ we choose $v = [v_1, v_2]^T$ as:

$$v_{1} = \ddot{y}_{ref_{1}} - \rho_{1,1}(\hat{z}_{2,1} - \dot{y}_{ref_{1}}) - \rho_{2,1}(z_{1,1} - y_{ref_{1}})$$

$$v_{2} = \ddot{y}_{ref_{2}} - \rho_{1,2}(\hat{z}_{2,2} - \dot{y}_{ref_{2}}) - \rho_{2,2}(z_{1,2} - y_{ref_{2}})$$
(23)

Now the coupling factors were chosen as $K_{cp}=10$ while the we consider arbitrary initial conditions for q_{1i},q_{2i} and $\dot{q}_{1i},\dot{q}_{2i}$. The controller was switched on after 5 seconds and after 10 seconds a perturbation torque $\tau_{pert}=10~Nm$ was applied to both link connections of all the robots. τ_{pert} was turned off after 15 seconds. For the trajectory $y_d \in R^2$ we chose an arbitrary smooth function. The following variables were chosen equally for all four robots:

\overline{L}	g	l_1	l_2	l_{c1}	l_{c2}	I_1	I_2
20	9.81	0.35	0.3	0.175	0.145	0.0064	0.004

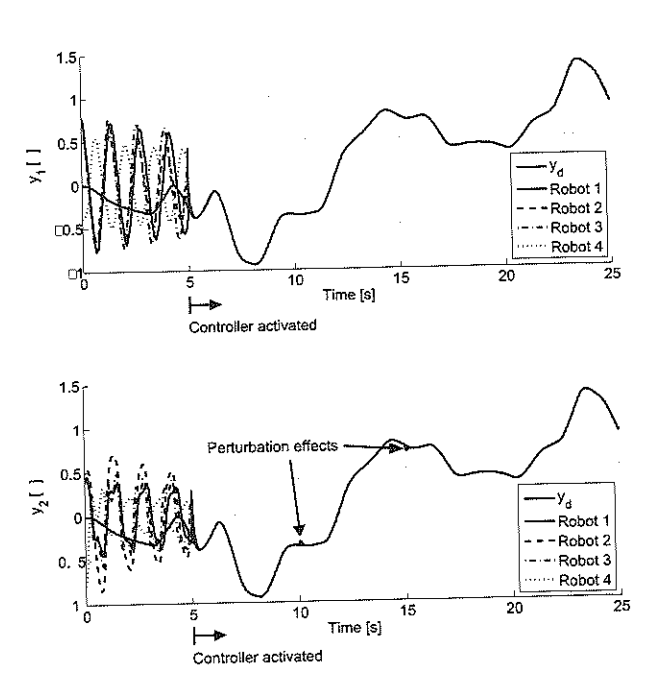
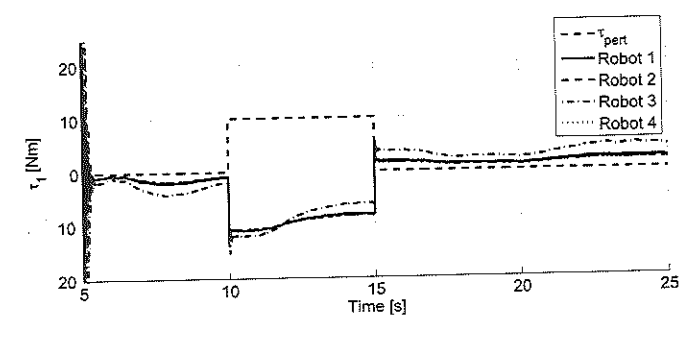


Fig. 1. (a) y_{d_1} and system output y_1 , (b) y_{d_2} and system output y_2

In Fig. 1 we can see the free oscillation of the uncontrolled robots in the first 5seconds. After this period the robots follow the arbitrary, user given trajectory y_d with actually very small errors. In Fig. 2 one can identify the torques generated to compensate the perturbation. Indeed, note that in Fig. 1, the effect of the



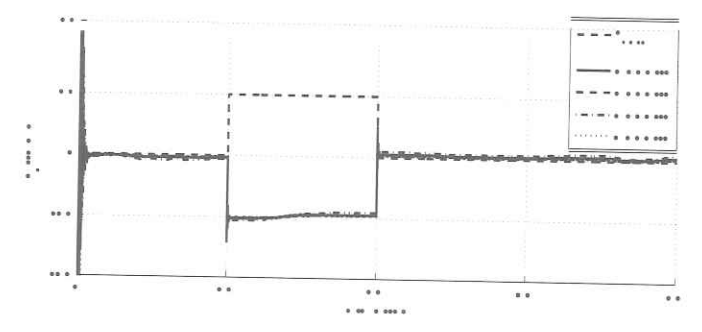


Fig. 2. (a) au_{pert_1} and system input au_1 , (b) au_{pert_2} and system input au_2

perturbation is actually very low (after 5 and after 10 seconds). This shows that the approach does not require the estimation of the perturbation.

4 Conclusions

In this work we have presented a robust control scheme that achieves synchronization of robot manipulators with an arbitrary number of degrees of freedom. It compensates unmodeled dynamics, uncertain or time-varying parameters as well as external perturbations and requires only the measurement of the angular positions at each point in time. The central feature of this approach is that the uncertainties are lumped into an extended state, which is reconstructed by a high-gain observer. Based on this estimation a linearizing-like control law is implemented that achieves the synchronization in combination with a mutual connection pattern of the robots. The methodology was demonstrated for the case of a 2 DOF robot manipulator and validated by numerical results. The proposed control scheme can also be applied to other mechanical systems, such as robot manipulators with linear degrees of freedom and in combination with other synchronization patterns.

References

- A. Pikovsky, M. Rosenblum, J. Kurths, Synchronization A universal concept in nonlinear sciences, Cambridge University Press, Cambridge, 2001
- [2] G. Renversez, Synchronization in two neurons: Results for a two-component dynamical model with time-delayed inhibition, Physica D 114 p. 147-171, 1998
- [3] B. Lading, E. Mosekilde, S. Yanchuk, Y. Maistrenko, Chaotic Synchronization between Coupled Pancreatic β-Cells, Prog. Theor. Phys. 139, p.164-177, 2000
- [4] J.J. Collins, I.N. Stewart, Coupled Nonlinear Oscillators and the Symmetries of Animal Gaits, Nonlinear Science Vol.3, p. 349-392, 1993
- [5] H. Kimura, K. Takase, Adaptive Running of a Quadruped Robot Using Forced Vibration and Synchronization, Journal of Vibration and Control 2006, May 2006
- [6] J.W. Hills, J.F. Jensen, Telepresence technology in medicine: principles and applications, Proceedings of the IEEE, Vol. 86, p.569-580, March 1998

- [7] H. Nijmeijer, A. Rodríguez-Angeles, Synchronization of Mechanical Systems, World Scientific Publishing, 2003
- [8] R. Femat, J. Alvarez-Ramírez, G. Fernández-Anaya, Adaptive synchronization of high-order chaotic systems: a feedback with low-order parametrization, Physica D 139 p. 231-246, 1999
- [9] R. Femat, R. Jauregui-Ortíz, G. Solís-Perales, A Chaos-Based Communication Scheme via Robust Asymptotic Feedback, IEEE Transactions on Circuits and Systems 1, Vol.48, p. 1161-1169, October 2001
- [10] G. Solís-Perales, S. Bowong, R. Femat, Synchronization of Dynamical Systems With Differente Order And Topology, 1st IFAC Conference on Analysis and Control of Chaotic Systems, p.175-180, June 2006
- [11] A. Isidori Nonlinear Control Systems, Springer Verlag, Berlin, 1989
- [12] R. Hensen, G. Angelis, M. Molengraft, A. Jaeger, J. Kok Grey-box modeling of friction: An experimental case-study, European Journal of Control, 6, p. 258-267, 2000

Signal and Image and Processing

Control of a nurse robot using voice commands and associative memories

Roberto A. Vázquez and Humberto Sossa

Centro de Investigación en Computación-IPN Av. Juan de Dios Batíz, esq. Miguel Othón de Mendizábal. Mexico City, 07738. Mexico Contact: ravem@ipn.mx, hsossa@cic.ipn.mx

(Paper received on February 29, 2008, accepted on April 15, 2008)

Abstract. NR-Alpha is a prototype of a surgical instrument server nurse robot. NR-Alpha is designed to provide to the surgeon the demanded surgery instruments. NR-Alpha perceives the surgeon's voice, recognizes the name of the instrument demanded and starts to look for the demanded instrument on the working area; once localized the instrument, NR-Alpha grapes it and finally reaches the hand of the surgeon to give him the demanded instrument. NR-Alpha is composed by three main modules: Artificial Vision Module (AVM), Voice Recognition Module (VRM) and Control Module (CM). In this paper, we describe how the VRM module could be implemented. To recognize the name of the instrument pronounced by the surgeon, VRM uses a dynamic associative memory (DAM). This DAM stores associations between a voice signals that encode the name of a surgery instrument and images of the corresponding instrument. Once the associative memory is trained, we would expect that when the surgeon pronounces, for example, "Forceps" the associative memory would recall the image of a forceps. Subsequently, the image recalled by the DAM could be used to localize the instrument. In order to test the accuracy of the proposal, we firstly train the DAM with associations of the instrument we would like the DAM learned. We then use a benchmark composed by 1800 voice signals to test the performance of the proposal.

1 Introduction

Robotics technology is developing dramatically. In this sense, a robot system is an alternative since accuracy for sensors and control system is increasing and computer technology for robots is rapidly developing. Robots are been used in increasingly complex surgical procedures. However these robots are not autonomous machines that carry out simple, pre-programmed instructions.

NR-Alpha is a surgical instrument server nurse robot (under development) composed by three main modules: An Artificial Vision Module (AVM), for the details refer to [11], A Voice Recognition Module (VRM) and Control Module (CM). In this paper we particularly emphasize on the implementation of the VRM module by means of reported associative memories.

An associative memory is a particular kind of neural network specially designed to recall output patterns in terms of input patterns that might appear altered by some kind

© E. V. Cuevas, M. A. Perez, D. Zaldivar, H. Sossa, R. Rojas (Eds.) Special Issue in Electronics and Biomedical Informatics, Computer Science and Informatics
Research in Computing Science 35, 2008, pp. 77-85



of noise, refer for example to [1], [2], [3], [4], [6], [7] and [8]. Most of these associative models have several constraints that limit their applicability in real life problems. In order to achieve the best performance the input patterns have to satisfy several conditions. Recently in [6] and [7] a new dynamic associative model (DAM) was proposed. This model can be used to recall a set of images even if these images suffer affine transformations. This model also has been applied to different pattern recognition problems. Refer for example to [6], [9] and [10].

In this paper we describe how the proposed associative model was implemented into the VRM for recognizing the name of the instrument pronounced by the surgeon. This DAM stores associations between a voice signals that encode the names of a surgery instruments and images of them. Once trained the associative memory we expect that when the surgeon says for example "Forceps" the associative memory recall the image of a forceps. Subsequently, the image recalled by the DAM could be used to localize the instrument. In order to test the accuracy of the proposal, we firstly train the DAM with associations of the instrument we would like the DAM learned, then during recognition, we use a benchmark composed by 1800 voice signals.

2 Description of the dynamic associative model

This model is not an iterative model as Hopfield's model [1]. The model emerges as an improvement of the model proposed in [4] which is not an iterative model. Let $\mathbf{x} \in \mathbf{R}^n$ and $\mathbf{y} \in \mathbf{R}^m$ an input and output pattern, respectively. An association between input pattern \mathbf{x} and output pattern \mathbf{y} is denoted as $\left(\mathbf{x}^k, \mathbf{y}^k\right)$, where k is the corresponding association. Associative memory: \mathbf{W} is represented by a matrix whose components w_{ij} can be seen as the synapses of the neural network. If $\mathbf{x}^k = \mathbf{y}^k \forall k = 1, \dots, p$ is auto-associative, otherwise it is hetero-associative. A distorted version of a pattern \mathbf{x}^k to be recalled will be denoted as \mathbf{x}^k . If an associative memory is fed with a distorted version of \mathbf{x}^k and the output obtained is exactly \mathbf{y}^k , we say that recalling is robust.

2.1 Building the associative memory

This model is bio-inspired in some biological ideas of human brain. Humans, in general, do not have problems recognizing patterns even if these are altered by noise. Several parts of the brain interact together in the process of learning and recalling a pattern. This model defines several interacting areas, one per association we would like the memory to learn. Also integrate the capability to adjust synapses in response to an input stimulus. Before an input pattern is learned or processed by the brain, it is hypothesized that it is transformed and codified by the brain. This process is simulated using the procedure introduced in [5].

This procedure allows computing codified patterns from input and output patterns denoted by $\overline{\mathbf{x}}$ and $\overline{\mathbf{y}}$ respectively; $\hat{\mathbf{x}}$ and $\hat{\mathbf{y}}$ are de-codifying patterns. Codified and de-codifying patterns are allocated in different interacting areas and d defines of much these areas are separated. On the other hand, d determines the noise supported by our model. In addition a simplified version of \mathbf{x}^k denoted by s_k is obtained as:

$$s_k = s(\mathbf{x}^k) = \mathbf{mid} \ \mathbf{x}^k \tag{1}$$

where mid operator is defined as mid $x = x_{(n+1)/2}$.

When the brain is stimulated by an input pattern, some regions of the brain (interacting areas) are stimulated and synapses belonging to those regions are modified. In this model, the most excited interacting area is call active region (AR) and could be estimated as follows:

(2) $ar = r(\mathbf{x}) = \arg\left(\min_{i=1}^{p} |s(\mathbf{x}) - s_i|\right)$

Once computed the codified patterns, the de-codifying patterns and s_k we can compute the synapses of the associative memory as follows:

Let $\{(\overline{\mathbf{x}}^k, \overline{\mathbf{y}}^k) | k = 1, ..., p\}$, $\overline{\mathbf{x}}^k \in \mathbf{R}^n$, $\overline{\mathbf{y}}^k \in \mathbf{R}^m$ a fundamental set of associations (codified patterns). Synapses of associative memory W are defined as:

$$w_{ij} = \overline{y}_i - \overline{x}_j \tag{3}$$

In short, building of the associative memory can be performed in three stages as:

- 1. Transform the fundamental set of association into codified and de-codifying patterns by means of previously described Procedure 1.
- 2. Compute simplified versions of input patterns by using equa-
- 3. Build ${f W}$ in terms of codified patterns by using equation 3.

2.2 Modifying synapses of the associative model

In this model, synapses could change in response to an input stimulus; but which synapses should be modified? There are synapses that can be drastically modified and they do not alter the behavior of the associative memory. In the contrary, there are synapses that only can be slightly modified to do not alter the behavior of the associative memory; we call this set of synapses the kernel of the associative memory and it is denoted by $\mathbf{K}_{\mathbf{w}}.$ In this model are defined two types of synapses: synapses that can be modified and do not alter the behavior of the associative memory and synapses belonging to the kernel of the associative memory. These last synapses play an important role in recalling patterns altered by some kind of noise.

Let $K_w \in \mathbb{R}^n$ the kernel of an associative memory W. A component of vector Kw is defined as:

$$kw_i = \mathbf{mid}\left(w_{ij}\right), j = 1, \dots, m \tag{4}$$

Synapses that belong to $\mathbf{K}_{\mathbf{w}}$ are modified as a response to an input stimulus. Input patterns stimulate some ARs, interact with these regions and then, according to those interactions, the corresponding synapses are modified. Synapses belonging to $\mathbf{K}_{\mathbf{W}}$ are modified according to the stimulus generated by the input pattern. This adjusting factor is denoted by Δw and can be computed as:

$$\Delta w = \Delta \left(\mathbf{x} \right) = s \left(\overline{\mathbf{x}}^{ar} \right) - s \left(\mathbf{x} \right) \tag{5}$$

where ar is the index of the AR.

Finally, synapses belonging to K_w are modified as:

$$\mathbf{K}_{\mathbf{W}} = \mathbf{K}_{\mathbf{W}} \oplus \left(\Delta w - \Delta w_{old}\right) \tag{6}$$

where operator \oplus is defined as $\mathbf{x} \oplus e = x_i + e \ \forall i = 1,...,m$. As you can appreciate, modification of $\mathbf{K}_{\mathbf{w}}$ in equation 6 depends of the previous value of Δw denoted by Δw_{old} obtained with the previous input pattern. Once trained the **DAM**, when it is used by first time, the value of Δw_{old} is set to zero.

2.3 Recalling a pattern using the proposed model

Once synapses of the associative memory have been modified in response to an input pattern, every component of vector \overline{y} can be recalled by using its corresponding input vector x as:

$$\overline{y}_i = \mathbf{mid}(w_{ij} + \overline{x}_j), j = 1, \dots, n$$
(7)

In short, pattern \overline{y} can be recalled by using its corresponding key vector \overline{x} or \tilde{x} in six stages as follows:

- 1. Obtain index of the active region ar by using equation 2.
- 2. Transform \mathbf{X}^k using de-codifying pattern $\hat{\mathbf{X}}^{ar}$ by applying the following transformation: $\hat{\mathbf{x}}^k = \mathbf{x}^k + \hat{\mathbf{x}}^{ar}$
- 3. Compute adjust factor $\Delta w = \Delta \left(\widehat{\mathbf{x}}\right)$ by using equation 5. 4. Modify synapses of associative memory \mathbf{W} that belong to $\mathbf{K}_{\mathbf{W}}$ by using equation 6.
- 5. Recall pattern $\widehat{\mathbf{y}}^k$ by using equation 7.
- 6. Obtain \mathbf{y}^k by transforming $\widehat{\mathbf{y}}^k$ using de-codifying pattern $\hat{\mathbf{y}}^{ar}$ by applying transformation: $\mathbf{y}^k = \hat{\mathbf{y}}^k - \hat{\mathbf{y}}^{ar}$.

The formal set of prepositions that support the correct functioning of this dynamic model and the main advantages again other classical models can be found in [12].

3 Experimental results

Several experiments were performed in order to test the accuracy of the proposal when a person pronounces the name on the instrument he needs. Firstly, we recorded a collection of signal voices. We recorded the name of five different instruments (backcock forceps, sponge forceps, adson forceps, allis forceps and rat tooth forceps).

Each signal voice was recorded in a wav file (PCM format, 44.1 KHz, 16 bits and mono). In average the duration of each sample was of 450 ms. Some samples of the signal voices are shown in Fig. 1. In total, 1960 signals were analyzed through the experiments.

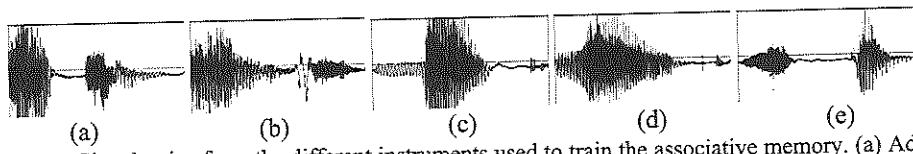


Fig. 1. Signal voice from the different instruments used to train the associative memory. (a) Adson. (b) Allis. (c) Backcock. (d) Rat tooth. (e) Sponge.

In addition, we proceeded to obtain an image of each instrument in order to associate it with its corresponding signal voice. Some images are shown in Fig 2.

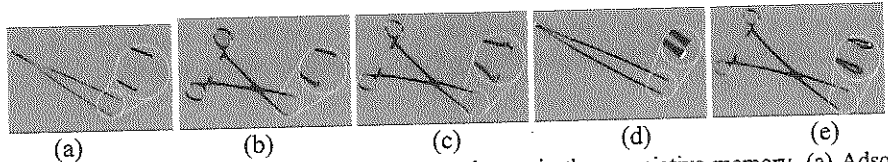


Fig. 2. Images from the different instruments used to train the associative memory. (a) Adson. (b) Allis. (c) Backcock. (d) Rat tooth. (e) Sponge.

In order to train the associative memory, we firstly transformed the signal sound of each instrument into a raw vector and the image of each instrument into a raw vector. Then each signal sound vector was associated with its corresponding image vector. Finally the associate memory was trained using the procedures described in section 2.

Experiment 1. In this experiment, we verified if the associative model was capable to recall the fundamental set of associations, in other words, if the DAM was able to recall the image associated to the signal voice used as input pattern. In average, the accuracy of the proposal in this experiment was of 100%, some examples are shown in Fig. 3.

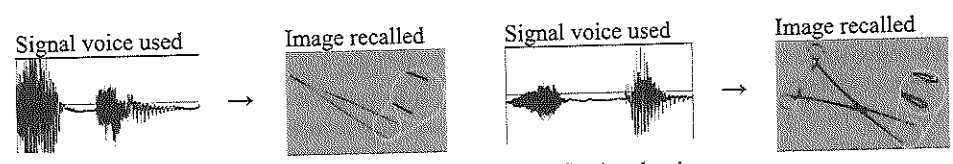


Fig. 3. Some examples of Images recalled using an specific signal voice.

Experiment 2. In this experiment, we verified if the DAM was able to recall the image associated to the signal voice used as input pattern, even if the signal voice is altered by additive noise (AN). To do this, each signal voice previously recorder was contaminated with additive noise altering from 2% until 90% of the information. 89 new samples were generated from each signal voice already recorder. This new set of signal voices was composed for 440 samples, some examples are shown in Fig. 4. In average, the accuracy of the proposal using this set of signal voices was of 71.3%.

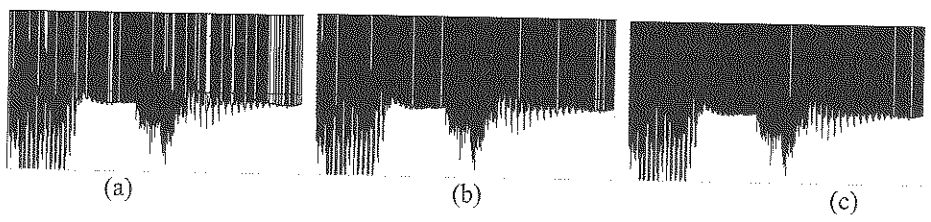


Fig. 4. (a-c) Signal voice of the adson instrument contaminated with additive noise.

Experiment 3. In this experiment, we verified if the DAM was able to recall the image associated to the signal voice used as input pattern, even if the signal voice is altered by subtractive noise (SN). To do this, each signal voice previously recorder was contaminated with subtractive noise altering from 2% until 90% of the information. 89 new samples were generated from each signal voice already recorder. This new set of signal voices was composed for 440 samples, some examples are shown in Fig. 5. In average, the accuracy of the proposal using this set of signal voices was of 71.6%.

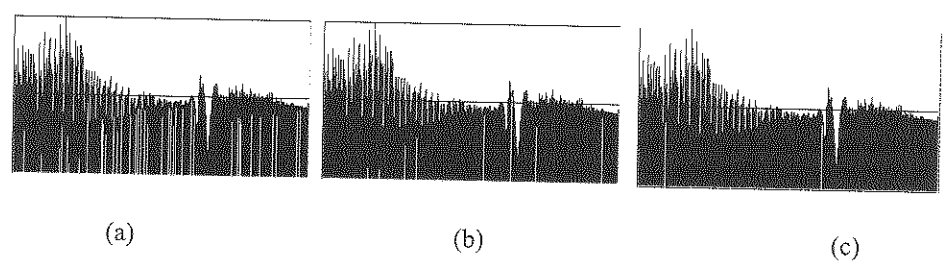


Fig. 5. (a-c) Signal voice of the allis instrument contaminated with subtractive noise.

Experiment 4. In this experiment, we verified if the DAM was able to recall the image associated to the signal voice used as input pattern, even if the signal voice is altered by mixed noise (MN). To do this, each signal voice previously recorder was contaminated with mixed noise altering from 2% until 90% of the information. 89 new samples were generated from each signal voice already recorder. This new set of signal voices was composed for 440 samples, some examples are shown in Fig. 6. In average, the accuracy of the proposal using this set of signal voices was of 79.55%.

Experiment 5. In this experiment, we verified if the DAM was able to recall the image associated to the signal voice used as input pattern, even if the signal voice is altered by Gaussian noise (GN). To do this, each signal voice previously recorder was contaminated with Gaussian noise altering from 2% until 90% of the information. 89 new samples were generated from each signal voice already recorder. This new set of signal voices was composed for 440 samples, some examples are shown in Fig. 7. In average, the accuracy of the proposal using this set of signal voices was of 74%.

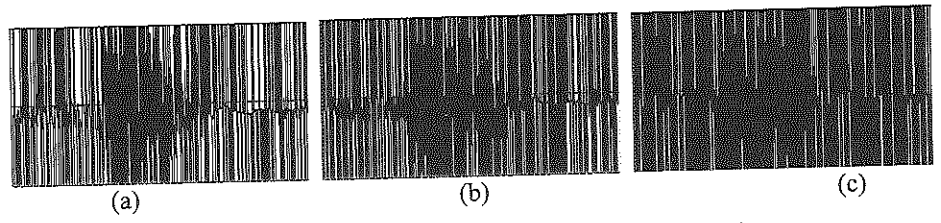


Fig. 6. Signal voice of the backcock instrument contaminated with mixed noise.

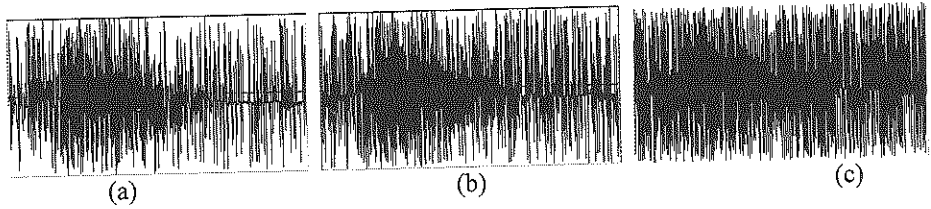


Fig. 7. (a-c) Signal voice of the rat tooth instrument contaminated with Gaussian noise.

Experiment 6. In this experiment, we verified if the DAM was able to recall the image associated to the signal voice used as input pattern, even if the signal voice is recorded at different tempo. To do this, each signal voice previously recorder was recorded 10 times. Ten new deformed samples (DEF) were recorded from each signal voice already recorder. This new set of signal voices was composed of 200 samples, some examples are shown in Fig. 8. In average, the accuracy of the proposal using this set of signal voices was of 32%.

Experiment 7. Despite of the low accuracy obtained, the results are encouraging because in more than the 50% of the samples, used on each experiment, a human is unable to perceive the name of the instrument. However, in order to increase the accuracy of the proposal we decided to apply the technique described in [10] for face recognition to the voice recognition problem. In [10], the authors suggest to compute a simplified version of the DAM model by using a random selection of stimulating points. For the details, refer to [10].

We tested again the accuracy of the proposal by using 1, then 2, them 3 until 50 stimulating points. In Fig. 9 it is shown the results obtained. As you can appreciate, the accuracy increases when the number of stimulating points increases. When we used more than 20 stimulating points the accuracy of the proposal was almost of 100% for the samples altered by additive, subtractive, mixed and Gaussian noise. Also we can appreciate that the accuracy slightly increases to 50% for the temporal deformed voice patterns.

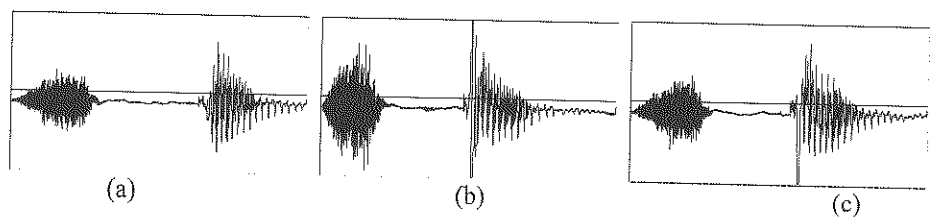


Fig. 8. (a-c) Deformed signal voice of the sponge instrument.

Accuracy of the proposal

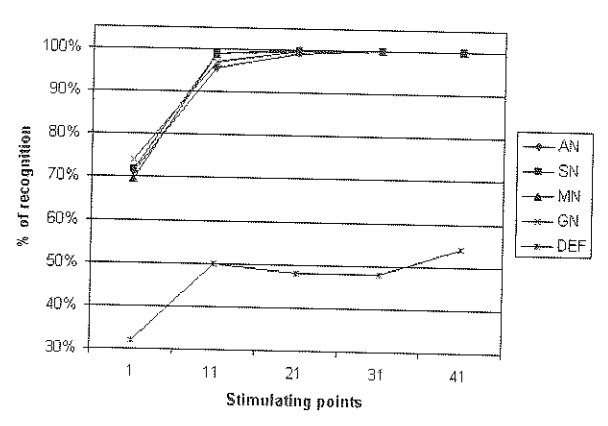


Fig. 9. Behavior of the proposal with the collections of altered signal voices using different number of stimulation points.

4 Conclusions

We have described how the VRM of NR-alpha prototype robot was implemented. We have demonstrated that associative memories, particularly dynamic associative memories can be used as powerful tools for voice recognition.

The accuracy of the proposed model was tested by using different sets of complex signal sounds and the result obtained supports the robustness of the proposals. We have studied the behavior of the model when a voice signal is contaminated with additive, subtractive, mixed, Gaussian noise and temporal deformations. The presented results are highly encouraged.

Nowadays we are applying some preprocessing techniques to increase the accuracy of the proposal when the voice signals are pronounced at different tempo by different people. Also we are integrating the VRM and AVM modules to localize an instrument using a voice command.

Acknowledgment. This work was economically supported by SIP-IPN under grants 20071438, 20082948 and CONACYT under grant 46805.

References

- [1] Hopfield, J. J.: Neural networks and physical systems with emergent collective computational abilities. *Proc. of the Nat. Academy of Sciences*, 79: 2554-2558 (1982)
- [2] Kohonen T.: Correlation matrix memories. IEEE Trans on Comp. 21(4):353-359 (1972)
- [3] Ritter G. X., Sussner P., Diaz de Leon J. L.: Morphological associative memories. IEEE Trans Neural Networks 9(2):281–293 (1998)
- [4] Sossa H., Barron R., Vazquez R. A.: New associative memories to recall real-valued patterns. In Alberto Sanfeliu, José Francisco Martínez Trinidad, Jesús Ariel Carrasco-Ochoa (Eds.) CIARP 2004. LNCS, vol. 3287, pp. 195-202, Springer (2004)
- [5] Sossa H., Barrón R., Vázquez R. A.: Transforming Fundamental set of Patterns to a Canonical Form to Improve Pattern Recall. *LNAI* 3315:687-696 (2004)
- [6] Vazquez R. A., Sossa H.: Associative Memories Applied to Image Categorization. In: Martínez-Trinidad, J.F., Carrasco Ochoa, J.A., Kittler, J. (eds.) CIARP 2006. LNCS, vol. 4225, pp. 549–558. Springer, Heidelberg (2006)
- [7] Vazquez R. A., Sossa H., Garro B. A.: A New Bi-directional Associative Memory. In: Gelbukh, A., Reyes-Garcia, C.A. (eds.) MICAI 2006. LNCS (LNAI), vol. 4293, pp. 367–380. Springer, Heidelberg (2006)
- [8] Sussner P., Valle M.: Gray-Scale Morphological Associative Memories. IEEE Trans. on Neural Networks, vol.17, No.3, pp.559-570 (2006)
- [9] Vazquez R. A., Sossa H., Garro B. A.: 3D Object recognition based on low frequencies response and random feature selections. In Alexander Gelbukh, A. F. Kuri Morales (Eds.): MICAI 2007. LNAI, vol. 4827, pp. 694-704 (2007)
- [10] Vazquez R. A., Sossa H., Garro B. A.: Low frequency responses and random feature selection applied to face recognition. In Mohamed Kamel, Aurelio Campilho (Eds.): ICIAR 2007. LNCS, vol. 4633, pp. 818-830, Springer (2007)
- [11] Sossa H., Vazquez R. A., Barron R.: Reconocimiento y localización de instrumental medico usando análisis automatizado de imágenes. Revista Mexicana de Ingeniería Biomédica, 26(2):75-85, SOMIB (2005)
- [12] Vazquez R. A., Sossa, H.: A new associative memory with dynamical synapses (submitted to Neural Processing Letters, 2007)

Detecting Scale-Sensitivity in Image Hierarchies for Coding and Compression

J. Alejandro Butrón Guillén¹ and Richard Harvey²

¹Centro Nacional de Actualización Docente CNAD Estanislao Ramírez s/n, col. Selene. México 13420, D.F. ²School of Computing Sciences, University of East Anglia Norwich, NR4 7TJ, UK.

Contact: abutron@cnad.edu.mx, rwh@cmp.uea.ac.uk

Abstract. This paper examines human sensitivity to errors introduced by two types of lossy image coders. Our interest is a special type of morphological scale-space tree called a sieve because such trees are thought to be useful for image understanding and other purposes, but we also examine a conventional lossy coder: JPEG. The paper introduces a new way of measuring image quality, a type of Turing test and we show how the method can be normalized to compare different images and coders. We conclude that content of the image can have a significant effect on the perception of image quality.

1 Introduction

Motivated by MPEG-7 and MPEG-4, image and video analysis and compression based on connected-set mathematical morphology ([1] for example) have become topics of some interest. Lossy compression based on such techniques typically involves deleting small-scale regions and/or coding regions using an approximation to their true shape. A key property of many connected set methods is their hierarchical structure [1], [2], in which the image is represented as a tree with small-scale regions as the leaves and root representing the whole image. Such trees can become large, it is therefore of some interest to know how many of the leaves may be deleted from a tree without affect the quality perceived by a human observer. The sensitivity of observers to the small scale contained in images is thus investigated and reported. Images are filtered with the sieve, a type of hierarchical connected-set representation, and a subjective test devised that allows us to measure the effect of deleting regions from the hierarchy.

The rest of the paper is organized as follows. In Section 2, we review the sieve algorithm and describe the hierarchical structure for decomposing images into hierarchies of contours. Section 3 presents the experimental setup for detecting the sensitivity to contours, together with a discussion of the results, and in Section 4 we make some initial conclusions for the development of a compressor based on the sieve.

© E. V. Cuevas, M. A. Perez, D. Zaldivar, H. Sossa, R. Rojas (Eds.) Special Issue in Electronics and Biomedical Informatics, Computer Science and Informatics
Research in Computing Science 35, 2008, pp. 87-96



2 The sieve algorithm

The sieve performs a non-linear decomposition of an image by removing extrema of increasing scale, and thus making a simplification of the input image. It is a filter based on graph-morphology [3] that removes features of the image without introducing new extrema. The theory is well established [4], [5], [6], [2], and what follows is a summary of this theory and a description of the hierarchical representation.

An example of a progressive simplification performed by the sieve is shown in Figure 1. This simplification is obtained by using the sieve at different increasing scales. The sieve treats the input image as a graph G=(V,E), where V represents the set of vertices for each pixel contained in the image, and E the set of edges that describe the connectivity between those vertices.

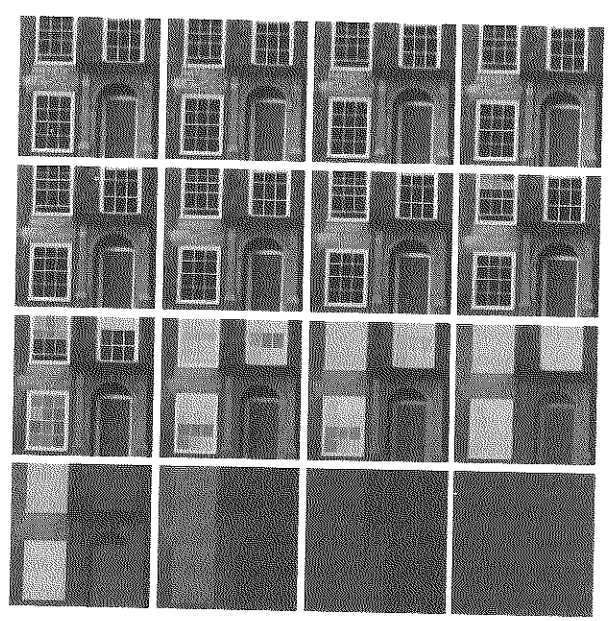


Fig. 1. Sieve decomposition of an original image (top left) processed at scales 2^n , with n=0 ... 15 (shown left-to-right). Note that, unlike wavelets, sieves can be applied at arbitrary scales.

An example of this representation is given in Figure 2 for a greyscale image of 4×4 pixels, where the vertices (V) are:

$$V = \{1, 2, 3, \dots, 14, 15, 16\} \tag{1}$$

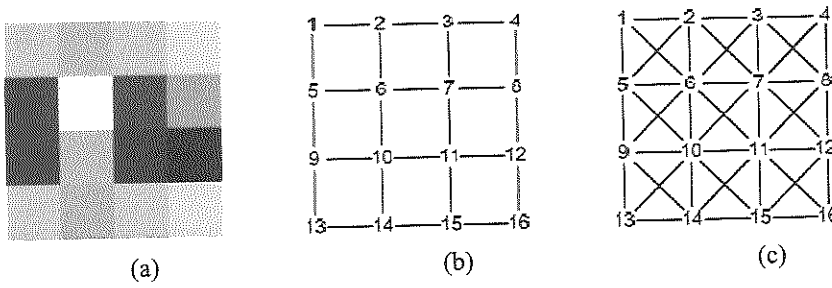


Fig. 2. Graph Representation: (a) Greyscale image. (b) Vertex labelling and the four-connectivity edges. (c) Vertex labelling and the eight-connectivity edges.

and for four-connectivity the set of edges E4,

$$E_4 = \{\{1,2\},\{1,5\},...,\{12,16\},\{15,16\}\}$$
 (2)

or using eight-connectivity the set of edges E₈,

$$E_8 = \{\{1,2\},\{1,5\},\{1,6\},...,\{11,16\},\{12,16\},\{15,16\}\}$$
 (3)

where the image intensities define a function f, of the vertex number f(v) with $v \in V$. Based on the connectivity between pixels of a given image, Cr(G) denotes the set of connected subsets C of size r, within G,

$$C_r(G, \nu) = \{ \xi \in C_r(G) \mid \nu \in \xi \}$$

$$\tag{4}$$

 ξ are the set of connected regions of size r that contain the vertex v. For example, for the image in Figure 2 the set of four-connected regions of size 2 for the vertex v = 10are

$$C_2(G,10) = \{\{6,10\}, \{9,10\}, \{10,11\}, \{10,14\}\}$$
 (5)

The sieve removes extrema (maxima or minima) by applying a morphological operator ϕ_s over $C_r(G)$. ϕ may be a morphological opening γ_r , closing ψ_r , or the alternating sequential filters \mathcal{M} and \mathcal{U} , defined on connected sets as an operator $\phi_r: \mathbf{Z}^v \to \mathbf{Z}^v$ for each integer $r \ge 1$, as

$$\gamma_r f(x) = \max_{\xi \in C_r(G, x)} \min_{u \in \xi} f(u)$$
 (6)

$$\psi_r f(x) = \min_{\xi \in C_r(G, x)} \max_{u \in \xi} f(u)$$
 (7)

$$\mathcal{M}_{r}f(x) = \gamma_{r}(\psi_{r}(f(x))) \tag{8}$$

$$\mathcal{H}_r f(x) = \psi_r(\gamma_r(f(x))) \tag{9}$$

The sieve operates on an image by applying the operator ϕ from scale one and increasing sequentially until no new maxima or minima are found. The differences between successive stages of a sieve are called granule functions, and contain all the connected sets that have been removed from the image for each scale s.

2.1 Sieve-trees

The complete sequence of granules that are obtained at the different stages of the sieve can be represented in a hierarchical structure, called the sieve tree [2], [7]. An example decomposition is shown in Figure 3. The original image is shown on the top right and successive simplifications are shown down the right-hand side. The granules are shown on the left and the containment of one region within another is indicated by an edge of the tree. The head region is seen to contain the face region and four children are linked from this node -- two eyes, a mouth and a nose. Each eye has two children. This tree has a depth of five and so is sometimes described as having five *levels*. The highest level nodes are nodes 1 and 2 which are at level 5, nodes 3, 4, 5 and 6 are all at level 4, node 7 is at level 3, node 8 is at level 2 and the root, node 9, is at level 1.

The sieve tree represents a transformation of the image to the granule domain, and it is possible to recover the original image by parsing the nodes of the tree and merging all the regions, taking in consideration the intensity profile for each node.

3 Visual comparisons between images

A graphical user interface (GUI) displays a group of images in a controlled environment with constant lighting and CRT displaying, and it is the interface in which the observer answers a subjective question about the originality of each image, as shown in Figure 4. The test set of sixteen images were captured at a resolution of 2,464 x 1,648 pixels, 24 bits per pixel, under natural conditions, using a Canon EOS 1D camera and recorded in uncompressed form. These were then resized to 640 x 428 pixels, 24 bits per pixel using the bicubic downsampling in Matlab. Figure 5 shows this test set. The images were processed at scales 0, 10 and 100 with the sieve algorithm, and also saved at quality levels of 20, 60 and 100, using the JPEG compressor. A total of 96 images were obtained from the original set, each image was displayed twice in a random order, having a total of 192 displayed images to 20 observers, students with good correct vision, same images with a disagreement were reshown a third time for a later vote. The viewing distance was variable depending on the observer and the time for the experiment was not limited.

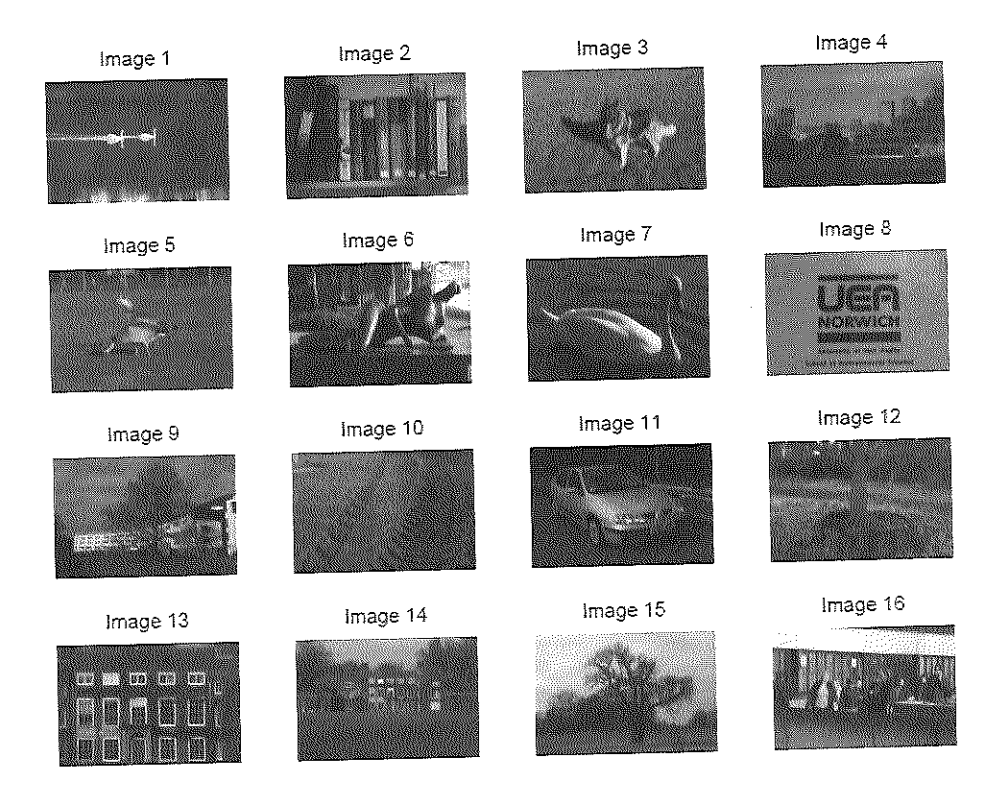


Fig. 5. Test set, taken under natural light conditions using a Canon EOS 1D digital camera, and recorded in uncompressed form. These were then resized to 640 x 428, 24 bits per pixel, using the downsampling in Matlab.

A decreasing score was obtained for all the images when sieved at scales 10 and 100, as shown in Figures 6(e, f), as the regions of small scale (and to which the eye is susceptible) were removed. As mentioned before, not all the images were accepted even when compressed at 100% with JPEG or sieved at area-scale of 0. This because, for comparing the acceptance of each image depending on their original score, the images compressed with JPEG and processed with the sieve algorithm were normalized with the value they obtained at this compressing value of 100% and area-scale of 0, for creating a "ratio of ratios" that considers the original score.

The results for the JPEG compressor are presented in Figure 7(a). The graph for JPEG 60% quality shows that some images improve against the originals at 100%. All the images decrease their acceptance when compressed with JPEG at 20% quality. Considering the same original scoring, Figure 7(b) shows the behaviour for the images when sieved at different scales. Only three images, 2, 8 and 7, have a scoring ratio of 0.8 or more at scale 10, the rest of the images are below 0.6. The graph for scale 100 shows the decreasing score for the images, arranged as in area-scale of 10.

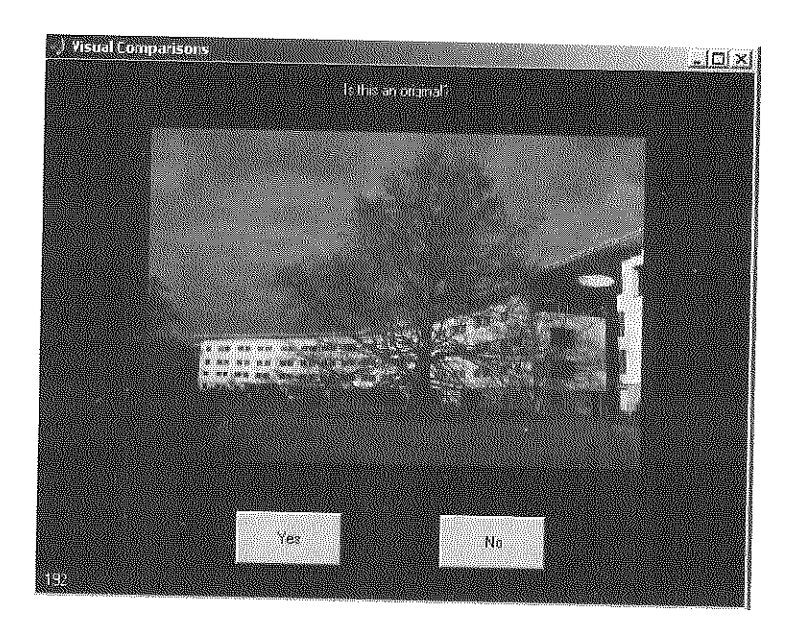


Fig. 4. Interface for a subjective test.

The acceptance of an image as an original depends not only in the compression quality or the scale at which they were sieved, but also in the contents of each image. Even when compressed at 100% quality with JPEG, not all the observers could identify them as originals. Figure 6(a) shows the fraction of observers that answered "yes" to the question "is this an original?" For image 1, 40% of the observers answered "yes" whereas for image 10, 95% answered "yes", illustrating the well known effect that the content of the image affects the visibility of compression errors. Only images 10 and 13 got a 95% acceptance. A similar behaviour is plotted in Figure 6(d), where the images were sieved at scale 0, and thus have the same quality level as when compressed at 100% with JPEG. The difference between Figure 6(a) and (d) is an indication of the variation in the experiment, since they are both acceptance ratios measured on identical sets.

Figure 6(b) (JPEG 60% quality) improves some scores and degrades others. Moving to Figure 6(c), all scores degrade with images 3, 10 and 13 degrading the least. A significant factor seems the presence of visual texture - JPEG artifacts are hard to spot in textured regions. Image 13 is slightly surprising, although we note it contains quite a lot of texture and the object boundaries align with the pixel grid, so are well represented by JPEG coding blocks.

The acceptance for all the images decreases in Figure 6(c), as the quality of the compressed file was of 20% only.

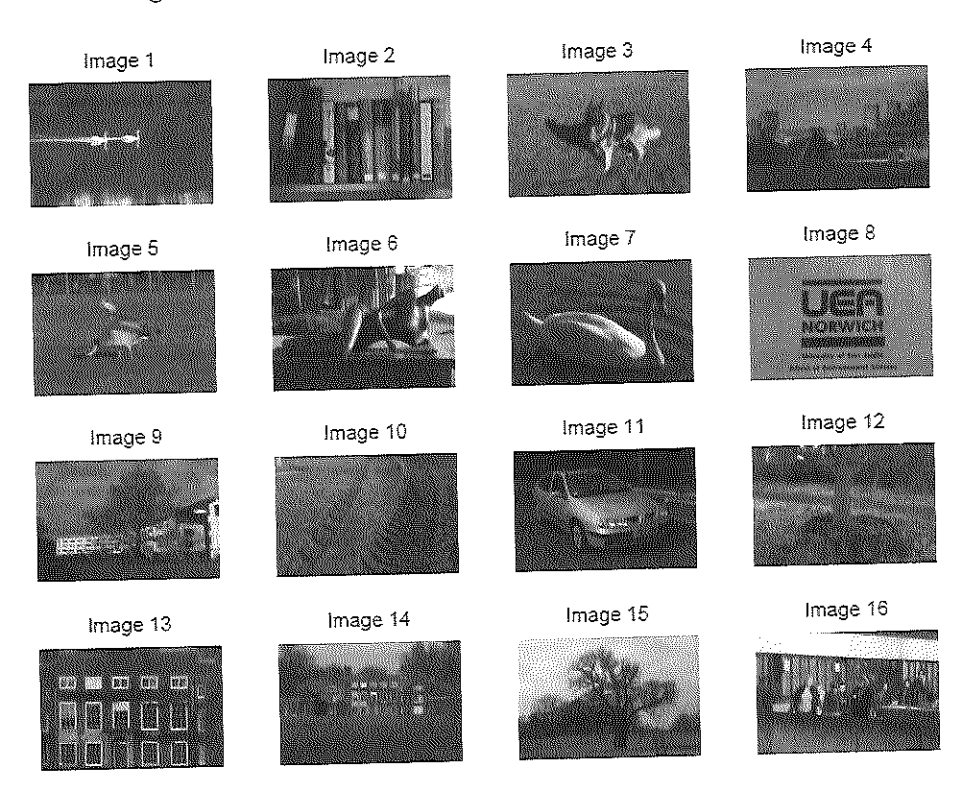


Fig. 5. Test set, taken under natural light conditions using a Canon EOS 1D digital camera, and recorded in uncompressed form. These were then resized to 640 x 428, 24 bits per pixel, using the downsampling in Matlab.

A decreasing score was obtained for all the images when sieved at scales 10 and 100, as shown in Figures 6(e, f), as the regions of small scale (and to which the eye is susceptible) were removed. As mentioned before, not all the images were accepted even when compressed at 100% with JPEG or sieved at area-scale of 0. This because, for comparing the acceptance of each image depending on their original score, the images compressed with JPEG and processed with the sieve algorithm were normalized with the value they obtained at this compressing value of 100% and area-scale of 0, for creating a "ratio of ratios" that considers the original score.

The results for the JPEG compressor are presented in Figure 7(a). The graph for JPEG 60% quality shows that some images improve against the originals at 100%. All the images decrease their acceptance when compressed with JPEG at 20% quality. Considering the same original scoring, Figure 7(b) shows the behaviour for the images when sieved at different scales. Only three images, 2, 8 and 7, have a scoring ratio of 0.8 or more at scale 10, the rest of the images are below 0.6. The graph for scale 100 shows the decreasing score for the images, arranged as in area-scale of 10.

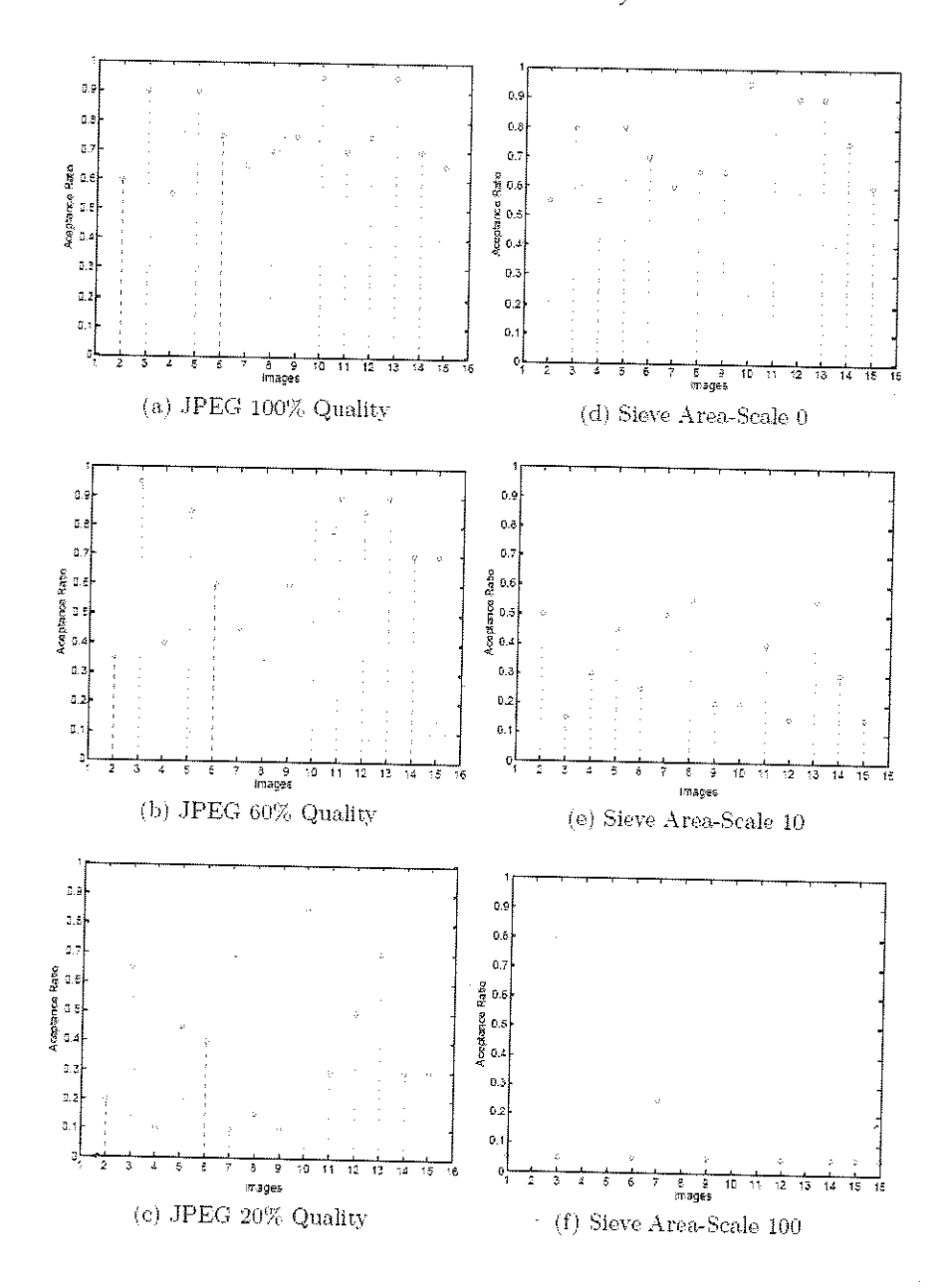
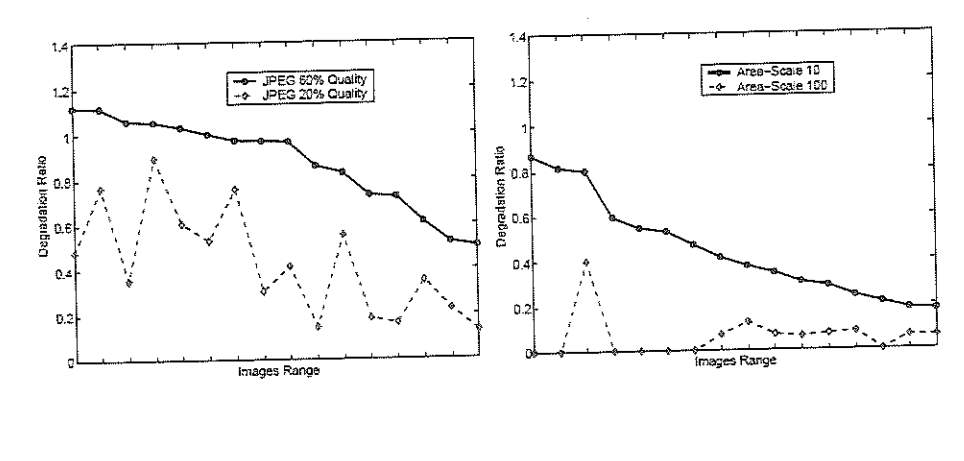


Fig. 6. Results of the subjective experiment. The x-axis is a number that identifies each of the images in the test set. The y-axis is the acceptance scores for each image when compressed at different quality levels and sieved at different area-scales.



(a) JPEG compressed images

(b) Sieved images

Fig. 7. Acceptance ratio of ratios for each normalized image with JPEG 100% quality and sieved at 0 area-scale. The images are arranged from higher score to lower. The JPEG range is 15,3,11,10,12,5,13,16,14,9,6,4,7,2,8,1 considering the 60% rate, and the sieve range is 2,8,7,13,4,5,11,14,1,6,16,9,15,10,12,3 considering the area-scale of 10.

Conclusion and directions for further research 4

The results of this experiment represent an indication of the susceptibility of the human eye to the small scale contained in an image. The images that were sieved at scale ten were easily detected and labeled as non-original by the observers. We can conclude that the observers were highly likely to detect the loss of even quite small scale regions. So, even if lossy compression is used, there may be a need to code smallscale regions, when using the sieve as the core of a compressor.

Future work will compare additional categories, like the CCIR/ITU-R 500 5-Point Scale, for improving the quality assessments. Also, it will be investigated how to integrate the "ratio of ratios" with other normalized scores, like Z-scores.

References

- P. Salembier, A. Oliveras, and L. Garrido (1998). Anti-extensive connected operators for image and sequence processing. IEEE Transactions on Image Processing, 7(4):555-570.
- J.A. Bangham, J. R. Hidalgo, and R. Harvey (1998). Robust morphological scale-space trees. In Proceedings of Noblesse Workshop on Non-linear Model-Based Image Analysis, pp. 133-139.

- J. A. Bangham, R. Harvey, Paul D. Ling, and Aldridge R. V. (1996). Morphological scalespace preserving transforms in many dimensions. Journal of Electronic Imaging, 5(3):283-299.
- J. A. Bangham, P. D. Ling, and R. Harvey (1996). Scale-space from nonlinear filters. IEEE Transactions on Pattern Analysis and Machine Intelligence, 18(5):520-528.
- J. A. Bangham, P. Chardaire, C. J. Pye, and P. D. Ling (1996). Multiscale nonlinear decomposition: the sieve decomposition theorem. IEEE Transactions on Pattern Analysis and Machine Intelligence, 18(5):529-539.
- R. Harvey, J. A. Bangham, and A. Bosson (1997). Scale-space filters and their robustness. In Springer, editor, Scale-Space Theory in Computer Vision, Lecture Notes in Computer Science, pp. 341-344.
- J. A. Bangham, J. Ruiz Hidalgo, and G. Cawley (1998). The segmentation of images via scale-space trees. In Proceedings of the 9th British Machine Vision Conference, pp. 33-43.

Smart Camera Design

Iván Olaf Hernández $^{\rm I},$ Miguel Enrique Bravo Zanoguera $^{\rm I},$ Guillermo Galaviz Yañez $^{\rm I}$

¹Universidad Autónoma de Baja California, Facultad de Ingeniería Blvd. Benito Juarez S/N, Mexicali, Baja California, México ivan.olaf@yahoo.com, bravometric@yahoo.com, ggalaviz@uabc.mx

(Paper received on February 29, 2008, accepted on April 15, 2008)

Abstract. The design and implementation of a smart device for image capture, processing and display is presented. The architecture is based on a CMOS image sensor and a pipelined processing structure implemented in a single FPGA device. The embedded system includes: I2C serial communication with the sensor, interpolation processing for demosaicing the Bayer pattern of the sensor, structure for color correction and image display in VGA format. The design holds the on-chip sophisticated functions of the image sensor. It can be used for low-cost vision systems that require real-time processing and portability

Keywords: FPGA, pipelined processing, VHDL, CMOS image sensor, Smart Camera.

1 Introduction

The design of a smart camera architecture based on a FPGA and a CMOS image sensor is presented. A Cyclone II FPGA from Altera is used as data pixel processor. A Micron's MT9T001 CMOS image sensor is used as the image capture element. Low level image processing operations were implemented using a pipelined architecture, obtaining a high data rate. After an initial latency, every pixel is computed at input data frequency, which gives real-time results.

The design was specified using VHDL. Since it is a standard language the design can be implemented in any FPGA, regardless of the manufacturer or the EDA tool used. This work was done from the scratch: the image capture stage is not based on a commercial camera with an analog or digital video output, instead of that a pipelined processing architecture was implemented to obtain color image from the sensor's raw digital output (Bayer patterned).

The whole system for image capture, processing and display was developed in a single FPGA. Different digital subsystems were implemented to do the following tasks:

- A component to write commands to the image sensor and control its functions. The I2C communication protocol was implemented
- A component to apply bilinear interpolation to extract the three color components for each pixel of the image sensor (Bayer patterned)
- A component that allows the display in the three color channels in VGA format.
- A component to apply a color correction matrix for suitable color perception image

© E. V. Cuevas, M. A. Perez, D. Zaldivar, H. Sossa, R. Rojas (Eds.) Special Issue in Electronics and Biomedical Informatics, Computer Science and Informatics
Research in Computing Science 35, 2008, pp. 97-106



A block diagram of the system is presented in Figure 1. The image processing block implements the pipelined structure to perform bilinear interpolation and color correction in real time using minimal memory resources. It is also possible to implement any other image operation that has the same structure. Furthermore, the architecture presented can be reconfigured since is implemented in a FPGA

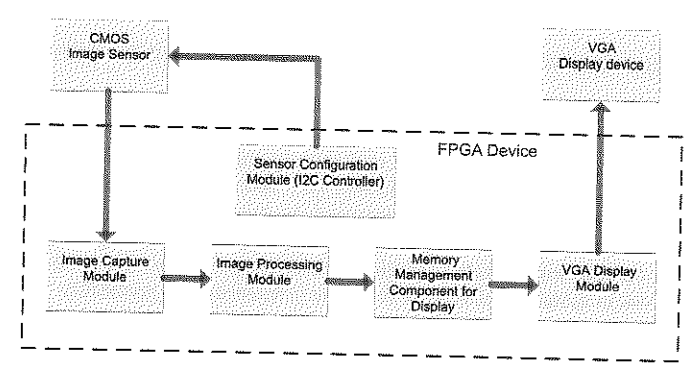


Fig. 1. Simplified scheme of the developed architecture.

2 MT9T001 Image Sensor

The MT9T001 is a CMOS active-pixel digital image sensor with an array of 2,048 horizontal by 1,536 vertical (QXGA format). It has an on chip analog-to-digital converter that provides 10 bits per pixel. It has a maximum pixel data rate of 48 megapixels per second. The sensor can be operated in its default mode or programmed by the user for frame size, exposure, gain setting, and other parameters. It is programmable through a simple two wire serial interface following the I2C protocol [1]The MT9T001 uses a color filter array with the Bayer pattern, in which every pixel has a filter of one of the primary colors. The MT9T001 image data is read out in a progressive scan. Valid image data is surrounded by horizontal blanking and vertical blanking (not valid data). The amount of horizontal blanking and vertical blanking is programmable. It is possible to modify the values of the control internal registers of the MT9T001 in order to change the window size and its location within the pixel array.

3 Image System Design in a FPGA

3.1 Control Interface for the MT9T001 Registers

The MT9T001 sensor can be programmed through a two wire serial interface that controls the reads and writes of the internal registers of the sensor using the I2C

master-slave protocol. In this work the sensor works as the slave. A design was done in a FPGA to implement the write sequence. Component I2C_ESCRITURA was realized to establish the write sequence to the sensor registers, it is subdivided in the components listed in table 1. Figure 2 shows a block diagram of component I2C ESCRITURA.

Table 1. Components list of I2C_ESCRITURA design

Components	Brief Description
I2C_WRA I2C_CNTR	State machine to realize the 16-bit write sequence Provides registers number and data to be written in them Obtains clock frequency of 100 kHz for I2C protocol

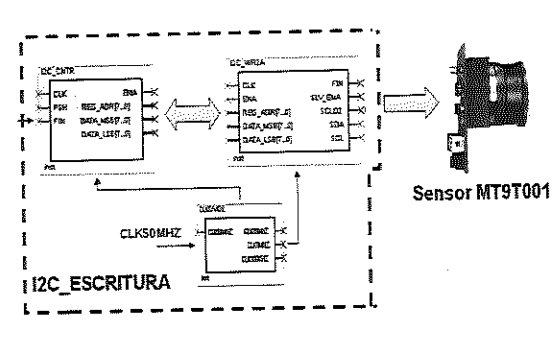


Fig. 2. Block diagram of the component I2C_ESCRITURA and its subcomponents.

3.2 Design to Obtain the Three Color Components of Every Pixel

The MT9T001 sensor uses a color filter array with the Bayer pattern, thus it is necessary to process this raw image in order to obtain the two missing color components for every pixel, using the color data of the adjacent pixels. The bilinear interpolation algorithm was selected for this task, since it is an algorithm that allows implementation using a regular and repetitive structure. The bilinear interpolation algorithm is widely used due to its low computation cost and because it offers an acceptable quality [2].

If an image sensor has the Bayer pattern as shown in figure 3b), the bilinear interpolation obtains the values of the missing colors by taking the average of the neighbor pixels; for instance, if it is located on a blue pixel it takes the average of the four red pixels and the four green pixels to obtain the red and green values respectively, in figure 3a) this idea is presented. From figure 3b), some examples for calculating pixel values are shown below:

If the pixel to work with is the blue pixel B_8 , the red and green values are obtained from:

$$R_8 = (R_2 + R_4 + R_{12} + R_{14})/4$$
 and $G_8 = (G_3 + G_7 + G_9 + G_{13})/4$

If the pixel to work with is the red pixel R_{12} the blue and green values are obtained from:

$$B_{12} = (B_6 + B_8 + B_{16} + B_{18})/4$$
 and $G_{12} = (G_7 + G_{11} + G_{13} + B_{17})/4$

If the pixel to work with is the green pixel G_7 the red and blue values are obtained from:

$$R_7 = (R_2 + R_{12})/2 \text{ and } B_7 = (B_6 + B_8)/2$$
a)
$$B_7 = (R_2 + R_{12})/2 \text{ and } B_7 = (B_6 + B_8)/2$$

$$B_7 = (R_2 + R_{12})/2 \text{ and } B_7 = (B_6 + B_8)/2$$

$$B_7 = (R_2 + R_{12})/2 \text{ and } B_7 = (B_6 + B_8)/2$$

$$G_7 = (R_2 + R_{12})/2 \text{ and } B_7 = (B_6 + B_8)/2$$

$$B_7 = (R_2 + R_{12})/2 \text{ and } B_7 = (B_6 + B_8)/2$$

$$B_7 = (R_2 + R_{12})/2 \text{ and } B_7 = (B_6 + B_8)/2$$

$$B_7 = (R_2 + R_{12})/2 \text{ and } B_7 = (B_6 + B_8)/2$$

$$B_7 = (R_2 + R_{12})/2 \text{ and } B_7 = (B_6 + B_8)/2$$

$$B_7 = (R_2 + R_{12})/2 \text{ and } B_7 = (B_6 + B_8)/2$$

$$B_7 = (R_2 + R_{12})/2 \text{ and } B_7 = (B_6 + B_8)/2$$

$$B_7 = (R_2 + R_{12})/2 \text{ and } B_7 = (B_6 + B_8)/2$$

$$B_7 = (R_2 + R_{12})/2 \text{ and } B_7 = (B_6 + B_8)/2$$

$$B_7 = (R_1 + R_1)/2 \text{ and } B_7 = (B_6 + B_8)/2$$

$$B_7 = (R_1 + R_1)/2 \text{ and } B_7 = (B_6 + B_8)/2$$

$$B_8 = (G_7 + B_8)/2 \text{ and } B_8 = (G_7 + B_8)/2$$

$$B_8 = (G_7 + B_8)/2 \text{ and } B_7 = (B_6 + B_8)/2$$

$$B_8 = (G_7 + B_8)/2 \text{ and } B_8 = (G_7 + B_8)/2$$

$$B_8 = (G_7 + B_8)/2 \text{ and } B_8 = (G_7 + B_8)/2$$

$$G_7 = (B_8 + B_8)/2 \text{ and } B_8 = (G_7 + B_8)/2$$

$$G_7 = (B_8 + B_8)/2 \text{ and } B_8 = (G_7 + B_8)/2$$

$$G_7 = (B_8 + B_8)/2 \text{ and } B_8 = (G_7 + B_8)/2$$

$$G_7 = (B_8 + B_8)/2 \text{ and } B_8 = (G_7 + B_8)/2$$

$$G_7 = (B_8 + B_8)/2 \text{ and } B_8 = (G_7 + B_8)/2$$

$$G_7 = (B_8 + B_8)/2 \text{ and } B_8 = (G_7 + B_8)/2$$

$$G_7 = (B_8 + B_8)/2 \text{ and } B_8 = (G_7 + B_8)/2$$

$$G_7 = (B_8 + B_8)/2 \text{ and } B_8 = (G_7 + B_8)/2$$

$$G_7 = (B_8 + B_8)/2 \text{ and } B_8 = (G_7 + B_8)/2$$

$$G_7 = (B_8 + B_8)/2 \text{ and } B_8 = (G_7 + B_8)/2$$

$$G_7 = (B_8 + B_8)/2 \text{ and } B_8 = (G_7 + B_8)/2$$

$$G_7 = (B_8 + B_8)/2 \text{ and } B_8 = (G_7 + B_8)/2$$

$$G_7 = (B_8 + B_8)/2 \text{ and } B_8 = (G_7 + B_8)/2$$

$$G_7 = (B_8 + B_8)/2 \text{ and } B_8 = (G_7 + B_8)/2$$

$$G_7 = (B_8 + B_8)/2 \text{ and } B_8 = (G_7 + B_8)/2$$

$$G_7 = (B_8 + B_8)/2 \text{ and } B_8 = (G_7 + B_8)/2$$

$$G_7 = (B_8 + B_8)/2 \text{ and } B_8 = (G_7 + B_8)/2$$

$$G_7 = (B_8 + B_8)/2 \text{ and } B_8 = (G_7 + B_8)/2$$

$$G_7 = (B_8 + B_8)/2 \text{ and } B_8 = (G_7 + B_8)/2$$

$$G_7 = (B_8 + B_8)/2 \text{ and } B_8 = (G_7 + B_8)/2$$

$$G_7 = (B_8 +$$

Fig. 3. a) The bilinear interpolation algorithm, b) shows the Bayer pattern

To implement these equations on hardware it is necessary to use adders and dividers. Divisions in powers of two can be implemented with right shift operations. VHDL allows these arithmetic and logical operations. The bilinear interpolation is a neighborhood operation similar to convolution filters with kernels of size 3x3.

The architecture of a general 2-D convolver presented in [3] was used. This architecture is shown in figure 4 and it can be observed that it only requires two line buffers to form the pipeline and three shift registers of three elements (pixels) to perform the 3x3 convolution window, which is used to have the necessary pixels for the operations with the eight neighbors. The use of two line buffers shouldn't be seen as a limitation, but as a design condition to use the minimal memory resources.

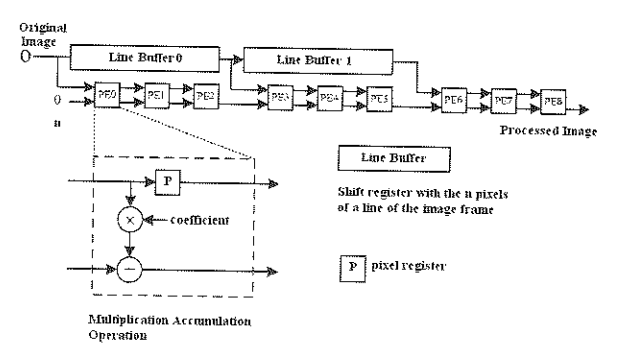


Fig. 4. Architecture to implement a general 2-D Convolver.

Subcomponents were created as a part of the major component PIPEBILINEAL, to implement the bilinear interpolation in a pipelined architecture. The component PIPE

creates the shift registers to form the pipeline. These registers must have the same number of elements as pixels in a line of the image frame. Since every pixel has 10 bits a considerable amount of memory is required. The VHDL coding style used forced the EDA software QUARTUS II to implement these shift registers in the dedicated memory blocks of the FPGA instead of misusing the available generic logic elements of the device (chapter 7 of [4] shows the VHDL coding styles). Component CONTPOS2 implements the counters that bring the pixel position relative to the center point of the convolution window. This position refers to the coordinates (row, column) of the corresponding pixel in the image frame and it is used to know if the pixel is located on a red, green or blue filter and to know which missing colors must be estimated. Component PIPECONV2 implements the registers to form the filter window and the hardware required to perform the arithmetic operations to obtain the bilinear interpolation, depending on the pixel position, it takes the required pixels from the window registers and performs the necessary operations. Component FRAMEBEGIN accepts the data and synchronization signals of the MT9T001 sensor. In figure 5 a block diagram of PIPEBILINEAL is shown.

Figure 6 shows the architecture to apply the pipelined bilinear interpolation, with an example of a 4x4 image frame size, where the line buffers for the pipeline have four pixels (as the four pixels in a line of the image frame). The necessary data to carry out the processing is stored in the three lower registers. These registers form the neighborhood window that is represented by a dashed line over the data frame in figure 8. The data stream is carried out pixel by pixel, line by line. In this architecture the pipeline orders the pixels in such a way that the operations can be performed in parallel. After a latency time of two lines and two pixels, the processed data is obtained at the input pixel data rate. Component PIPECONV takes into account the conditions where the window is on the edges of the image frame, for those cases it is considered that the missing pixels have a null value.

Table 2. Components list of PIPEBILINEAL design

Components	Brief Description
PIPE	Creates the shift registers to form the pipeline.
CONTPOS2	Brings the nixel position in the image frame.
PIPECONV2	interpolation operations
FRAMEBEGIN	Accepts the sensor's data and synchronization signals

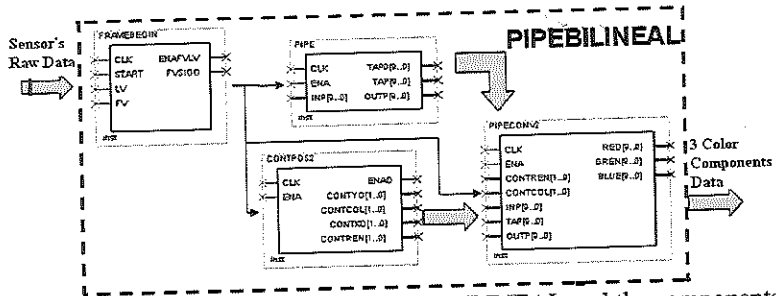


Fig. 5. Block diagram of the component PIPEBILINEAL and the components that conforms it

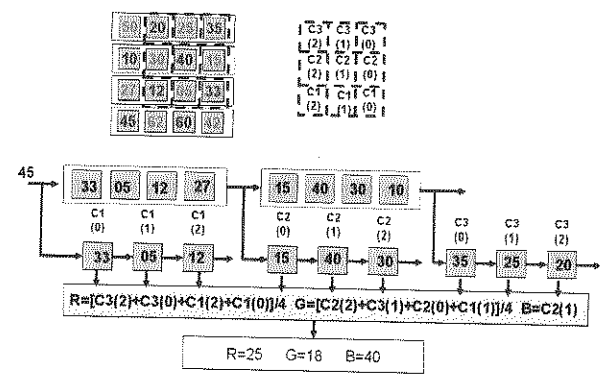


Fig.6. Pipelined architecture to implement bilinear interpolation, showing an example with a 4x4 image frame size.

3.3 Real Time Display of the Interpolated Data in Three Color Channels.

To carry out the real time display of the interpolated pixels (the obtained pixels from applying the bilinear interpolation process), alternatives where looked to utilizes the minimum of memory and it was concluded that with three memory arrays, every one of them with two line buffers, it would be sufficient to capture and display in real time. For major comprehension, in figure 7 are represented two arrays (RGB1, RGB2) of three buffers each one. The capture and display process is explained next:

After the latency of the bilinear interpolation is taken into account (figure 7a), the first interpolated data line is stored in the RGB1 array (figure 7b). Then, the second interpolated data line is stored in the RGB2 array while the content of RGB1 is read out for display (figure 7c); these steps are repeated nonstop. In figure 7, the signal "capture of line" represents the line valid signal from the sensor and the signal "display of line" represents the valid display line period of the VGA format. The data begins to be displayed after the interpolation latency and after the first interpolated data line is stored (figure 7c). For this process to run, the capture cycle must have the same duration as the display cycle and be synchronized. The 48Mhz clock signal from the sensor acts as the master clock and a derived 24Mhz clock signal is used for the display cycle in VGA format; therefore, synchronizing the capture and display cycles. The 24 MHz clock signal generates a frame rate of 53 frames/s for the display in VGA format. The I2C_ESCRITURA component was used to configure a 640x480 image frame size (VGA) and to modify the horizontal and vertical blanking duration accordingly, so the capture and display cycles were synchronized.

The DESP_REAL4 module was created for the real time display and it is subdivided in the components shown in figure 8 and in table 3. The BUFDESP4 component accepts the interpolated data coming from the PIPEBILINEAL component generates the counters and provides the address and enable signals to write and read to each of the color channels memory. The components BUFRED, BUFGREEN and BUFBLUE are memory blocks containing each one a two line buffers, each component stores on of the three color channels. These memory blocks have separated port, enable and clock

signals for write and read, and a VHDL coding style was used in order to implement dual port and dual clock RAM memory utilizing the dedicated memory blocks of the FPGA, as it is recommended in chapter 7 of [4]. The component VGA5 generates the synchronization signals for the VGA format and accepts the three data ports coming from the components BUFRED, BUFGREEN and BUFBLUE, providing the VGA display in the three color channels. The component CLKDIVIDE divides the frequency of the master clock from 48 MHz to a 24 MHz clock signal.

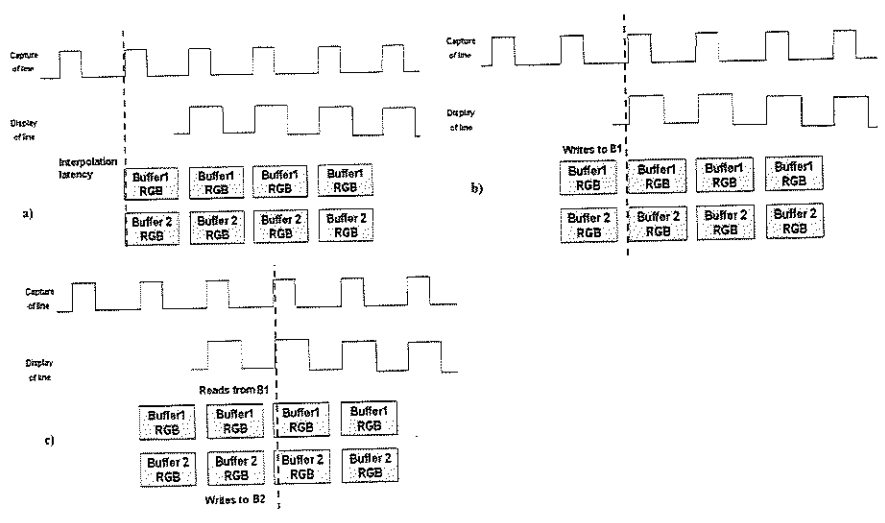


Fig.7. Management of memory to carry out the capture and display of the interpolated data in the three color channels

3.4 Color Correction

A color correction is applied since the spectral response of the CMOS image sensor is different that the response of the human eye, and also different from the response of the display device [5]. The color correction multiplies a 3x3 matrix with the vector formed of the red (R), green (G) and blue (B) values of every interpolated pixel, as it is

formed of the red (R), green (G) and blue (B) values of every interpolated pixel, as it is shown next:
$$\begin{bmatrix} R' \\ G' \\ B' \end{bmatrix} = \begin{bmatrix} r_1 & r_2 & r_3 \\ g_1 & g_2 & g_3 \\ b_1 & b_2 & b_3 \end{bmatrix} \begin{bmatrix} R \\ G \\ B \end{bmatrix}, \text{ or } \begin{bmatrix} R' = r_1R + r_2G + r_3B \\ G' = g_1R + g_2G + g_3B, \\ B' = b_1R + b_2G + b_3B \end{bmatrix} \text{ where } \begin{bmatrix} R \\ G \\ B \end{bmatrix} = \text{RGB}$$

values of the interpolated pixel, $\begin{bmatrix} R' \\ G' \end{bmatrix}$ = RGB values of the corrected pixel and

$$\begin{bmatrix} r_1 & r_2 & r_3 \\ g_1 & g_2 & g_3 \\ b_1 & b_2 & b_3 \end{bmatrix}$$
 is the correction matrix.

Typically the coefficients have values $r_1 > 1, r_2 < 1, r_3 < 1$, $g_1 < 1, g_2 > 1, g_3 < 1$, $b_1 < 1, b_2 < 1, b_3 > 1$. Where the sum of the values of each coefficient set must be equal to one to maintain color balance [6]. For color correction implementation, the product of the coefficient fractional part by the interpolated data (R, G or B), and the product of the coefficient integer part by the interpolated data, are obtained separately, and then these products are added resulting an integer number (disregarding the fractional part). This is done for every interpolated data, these results are added and limited to a possible maximum or to zero if it is a negative result. Figure 9 shows the structure to obtain the equation for the corrected red (R'), for the equations of the corrected green and blue (G', B'), the same structure is used with the corresponded coefficients. The component MULTADD5 was designed to have a structure required to apply the correction matrix, and the values of the coefficients will depend of user application.

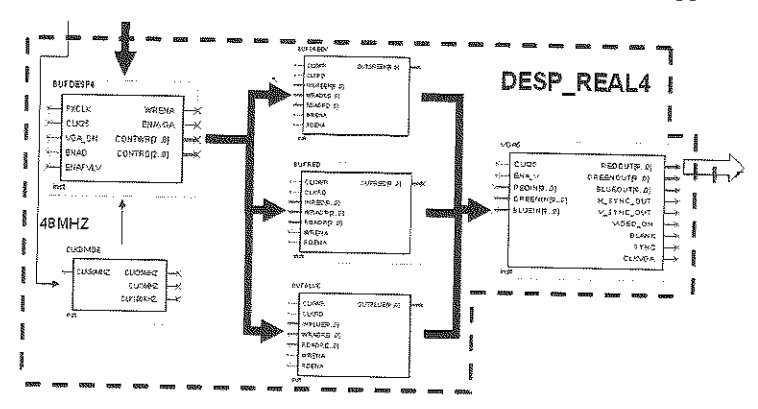


Fig.8. Block diagram of DESP_REAL4 showing its components

Table 3. List of components of the design DESP_REAL4

Components	Brief Description
BUFDESP4	Accepts interpolated data and generates write/read signals for the RAM arrays.
BUFRED,	Each one creates a memory block containing two line buffers, the
BUFGREEN & BUFBLUE	blocks are dual port and dual clock RAM, each component stores one of the three color channels.
VGA5	Generates the synchronization signals for VGA format in three color channels
CLKDIVIDE	Obtains the 24 MHz clock signal for the VGA display

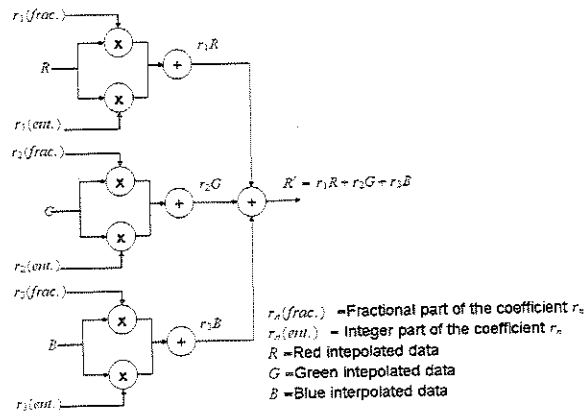


Fig.9. Structure to obtain the equation for the corrected red R'.

4. Results and Discussion

The top level design called DESP_BAYER3 joins the components to carry out the sensor configuration (I2C_ESCRITURA), the bilinear interpolation (PIPEBILINEAL), the color correction (MULTADD5) and the real time display in the three color channels (DESP_REAL4.vhd). Figure 10 shows a block diagram of DESP_BAYER3.

In this system the initial latency time t_i , is the sum of the latencies provoked by the interpolation processing $t_i = (n+2)1/f$ (time of capturing two lines and two pixels), the real time display process $t_d = (n)1/f$ (time of capturing one line) and the color correction structure $t_c = 1/f$. After a latency time t_l described by equation 1, the system begins to display image from the sensor in VGA format.

$$t_1 = t_1 + t_2 + t_3 = (2n+3)1/f$$
 (1)

Where n is the number of pixels in a line of the image frame and f is the frequency of the clock.

The resources utilized from the FPGA Cyclone II to implement the system DESP_BAYER3 are shown in table 4, and represent an optimized design, leaving plenty of free resources, especially for memory.

Table 4. Utilized resources of the FPGA Cyclone II

FPGA used resources	Used elements /total elements	Percentage
Total logic elements	930/33,216	28%
Total memory bits	51,160/483,840	11%
9-bit embedded multipliers	10/70	14%

It is important to mention, that within the VHDL codes, exist a list of parameters used by the components of the system in such a way that values of number of pixels in a line and number of bits in a pixel can be configured, also the pipelined interpolation processing architecture can be configured in the number of line buffers, the number of register for the filter window.

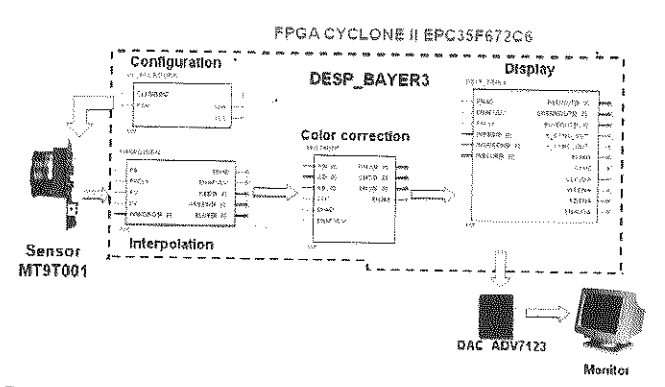


Fig. 10. System that performs the sensor configuration, the bilinear interpolation, the color correction and the real time display in the three color channels.

5. Conclusions

The smart camera system developed speeds up image processing of the interpolation and color correction algorithms, obtaining results at the pixel input data rate after an initial latency required to store two lines of the image frame. This system can be used in software based vision systems as a subsystem to speed up processing of low level image operations or it can be used as stand alone system. The resources utilized by the implemented system are just a low percentage of the full FPGA device used, thus the free resources can be used to implement other processing architecture, or to integrate other connectivity capabilities using the same Cyclone II device.

6. References

- 1. 1/2-Inch 3-Megapixel CMOS Digital Image Sensor MT9T001P12STC, Micron Technology, Inc (2004)
- A Study of Spatial Color Interpolation Algorithms for Single-Detector Digital Cameras. Stanford University, http://scien.stanford.edu/class/psych221/projects/99/tingchen/index.htm
- Chi-Jeng Chang, Zen-Yi Huang, Hsin-Yen Li, Kai-Ting Hu, and Wen-Chih Tseng.: Pipelined Operation of Image Capturing and Processing. In: 5th IEEE Conference on Nanotechnology, Nagoya, Japan (2005)
- Quartus II Handbook, Volume 1, 7 Recommended HDL Coding Styles. Altera Corporation (2007)
- 5. Color Correction for Image Sensors Application Notes. Image Sensor Solutions. Kodak (2003)
- 6. Color Correction Matrix Application Note. Lumenera Corporation (2005)

Object recognition using coupled filters

Jorge Hernández-Constante¹, Josué Álvarez-Borrego², Marco A. Cedano-Olvera³

¹Universidad de Guadalajara, División de Electrónica y Computación, Departamento de Electrónica, Av. Revolución 1500, Módulo "O", S.R. C.P. 44430, Guadalajara, Jal., México.

²Centro de Investigación Científica y de Educación Superior de Ensenada, División de Física Aplicada, Departamento de Optica, km. 107 carretera Tijuana-Ensenada B.C. C.P. 22860, Méxi-

josue@cicese.mx

³Universidad de Guadalajara, División de Electrónica y Computación, Departamento de Computación, Av. Revolución 1500, Módulo "O", S.R. C.P. 44430, Guadalajara, Jal., México. marco.cedano@cucei.udg.mx

Correspondent author: jorge.constante@red.cucei.udg.mx

(Paper received on February 29, 2008, accepted on April 15, 2008)

Abstract. There are many advantages using artificial vision systems to implement quality control systems, in particular those processes where it is impossible to use other methods. However, efficient real-time vision algorithms depend on appropriate relationship between speed and computation cost. Coupled filters applications have produced remarkable results due to its efficiency for real-time object recognition. In this work, one pattern recognition application using coupled filters is implemented. Some results during an industrial-nutritious process assembling are presented.

1 Introduction

Some industries have been looking for to automate their processes to improve quality products. There are different alternatives: using pattern recognition [1], [2], [3], [4], to calculate sausage quality according to their scab, using a vision system and fuzzy logic techniques for extraction sausages' characteristics [5], [6], wood quality analysis based on information on color and texture [7], and wood inspection based on color and texture without supervised grouping [8], [9]. Originally these processes could only be assured by human beings due to the heuristic nature of the quality evaluation procedure.

This work presents the application of algorithms for pattern recognition, using coupled filters; its intended purpose is to identifying a toothpick's assembling quality in chocolate pops.

This work is organized as follows: section 2 presents a brief description of coupling filters theory. Section 3 describes implementation while section 4 shows results obtained. Section 5 discusses some conclusions and comparisons.

© E. V. Cuevas, M. A. Perez, D. Zaldivar, H. Sossa, R. Rojas (Eds.) Special Issue in Electronics and Biomedical Informatics, Computer Science and Informatics
Research in Computing Science 35, 2008, pp. 107-116



2 Coupling filters

An important problem within the image analysis field is the detection of changes or presence of an object in a given scene. Such problems normally appear in remote sensors when monitoring patrons of growth in urban areas, climate prediction starting with images from a satellite, diagnosis of illnesses starting from medical images, detection of objects starting from radar images, and automation using vision robotics and such. Variation detection is also useful in alignment or space registration of two image scenes of different instants or using different sensors.

Presence of a well-known object in a scene can be detected looking for coupling localization among object's reference image h(m,n) and test pop f(m,n). Reference image coupling can be conducted by looking for h(m,n) displacement where coupling energy is minimum. A displacement (p,q), is defined as coupling energy.

$$\sigma_{\eta}^{2}(p,q) \underline{\Delta} \sum_{m} \sum_{n} \left[f(m,n) - h(m-p,n-q) \right]^{2}$$

$$= \sum_{m} \sum_{n} \left| f(m,n)^{2} \right| - 2 \sum_{m} \sum_{n} f(m,n) h(m-p,n-q) + \sum_{m} \sum_{n} \left| h(m,n)^{2} \right|$$
(1)

In order to make $\sigma_{\eta}^2(p,q)$ able to reach a minimum, it is enough to maximize cross-correlation

$$\operatorname{Max}^{c} f_{h}(p,q) \underline{\Delta} \sum_{m} \sum_{n} f(m,n) h(m-p,n-q) \quad \forall (p,q)$$
 (2)

From Cauchy-Schwarz inequality, we obtain

$$\left|c_{fh}\right| = \left|\sum_{m}\sum_{n}f(m,n)h(m-p,n-q)\right| \le \left[\sum_{m}\sum_{n}\left|f(m,n)\right|^{2}\right]^{\frac{1}{2}} \left[\sum_{m}\sum_{n}\left|h(m,n)\right|^{2}\right]^{\frac{1}{2}}$$
(3)

Where equality happens if and only if $f(m,n) = \delta h(m-p, n-q)$; δ is an arbitrary constant and it can be similar to 1. This means that cross-correlation $c_{fh}(p,q)$ achieves the maximum value when displaced position of reference image matches to the observed image. It is calculated as:

$$\max_{c_{fh}}(p,q) = \sum_{m} \sum_{n} |f(m,n)|^2 > 0$$
 (4)

Thus, a given object h(m,n) is able to search within the scene by searching cross-correlation function peaks (see Fig. 1).

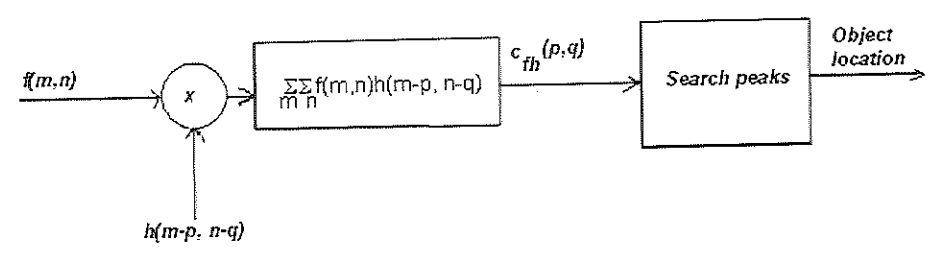


Fig. 1. Image reference coupling using area correlation.

Cross-correlation $c_{fh}(p,q)$, it is also called *area correlation*. It can either be evaluated directly or using the Fourier inverse transform of Equation 5.

$$C_{fh}(\omega_1, \omega_2) \underline{\triangle} \Im \{c_{fh}(p, q)\} = F(\omega_1, \omega_2) H^{\bullet}(\omega_1, \omega_2)$$
(5)

The problem of coupling filters turns out finding a linear filter g(m,n) which maximizes signal to noise relationship of output (SNR)

$$SNR \triangleq \frac{\left| s(0,0) \right|^2}{\sum_{m} \sum_{n} E \left[\left| g(m,n) \Theta \eta(m,n) \right|^2 \right]}$$
 (6)

Where, it is defined such that

$$s(m,n)\underline{\Delta}g(m,n)\Theta h(m-m_0,n-n_0)$$
(7)

being Θ the cross-correlation operation. Here s(m,n) represents the signal content at the output, filtering $g(m,n)\Theta f(m,n)$. The result using the coupled frequency filter is:

$$G(\omega_1, \omega_2) = \frac{H^*(\omega_1, \omega_2)}{S_{\eta}(\omega_1, \omega_2)} e^{(-j\omega_1 m_0 + \omega_2 n_0)}$$
(8)

While such a result might be an impulse signal.

$$g(m,n) = r_{\eta}^{-}(m,n)\Theta h(-m - m_{0}, -n - n_{0})$$
(9)

Considering that

$$r_{\eta}^{-}(m,n)\underline{\Delta}\mathfrak{I}^{-1}\left[\frac{1}{S_{\eta}(\omega_{1},\omega_{2})}\right] \tag{10}$$

Due to all above-mentioned output of coupled filter can be written as

$$g(m,n)\Theta f(m,n) = h(-m - m_0, -n - n_0)\Theta f(m,n)$$

$$= \sum_{i} \sum_{j} f(i,j)h(i - m - m_0, j - n - n_0)$$
(11)

Where cfh(m+m0, n+n0) is area correlation of f(m,n) with h(m+m0, n+n0). If (m0,n0) were known, then SNR would be maximized in (m,n)=(0,0), as it would be expected in equation 11. In practice these displacement values are known. Therefore, we calculate correlation cfh(m,n) and we look for localization of maximum that gives (m0,n0). Consequently, coupled filter can be implemented as an area correlator with a pre-processing filter that can be, in some cases, a high pass filter. Highly correlated random fields, usual monochrome images $r_0(m,n)$ represent a high pass filter.

3 Implementation

Methodology to use consists basically of a pre-processing stage followed by an application stage of cross-correlation. Preprocessing stage consists of two steps: first vision system that needs to identify toothpick position inside optic system view field. Second step vision system is to identify sub image that represents to toothpick and separate it of marshmallow bar. This operation is carried out with segmentation of original image in gray levels, applying a threshold T to image. According with human inspectors, quality pops depends on factors that include errors in toothpick position and rotation. Consequently, these characterization parameters have to be evaluated to determine quality pop norms. In correlation plane, toothpick localization input scene is achieved finding maximum to plane and its respective coordinates [x_max, y_max] that determine maximum correlation respect to center. These coordinates define first two characterization parameters. Valor_max of correlation diminishes when input patterns strays of reference. Therefore, the third characterization parameter is maximum correlation magnitude defined as valor_max. This parameter is used to determine relative toothpick lateral and angular position.

Coupled space filter simulates the correlation against a holographic filter. For example let us take case of chocolate pop. At Fig. 2(a) is shown the pop that will be the reference image, and 2(b) show test pop with toothpick rotated 5 degrees.

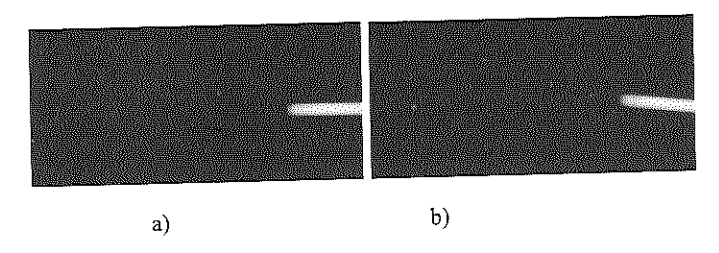


Fig. 2 (a) Reference object. (b) Test pop with toothpick rotated 5 degrees.

We want to find toothpick position to determine if test pop, shown in Fig. 2(b), passes quality control by means of parameters defined in this work: coordinates of maximum position, their value and correlation factor.

We make a space coupled filter for test pop applying the bidimensional discreet Fourier's transformation, changing previously component of frequency zero to spectrum center with Fast Fourier Transform (FFT), and later we return to original domain with the inverse FFT. Then we simulate optic correlator applying to the corresponding algorithm, which consists on changing the component of frequency zero to spectrum center with Fast Fourier Transform (FFT), and then we apply the bidimensional discreet Fourier Transform, at once we return it to its original domain with the inverse FFT. Lastly, we obtain square magnitude multiplying optical correlation with its conjugated complex (using a detector of square law) where we can observe that correlation maximum is a little wide. See Fig. 3.

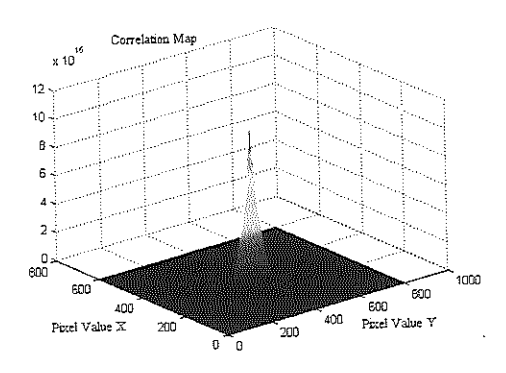


Fig. 3. Maximum correlation.

If coupled filters algorithm is now considered, according to the following block diagram in Fig. 4a, it can be noticed that Coupled Space Filter consists of an object conjugated complex version of the Fourier Transform multiplied by a proportional factor, giving us as a result correlation parameters pick which will provide us the correct letter E identification (See Fig. 4b). Parameters used for identification were coordinated x and y of the pick to identify letter E case. In this case the following values were obtained: x_peak=177 y y_peak = 190.

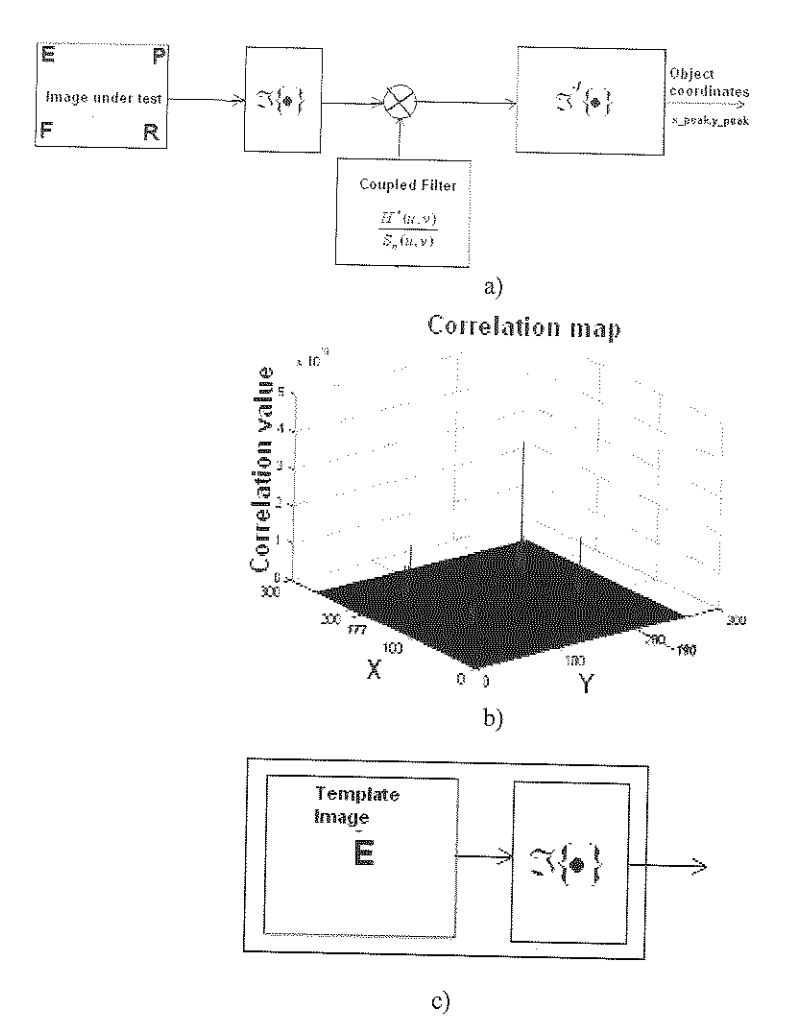


Fig. 4 Coupled Filter Algorithm for the correct letter E identification case a) block diagram b) correlation map c) template image.

4 Results

In this section, algorithms results are described used in this work. We begin with results obtained using crossed correlation algorithm where we consider three cases that are presented in production of chocolate pops and that they consist on the position, in rotation and in overlapping of pop's toothpick. At once we show results obtained applying coupled filters algorithm to pop's toothpick cases of position and rotation. Finally we show results obtained when applying adjournment and rotation algorithms, also applied to toothpick cases of position and rotation. For last two mentioned algorithms, toothpick case overlapped was not considered because any pop with the toothpick overlapped passes required quality control by the candy company. The results obtained when applying coupled filters to groups A and B are shown in Figs. 5 and 6. Table 4.1 contains these results. The values in boldface in second column of Table 4.1 indicate that those pops didn't pass the quality control, that is to say, they are rejected for smaller abscissa values of 244, corresponding with threshold settled down by the candy company.

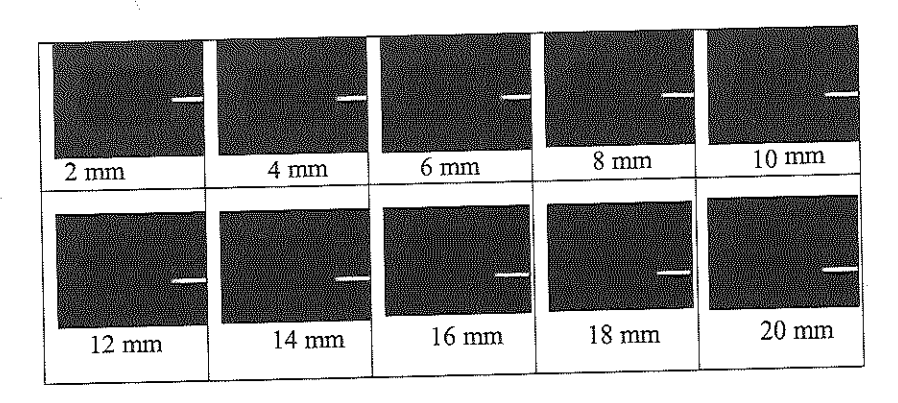


Fig. 5. Group A chocolate pops where from position of 2mm at 10mm of central position are pops with the toothpick with acceptable quality, and of 12mm at 20mm of the central position present an unacceptable quality.

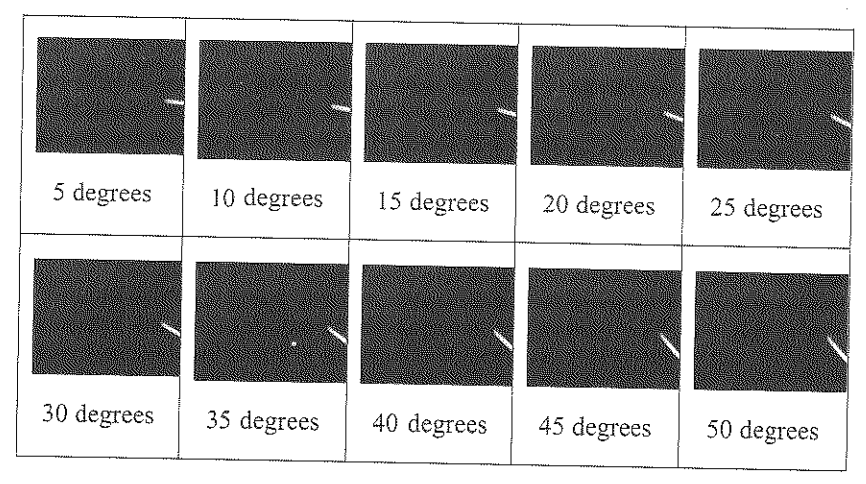


Fig. 6. Group B of chocolate pops where orientation of 5 to 45 degrees of central position are toothpick pops with acceptable quality, and more than 45 degrees, one with toothpick to 50 degrees of central position orientation presents an unacceptable quality.

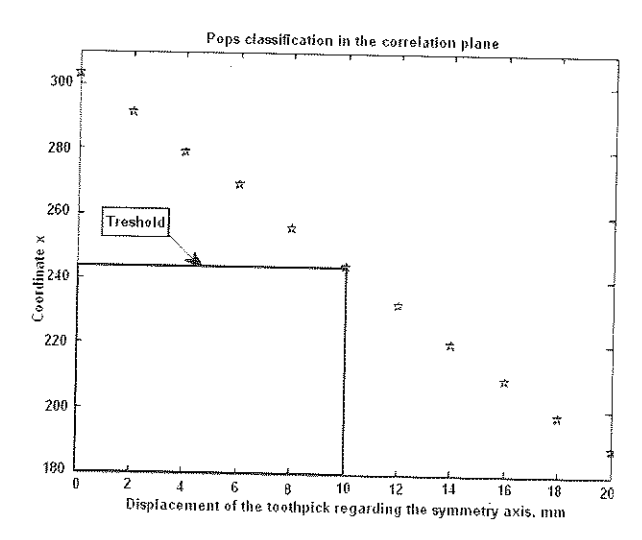


Fig. 7 Rate among displacement Δx and maximum abscissa.

In Fig. 7 is shown coordinate x in function to toothpick distance regarding their wanted position. These results correspond to variations in position of each 2 mm to observe their behavior.

Table 4.1. Represents parameters obtained for certain displacement Δx regarding toothpick of central position.

Δx Mm	Maximum Coordinates x_max , y_max	Maximum value valor_max	FC
0	303, 403	1.0636e+016	7.5545e+018 1.7539e+019 1.3052e+019 1.2740e+019 1.2806e+019 1.1302e+019 1.1162e+019 1.0180e+019 1.0214e+019 9.7052e+018
2	291, 425	1.0435e+016	
4	279, 452	9.5644e+015	
6	269, 435	9.1866e+015	
8	256, 434	8.6584e+015	
10	244, 434	9.1991e+015	
12	232, 436	8.6343e+015	
14	220, 449	7.8206e+015	
16	209, 439	7.1238e+015	
18	198, 450	7.6832e+015	
20	188, 462	7.5357e+015	

The statistical procedure of the results is now presented: The most important thing for this work is the statistical R^2 , the determination coefficient, which represents the quality pattern and it indicates what so well the movement of the toothpick is explained by the pattern.

Table 4.2 Characterization of coupled filters algorithm by means of regression analysis using Statgraphics software.

Data Set	P-Value for Pattern parameters	Determination Coefficient R^2
A	C: 0.0000 X: 0.0000	99.9505 %
В	C:0.0012 X: 0.0000 Y: 0.1633	99.9505 %
	Set A	Set Pattern parameters A C: 0.0000 X: 0.0000 Y: 0.7660 B C:0.0012 X: 0.0000

As it is appreciated, in both cases the coefficient R2 is bigger than 90%, what is considered a model of good quality.

5 Conclusions

The proposed system has been able to discriminate between objects that can be accepted, or those that present good assembling quality, and those that should be rejected by not fulfilling quality requirements. That is how it has been able to determine the thresholds that mark difference between the quality and the non quality products. These values have been expressed in pixels and they have been established in the following way:

For coupled filter, the acceptance threshold of displaced toothpicks is 244 pixels in abscissas axis (this is equal to the 10 mm settled down by the candy company), the acceptance threshold regarding toothpicks orientation is given by an ordinate of 425 pixels and 219 pixels for the abscissa (these values represent the limit settled down by candy company and they correspond to a maximum rotation of 45 degrees).

Coupled filters are best fitted for this usage, values obtained with traslation and rotation filters provided the following results [10]: displacement limit was established at 196 pixels, corresponding to a 10 mm maximum boundary set by the candy company. Rotation limit is 35 pixels, which represents maximum rotation admitted (equal to 45 degrees), for angle measures over 45 degrees, rotation filters don't discriminate on a wide range basis.

6 References

- González-F. Kober V. and Álvarez-B. Adaptive synthetic discriminant function filters for pattern recognition, Optical Engineering 45_5_, 057005 May 2006, pp 1-9.
- Kober V., Mozerov M. and Alvarez-B. Pattern recognition based on rank correlations, Proc. Spie's Optical Science and Technology 49th Annual Meeting 2-6 August in Denver Colorado USA vol. 5558, 2006 pp 1-6.
- 3. Diaz-R, Kober V., and Álvarez-B. Pattern recognition with an adaptive joint transform correlator, Vol. 45, No. 23 Applied Optics 5929, 10 August 2006, pp 1-13.
- 4. Kober, V., Díaz-Ramírez V. H., González-Fraga, J. A. and Josué Álvarez-Borrego. Real time pattern recognition with adaptive correlation filters. In: G. Obinata and A. Dutta, "Vision systems, segmentation and pattern recognition", Chapter 27 Editorial Collegiums, Printed in Croatia., 2007, 515 p.
- Kyllönen J., Pietikäinen M. Visual inspection of Parquet Slabs by Combining color and Textures, FIN http://www2.automaatioseura.fi/jaostot/mvn, 1995, pp 1-4.
- Hirvonen J. Vision Pulp Analyzer, VTT Industrial Systems, Finland, http://www.vtt.fi/tuo/indexe.html, 2002, pp 1-4.
- 7. Gonzalez R. Digital Image Processing, Addison-Wesley, 1992, pp 628-631.
- Skalak D. Prototype Selection for Composite Nearest Neighbor Classifiers, Thesis, University of Massachusetts, Amherst, MA 01003-46101997, 1997, pp 1-14.
- Carew T. Automation of painted slate inspection, School of Electronic Engineering, Dublin City University, Ireland 2002, pp 9-29.
- Hernández J, et al Discriminación entre calidad de paletas mediante un sistema digital que detecta posición y rotación de objetos, CONCIBE 2007, Universidad de Guadalajara, 2005, pp 1-6.

Mixed Analog-Digital Implementation of the Semidiscrete Wavelet Transform

Marco A. Gurrola-Navarro and Guillermo Espinosa-Flores-Verdad

National Institute for Astrophysics Optics and Electronics Electronics Department Tonantzintla, Mexico magurrola@inaoep.mx, gespino@inaoep.mx

(Paper received on February 29, 2008, accepted on April 15, 2008)

Abstract. In the present work is proposed a mixed approach to implement the two parts of the wavelet transform: the direct transform using analog filters and the inverse transform by digital filters. A set of continuous time signals, constituting the wavelet transform, is obtained from the original signal using analog filters. This set of signals is digitalized and then the inverse wavelet transform can be numerically applied. The digital filters are specially designed to compensate linear variations on the analog devices as well as the effects of the finite number of scales in the system. The difference between the reconstructed and the original signal can be as low as be required.

1 Introduction

The Wavelet Transform (WT) maps a time signal to a function depending on two variables: time location and scale. The WT allows the representation of a signal simultaneously in time and frequency, and is "particularly useful for analyzing signals which can best be described as aperiodic, noisy, intermittent, transient and so on" [1]. Denoising, compression, pattern recognition and enhancement are some of the techniques specially developed to be applied in the wavelet domain and are used in application areas as image processing, medicine, engineering, physics, etc. [1][2][3].

In the most works about the WT its numerical implementation by software or digital hardware is supposed. Only few works deal with the alternative to carry out the WT using analog circuits. In this work is taken the approach to implement the WT by convolution in continuous time filters [4][5][6][7][8][9]. In particular, the set of continuous band-pass filters defined in [9] is here taken to perform the direct WT, whereas the inverse transform is numerically developed using a wavelet which is constructed as is explained in [10].

The proposal of the analog implementation of the direct WT in combination with a numerical implementation of the inverse WT is an original contribution of this work. Additionally, in this paper is explained how to fit the numerical wavelets to compensate linear deviations on the analog wavelets due to non-ideal devices, and how to design two lateral filters to compensate the effects due to the

© E. V. Cuevas, M. A. Perez, D. Zaldivar, H. Sossa, R. Rojas (Eds.) Special Issue in Electronics and Biomedical Informatics, Computer Science and Informatics
Research in Computing Science 35, 2008, pp. 117-124



finite number of scales in the system. This corrections make possible to obtain an error between the reconstructed and the original signals as low as be required.

Section 2 is a review of the theoretical bases of the semidiscrete WT. The compensation of the variations on the analog wavelets and the effects of the finite number of scales are explained in sections 3 and 4. A simulation example is shown in section 5. And the conclusions are depicted in section 6.

2 Semidiscrete Wavelet Transform

Given a function f(t), in this work the complex conjugated is denoted by $f^*(t)$ and its Fourier transform is denoted by the respective upper case letter, $F(\omega)$, except H(s) representing the Laplace transform of h(t).

2.1 General Principles

The direct and inverse semidiscrete WT of a function f(t) respect to the prototype wavelet $\psi(t)$ are given by [11][10]

$$w_m(b) = \int_{-\infty}^{\infty} f_{in}(t)\psi_m(t-b)dt, \qquad (1)$$

$$f_{out}(t) = \sum_{m} \int_{-\infty}^{\infty} w_m(b) \chi_m(t-b) db, \qquad (2)$$

where $m \in \mathbb{Z}$, and

$$\psi_m(t) = r^{-m}\psi(r^{-m}t), \qquad (3)$$

for a selected value $1 < r \in \mathbb{R}$. As can be seen, the semidiscrete WT is defined by the set of continuous functions $w_m(t)$.

To be used as semidiscrete wavelet, $\psi(t)$ must be bounded and integrable, must fulfill the admissibility condition

$$\int_{-\infty}^{\infty} \frac{|\Psi(\omega)|^2}{\omega} d\omega < \infty, \text{ for } \omega > 0,$$
(4)

and must satisfy the stability condition: there exist two constants A and B, with $0 < A \le B < \infty$, such that for every $\omega > 0$

$$A \le \sum_{m} |\Psi(r^m \omega)|^2 \le B. \tag{5}$$

To achieve perfect reconstruction, for $\omega > 0$ must be verified

$$\sum_{m} \Psi^*(r^m \omega) X(r^m \omega) = 1.$$
 (6)

Analog Wavelet Filters 2.2

Work [9] shows that any continuous linear filter described in the Laplace domain

$$H(s) = \frac{p_1 s + p_2 s^2 + \dots + p_{d-1} s^{d-1}}{q_0 + q_1 s + \dots + q_{d-1} s^{d-1} + s^d},$$
 (7)

where $2 \leq d \in \mathbb{Z}$, $p_1, \dots, p_{d-1}, q_0, \dots, q_{d-1} \in \mathbb{R}$, with at least one p different to zero, and denominator is a strictly Hurwitz polynomial, has an impulse response h(t), such that $\psi(t) = h(-t)$ is a semidiscrete wavelet for any value r > 1, i.e. $\psi(t)$ is bounded, is integrable, and satisfies the admissibility (4) and stability (5)

Therefore, the equation (1) can be implemented in a continuous time filter by the convolution between the input signal $f_{in}(t)$ and the impulse response

Numerical Wavelets

In the work [10] is defined the function

$$X(\omega) = \frac{\Psi(\omega)}{\sum_{m} |\Psi(r^{m}\omega)|^{2}},$$
(8)

which fulfills the condition for perfect reconstruction (6) as can be easy probed by direct substitution.

Having the numerical representation of $\chi(t)$, the inverse WT (2) can be numerically implemented after the analog-to-digital conversion of $w_m(t)$.

Compensation of Linear Variations 3

Suppose that the functions $H_{\psi_m}(j\omega) = \Psi^*(r^m\omega)$ are implemented with analog circuits and that variations in the time constants are introduced due to deviations on the nominal values of the analog devices.

If the deviations introduce only linear changes in the filter responses (without distortion), then the effects can be compensated using the function

$$\bar{\mathbf{X}}_{m}(\omega) = \frac{\Psi^{*}(r^{m}\omega)}{\bar{\Psi}_{m}^{*}(\omega)} \mathbf{X}(r^{m}\omega), \qquad (9)$$

where $\bar{\Psi}_m^*(\omega)$ is the actually implemented analog m filter.

Making direct substitutions can be easily verified that the functions $\bar{\Psi}_m(\omega)$ and $\bar{\mathbf{X}}_m(\omega)$ fulfill condition (6).

4 Compensation of Bandpass Behavior

In practice only systems with a finite number of filters can be implemented. The filters go from the lower scale m_a up to the higher scale m_b . The operative frequency range of the system can be established as $\omega \in (\omega_b, \omega_a)$, where ω_a and ω_b are the central frequencies of the first and last filters, $\Psi_{m_a}(\omega)$ and $\Psi_{m_b}(\omega)$. However the lacking filters of scales lower than m_a and higher than m_b will bring about the unfulfillment of condition (6), introducing a band pass behavior in the finite sum $\sum_{m=m_a}^{m_b} \Psi^*(r^m \omega) X(r^m \omega)$.

This band-pass behavior can be compensated on $\omega \in (\omega_b, \omega_a)$ redefining the next lateral filters which involve n extra scales at each side.

$$\bar{\mathbf{X}}_{m_a}(\omega) = \frac{\sum_{m=m_a-n}^{m_a} \Psi_m^*(\omega) \mathbf{X}_m(\omega)}{\bar{\Psi}_{m_a}^*(\omega)}, \qquad (10)$$

$$\bar{\mathbf{X}}_{m_b}(\omega) = \frac{\sum_{m=m_b}^{m_b+n} \Psi_m^*(\omega) \mathbf{X}_m(\omega)}{\bar{\Psi}_{m_b}^*(\omega)}.$$
 (11)

The functions $\bar{\Psi}_m(\omega), \bar{\bf X}_m(\omega), \bar{\bf X}_{m_a}(\omega)$ and $, \bar{\bf X}_{m_b}(\omega)$ satisfies

$$\bar{\Psi}_{m_a}^*(\omega)\bar{X}_{m_a}(\omega) + \sum_{m=m_a+1}^{m_b-1} \bar{\Psi}_m^*(\omega)\bar{X}_m(\omega) + \bar{\Psi}_{m_b}^*(\omega)\bar{X}_{m_b}(\omega) =
= \sum_{m=m_a-n}^{m_b+n} \Psi^*(r^m\omega)X(r^m\omega) \approx 1, \text{ for } \omega \in (\omega_b, \omega_a).$$
(12)

As larger is n the error of reconstruction will be lower, as can be seen in the example of next section.

5 Simulated Example

For the WT system of this example a value $r=\sqrt[3]{10}$ was selected, obtaining three scales per decade. The prototype filter is given by

$$H_{\psi_0}(s) = \frac{(s\omega_c/q)^2}{(s^2 + s\omega_c/q + \omega_c)^2},$$
 (13)

where $\omega_c = 2\pi \times 10 \,\mathrm{Hz}$ and $q = \sqrt{1/2}$.

The system has 7 filters from $m_a=0$ to $m_a=6$ and operates in the frequency range (0.1 Hz, 10 Hz). Only two extra scales (n=2) were considered at each side to construct the lateral filters.

Table 1 shows the central frequency of the filters $H_{\psi_m}(s)$.

Fig. 1 shows the ideal analog $\psi_0(t)$ and numerical $\chi_0(t)$ wavelets.

Fig. 2-a shows the spectrums of $H_{\psi_m}(j\omega)$, both ideal and with simulated linear variations. The variations was introduced with Gaussian deviations of $20\% = 3\sigma$ in the poles of the transference function. The variations has been overdone for illustrative purposes, even though uniform variations with values as low as 1% can be achieved in actual analog integrated circuits when mismatch

design guidelines are carefully followed. Fig. 2-b shows the spectrums of $\bar{X}_m(\omega)$ for m=1 to m=5. Fig. 2-c shows the spectrums of the lateral filters $\bar{\mathbf{X}}_{m_a}(\omega)$ and $\bar{\mathbf{X}}_{m_b}(\omega)$.

Fig. 3-a shows a probe signal $f_{in}(t)$ which includes a chirp signal and oscillations of 0.1, 1.0 and 10 Hz. Fig. 3-b shows the wavelet transform $w_m(t)$ of the signal $f_{in}(t)$. Fig. 3-c shows the difference between the reconstructed signal $f_{out}(t)$ and the probe signal $f_{in}(t)$ (the reconstructed signal was not included because in the resolution of the graphics the differences respect to the probe signal can not be appreciated).

Table 2 shows the the maximum difference $f_{out}(t) - f_{in}(t)$ as a function of the amount of extra scales (n) that was considered in the construction of the lateral filters.

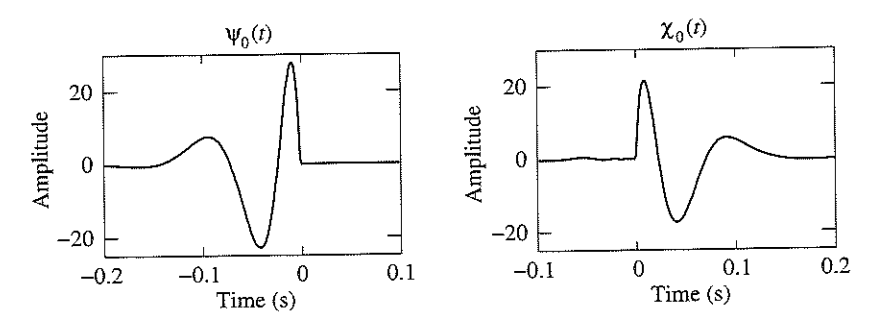


Fig. 1. Analog prototype wavelet $\psi_0(t)$ and numerical wavelet $\chi_0(t)$.

Table 1. Central frequency of the filters $H_{\psi_m}(s)$.

filter (Central Freq.
m	(Hz)
0	$10.0~\mathrm{Hz}$
1	$4.64~\mathrm{Hz}$
2	$2.15~\mathrm{Hz}$
3	$1.00~\mathrm{Hz}$
4	$0.464~\mathrm{Hz}$
5	$0.215~\mathrm{Hz}$
6	0.100 Hz

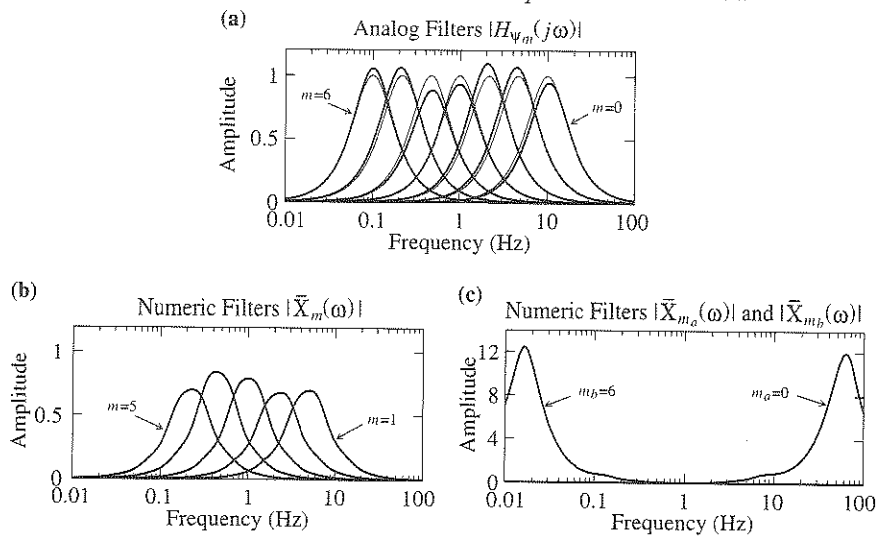


Fig. 2. a) Spectrums of the exact (thick) analog filters $H_{\psi_m}(j\omega)$, and with simulated linear variations (bold). b) Spectrums of the numerical filters $\bar{\mathbf{X}}_m(\omega)$ compensating linear variations. c) Spectrums of the numerical lateral filters, $\bar{\mathbf{X}}_{m_a}(\omega)$ and $\bar{\mathbf{X}}_{m_b}(\omega)$, compensating linear variations and band-pass behavior.

6 Conclusions

A mixed analog-digital approach to implement the WT has been explained, including a numerical compensation of the variations on the nominal values of the analog devices, as well as a method to numerically compensate the band-pass effects of the system due to the finite number of scales.

A simulated example has been presented, where the analysis capabilities of the analog direct WT, and the reconstruction virtues of the numerical inverse WT could be graphically appreciated.

The proposed methodology has been developed at the level of the linear systems theory, then, it can be applicable at any frequency, with the only limitations of the analog-to-digital conversion and the numerical processing rates.

Acknowledgments

 ${\rm M.\,A.\,Gurrola\,thanks\,Mexican\,Council}$ for Science and Technology (CONACYT) for his Doctoral Scholarship.

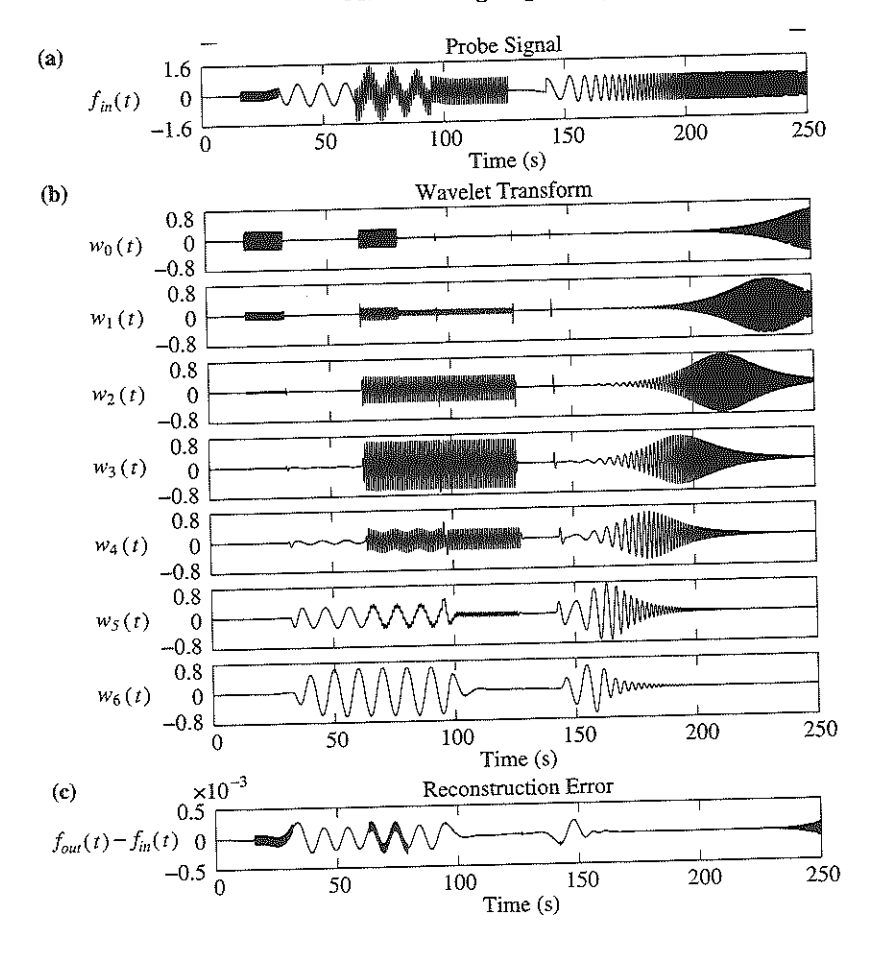


Fig. 3. a) Probe signal $f_{in}(t)$ including a chirp signal and oscillations of 0.1, 1.0 and 10 Hz. b) Wavelet transform $w_m(t)$. c) Error of reconstruction $f_{out}(t) - f_{in}(t)$.

References

- Addison, P.S.: The Illustrated Wavelet Transform Handbook: Applications in Science, Engineering, Medicine and Finance. Institute of Physics Publishing, Bristol (2002)
- Unser, M., Aldroubi, A.: A review of wavelets in biomedical applications. In: Proceedings of the IEEE. Volume 84. (1996) 626–638
- 3. Sadowsky, J.: Investigation of signal characteristics using the continuous wavelet transform. Johns Hopkins APL Thechnical Digest 17 (1996) 258–269
- Lin, J., et al.: Analog vlsi implementations of auditory wavelet transforms using switched-capacitor circuits. IEEE Trans. Circuits Syst. I 41 (1994) 572–583
- Ortiz-Balbuena, L., et al.: Wavelets generation using laguerre analog adaptive filter. In: IEEE ISCAS'96. Volume 1. (1996) 325–328

Table 2. Maximum difference, $f_{out}(t) - f_{in}(t)$, as a function of the number n of extra scales considered in the lateral filters $\bar{X}_{m_a}(\omega)$ and $\bar{X}_{m_b}(\omega)$.

xtra scales	max. error
n	
0	1.1×10^{-1}
1	5.9×10^{-3}
2	2.7×10^{-4}
3	1.3×10^{-5}
4	6.3×10^{-7}
5	2.9×10^{-8}

The maximum amplitude of $f_{in}(t)$ is 1.5

- Kamada, H., Aoshima, N.: Analog gabor transform filter with complex first order system. In: Proc. 36th SICE Annual Conference, International Session Papers. (1997) 925–930
- Chen, D., Harris, J.G.: An analog vlsi circuit implementing an orthogonal continuous wavelet transform. In: Proc. IEEE International Conference on Electronics, Circuits and Systems. Volume 2. (1998) 139–142
- 8. Haddad, S.A.P., et al.: Analog wavelet transform employing dynamic translinear circuits for cardiac signal characterization. In: Proc. IEEE International Symposium on Circuits and Systems. Volume 1. (2003) I-121 I-124
- 9. Gurrola-Navarro, M.A., Espinosa-Flores-Verdad, G.: Direct and inverse wavelet transform implemented usign continuous filters. In: Proc. IEEE 48th Midwest Symposium on Circuits and Systems. Volume 2. (2005) 1051–1054
- 10. Chui, C.K.: Wavelet Analysis and its Applications Volume 1: An Introduction To Wavelets. Harcourt Publishers Ltd, San Diego (1992)
- Mallat, S., Zhong, S.: Characterization of signals from multiscale edges. IEEE Trans. Pattern Anal. Machine Intell. 14 (1992) 710-732

Computer Science and Embedded Architecture

•	

Improving search and publish of knowledge by means of ontology in a Virtual Learning Environment

Héctor Diez-Rodríguez, and José Oscar Olmedo-Aguirre

Centro de Investigación y de Estudios Avanzados del I.P.N.

Ave. Instituto Politécnico Nacional 2508

Colonia San Pedro Zacatenco CP 07360, México-DF

hdiez@computacion.cs.cinvestav.mx, oolmedo@cs.cinvestav.mx

(Paper received on February 24, 2008, accepted on April 15, 2008)

Abstract. Online Problem-based learning environments afford many opportunities engage in collaborative knowledge construction. Problem-based Learning (PBL) is widely collaborative. In PBL, students work in small groups with the guidance of a facilitator learning through solving problem, and reflecting on their experience. The combination of Information and Communication Technology with pedagogical methods produces a new quality that favors the task of generating, transmitting and sharing knowledge The use of ontologies to represent knowledge of specifically domain improves the management of information in the Virtual Learning Environment since it allows the automatic reasoning and it facilitates processes search and recovery of knowledge. In this paper we present a constructivist paradigm for VLE that includes automated mechanisms of search and publish of knowledge integrated in an environment, based on use ontologies that describe learning domain to help students in PBL.

1 Introduction

A Virtual Learning Environment (VLE) increases productivity in education because it provides access to learning materials at any time and at any place. VLE leads from mere information transmission to knowledge construction.

A Constructivist VLE comprises adaptable and contextual spaces that favor an independent work of students, with the purpose of offering non sequential approaches that foment free association of ideas. They are an additional complement for the enrichment of the received education that foments practical ways to design educational activities and to organize information agree to requirements of constructivist approach of education

Proposals that implement a constructivist approach [1] [2] in the educational process have made emphasis in the experimentation phase of knowledge generation and experiences with their use have shown that it can foment interest in learning and working in group to acquire new knowledge. Nevertheless, its effectiveness is limited because most VLE has no appropriate automated mechanisms to reuse and to integrate the generated knowledge and does not motivate students to search for previously known solutions neither to publish new knowledge.

© E. V. Cuevas, M. A. Perez, D. Zaldivar, H. Sossa, R. Rojas (Eds.) Special Issue in Electronics and Biomedical Informatics, Computer Science and Informatics
Research in Computing Science 35, 2008, pp. 127-136



Although students who use these educational environments also have access to information retrieval tools for the Internet (for example Google, Lycos and CiteSeer), a proliferation of superfluous data obtained under these conditions does not imply any form of validation or trustworthiness. In addition the overabundance of the search results leads to the problem known as *cognitive overload*.

Application of ontology to model related components of learning materials would contribute to effective reuse of knowledge. An organizational structure of generalized knowledge with pedagogical purposes can be helpful when a knowledge repository is incorporated into a comprehensive pedagogical design. However, in the broader literature, there is a lack of formal ontology description of knowledge repository for pedagogical design.

In this paper we present a constructivist paradigm for VLE that includes automated mechanisms for knowledge searching and publishing, based on an ontology that describes a learning domain to help students in Problem Based Learning [3]. Students following a systematic procedure can discover and examine contents using pre-designed devices (Learning Objects, LO) to create, validate and publish new knowledge that can be used in the form of learning objects, with a well defined interface that allows and facilitates its reusability. The main contribution in this paper is on adopting the ontological representation of knowledge for searching and discovering content in known repositories of educative materials.

The rest of paper is structured in the following way. In section 2 "Knowledge representation and management in a Virtual Learning Environment" we analyze the concept of ontology and apply it in a VLE design that delivers instructional materials as Learning Objects. In section "Use of ontology in a guided solution of problem" we show how to describe a problem domain in an ontological structure and how to use this representation to help students in a problem resolution strategy. In section "EnEMoCi: Virtual Learning Environment" we present the EnEMoCi's search and publish mechanism, illustrating it with a case of study. In section "Related Works" we show a related solution. Finally in section "Conclusions" we present some concluding remarks and future work.

2 Representation and management of knowledge in a Virtual Learning Environment

Knowledge management is the systematic process of detecting, selecting, organizing, displaying and using highly structured information originated from an organization, with the purpose of cooperatively operating knowledge-based resources to give the right piece of knowledge to the right person at the right moment.

Ontological models for knowledge management in a VLE specify the generic structure of the learning material shared on a knowledge repository. A VLE that actualizes such a structure allows users to play an active role in pedagogical development through semantically relevant knowledge searching. The purpose of representing concepts in an ontological representation is to standardize and to improve the methods of searching and discovery of knowledge for an agile manner of delivering instructional material.

2.1 Learning Objects to represent knowledge in a Virtual Learning Environment

Learning Objects (LO) are a new way of thinking about learning material. A LO is a unit of digital resource that can be shared to support teaching and learning [4] [5]. Because knowledge can be displayed in many ways, for example by narrative descriptions, graphical illustrations, and program simulations, Learning Objects are suitable to represent them and are used for knowledge sharing in a VLE [6] [7] [8].

In the VLE field, there are emerging standards for describing learning resources, and among them, Learning Objects Metadata (LOM) [9] is gaining acceptance. LOM describes metadata for learning objects and it is gradually becoming the reference standard for educational system managing learning objects of many kind. However this standard lacks flexibility, because it cannot allow interoperability between systems.

Ontologies as conceptual model in management knowledge in a Virtual 2.2 Learning Environment

Ontology is the science that studies the explicit formal specification of the terms of a knowledge domain and the relations among them [10] [11]. Many different definitions of the term have been proposed so far. One of most widely quoted and well-known definition of ontology was given by Gruber "Ontology is an explicit specification of a conceptualization" [12].

The use of ontologies in an educational environment is not new [13] [14] [15]. Bloom defines a taxonomy of educative goals in which the category 'contents' has a roll that specifies the concepts that were taught in a course [13]. Bloom's taxonomy of education objectives is a framework which has been widely used in all disciplines. The original Bloom's framework includes six levels of learning: knowledge, comprehension, application, analysis, synthesis and evaluation. Given the recent development in the knowledge management field, this description is no longer appropriate in nowadays VLE context.

Nevertheless, investigations that use ontology in a VLE have been focused in two fundamental focuses [16]:

- Interoperability and classification of the Learning Objects used in Learning Management Systems (LMS) [17]. The ontologies define a vocabulary that is shared by the applications including entries for the Learning Objects it contains.
- Generation of adaptable Learning Environment [18] [19]. The ontologies describe roles and contents that allow personalizing a learning process.

Ontology has been receiving considerable attention in the learning research community. In the Learning Objects field, ontology is typically a network of semantically related knowledge for a specific instructional domain.

The role of ontologies in a VLE is often underestimated. They can be useful for systems that have to intercommunicate according to an agreed protocol (interoperability) and for the system development process (for specification, reusability, and reliability).

2.3 Ontology versus Learning Objects metadata

There have been metadata standard for Learning Objects, such as those proposed in Dublin Core [20], IEEE LTSC [21] and IMS Guide [22]. These standards are used to represent individual Learning Objects at the collection level, which is similar to library catalogue systems. However, to use Learning Objects to support teaching and learning at the knowledge sharing level for a specific domain, knowledge schema must be applied to a Learning Objects repository for such domain [23] [24]. This is because Learning Objects can be organized in a variety of ways depending upon complex intracontext and inter-context where they can be deployed. When a virtual Learning Objects repository is huge and is distributed on the Internet, the use of metadata and keywords only to search for the needed Learning Objects is inefficient and ineffective since many of the potential associations with the various learning aspects are bypassed [25]. This has lead to approaches to Semantic Web applications that model the relationships between Learning Objects using formal ontologies [26].

While metadata describe the artifacts of Learning Objects that are shared by diverse domains, ontology represent a knowledge domain that shares the relationships of Learning Objects within a specific context. There has been moderate literature on ontologies associated with Learning Objects [19] [27]. However, few research reports have provided explicit generic structure of ontologies for knowledge sharing.

Metadata standards of Learning Objects intend to generalize taxonomies and vocabularies for Learning Objects repositories for all disciplines [20], [21], [22], [28], [29], [30]. There is a tacit ontology behind a metadata standard. Such a tacit ontology is too complicated to present because the semantic relationships between all Learning Objects are hard to be standardized. Without the support of ontologies, tagging all types of metadata and relevant keywords to every Learning Object could be prohibitively expensive and will eventually make any search engine practically powerless. On the other hand, specific domain ontology for Learning Objects repositories serves as a map and suggests paths for retrieving candidate Learning Objects to attain certain pedagogical objectives.

3 Use of ontology in a guided solution of problem

In Problem-Based Learning (PBL), while students are identifying crucial parts of the problem, they are also conceiving possible solutions. These solutions can be characterized according to the description along with the restrictions of the problem domain to guide the student to a good solution.

In all problem domains that are more susceptible than others of having a better formalization exist fundamental concepts that may be classified with the basic ontological relationships of *subclass of* and *part of*.

The ontologies involved in the guided solution of problems organize knowledge in two categories: Concepts and Solutions. The Concepts class describes the problem domain, whereas the Solutions class describes the existing algorithms. For example in a domain of graph algorithms used in computer science, the former class comprises graph, directed graph, shortest path and maximum flow subclasses, whereas the

the latter class comprises the Bellman-Ford, Dijkstra, and Kruskal algorithms as subclasses.

The Concepts class organizes in subclasses concepts describing a problem domain and each subclass has the name and solvewith properties. The name property is used to identify class or subclass. The solvewith property associates concepts with solutions. The Solutions class organizes solutions that solve problems in this domain. Each subclass that belongs to this category has several properties. A description property has a brief narrative description of the solution to the students. The properties enlacePW and enlaceOA contain pointers to educative materials (Learning Objects) that describe solutions. The enlacePW property has a link to the main Learning Objects that describe a solution and it is normally elaborated by an expert. The enlaceOA property has more Learning Objects that further develop a solution description. These Learning Objects are elaborated by students and professors. This links allow navigation to review the educational material stored in a Learning Objects Repository. These materials are implementations of a solution and complement an exposed description solution in the main Learning Object.

EnEMoCi: Virtual Learning Environment

EnEMoCi is a VLE that provides high-level services for discovery, searching and publishing of knowledge, though it also provides the functionality of a learning management system to conduct the administrative tasks involved in teaching a course. The knowledge level services facilitate a constructivist approach to education. Besides users can perform knowledge administration upon learning objects by means of a dedicated layer that manage a knowledge involved in solving problems by means of ontologies.

Searching for knowledge 4.1

In EnEMoCi, searching for the set of solutions to a problem given by a query consists on determining the set of Learning Objects that represents an appropriate set of solutions to the problem. Algorithm SEARCH shown in Figure 1 retrieves all the known solutions that can better solve the given problem.

Algorithm Search receives as inputs an ONTOLOGY and a QUERY (an abstract narrative description of the problem), and returns as outputs the set of SOLUTIONS that solves the QUERY according to the ONTOLOGY and the set of LEARNINGOBJECTS associated with the SOLUTIONS. As the ONTOLOGY has a hierarchical structure, the search starts in the top of the structure descending by a breath-first traversal from the most general to the more specialized concept.

The algorithm begins by getting all the WORDS extracted from the QUERY (line 2). The algorithm iterates FORALL WORD IN WORDS (lines 3 through 10) and FORALL CONCEPT IN ONTOLOGY (lines 5 trough 9) to find those CONCEPTs whose property NAME is the root of a discriminating WORD. In case the NAME identifies an abstract CONCEPT in the ONTOLOGY (lines 6 through 8), a new entry in the SOLUTION array is defined to associate the NAME to the SOLUTION obtained from property SOLVEWITH of CONCEPT (line 7). The set of all final SOLUTIONS are obtained by intersecting all partial solutions (lines 10 through 13) and the set of all LEARNINGOBJECTS are obtained by joining the sets of Learning Objects given by property ENLACEPW of each final solution (lines 14 through 16).

```
ALGORITHM SEARCH
INPUT ONTOLOGY, QUERY
OUTPUT SOLUTIONS, LEARNINGOBJECTS
BEGIN
1 SOLUTIONS, LEARNING OBJECTS ← Ø
2 Words ← Split(Query)) \ NonDiscriminantWords
3 FORALL WORD IN WORDS DO
    NAME ← LEXICON.GETSTEM(WORD)
5
   FORALL CONCEPT IN ONTOLOGY
6
     IF CONCEPT.NAME=NAME THEN
7
       SOLUTION[CONCEPT.NAME] ← CONCEPT.SOLVEWITH
8
     END IF
9 END FORALL
10 END FORALL
11 FORALL S IN DOM(SOLUTION) DO
12 SOLUTIONS \leftarrow SOLUTIONS \cap SOLUTION[S]
13 END FORALL
14 FORALL S IN SOLUTIONS DO
15 LEARNINGOBJECTS ← LEARNINGOBJECTS ∪ S.ENLACEPW
16 END FORALL
END
```

Fig. 1. SEARCH Algorithm

In this algorithm, function SPLIT(QUERY) returns the set of all WORDS (with no duplicates) that appear in QUERY, function GETSTEM(WORD) returns the root of WORD by using a LEXICON such as WordNet [31]. The algorithm uses dynamic associative arrays (like those found in JavaScript) in which a new entry is defined by assignment (as in line 7). There are no duplicated entries for this array. Associative arrays have an intrinsic function DOM() that returns the set of all elements for which an entry for the array is defined. Predefined set NonDiscriminantingWords contains frequently used words, among articles, pronouns, and verbs, which do not contribute to determine the problem domain. The operations of union (\cup), intersection (\cap) and difference (\setminus) for generic sets have their usual meaning. The algorithm also uses high-level iterator FORALL that has the form FORALL ELEMENT IN SET DO ACTION END, meaning that variable ELEMENT is instantiated with each member of SET, if non-empty, to perform the given ACTION upon ELEMENT. For the ONTOLOGY, the iterator traverses the hierarchy of nodes in a breath-first manner beginning by the top node, as explained before.

Because a problem generally involves concepts whose solutions may completely differ from others, the algorithm returns no solution when SOLUTIONS is empty. When no solution is found, it indicates that there is some inconsistency in the QUERY.

Publish of knowledge 4.2

Publication consists on augmenting a centralized repository of Learning Objects with the known solutions for the problem. The publication process is lead by an instruction facilitator. In practice, Learning Objects can be either permanent or temporal, according to their duration in the repository. Permanent Learning Objects are elaborated by experts (generally the facilitators) to be used as reference in the subject matter and represents the most complete information available. Temporal Learning Objects are elaborated by students as incomplete, tentative, discardable solutions that arise during the problem solving.

Case of study 4.3

In a Computational Algorithms course it is asked to the students to solve the following problem: "A road map contains information about 20 cities and the roads that connect them have a length given in kilometers. There is always at least one route between any two cities of the map. The problem consists in finding an optimal route between any two cities that minimizes the distance covered by the route. "

Following the PBL methodology, the students start their activities by identifying the learning objectives they have. For this problem, the learning objective can be specified in abstract terms by the query "Finding the shortest path in a directed graph".

Documents related to the specified query were obtained from a search engine like Google [32] that comprises databases containing million of documents organized by classical information retrieval methods. Table 1 summarizes the first ten results the search engine returned to answer the query. From the list of results, the students have to decide which information is most appropriate by examining each result. It was observed that only 30% from the retrieved information is useful for the students, because they contain enough information (theoretical explanations and algorithms) related to the purpose of the query, so that the students can satisfy their learning objectives.

Table 1. Search results from Google. (*) The link has information useful for students

Links quantity	Description	Average (%)
1	Dijkstra's Algorithm Description	10 (*)
2	Directed weighed Graph theory and	20 (*)
	Dijkstra's Algorithm Description	
5	Data structure exercises	50
1	Floyd's Algorithm application paper	10
1	The link could not be shown	10

Nevertheless, if the learning objective that the students have identified can be situated in an ontological domain of Computational Algorithms, then more precise results to that query could be obtained by using the RIbONTOMiddleware, a nonconventional search engine based on ontology containing those abstract terms. The results obtained by using the RIbONTOMiddleware to the same query are summarized in Table 2.

Table 2. Search results using RIbONTOMiddleware.

Solutions

Bellman-Ford Algorithm

Floyd-Warshall Algorithm

Dijkstra Algorithm

By using this search engine based on context ontology the following conclusions can be derived: (1) 100 % of the retrieved information is useful for the students, and (2) the number of links was reduced significantly with respect to the results obtained from the Google search engine.

5 Related work

Snae propose the O-DEST system [19] that comprises ontology for e-learning process, such as course syllabus, teaching methods and learning activities. However the description only refers to pedagogical rolls and activities, and it does not approach the use of knowledge search mechanisms. In [33] a revision of the Learning Management System (LMS) concept is presented. It proposes ontology based on the most recent definitions that facilitate the evaluation, selection and implantation of a LMS, but it cannot able to extent to other domains. In [34] is presented COFALE, a system to support a flexible learning. The system support to implement problem based learning allows an adaptable use of: presentation of learning contents, pedagogical resources and evaluation generation. Nevertheless, these systems do not include search and discovery knowledge mechanisms, that they allow the reusability of the generated knowledge.

6 Conclusion

In this paper we present the EnEMoCi Virtual Learning Environment that approaches problem-based learning, guides students through the problem solving activities and implement a methodology for searching and publishing of knowledge. The domain description is based on ontology that optimizes the application of knowledge based systems, development and interoperability.

The use of EnEMoCi has demonstrated that a retrieval mechanism based on context ontologies reduce the links amount that students should navigate.

An ontological model would help a user to search learning objects by reducing the mental search space. Our proposed ontological model has explicit descriptions of pedagogical intentions. In comparison with general topic maps, the semantic network repre-

sented by ontological model is formalized for problem solving in the pedagogical development domain. From the viewpoint of knowledge sharing, our ontological model can be considered as a framework for pedagogical development based on common pedagogical design patterns.

Ontology does not replace individual learning objects metadata, rather it adds explicit relationships between learning objects that would help the user to conduct unstructured pedagogical development. As a result, the use of ontology would allow students to utilize well-known knowledge in an efficient manner. A formalized learning objects category can help a community in developing aspects of its ontology, especially when the learning objects repository is incorporated into a learning system.

The future work is focused in improving response time to query and a development of appropriate update services for generated knowledge automation publication in a Learning Objects Repository.

Acknowledgement. This research was supported by Secretaría de Educación Pública (SEP) of Mexican government.

References

- H. Zhuge, and Y. Li, (2004), Active E-Course for Constructivist Learning, Proceedings of the 13th International World Wide Web Conference, pp. 246-247.
- L.P. Maia, F. Berenger, and A.G. Pacheco, (2005), A Constructivist Framework for Operating Systems Education: a Pedagogic Proposal Using the SOsim, Proceedings of the 10th Annual SIGCSE Conference on Innovation and Technology in Computer Science Education, pp: 218-222.
- H.S., Barrows, (2000), Problem-Based Learning Applied to Medical Education.
- 4. D.A. Willey, (2000), Connecting learning objects to instructional design theory: A definition, a metaphor, and a taxonomy, In D.A. Wiley (Ed.), The Instructional use of Learning Objects.
- 5. D.A. Willey, and E.K. Edwards, (2002), Online self-organizing social system: The decentralized future of online learning, Quarterly Review of Distance Education, 3(1):33-46.
- E.B. Cohen, and M. Nycz, (2006), Learning objects and e-learning: An Informing Science Perspective, Interdisciplinary Journal of Knowledge and Learning Objects, 2:23-34.
- B. Collis, and A. Strijker, (2003), Re-usable learning objects in context, International Journal on E-Learning, 2(4):5-16.
- G. Singh, L. Hawkins, and G. Whymark, (2007), An integrated model of a collaborative knowledge building, Interdisciplinary Journal of Knowledge and Learning Objects, 3:85-
- C. Knight, D. Gaševič, and G. Richards, (2006), An ontology-based framework for bridging learning design and learning content, Journal of Education Technology & Society: Special Issue on Current Research in Learning Design, 9(1):23-37.
- 10. T. Gruber, (1995), Toward principles for the design of ontologies used for knowledge sharing, International Journal of Human and Computer studies, 43(5/6):907-928.
- N. Guarino, (1995), Formal ontology, conceptual analysis and knowledge representation, International Journal of Human and Computer studies, 43(5/6):625-640
- T. Gruber, (1993), A translation approach to portable ontology specifications, Knowledge Acquisition, 5(2):199-220.

- 13. B.S. Bloom, (1956), Taxonomy of educational objectives. The classification of educational goals, Handbook I: Cognitive domain, New York, Longmans, Green.
- I. Friss, J. Azpiazu, and A. Silva, (2003), Use of Ontologies in a Learning Environment Model, Proceedings of Computers and Advanced Technology in Education (CATE'03), Greece.
- A. Dong, and H. Li, (2005), Ontology-Based Information Integration in Virtual Learning Environment, Proceedings of IEEE/WIC/ACM International Conference on Web Intelligence (WI'05), pp. 762-765.
- J. Breuker, A. Muntjewerff, and B. Bredeweg, (1999), Ontological Modeling for Designing Educational Systems, Proceedings of the Workshop on Ontologies for Educational System.
- 17. P. Mohan, and B.K. Daniel, (2004), A New Distance Educational Model for the University of the West Indies: A Learning Objects Approach, Proceedings of the IEEE International Conference on Advanced Learning Technologies, pp. 938-942.
- K. Verbert, D. Gaševič, J. Jovanovič, and E. Duval, (2005), Ontology-based Learning Content Repurposing, In Proceedings of WWW'2005, pp. 1141-1141.
- C. Snae, and M. Brueckner, (2007), Ontology-driven e-learning system based on roles and activities for Thai learning environment, Interdisciplinary Journal of Knowledge and Learning Objects, 3:1-17.
- 20. Dublin Core Metadata Initiative, Retrieved from http://dublincore.org
- 21. IEEE Learning Technology Standards Committee, Retrieved from http://ieeeltsc.org
- IMS Meta-data Best Practice Guide for IEE 1484.12.1-2002. Standard for Learning Object Metadata Version 1.3 Final Specification, Retrieved from http://www.imsproject.org/metadata/
- K. Harman, and A. Koohang, (2005), Discussion board: A learning object, Interdisciplinary Journal of Knowledge and Learning Objects, 1:67-77.
- A. Koohang, (2004), Creating learning objects in collaborative e-learning setting, Issues in Information System, 4(2):584-590.
- P.N. Mustaro, and L.F. Silveira, (2006), Learning objects: Adaptive retrieval through learning style, Interdisciplinary Journal of Knowledge and Learning Objects, 2:35-46.
- 26. M.A. Silicia, and M. Lytras, (2005), On the representation of change according to different ontologies of learning, International Journal of Learning and Change, 1(1):66-79.
- A. Zouaq, R. Nkambou, and C. Frasson, (2007), An integrated approach for automatic aggregation of learning knowledge objects, Interdisciplinary Journal of Knowledge and Learning Objects, 3:135-162.
- V.N. Convertini, D. Albanese, A. Marengo, V. Marengo, and M. Scalera, (2007), The OSEL taxonomy for classification of learning objects, Interdisciplinary Journal of Knowledge and Learning Objects, 2:125-138.
- 29. N. Friesen, (2005), Interoperability and learning objects: An overview of e-learning standardization, Interdisciplinary Journal of Knowledge and Learning Objects, 1: 23-31.
- K. Yordanova, (2007), Meta-data application in development, exchange and delivery of digital reusable learning content, Interdisciplinary Journal of Knowledge and Learning Objects, 3:229-237.
- 31. WordNet, Retrieved from http://wordnet.princeton.edu/
- 32. Google, Retrieved from http://www.google.com.mx/
- 33. G. Diaz, and M.A. Perez, (2006), Towards an ontology of LMS: A Conceptual Framework, 8th International Conference on Enterprise Information System, pp. 161-164.
- V. Minh, (2006), COFALE: An Authoring System for Supporting Cognitive Flexibility, Proceedings of Sixth International Conference on Advanced Learning Technologies, ICALT'06.

Construction of an optimal solution for a Real-World Routing-Scheduling-Loading Problem

José F. Delgado O.¹, Laura Cruz-Reyes¹, Juan J. González B.¹, Héctor Fraire H.¹, Rodolfo A. Pazos R.²

¹ Instituto Tecnológico de Ciudad Madero, México (ITCM)
² Centro de Nacional de Investigación y Desarrollo Tecnológico, México (CENIDET)
Email: francisco.delgado.orta@gmail.com, lcruzreyes@prodigy.net.mx,
jjgonzalezbarbosa@hotmail.com, hfraire@prodigy.net.mx, pazos@sd-cenidet.com.mx

(Paper received on February 29, 2008, accepted on April 15, 2008)

Abstract. This work presents an exact method for the Routing-Loading-Scheduling Problem (RoSLoP). The objective of RoSLoP consists of optimizing the delivery process of bottled products in a company study case. RoSLoP, formulated through the well-known Vehicle Routing Problem (VRP), has been solved as a rich VRP variant through approximate methods. The exact method uses a linear transformation function, which allows the reduction of the complexity of the problem to an integer programming problem. The optimal solution to this method establishes metrics of performance for approximate methods, which reach an efficiency of 100% in distance traveled and 75% in vehicles used, objectives of VRP. The transformation function reduces the computation time from 55 to four seconds. These results demonstrate the advantages of the modeling mathematical to reduce the dimensionality of problems NP-hard, which permits to obtain an optimal solution of RoSLoP. This modeling can be applied to get optimal solutions for real-world problems.

Keywords: Optimization, Routing-Scheduling-Loading Problem (RoSLoP), Vehicle Routing Problem (VRP), rich VRP.

1 Introduction

The distribution and delivery processes are inherent to many manufacturing companies; in other cases, it is the main function of several service businesses. Though this could be considered in consequential, however, merchandise delivery in due time with the minimum quantity of resources, reduces operation costs, yielding savings between 5 to 20 % in total costs of products [1].

In recent years, many researchers have approached transportation problems based on real situations in two ways: formulating rich models of solution and developing efficient algorithms to solve them. RoSLoP, defined in [2] and extended in [3], is a high-complexity problem due its dimensionality.

RoSLoP formulation, associated with the transportation of bottled products in a company located in north eastern Mexico, satisfies the needs of the logistics group of the company. The application of a meta-heuristic algorithm based on an ant colony system (presented in [3]) to the RoSLoP problem permits to generate feasible

© E. V. Cuevas, M. A. Perez, D. Zaldivar, H. Sossa, R. Rojas (Eds.) Special Issue in Electronics and Biomedical Informatics, Computer Science and Informatics
Research in Computing Science 35, 2008, pp. 137-146



solutions. However, performance metrics that measure the quality of the obtained solutions have not been created for this method. This work presents a new formulation for RoSLoP, based on reported methods in the literature for VRP variants, which uses a mathematical artifice that permits reducing the dimensionality of the problem and its solution as an integer programming problem. Therefore, the solution obtained is used as a measure of performance for heuristic algorithms.

This paper shows the exact method based on the solution of 12 VRP variants: CVRP, VRPM, HVRP, VRPTW, SDVRP, sdVRP, VRPMTW, OVRP, sdVRP, CCVRP, DDVRP and MDVRP. These variants and the sate of art of with rich VRP variants are described in section 2 and 3. Sections 4 and 5 are devoted to describe RoSLoP and the exact method. Section 6 show the experimentation with real-world instances; and section 7 presents the conclusions for future applications of this work.

2 The Vehicle Routing Problem (VRP)

VRP, defined by Dantzig in [4], is a classic problem of combinatorial optimization. It consists in one or various depots, a fleet of m available vehicles and a set of n customers to be visited, joined through a graph G(V,E), where:

 $V=\{v_0, v_1, v_2, ..., v_n\}$ is the set of vertex v_i such that, v_0 is the depot and the rest of the vertex represent the customers; each customer has a demand q_i of goods to be satisfied by the depot.

 $E=\{(v_b \ v_j) \mid v_b v_j \in V, i \neq j\}$ is the set of edges where each edge has an associated value c_{ij} that represents the transportation cost from v_i to v_i .

The VRP consists of obtaining a set R of routes with a total minimum cost such that: each route starts and ends at the depot, each vertex $v_i \in V - \{v_0\}$ is visited only once by a route and the length of each route must be less than or equal to L. So, the main objective is to obtain a configuration with the minimum quantity of vehicles and traveled distance for satisfying all the customer demands.

2.1 Variants of VRP

The most known variants of VRP add several constraints to the basic VRP such as capacity of the vehicles (CVRP) [4], independent service schedules at the customers facilities (VRPTW-VRPMTW) [5], multiple depots to satisfy the demands (MDVRP) [6]; customers to be satisfied by different vehicles (SDVRP) [7], a set of available vehicles to satisfy the orders (sdVRP) [8], customers that can ask and return goods to the depot (VRPPD) [9], dynamic facilities (DVRP) [10], line-haul and back-haul orders (VRPB) [11], stochastic demands and schedules (SVRP) [8], multiple use of the vehicles (VRPM) [12], a heterogeneous fleet to delivery the orders (HVRP) [13], orders to be satisfied in several days (PVRP) [6], constrained capacities of the customers for docking and loading the vehicles (CCVRP) [3], transit restrictions on the roads (rdVRP) [3], depots that can ask for goods to another depots (DDVRP) [3] and vehicles that can end its travel in several facilities (OVRP). A rich VRP variant, defined in [1] as an Extended Vehicle Routing Problem, is an application of VRP for

real transportation problems. It is based on the Dantzig's formulation; however, it requires the addition of restrictions that represent the combination of many variants in a problem; which increases its complexity, making more difficult the computation of an optimal solution through exact algorithms.

Related works of rich VRP variants 3

Recent works have approached the solution of rich VRP problems like the DOMinant Project [14], which solves five variants of VRP in a transportation problem of goods among industrial facilities located in Norway. Goel [15] solves four VRP variants in a problem of sending packages for several companies. Pisinger [16] and Cano [17] solve transportation problems with five VRP variants.

RoSLoP was formulated initially in [18] with six VRP variants. Due a requirement of the company it was necessary to formulate a VRP with 11 variants in [19]. This new formulation allows the solution of instances of 12 VRP variants. Table 1 details the variants solved by various authors.

Solved variants Autor	CVRP	VRPTW	VRPMTW	OVRP	VRPPD	MDVRP	SDVRP	sdVRP	VRPM	HVRP	CCVRP	DDVRP	rdVRP
Hasle [14]	✓	✓	✓						✓	✓			
Goel [15]	✓	✓							✓	✓			
Pisinger [16]	✓	1		✓		✓		✓					
Cano [17]	✓	✓					✓	<u> </u>	✓	✓			
Cruz et al. [2]	1	1				1	✓		✓	1			
Cruz et al. [3]	√	✓	1			✓	✓	✓	1	✓	1	1	✓
This work	✓	✓	✓	√		√	✓	√	✓	1	1	✓	V

Table 1. Related works about known rich VRP variants

A study of complexity factors of the base case of the problem is presented in Table 2. Rangel's mathematical formulation [18] requires 26 integer variables to solve 30 restrictions. Herrera's approach [19] needs 29 integer variables to solve 30 restrictions of the formulation. The proposed formulation contains 22 integer variables and 15 restrictions to solve 12 VRP variants.

Complexity Elements Method	Number of integer variables	Number of Restrictions	Solved VRP variants	Solver
Rangel [18]	26	30	6	Heuristic
Herrera [19]	2 ⁹	30	11	Heuristic
This work	2^{2}	15	12	Exact

Table 2. Complexity of the mathematical models created to RoSLoP

4 Definition of RoSLoP

RoSLoP, immersed in the logistics activity of the company study case, involves a subset of three tasks: routing, scheduling and loading. The mathematical model of RoSLoP was formulated with two classical problems: routing and scheduling through VRP and the loading through the Bin Packing Problem (BPP). Fig. 1 shows RoSLoP and its relation with VRP-BPP.

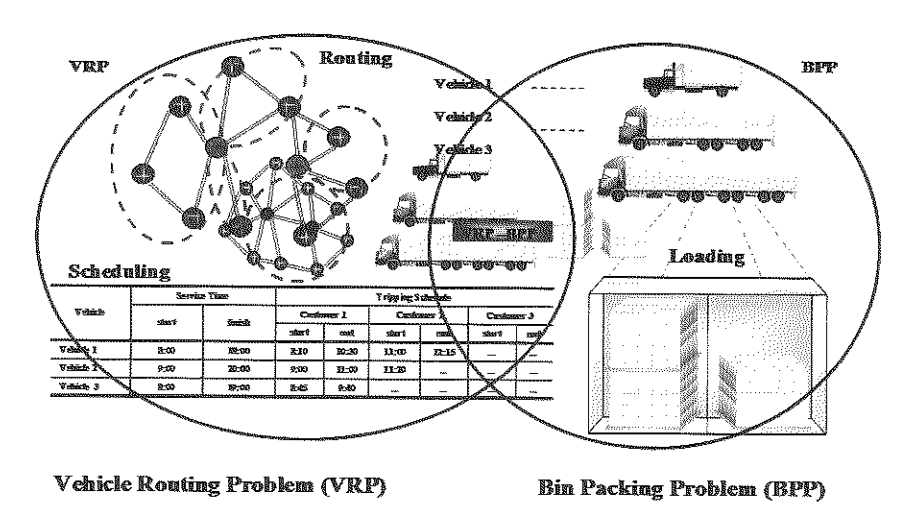


Fig. 1. Definition of the Routing-Scheduling-Loading Problem (RoSLoP)

The case of study contains the next elements:

- A set of *ORDERS* to be satisfied at the facilities of the customers, formed by boxes of products with different attributes such as weight, high, product type, supported weight, packing type and beverage type.
- A set of *n* customers with independent service schedules at a facility *j* [start_service_j, end_service_j] and a finite capacity of attention of the vehicles.
- A set of depots with independent schedules, which have the possibility to request goods to other depots.
- A fleet of vehicles with heterogeneous capacity *Vehicles_d* to transport goods, with a service time *service_time_v* and a time for attention at the facilities of the customers. The attention time *tm_{vj}* depends on the capacity of the vehicle and the available people for docking and loading the vehicles.
- A set of roads represented by the edges of the graph. Each road has an assigned cost C_{ij} , each one with a threshold of allowed weight $MAXLoad_{vj}$ for a determined vehicle v that travels towards a facility j, and a travel time t_{ij} from facility i to j.

The objective of RoSLoP is to get a configuration that allows the satisfaction of the set of *ORDERS* at the set of the customer facilities, minimizing the number of vehicles used and the distance traveled. This new formulation includes a model with 12 variants of VRP: CVRP, VRPTW, VRPMTW, MDVRP, SDVRP, sdVRP, VRPM, HVRP, CCVRP, DDVRP, rdVRP and OVRP, described in section 2.1.

Formulation of RoSLoP 5

Input sets

AMP OF STEE	
C	Set of customer facilities or vertex of the associated graph
ORDERS	Set orders to be satisfied
D	Set of depots to satisfy all the customer demands
Vehicles _d	Set of available vehicles in a depot d
K	Set of all existent routes in a graph
K_d	Set of routes to be covered by a depot $d \in D$
Pallets _v	Set of containers of a vehicle v . Each container has an associated pair $(h_{palletij}, w_{palletij})$, which represents the high and weight of a container i when a customer j is visited by a vehicle v .
ITEMS _i	A set of units of ORDERS for a customer j.

Parameters

Capacity of a vehicle ν to visit a customer j .			
Service time of vehicle v.			
Maneuver time of a vehicle v at facility j , associated to vehicle docking and loading			
Upper limit for the load to be assigned to vehicle ν to visit facility j			
Upper limit fot the number of vehicles attended simultaneously at a facility j.			
The time when a facility j starts its operation			
The time when a facility j ends its operation			
Transportation cost to travel from facility i to j			
Transportation time to travel from facility i to j			

Real variables

Real valla	nie2				
$Load_{vi}$	Assigned load in a vehicle v to visit facility j.				
arrive _{ik}	Arrival time of a vehicle to facility i using route k.				
left _{ik}	Departure time of a vehicle from a facility i using route k .				
φ_k	Associated cost to travel by route k.				
t_k	Travel cost of a vehicle by route k.				

Integer variables

integer variables					
Xiik	1 if the edge (i, j) is visited on route k , 0 in otherwise				
Viste	1 if vehicle v is assigned to route k , 0 in otherwise				

5.1 Preprocessing of the instance of RoSLoP

The preprocessing of an instance is carried out through a linear transformation function, which normalizes the load objects of the problem. Load objects are defined as n-dimensional objects. They are transformed into a set of real numbers where each number represents an n-dimensional object. The function of transformation is illustrated in Fig. 2, in which, an order of a customer j is transformed. This function represents the relationship between the dimensions of the objects. It consists of two steps: 1) the construction of units of load and 2) the transformation of these units in a representative set of real numbers.

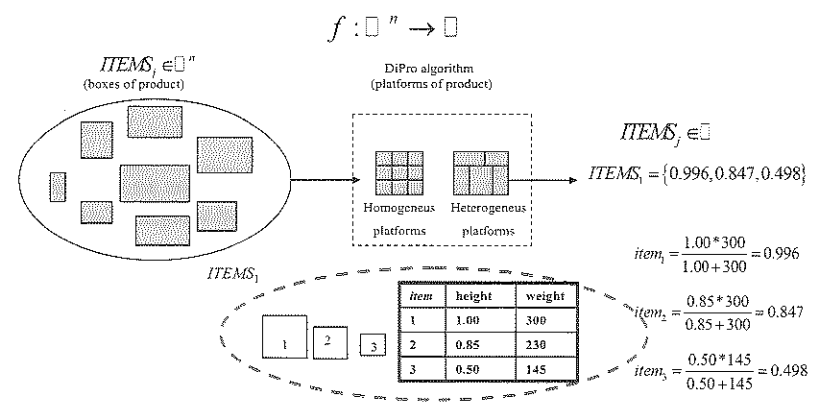


Fig 2. Transformation of the orders dataset of the case study

The construction of load units is done through the DiPro is invoked. As a result, two kinds of units are created: homogeneous and heterogeneous platforms. Homogeneous platforms are constituted by products of the same type, while heterogeneous platform are constituted with different types of products with similar characteristics. Both, Homogeneus and Heterogeneus platforms are defined as a set $ITEMS_j = \{ \forall (w_i, h_i) \}$. Then, each pair (w_i, h_i) is transformed into a number $item_i$ using the following expression (1). A detailed review of DiPro is presented in [20].

the following expression (1). A detailed review of DiPro is presented in [20].
$$item_{i} = \frac{h_{i}w_{i}}{h_{i} + w_{i}} \qquad i \in ITEMS_{j}$$
 (1)

The capacity $Capacity_{vj}$ of a vehicle v to visit node j is transformed likewise. Each container that belongs to a trailer has two attributes: a high $hpallet_{ij}$ and weight $wpallet_{ij}$ of the assigned load to visit customer j. The width of the load is determined by a categorization of products, asked the company to group the products. This is necessary for adjusting the load to the containers. The transformation of the vehicles dimensions is shown in Fig. 3.

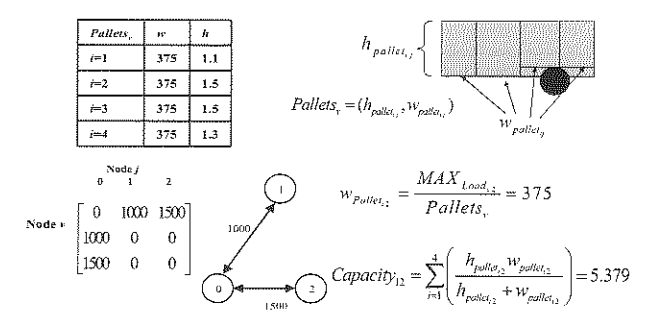


Fig. 3. Transformation of the vehicles dimensions

It is assumed that the weight of the load to be assigned to each container must be uniform. Expression (2) is used to obtain the capacity of the vehicle. This expression ensures that the dimensions of the load objects and the vehicles are equivalent.

$$Capacity_{ij} = \sum_{i=1}^{Pallets_i} \frac{h_{pallet_{ij}} w_{pallet_{ij}}}{h_{pallet_{ij}} + w_{pallet_{ij}}} \qquad j \in C, v \in Vehicles_d$$

$$Load_{ij} = \sum_{i=1}^{Pallets_i} \frac{h_{pallet_{ij}} w_{pallet_{ij}}}{h_{pallet_{ij}} + w_{pallet_{ij}}} \qquad j \in C \cup D, k \in K_d$$
(3)

$$Load_{ij} = \sum_{r \in TEMS_j} item_r \sum_{i \in C \cup D} x_{ijk} \qquad j \in C \cup D, k \in K_d$$
 (3)

Once defined the input parameters, instance preprocessing is performed. These elements are used to formulate the integer programming model. The combination of these elements generates the solution to the related rich VRP.

Mathematical model to solve the rich VRP 5.2

The objective of RoSLoP is to minimize the assigned vehicles and the distance traveled, visiting all the customer facilities and satisfying the demands. Each route k is constituted by a subset of facilities to be visited and a length φ_k . Expression (4) is used to get the maximum covering set established by the use of variant HVRP. Expressions (5)-(6) permit obtaining the length and the travel time on a route k.

$$|K_{d}| = |Vehicles_{d}| \left[\frac{max(ITEMS_{j})}{min(Capacity_{vj})} \right] \qquad K_{d} \in K$$

$$\varphi_{k} = \sum_{j \in C \cup D} \sum_{i \in C \cup D} c_{ij} x_{ijk} \qquad k \in K, v \in Vehicles_{d}$$

$$t_{k} = \sum_{j \in C \cup D} \sum_{i \in C \cup D} \sum_{j \in C \cup D} \sum_{v \in Vehicles_{d}} t m_{vj} x_{ijk} y_{vk} \qquad k \in K_{d}$$

$$(5)$$

$$\varphi_{k} = \sum_{i \in C \setminus D} \sum_{i \in C \setminus D} c_{ij} x_{ijk} \qquad k \in K, v \in Vehicles_{d}$$
 (5)

$$t_{k} = \sum_{j \in C \cup D} \sum_{i \in C \cup D} t_{ij} x_{ijk} + \sum_{i \in C \cup D} \sum_{j \in C \cup D} \sum_{v \in Vehicles_d} t m_{vj} x_{ijk} y_{vk} \qquad k \in K_d$$
 (6)

The objective function of the problem, defined by expression (7), minimizes the number of assigned vehicles and the length of all the routes generated. Expressions (8) - (10) are used to generate feasible routes and solve the related TSP problem. Expression (8) restricts each edge (i, j) on a route k to be traversed only once. Expression (9) ensures that route k is continuous. Expression (10) is used to optimize the covering set related with the objective function. These expressions solve variants DDVRP and MDVRP.

$$\min \sum_{k \in K_1} \sum_{\text{withinker}} \varphi_k y_{vk} \tag{7}$$

$$\sum_{k \in K_d, j \in C \cup D} x_{ijk} = 1 \qquad k \in K_d, j \in C \cup D$$
 (8)

$$\min \sum_{k \in K_d} \sum_{v \in Vohicles_d} \varphi_k y_{vk}$$

$$\sum_{i \in C \cup D} x_{ijk} = 1$$

$$\sum_{i \in C \cup D} x_{jjk} - \sum_{i \in C \cup D} x_{jik} = 0$$

$$k \in K_d, j \in C \cup D$$

$$k \in K_d, j \in C \cup D$$

$$(9)$$

$$\sum_{i \in C \cup D} \sum_{j \in C \cup D} x_{ijk} \ge 1 \qquad k \in K_d$$
 (10)

Expressions (11)-(14), formulated in [5], calculate the time used by a vehicle assigned to route k. Expression (14) ensures that the use of a vehicle does not exceed the attention time at facility j.

These expressions permit solving the variants VRPTW, VRPMTW and VRPM. The variants CCVRP and SDVRP are solved using the expression (15), which ensures that two routes k and k' do not intersect each other at a facility j.

$$t_k y_{i,k} \le service_time_i$$
 $k \in K_d; v \in Vehicles_d$ (11)

$$left_{jk} \geq arrive_{jk} \sum_{l \in C \cup D} t_{ij} x_{ijk} + \sum_{v \in Vehicles_d} tm_{vj} y_{vk} \qquad \qquad j \in C \cup D, k \in K_d \tag{12}$$

$$arrive_{jk} \sum_{i \in C \cup D} x_{ijk} = \sum_{i \in C \cup D} t_{ij} x_{ijk} \qquad j \in C \cup D, k \in K_{\sigma}$$
 (13)

$$start_service_j \le arrive_{jk} \le end_service_j \qquad j \in C, k \in K_d$$
 (14)

$$arrive_{jk} \le left_{jk} \le arrive_{jk}, \qquad k < k', \forall k, \forall k' \in K_d$$
 (15)

Expressions (16)-(18), formulated in [1] and combined with the linear transformation function, define the restrictions for variants CVRP, sdVRP, rdVRP and HVRP. Expression (16) establishes that a vehicle is assigned to a route k. Expression (17) ensures that vehicle capacities are not exceeded. Equation (18) establishes that all goods must be delivered and all demands are satisfied. The relaxation of the model that permits the solution of the variant OVRP consists of the reformulation of expression (9) through expression (19).

$$\sum_{v \in Vehicles} y_{vk} \le 1 \qquad \qquad k \in K_d \tag{16}$$

$$Load_{v_j} \le Capacity_{v_j} y_{v_k} \qquad \qquad k \in K_d; v \in Vehicles_d$$
 (17)

$$\left| ITEMS_{j} \right| - \sum_{j \in C} Load_{ij} = 0 \qquad j \in C \cup D$$
 (18)

$$\sum_{i \in C \cup D} x_{ijk} - \sum_{i \in C \cup D} x_{jik} \le 1 \qquad k \in K_d, j \in C \cup D$$
 (19)

The right side of expression (19) is 0 when a route starts and ends at a depot; otherwise, when the right side has the value 1 means that route starts at a depot and finishes at a different facility.

6 Experimentation

Real instances were provided by the bottling company. They were solved using the approximate algorithm called Heuristics-Based System for Assignment of Routes, Schedules and Loads (HBS-ARSL) proposed in [3] and an exact method. Both were tested on a set of VRP variants that are present in the test data set: VRPTW, VRPMTW, sdVRP, SDVRP, rdVRP, CCVRP, DDVRP, CVRP y HVRP. The HBS-ARSL algorithm was coded in C# and it was executed during two minutes to observe the time when it reaches the best solution. The implementation of the exact method was coded in C# and uses the LINDO API v4.1. A set of 12 test instances were selected from the database of the company, which contains 312 instances classified by the date of the orders; the database contains also 1257 orders and 356 products in its catalogues. Eight available vehicles were disposed. The results are shown in Table 3.

HBS-ARSI **ORDERS** Exact method Instance n /KDistance Vehicles Time Distance Vehicles Used Traveled Used (secs) Traveled (secs) 06/12/2005 5 158 1444 4 51.33 1444 3 3.09 3.32 09/12/2005 5 5 171 1580 5 23.64 1580 5 2500 5.03 12/12/2005 7 9 250 2500 6 38.52 6 01/01/2006 286 2560 7 75.42 2560 6 3.42 9 6 1340 4 1340 2.97 03/01/2006 4 4 116 63.00 4 4.53 07/02/2006 9 288 2660 7 83.71 2660 6 1980 5 3.85 7 208 1980 5 55.57 13/02/2006 5 06/03/2006 7 224 1960 32.16 1960 5 3.36 5 6 09/03/2006 9 269 2570 6 76.18 2570 6 3.85 6 7 22/04/2006 381 3358 7 57.35 3358 5.24 8 11 2350 4.86 6 6 14/06/2006 8 245 2350 90.84 4.53 04/07/2006 270 2640 72.49 2640 6 9 6 55.27 4.00 2245.16 5.66 2245.16 5.33 Average 8 238.83

Table 3. Experimentation with real-world instances, provided by the bottling company

Analysis of Results

The exact method obtained the optimal solution for the 12 instances of the test data set; which permits to measure the performance of the algorithm HBS-ARSL when solving the related rich VRP variant. Table 3 shows that HBS-ARSL reaches the optimal solution in 100% of the cases considering the distance traveled and in 75% considering the number of vehicles assigned. These results reveal as consequence, the need of improving the search techniques of HBS-ARLS to reach 100% of efficiency. The best solutions of HBS-ARLS were obtained in 55.27 seconds on average, while the exact method reaches the optimal solutions in 4 seconds, permitting a reduction of 92% in execution time; which reveals the advantages of the transformation function used to reduce the execution time and the computation of the optimal solution.

8 Conclusions and Future Works

This work presented a mathematical formulation and a linear transformation function, which make possible to obtain the optimal solution for the rich VRP variant related to RoSLoP. It was demonstrated that, the use of mathematical artifices can be used to reduce the dimensionality generated by the solution of many VRP variants. This allowed the obtaining an optimal solution through the formulated integer problem. It could be advantageous when an exact solution is needed for problems classified as NP-Hard as VRP or BPP. However, this transformation function has the restrictive condition of the dependence of domain for this application. Therefore, it is proposed the construction of a transformation function, which is able to reduce the dimension of some specific problems as BPP to a representative set. This can be used to obtain the optimal solution for other real-world problems.

References

- Toth P. Vigo D, editors. The vehicle routing problem, SIAM Monographs on Discrete Mathematics and Applications. Society for Industrial and Applied Mathematics. (2001)
- Cruz L. et al.: A Distributed Metaheuristic for Solving a Real-World Scheduling-Routing-Loading Problem, ISPA 2007, Ivan Stojmenovic (eds.), Springer Verlag, pp. 68-77. (2007)
- Cruz L. et al.: An Ant Colony System to solve Routing Problems applied to the delivery of bottled products, ISMIS 2008, in Aijun An (eds.), Springer Verlag. pp. 329-338. (2008)
- Shaw P.: Using Constraint Programming and Local Search Methods to Solve Vehicle Routing Problems," 40 Conference on Principles and Practice of Constraint Programming (CP 98), M. Maher and JF. Puget (eds.), Springer-Verlag, pp. 417-431. (1998)
- Cordeau, F., Desaulniers, G., Desrosiers, J., Solomon, M., Soumis, F.: The VRP with time windows. Technical Report Cahiers du GERAD G-99-13, Ecole des Hautes 'Etudes Commerciales de Montreal (1999)
- Mingozzi A.: An exact Algorithm for Period and Multi-Depot Vehicle Routing Problems. Department of Mathematics, University of Bologna, Bologna, Italy. (2003)
- Archetti C., R. Mansini and M.G. Speranza.: The Vehicle Routing Problem with capacity 2 and 3, General Distances and Multiple Customer Visits. Operational Research in Land and Resources Manangement, p. 102. (2001)
- Thangiah S.: A Site Dependent Vehicle Routing Problem with Complex Road Constraints.
 Artificial Intelligence and Robotics Laboratory, Slippery Rock University, U.S.A. (2003)
- Dorronsoro B.: The VRP Web. AUREN. Language and Computation Sciences of the University of Malaga. http://neo.lcc.uma.es/radi-aeb/WebVRP. (2005)
- Bianchi Leonora.: Notes on Dynamic Vehicle Routing. Technical Report IDSIA-05-01.
 IDSIA Istituto Dalle Molle di Studi sull'Intelligenza Artificiale. Switzerland. (2000)
- Jacobs Blescha and Mark Goetshalckx.: The Vehicle Routing Problem with Backhauls: Properties and Solution Algorithms. Techincal report MHRC-TR-88-13, Georgia Institute of Technology. (1993)
- 12. Fleischmann B.: The Vehicle routing problem with multiple use of vehicles. Working paper, Fachbereigh Wirtschaftswissenschaften, Universitt Hamburg. (1990)
- Taillard, E.: A Heuristic Column Generation Method For the Heterogeneous Fleet VRP. Istituto Dalle Moli di Studi sull Inteligenza Artificiale, Switzerland. CRI-96-03. (1996)
- Hasle G., O. Kloster, E. J. Nilssen, A. Riise, T. Flatberg.: Dynamic and Stochastic Vehicle Routing in Practice. Operations Research/Computer Science Interfaces Series, Springer, Vol. 38, pp 45-68, (2007).
- Goel, A.; Gruhn, V. Solving a Dynamic Real-Life Vehicle Routing Problem. Haasis, H.-D.et al. (Ed.): Operations Research Proceedings 2005, Bremen, Deutschland. (2005)
- 16. D. Pisinger and S. Ropke, A General Heuristic for Vehicle Routing Problems, tech. report, Dept. of Computer Science, Univ. Copenhagen. (2005)
- I. Cano, I. Litvinchev, R. Palacios and G. Naranjo.: Modeling Vehicle Routing in a Star-Case Transporation Network. XVI International Congress of Computation (CIC-IPN). (2005)
- 18. Herrera, J. Development of a methodology based on heuristics for the integral solution of routing, scheduling and loading problems on distribution and delivery processes of products. Master's Thesis. Posgrado en Ciencias de la Computación. Instituto Tecnológico de Ciudad Madero, México. (2006).
- Rangel, N. Analysis of the routing, scheduling and loading problems in a Products Distributor. Master's Thesis. Posgrado en Ciencias de la Computación. Instituto Tecnológico de Ciudad Madero, México. (2005).
- Cruz L. et al.: DiPro: An Algorithm for the Packing in Product Transportation Problems with Multiple Loading and Routing Variants, MICAI 2007, in Alexander Gelbukh and Angel Fernando Kuri Morales (eds.), Springer-Verlag, pp. 1078-1088. (2007)

Efficient Pattern Recalling using Parallel Alpha-Beta Associative Memories

Mario Aldape-Pérez, Cornelio Yáñez-Márquez, and Oscar Camacho-Nieto

Center for Computing Research, CIC
National Polytechnic Institute, IPN
Mexico City, Mexico
Contact: mario@aldape.org.mx, cyanez@cic.ipn.mx
oscarc@cic.ipn.mx
http://www.aldape.org.mx

(Paper received on February 29, 2008, accepted on April 15, 2008)

Abstract. Associative memories have a number of properties, including a rapid, compute efficient best-match and intrinsic noise tolerance that make them ideal for many applications [1-4]. However, a significant bottleneck to the use of associative memories in real-time systems is the amount of data that requires processing. The aim of this paper is to present the work that produced a dedicated hardware design, implemented on a field programmable gate array (FPGA) that applies the Alpha-Beta Associative Memories model for pattern recognition tasks. Along the experimental phase, performance of the proposed associative memory architecture is measured by learning large sequences of symbols and recalling them successfully.

1 Introduction

An associative memory M is a system that relates input patterns and output patterns as follows: $x \to M \to y$ with x and y, respectively, the input and output pattern vectors. Each input vector forms an association with its corresponding output vector. For each k integer and positive, the corresponding association will be denoted as: (x^k, y^k) . An Associative memory M is represented by a matrix whose ij-th component is m_{ij} [5]. Memory M is generated from an a priori finite set of known associations, called the fundamental set of associations. If μ is an index, the fundamental set is represented as: $\{(x^\mu, y^\mu) \mid \mu = 1, 2, ..., p\}$ with p as the cardinality of the set. The patterns that form the fundamental set are called fundamental patterns. If it holds that $x^\mu = y^\mu \ \forall \mu \in \{1, 2, ..., p\}$ M is auto-associative, otherwise it is heteroassociative; in this case, it is possible to establish that $\exists \mu \in \{1, 2, ..., p\}$ for which $x^\mu \neq y^\mu$. If we consider the fundamental set of patterns $\{(x^\mu, y^\mu) \mid \mu = 1, 2, ..., p\}$ where n and m are the dimensions of the input patterns and output patterns, respectively, it is said that $x^\mu \in A^n$, $A = \{0,1\}$ and $y^\mu \in A^m$. Then the j-th component of an input pattern is represented

© E. V. Cuevas, M. A. Perez, D. Zaldivar, H. Sossa, R. Rojas (Eds.) Special Issue in Electronics and Biomedical Informatics, Computer Science and Informatics
Research in Computing Science 35, 2008, pp. 147-156



as $y_j^\mu \in A$. A distorted version of a pattern x^k to be recuperated will be denoted as \tilde{x}^k . If when feeding an unknown input pattern x^ω with $\omega \in \{1,2,...,k,...,p\}$ to an associative memory \mathbf{M} , it happens that the output corresponds exactly to the associated pattern y^ω , it is said that recuperation is correct.

2 Alpha-Beta Associative Memories

Alpha-Beta Associative Memories mathematical foundations are based on two binary operators: α and β . Alpha operator is used during the learning phase while Beta operator is used during the recalling phase. The mathematical properties within these operators, allow the $\alpha\beta$ associative memories to exhibit similar characteristics to the binary version of the morphological associative memories, in the sense of: learning capacity, type and amount of noise against which the memory is robust, and the sufficient conditions for perfect recall [6]. First, we define set $A = \{0,1\}$ and set $B = \{00,01,10\}$ so α and β operators can be defined as in Table 1.

Table 1. Alpha and Beta operators.

	$\alpha:A \times$	$A \rightarrow B$
X	у	$\alpha(x,y)$
0	0	01
0	1	00
1	0	10
1	1	01

	$B:B \times B$	$A \to A$
Х	у	$\beta(x,y)$
00	0	0
00	1	0
01	0	0
01	1	1
10	0	1
10	1	1

These two binary operators along with maximum (\vee) and minimum (\wedge) operators establish the mathematical tools around the Alpha-Beta model. According to the type of operator that is used during the learning phase, two kinds of Alpha-Beta Associative Memories are obtained. If maximum operator (\vee) is used, Alpha-Beta Associative Memory of type MAX will be obtained, denoted as M; analogously, if minimum operator (\wedge) is used, Alpha-Beta Associative Memory of type min will be obtained, denoted as W [7].

In order to understand how the learning and recalling phases are carried out, some matrix operations definitions are required.

- α max Operation: $P_{mxr} \nabla_{\alpha} Q_{rxn} = [f_{ij}^{\alpha}]_{mxn}$, where $f_{ij}^{\alpha} = \bigvee_{k=1}^{r} \alpha(p_{ik}, q_{kj})$
- α min Operation: $P_{mxr}\Delta_{\alpha}Q_{rxn} = [f_{ij}^{\alpha}]_{mxn}$, where $f_{ij}^{\alpha} = \wedge_{k=1}^{r}\alpha(p_{ik}, q_{kj})$
- β max Operation: $P_{mxr} \nabla_{\beta} Q_{rxn} = [f_{ij}^{\beta}]_{mxn}$, where $f_{ij}^{\beta} = \bigvee_{k=1}^{r} \beta(p_{ik}, q_{kj})$
- β min Operation: $P_{mxr}\Delta_{\beta}Q_{rxn} = [f_{ij}^{\beta}]_{mxn}$, where $f_{ij}^{\beta} = \wedge_{k=1}^{r}\beta(p_{ik}, q_{kj})$

Whenever a column vector of dimension m is operated with a row vector of dimension n, both operations ∇_{α} and Δ_{α} , are represented by \oplus ; consequently, the following expression is valid:

$$y\nabla_{\alpha}x^{\prime} = y \oplus x^{\prime} = y\Delta_{\alpha}x^{\prime} \tag{1}$$

If we consider the fundamental set of patterns $\{(x^{\mu}, y^{\mu}) \mid \mu = 1, 2, ..., p\}$ then the ij -th entry of the matrix $y^{\mu} \oplus (x^{\mu})'$ is expressed as follows:

$$\left[y^{\mu} \oplus \left(x^{\mu}\right)^{t}\right]_{ii} = \alpha(y_{i}^{\mu}, x_{j}^{\mu}) \tag{2}$$

2.1 Learning Phase

Find the adequate operators and a way to generate a matrix **M** that will store the *p* associations of the fundamental set $\{(x^1, y^1), (x^2, y^2), (x^3, y^3), ..., (x^p, y^p)\}$, where $x^{\mu} \in A^n$ and $y^{\mu} \in A^m$ $\forall \mu \in \{1, 2, ..., p\}$.

Step 1. For each fundamental pattern association $\{(x^{\mu}, y^{\mu}) | \mu = 1, 2, ..., p\}$, generate p matrices according to the following rule:

$$\left[y^{\mu} \oplus \left(x^{\mu}\right)^{t}\right]_{T} \tag{3}$$

Step 2. In order to obtain an Alpha-Beta Associative Memory of type MAX, apply the binary MAX operator (\vee) according to the following rule:

$$\mathbf{M} = \vee_{\mu=1}^{p} \left[y^{\mu} \oplus \left(x^{\mu} \right)^{t} \right] \tag{4}$$

Consequently, the ij -th entry of an Alpha-Beta Associative Memory of type MAX is given by the following expression:

$$v_{ii} = \vee_{\mu=1}^{p} = \alpha(y_i^{\mu}, x_i^{\mu})$$
 (5)

Step 3. In order to obtain an Alpha-Beta Associative Memory of type min, apply the binary min operator (\wedge) according to the following rule:

$$\mathbf{W} = \wedge_{\mu=1}^{p} \left[y^{\mu} \oplus \left(x^{\mu} \right)^{\prime} \right] \tag{6}$$

Analogously, the *ij* -th* entry of an Alpha-Beta Associative Memory of type min is given by the following expression:

$$\psi_{ij} = \bigwedge_{\mu=1}^{p} = \alpha(y_i^{\mu}, x_j^{\mu}) \tag{7}$$

2.2 Recalling Phase

Find the adequate operators and sufficient conditions to obtain the fundamental output pattern y^{μ} , when either the memory \mathbf{M} or the memory \mathbf{W} is operated with the fundamental input pattern x^{μ} .

- **Step 1**. An unknown input pattern x^{ω} with $\omega \in \{1, 2, ..., p\}$ is presented to the Alpha-Beta Associative Memory.
- **Step 2**. In order to obtain an unknown output pattern y^{ω} with $\omega \in \{1, 2, ..., p\}$, an Alpha-Beta Associative Memory of type MAX will be used according to the following rule:

$$\mathbf{M}\Delta_{\beta}x^{\omega} = \bigwedge_{j=1}^{n} \beta(v_{ij}, x_{j}^{\omega}) = \bigwedge_{j=1}^{n} \left\{ \left[\bigvee_{\mu=1}^{p} \alpha(y_{i}^{\mu}, x_{j}^{\mu}) \right], x_{j}^{\omega} \right\}$$
(8)

Step 3. In order to obtain an unknown output pattern y^{ω} with $\{\omega = 1, 2, ..., p\}$, an Alpha-Beta Associative Memory of type min will be used according to the following rule:

$$\mathbf{W}\nabla_{\beta}x^{\omega} = \bigvee_{i=1}^{n} \beta(\psi_{ij}, x_{i}^{\omega}) = \bigvee_{i=1}^{n} \left\{ \left[\bigwedge_{\mu=1}^{p} \alpha(y_{i}^{\mu}, x_{i}^{\mu})\right], x_{i}^{\omega} \right\}$$

$$\tag{9}$$

Without dependence on the Alpha-Beta Associative Memory type used throughout the recalling phase, a column vector of dimension *m* will be obtained.

3 Numerical Results

Let p=5, n=4, m=4. Given the fundamental patterns $\{(x^{\mu},y^{\mu}) \mid \mu=1,2,...,p\}$, obtain an Alpha-Beta Associative Memory. The fundamental associations will be denoted as: $\{(x^1,y^1),(x^2,y^2),...,(x^5,y^5)\}$.

$$x^{1} = \begin{bmatrix} 1 \\ 1 \\ 0 \\ 1 \end{bmatrix} \qquad x^{2} = \begin{bmatrix} 0 \\ 0 \\ 0 \\ 1 \end{bmatrix} \qquad x^{3} = \begin{bmatrix} 0 \\ 1 \\ 1 \\ 1 \end{bmatrix} \qquad x^{4} = \begin{bmatrix} 0 \\ 1 \\ 0 \\ 0 \end{bmatrix} \qquad x^{5} = \begin{bmatrix} 1 \\ 0 \\ 1 \\ 1 \end{bmatrix}$$

$$y^{1} = \begin{bmatrix} 1 \\ 1 \\ 0 \\ 1 \end{bmatrix} \qquad y^{2} = \begin{bmatrix} 1 \\ 0 \\ 0 \\ 1 \end{bmatrix} \qquad y^{3} = \begin{bmatrix} 1 \\ 1 \\ 1 \\ 1 \end{bmatrix} \qquad y^{4} = \begin{bmatrix} 1 \\ 1 \\ 0 \\ 0 \end{bmatrix} \qquad y^{5} = \begin{bmatrix} 1 \\ 0 \\ 1 \\ 1 \end{bmatrix}$$

Learning Phase 3.1

Obtain the corresponding matrices $M_1, M_2, ..., M_5$, according to step 1, indicated in section 2.1.

According to step 2 in section 2.1, an Alpha-Beta Associative Memory of type MAX denoted by M, is obtained. Analogously, according to step 3 in section 2.1, an Alpha-Beta Associative Memory of type min denoted by W, is obtained.

Recalling Phase 3.2

Obtain the corresponding output patterns, by performing the operations $\mathbf{M}\Delta_{\beta}x^{\omega}$, $\forall \mu \in \{1,2,\ldots,p\}$ as stated in section 2.2. Due to paper space limitations, only the Alpha-Beta MAX type recalling phase results are shown.

Fig. 1. Alpha unit.

The reader can easily verify that the Alpha-Beta min type recalling phase also recalls the whole fundamental set of patterns perfectly.

4 Implementation Details

As previously mentioned, the main goal of this paper is to derive an efficient implementation of the Alpha-Beta Associative Memories which exploits the inherent parallelism of this mathematical model, targeted towards FPGAs. The Alpha operator implementation is shown in Figure 1, while the Beta operator implementation is shown in Figure 2.

The proposed architecture works with a 50 MHz master clock, which implies a 20ns period. As is it shown in Figure 3, the learning phase is implemented with 5 registers, 1 MAX/min block and 2 external 10ns SRAM chips (mounted on the same board), that allow 1MB of data storage, 8 Alpha blocks that allow byte processing instead of bit processing, resulting in an eight times faster learning phase compared against [8].

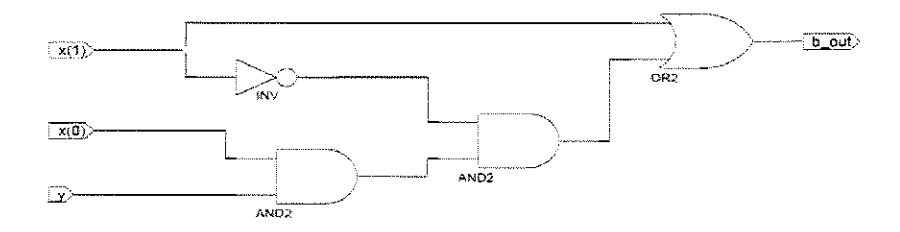


Fig. 2. Beta unit.

There are two remarkable topics to be taken into consideration. The former concerns about the amount of logic resources that are needed to implement the two binary operators (Alpha and Beta). The latter results from the fact that most of the components that constitute the learning phase are combinatorial circuits. Hence, it is possible to read data from the external SRAM memory at the same time that a new bit is shifted to the Alpha blocks.

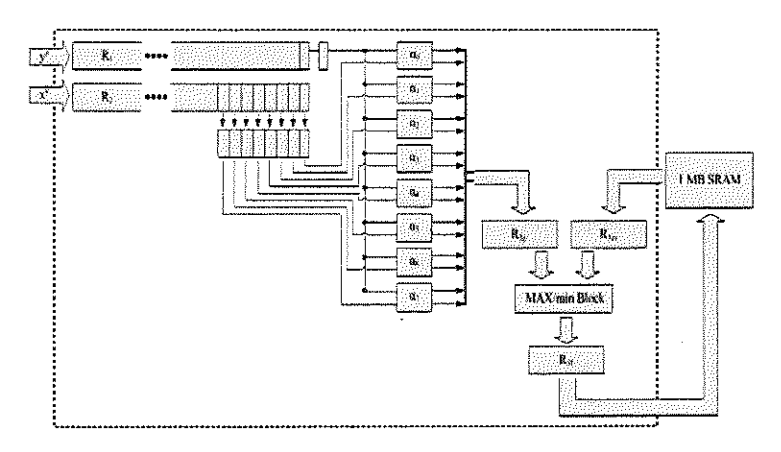


Fig. 3. Learning Phase Architecture.

As it is shown in Figure 4, the recalling phase is implemented with 4 registers, 8 Beta block, 1 min/MAX block and the same 2 external 10ns SRAM chips that were used to store the fundamental associations during the learning phase. The recalling phase is executed as follows. Firstly, R_{3m} receives one data word from the Alpha-Beta Associative Memory (stored in the 2 external 10ns SRAM chips). Then, R_i receives the unknown input pattern. Finally, R_2 stores the recalled output pattern.

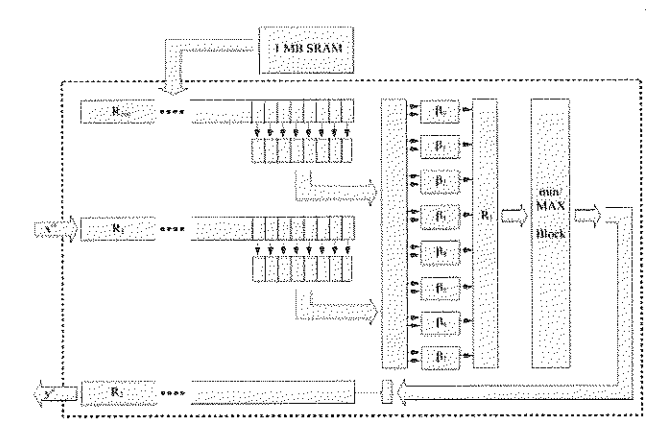


Fig. 4. Recalling Phase Architecture.

5 Experimental Results

The experimental phase was carried out in two stages. In the first one, the same fundamental set of patterns that was presented in section 3, was downloaded to the proposed architecture. The performance results are shown in Figure 5 and Figure 6. As expected, the entire fundamental set of patterns was perfectly recalled. In order to estimate how the Alpha-Beta Associative Memory model performs with high dimensional data, 20 binary images obtained from the Third International Fingerprint Verification Competition (FVC2004) were used as fundamental patterns (Figure 7). Originally, each one of these images is 160 by 120 pixels.

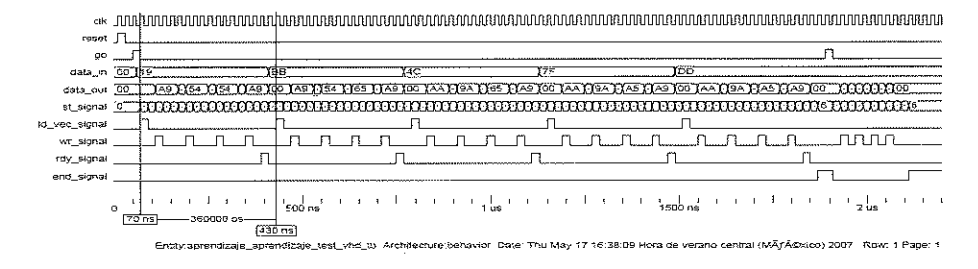


Fig. 5. Learning Phase Performance.

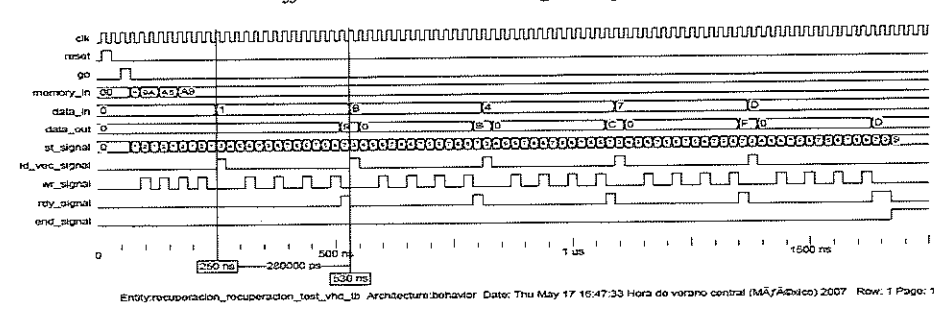


Fig. 6. Recalling Phase Performance.

The Advanced Batch Converter image editor was used to modify the fingerprints dimensions, such that it was possible to keep the pattern associations over the previously mentioned SRAM chips. The experimental phase was carried out as follows: after the register initialization process was concluded, the first association was learned and recalled. Subsequently, the first and second associations were learned and recalled; after that, the same procedure continued in a consecutive manner until the fundamental set of patterns was completely learned and recalled. The above mentioned procedure was executed 10 times, each time changing the fundamental patterns order randomly. A relevant thing to mention about the recalling criterion that was used along the experimental phase is that, in this case, perfect recall means that all of the 1600 bits were exactly recovered. Particularly, outstanding results were achieved by both types of Alpha-Beta Associative Memories (the whole fundamental set of patterns was perfectly recalled).

6 Conclusions and Ongoing Research

In this paper, we introduced a simple but efficient implementation of the Alpha-Beta Associative Memories which exploits the inherent parallelism of this mathematical model targeted towards FPGAs that overcomes a serious challenge in pattern recognition tasks (bottle-neck problems due to high dimensional data). A relevant thing to mention is that after a fundamental pattern is downloaded to the proposed architecture, each bit is learned in 90 ns, which fulfils one of the main purposes of this paper. Moreover, if the learning rate is known, it is possible to estimate the learning phase duration even with high dimensional fundamental patterns. Usually, this situation takes place when the fundamental patterns are RGB images. It is worth to mention that the proposed architecture can be easily adapted to work as an Alpha-Beta bi-directional associative memory [6-7].

Fig. 7. Fundamental Patterns.

Acknowledgments

The authors of the present paper would like to thank the following institutions for their economical support to develop this work: National Polytechnic Institute, Mexico (CIC, SIP, PIFI, COFAA), CONACyT and SNI.

References

- Yáñez-Márquez, C., Felipe-Riverón, E. M., López-Yáñez, I., and Flores-Carapia, R. (2006). A Novel Approach to Automatic Color Matching, LNCS 4225: 529-538.
- Acevedo-Mosqueda, M. E., Yáñez-Márquez, C., and López-Yáñez, I. (2006). Alpha-Beta Bidirectional Associative Memories Based Translator, IJCSNS 6: 190-194.
- Yáñez-Márquez, C., Sánchez-Fernández, L. P., and López-Yáñez, I. (2006). Alpha-Beta Associative Memories for Gray Level Patterns, LNCS 3971: 818-823.
- Sossa, H., Barrón, R., Cuevas, F., and Aguilar, C. (2005). Associative Gray Level Pattern Processing using Binary Decomposition and α β Memories, Neural Processing Letters, 22: 85-111.
- Kohonen, T. (1972). Correlation Matrix Memories, IEEE Transactions on Computers, 21: 353-359.
- Acevedo-Mosqueda, M. E., Yáñez-Márquez, C., and López-Yáñez, I. (2006). A New Model of BAM: Alpha-Beta Bidirectional Associative Memories, LNCS 4263: 286-295.
- Acevedo-Mosqueda, M. E., Yáñez-Márquez, C., and López-Yáñez, I. (2007). Alpha-Beta bidirectional associative memories: theory and applications, Neural Processing Letters, 26: 1-40.
- 8. Yáñez-Márquez C. (2002). Associative memories based on order relations and binary operators (in Spanish) PhD Thesis, Center for Computing Research, México.

Synchronization of complex networks with nonidentical nodes

Gualberto Solís-Perales* and Daniela Valle-Rodríguez

Departamento de Electrónica, CUCEI, U. de G., Av. Revolución 1500, Guadalajara Jalisco, México * Corresponding Author, e-mail: gualberto.solis@cucei.udg.mx (Paper received on February 29, 2008, accepted on April 15, 2008)

Abstract. In this communication we present the synchronization of complex networks adding a derivative coupling term in the network equation. This is, using a simple derivative action the synchronous behavior of a complex network is achieved. We consider strictly different chaotic systems in nodes. We show that the derivative term leads to the synchronous behavior in networks that has three different dynamical models in nodes, whereas when there is no derivative term the network is leaded to an equilibrium point. Numerical simulation are provided to illustrate the result.

Keywords: Complex Networks, Synchronization, Chaos

1 Introduction

Network are everywhere in nature, a network can be seen as a set of objects connected or linked with some strength coupling. The study of this class of dynamical system has attracted a lot of attention see for instance[1],[2],[3]. Complex networks involves a common phenomenon between dynamical systems, synchronization [4], moreover synchronization of chaotic systems is still an open topic (refer to [5],[6],[7]). Therefore synchronization of complex networks is a challenging recent problem under study. Examples of networks are so diverse, individuals in a community, where every person is represented as a node; the internet, which is a set of routers connected by physical or virtual connections; the Web, where virtual web documents can be accessed via other web links [8], or others web documents can be accessed via this web. Biological networks, where an important issue is to understand the interaction between cells [9]; in protein interactions, it has been shown that this interaction is highly heterogeneous [10]; epidemic spreading studies [11]; until collaboration networks [12]; thus understanding the synchronization of complex networks is an essential issue in science and technology.

The problem of network synchronization has been studied departing from the determination of the appropriate coupling strength (see for instance [2],[13]), and assuming that every system in each node is equal to any other system in the network. However, these assumptions are not realistic, since the nodes in a network

© E. V. Cuevas, M. A. Perez, D. Zaldivar, H. Sossa, R. Rojas (Eds.) Special Issue in Electronics and Biomedical Informatics, Computer Science and Informatics
Research in Computing Science 35, 2008, pp. 157-164



community, internet, webs etc. are in general different. In this sense we deal with the particular problem of synchronize a network which nodes are represented by nonidentical chaotic systems. Moreover, we seek for synchronization of the network in a chaotic attractor, neither into a limit cycle nor an equilibrium point. Maovin and Donghua [14] reported the synchronization of a complex network assuming unknown the dynamics in each node and the strength coupling functions, authors used the LaSalle invariance principle and a simple linear controller. However, they assume that there is an isolated dynamics to which the nodes in the network are synchronized. This is a strong assumption, since the behavior of the network depends on the collective dynamics and not on an isolated node. Other approach to control and synchronization of complex network is provided in [15] where they considered a synchronization scheme assuming that a few nodes are controlled via a proportional term. Nevertheless, the synchronization objective was to stabilize the global behavior in an equilibrium point and not in a chaotic attractor. Gua-Ping and coworkers [16] reported an approach to synchronize a dynamical complex network using state observers, but the synchronization is achieved via solving a LMI, solution of this kind of inequalities requires a great computational capacities for networks with many nodes, which represents a consumption of resources.

We present an approach that consider a derivative coupling term in the network equation to improve the synchronous behavior. To this end, we propose to synchronize scale-free networks and small-world networks with nonidentical nodes. The derivative term lead the global behavior of the network to a chaotic attractor. Compared with the standard coupling, the derivative coupling under certain network topology reaches the chaotic synchronous behavior, whereas the standard coupling lead the network to the equilibrium ir a limit cycle.

The paper is organized as follows. In Section II the model for the complex networks dynamics is described, in Section III we propose the derivative term to improve the synchronization behavior, results on synchronization of scale-free and small-world networks are illustrated in Section IV and finally, the work is closed with some concluding remarks in section V.

Model of dynamical complex networks

Consider a dynamical complex network with N identical nodes and diffusive couplings, which every node is an identical n-dimensional dynamical system and with state equation given by

$$\dot{x}_i = f(x_i) + c \sum_{j=1}^{N} a_{i,j} \Gamma(x_j - x_i)
y_i = x_i$$
(1)

where $x_i = (x_{i1}, x_{i2}, \dots, x_{in})^T \in \mathbb{R}^n$ is the state vector for the i - th node, $f: \mathbb{R}^n \times \mathbb{R} \to \mathbb{R}^n$ is a smooth nonlinear vector field, c > 0 stands for the coupling strength, the constant matrix $\Gamma = diag(\gamma_1, \gamma_2, \dots, \gamma_n)$ is a diagonal matrix with $\gamma_k = 1$ for the k - th state, this means that two nodes are coupled via the k - th state variable. In other words, matrix Γ determines by which variables the oscillators are coupled.

Now, the coupling coefficients $a_{i,j}$ are the incomes of a real matrix A, if it is a connection between node i and node j ($j \neq i$), therefore $a_{ij} = a_{ji} = 1$; otherwise, $a_{i,j} = a_{j,i} = 0 (j \neq i)$. Then the coupling matrix is diagonal and irreducible if we consider that there are no isolated nodes, thus, we know that zero is an eigenvalue of A with multiplicity 1, and the others eigenvalues of A are strictly positive. Network synchronization is defined as follows

Definition 1. A complex network is Completely Synchronized if every node synchronizes each other, $\lim_{t\to\infty} ||x_i-x_j||\to 0$ for all $1\leq i,j\leq N$.

2.1 The proposed derivative coupling

We consider that the vector fields $f(x_i)$ in every node of the network are in general nonidentical. This is a realistic consideration since in real networks dynamical system in a node is in general different. Therefore, the main contribution is the modification of the equation (1) by adding a derivative coupling term, with this new term the synchronization behavior of the network is investigated. With these modifications we can rewrite (1) as follows

$$\dot{x}_i = f(x_i) + c_P \sum_{j=1}^{N} a_{i,j} \Gamma(x_j - x_i) + c_D \sum_{j=1}^{N} a_{i,j} \Gamma(\dot{x}_j - \dot{x}_i)$$
 (2)

where we have added the derivative part, c_P and c_D are the Proportional and Derivative coupling strength respectively. The derivative term is such that the network dynamics is increased in the sense that the interconnection between nodes are provided by the time variation of the linking state. Therefore, the linking of the nodes in the network are composed by the states and the time derivative of the states. With this modification we look for the synchronization of complex networks in a chaotic attractor which is defined by the collective behavior of the network.

3 Results on synchronization

We seek for complete synchronization of a network in a synchronization manifold $\Psi(x)$, in other words, synchronization of the network in a chaotic attractor. Where the synchronization manifold is given by $\Psi(x) = x_1 = x_2 = \cdots = x_N$ and correspond to the synchronized behavior. It is clear that x_i for some i could be seen as a solution of an isolated system which in this case is uncertain. The synchronization manifold $\Psi(x)$ is a result of the collective behavior and it is not

known a prior.

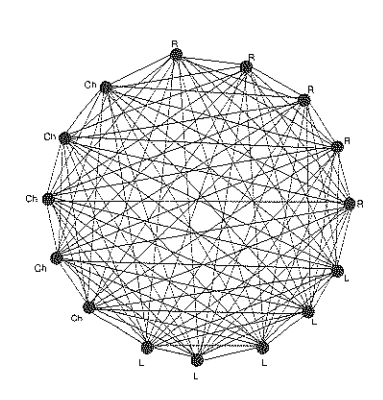


Fig. 1. Small-World complex network, where R, L, Ch stand for the Rössler, Lorenz and Chen systems respectively.

3.1 Synchronization of Small-World Networks

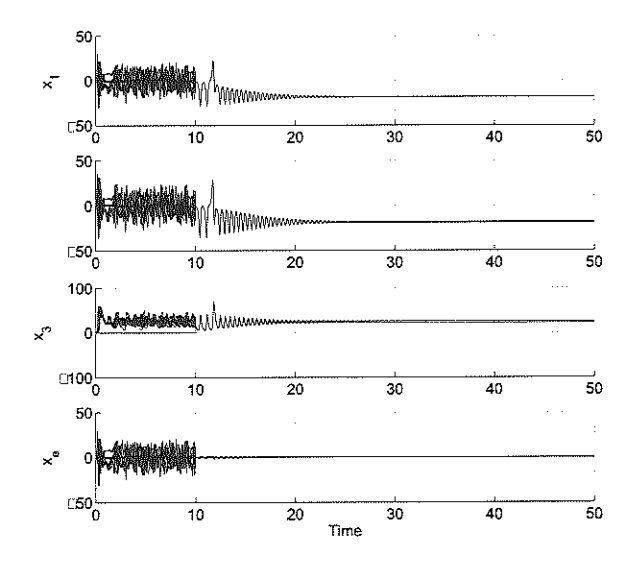
Small world networks are characterized by possessing a relatively small average path length. The average path length, is defined as the mean distance between two nodes, averaged over all pair of nodes. To illustrate the result, let us consider a network with three autonomous chaotic systems given by the Rössler, Chen and Lorenz systems

$$\dot{x}_1 = -x_2 - x_3
\dot{x}_2 = x_1 + ax_2
\dot{x}_3 = (x_1 - d)x_3 + b$$
(3)

$$\dot{x_1} = \sigma(x_2 - x_1)
\dot{x_2} = \rho x_1 + \beta x_2 - x_1 x_3
\dot{x_3} = x_1 x_2 - \alpha x_3$$
(4)

$$\dot{x_1} = s(x_2 - x_1)
\dot{x_2} = rx_1 - x_1x_3 + x_2
\dot{x_3} = x_1x_2 - gx_3$$
(5)

Where the parameters for the system in node i-th, are different, which represents nonidentical dynamical systems. Thus, the network considered for this case is illustrated in Figure 1, where 5 Rössler systems, 5 Chen systems and 5 Lorenz systems were connected and with $\Gamma = diag(1,1,1)$.



 ${\bf Fig.\,2.}\ {\bf Stabilization}\ {\bf of}\ {\bf the}\ {\bf Small-World}\ {\bf complex}\ {\bf network}\ {\bf at}\ {\bf an}\ {\bf equilibrium}.$

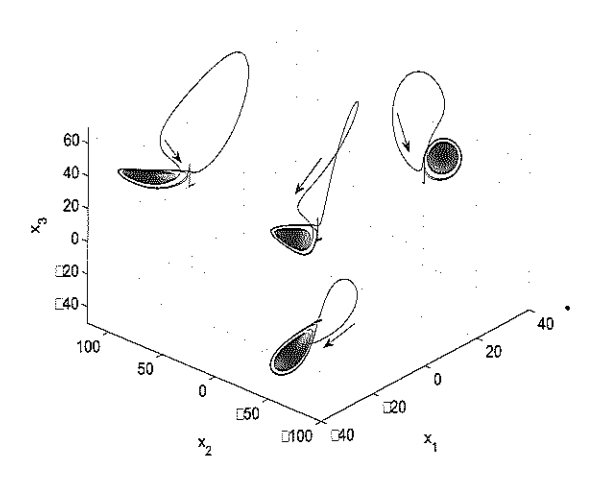


Fig. 3. Attractor for the stabilization of the network.

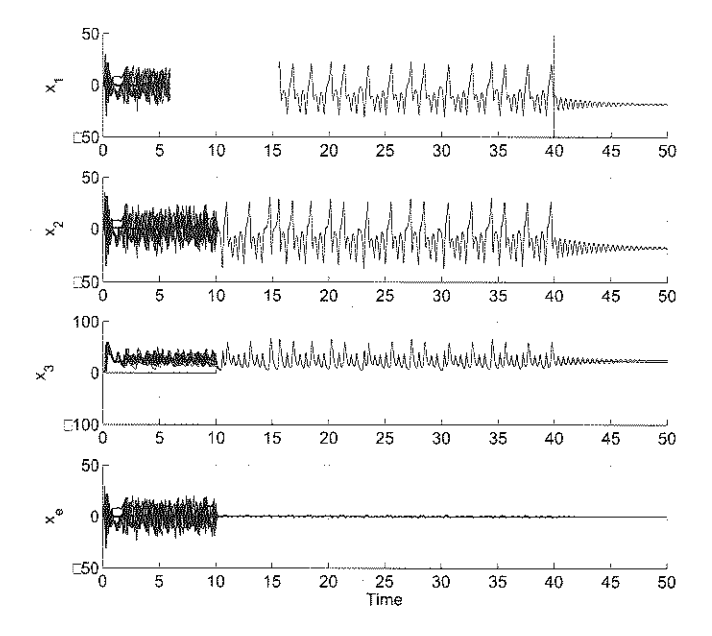


Fig. 4. Synchronization of the network.

The behavior of the network with no derivative coupling is illustrated in Figure 2, where the connection was activated at t=10sec. It can be observe that the dynamics of the network is leaded to an equilibrium point. This means that with this network topology the synchronization is achieved but in an equilibrium, this is, the the collective behavior is such that inhibits the chaotic behavior in each node. It is important to note that there is no value for the coupling parameter c_P such that the network synchronizes in a chaotic attractor, for this case we use $c_P=15$.

In Figure 3 the attractor of one node in the network and its corresponding canonical projections are illustrated. The trajectories of each system in the network are driven to an equilibrium point. A conjecture for this behavior can be the fact that the system in the network are strictly different, this means that, since each system in the network possess a strictly different vector fields and the corresponding trajectories are also different.

Therefore, in order to obtain chaotic synchronization in the network, we use the modified equation (2). Thus, considering the same network topology but with $c_P = 15$ and $c_D = 1$ the synchronization in the chaotic attractor is obtained. The time evolution is illustrated in Figure 4. Where we have connected the network

at $t=10 {\rm sec.}$ using the derivative coupling. At $t=40 {\rm sec.}$ the derivative coupling is disconnected and the behavior is leaded again to the equilibrium point.

In Figure 5 the chaotic attractor of a single node is presented as well as its corresponding canonical projections. This attractor was obtained using the derivative coupling, and again after a period of time the derivative coupling is disconnected and the trajectory is leaded to an equilibrium point. Note that, in Figure 4, the corresponding error $x_e = x_i - x_j$ for $j = 1, 2, \ldots, N$, this is, the error of the output of node *i*-th, and the node *j*-th, for all *j*.

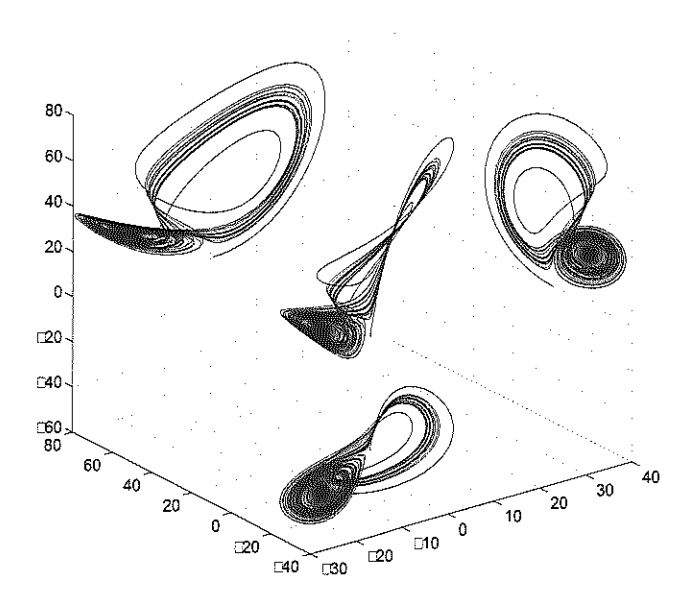


Fig. 5. Synchronization of the network in a chaotic attractor.

4 Conclusions

In this communication we illustrated the synchronization of a complex small-world network. The main contribution is that using a derivative coupling, a network with non identical systems in nodes can reach the synchronous behavior. We show that the network is leaded to an equilibrium point if the coupling factor is increased, but using the derivative coupling the synchronization in a chaotic

attractor is obtained. The next step is apply this derivative coupling to scale-free networks which is still under study.

References

- D. J. Watts and S. H. Strogatz, Collective dynamics of small world networks, Nature, vol. 393, pp. 440-442, June 1998.
- S. Boccaleti, V. Latora, Y. Moreno, M. Chavez and D.U. Hwang, Complex networks: Structure and Dynamics, Phys. Reports, 424 (2006) 175-308
- X.F. Wang and G. Chen, Complex networks: Small-world, scale-free and beyond, IEEE Circuts and Systs. Magazine, (2003) 6-20
- V. S. Afraimovich, N. N. Verichev and M. I. Rabinovich, Stochastic synchronization of oscillations in dissipative systems, Radiophys and Quantum Electronics, 29 (1986) 747-751
- L.M. Pecora and T.L. Carroll, Synchronization in chaotic systems, Phys. Rev. Letts., 64 (1990) 821-824.
- R. Femat, J. Alvarez-Ramírez and G. Fernandez Anaya, Adaptive synchronization of high order chaotic systems: A feedback with low parameterization, *Phys. D*, 139, 231-246, 2000
- R. Femat and G. Solís-Perales, On the chaos synchronization phenomena, Phys. Lett. A, 262 (1999) 50-60.
- B.A. Huberman and L.A. Adamic, Growth dynamics of the World-Wide Web, Nature, 401 (1999) 131.
- 9. A.L. Barabási and Z.N. Oltvai, Nature Reviwes Genetics, 5 (2004) 101-113.
- R. Pastor-Satorras, E. Smith and R.V. Solé, Evolving protein interaction networks through gene duplication, Jour. of Theoretical Biology, 222 (2003) 199-210
- R. Pastor-Satorras and A. Vespignani, Epidemic spreading in scale-free networks, Phys. Rev. Letts., 86 (2001) 3200-3203
- A.L. Barabási, H. Jeong, Z. Nda, E. Ravasz, A. Schubert and T. Vicsek, Evolution of the social network of scientific collaborations, *Physica A*, 311, (2002) 590-614
- X.F. Wang and G. Chen, Synchrnoization in scale-free dynamical Networks: Robustness and Fragility, IEEE Trans. on Circs. and Systs. 1, 49 (2002) 54-62.
- M. Chen and D. Zhou, Synchronization in uncertain complex networks, Chaos 16 (2006) 013101
- X. Li, X. Wang and G. Chen, Pinning a complex dynamical network to its equilibrium, IEEE Trans. Circs., and Systs. I, 51, No. 10, (2004) 2074-2087
- G.P. Jiang, W.K-S. Tang and G. Chen, A state-observer-based approach for synchronization in complex dynamical networks, *IEEE Trans. Circs.*, and Systs. I, 53, No.

Hot Rolling Scheduling Optimization Problem

Carlos A. Hernández Carreón¹, Héctor J. Fraire Huacuja², Karla Espriella Fernandez¹, Guadalupe Castilla Valdez², Juana E. Mancilla Tolama¹

 ¹IPN, E.S.I.M.E. Azcapotzalco
 Av. de las Granjas No. 682 Col. Santa Catarina 02250-Azcapotzalco, México, D. F.
 ² Instituto Tecnológico de Ciudad Madero.
 1o. de Mayo y Sor Juana I. de la Cruz S/N. 89440-Cd. Madero, Tamaulipas, México

Contact: cahc05@yahoo.com.mx, hfraire@prodigy.net.mx, karla rouge@yahoo.com, gpe_cas@yahoo.com.mx, emtolama@hotmail.com

(Paper received on February 29, 2008, accepted on April 15, 2008)

Abstract. In this paper the problem of minimizing the hot rolling time using genetic algorithms of a steel strip is approached. Unlike the traditional approaches in this work the steel chemical composition of the strip is incorporated as a problem parameter allowing the automatically setup of the hot mill for different steels. To validate the approach, a six-stand rolling mill is modeled as an optimization constrained problem. The used set of problem instances were built with realistic data of industrial schedules. In this paper the mathematical model and the instances set are completely described. To evaluate the model quality we present the results obtained with a solution method based on genetic algorithms (GA). The global rolling time obtained solving the modeled problem with a genetic algorithm (GA) is 0.051% better than the industrial time. The generated rolling schedule diminishes the equipment damage risks because it produces softer reductions than the rolling schedule proposed by the manufacturer. Currently we are developing new solution methods using different metaheuristics.

Keywords: genetic algorithm, hot rolling scheduling

1 Introduction

Steel hot rolling is one of the most important metalworking processes in comparison with any other deformation process, aimed to manufacture products of relatively large dimensions (sheets, strips, plates, foils, etc.), at high speeds [1]. The rolling mill reduces the thickness steel slab by rolling two driven work rolls in a mill stand (as we can see in Fig. 1). Due to high operational costs of a rolling mill is not acceptable to setup the rolling schedule in an empirical way.

© E. V. Cuevas, M. A. Perez, D. Zaldivar, H. Sossa, R. Rojas (Eds.) Special Issue in Electronics and Biomedical Informatics, Computer Science and Informatics
Research in Computing Science 35, 2008, pp. 165-174



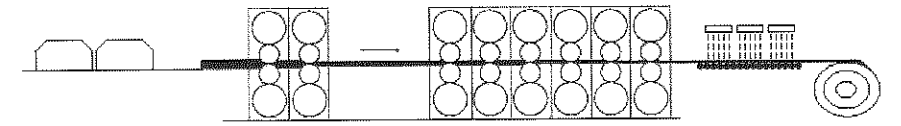


Fig. 1. Hot rolling process

The hot rolling scheduling problem consist in determining the reductions for every rolling pass to obtain the final thickness, considering that the rolling power should be lower than the motor power.

2 Related works

The hot rolling scheduling problem has been the subject of several research works. Nolle & Armstrong propose the optimization of a 7-stand hot rolling mill using simulated annealing (SA) and genetic algorithms (GA) [2]. The goal was to optimize the surface quality of a steel slab. In this work the SA shows a better performance than GA. Oduguwa & Tiwari propose a general methodology to solve problems of sequential processes using GA [3]. The proposal consists in a binary representation of the full set of parameters as a sub-set of strings. An application to multi-pass hot rolling was given, using a multi-objective model. The goal was to maximize the system productivity, optimizing the roll force. Chakraborti [4] applied GA to the problem of minimizing hot rolling time in a reversing mill stand, determining the optimum number of odd passes. In this work the efficiency of GA to calculate a hot rolling schedule, with respect to traditional methods, is demonstrated. Another contribution of Chakraborti [5] was the study of surface profiles of slab rolled. In this case, two objective functions were applied to evaluate the wearing and deflection rolls as the main factors of the variation of the thickness during rolling process. The GA produces good quality solutions with respect to the solutions corresponding to the industrial data [6]. Other approaches to determine hot rolling schedules have been applied as neural network [7, 8], fuzzy logic [9], and finite element methods [10]. Currently the more successfully approach to solve the hot rolling scheduling problem is the genetic algorithm.

In this work the steel chemical composition of the strip is incorporated, as a problem parameter, allowing the automatically setup of the hot mill for different steels. To validate the approach, a six-stand rolling mill is modeled as an optimization constrained problem and a set of industrial instances is used.

3 Hot rolling model

The process parameters to roll the steel are obtained using a rolling model. Fig. 2 shows the hot rolling schedule flowchart to calculate the parameters, for a rolling mill with n deformation passes of the roll stand i.

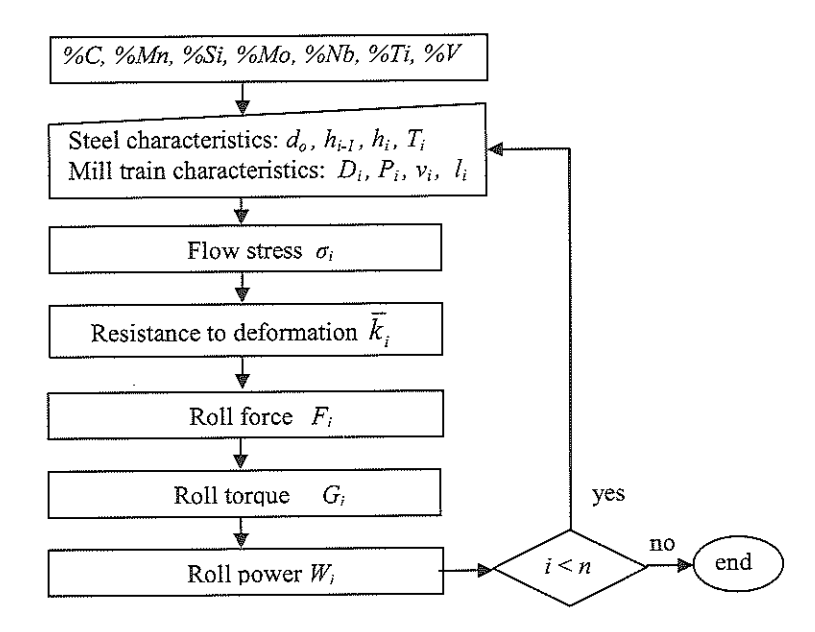


Fig. 2. Hot rolling schedule flowchart.

In this work we use the Hernández model to predict the flow stress of any kind of steel independently of the chemical composition [11-14]. The flow stress parameters include the temperature, the strain, strain rate, grain size and the chemical composition of the rolling steel.

The hot rolling model is used to calculate the flow stress and the resistance to deformation in two steps. The first step uses a stress-strain curve model to calculate the flow stress as follows:

```
Let
      Z_i the Zener-Hollomon parameter in stand i,
      A = (12.19 + 65.58 \cdot \%C - 49.05 \cdot \%Nb) \exp(7.076 \cdot Q) and
      Q = 267,000-253552·%C +1010·%Mn +33,620.7·%Si + 35,651.28·%Mo +93,680.52·%Ti 0.5919+ 70,729.85·%Nb<sup>0.5649</sup>+ 31,673.46·%V
       where:
                %C : percentage weight of carbon.
                %Mn: percentage weight of Manganese.
                %Si : percentage weight of Silicon.
                %Mo: percentage weight of molybdenum.
                %Nb: percentage weight of Niobium.
                %Ti : percentage weight of Titanium.
                %V : percentage weight of Vanadium.
```

Once the above parameters are determined, the flow stress is calculated using expression (1).

 $\sigma_i = B_i \cdot [1 - \exp(-C_i \varepsilon_i)]^{n_i} - B^i_i \left\{ 1 - \exp\left[-K_i \left(\frac{\varepsilon_i - a\varepsilon_{p_i}}{\varepsilon_{p_i}}\right)^{m_i}\right] \right\}$ (1)

where:

a: empirical parameter with value 0.95.

 ε_i : steel strain in stand *i*.

 ε_p : peak strain for a given steel composition.

 Z_i : Zener-Hollomon parameter in stand i.

B, B'_b K_b C_i : parameters dependent of Z/A.

$$A = (12.19 + 65.58 \cdot \%C - 49.05 \cdot \%Nb) \exp(7.076E - 05 \cdot Q)$$
 (2)

$$Q = 267,000 - 253552 \cdot \%C + 1010 \cdot \%Mn + 33,620.7 \cdot \%Si + 35,651.28 \cdot \%Mo +93,680.52 \cdot \%Ti^{0.5919} + 70,729.85 \cdot \%Nb^{0.5649} + 31,673.46 \cdot \%V$$
(3)

In the second step, the resistance to deformation [15, 16] is calculated as follows:

$$\overline{k}_{i} = \frac{1}{\alpha_{i}} \int_{\alpha_{i}}^{\alpha} \sigma_{i} d\alpha_{i} \tag{4}$$

where:

 α_i : angle between the steel and the roll in stand i.

 σ_i : plane flow stress in stand i.

Then the rolling forces to deform the steel can be calculated. The constitutive model equations applied in this work have been validated with industrial data [17]. The rollseparating force F can be calculated using different mathematical models, like rolling theories of Sims [18], Cook & McCrum [19] and Alexander & Ford [20], in this work is used the Alexander & Ford model.

The roll force is calculated using:

$$F_{i} = \frac{X}{4} w \cdot L_{i} \cdot (\pi + z_{a_{i}}) \cdot \overline{k}_{i}$$
 (5)

where:

X: parameter with value 1.07

 L_i : contact arc between the roll and the steel in stand i.

w: steel width.

 z_{ai} : geometrical parameter in stand i.

 k_i : resistance to deformation in stand I, as calculated with (4)

The roll torque is required, applying a variant of equation (1). The model of Alexander & Ford was used [20]. The energy consumption or the rolling work for a given pass can be determined by an empirical expression that takes into account rolling torque. With this formulation, overloading of the main motor can be assessed.calculated using:

$$G_i = 250 \cdot w \cdot R'_i \cdot \Delta h_i \left(\pi + \frac{z_{a_i}^2}{z_{p_i}} \right) \cdot \bar{k}_t$$
 (6)

where:

 R'_{i} : roll radius with correction plane in stand i.

 za_i : geometrical parameter in stand i. zp_i : geometrical parameter in stand i.

 Δh_i : difference between the final and the initial thickness in stand i.

Finally the rolling power can be calculated as follows:

$$W_i = 2 \pi \cdot G_i \frac{RPM_i}{60} \tag{7}$$

where:

 G_i : roll torque in stand i.

 RPM_i = revolutions turns per minute in stand i.

4 Instance description

Industrial data was obtained from the Hylsa Monterrey Company and from the software HSMM of INTEG Process Group [21]. Table 1 shows the chemical compositions of the steels considered in this work. The first column contains the steel identifier. From column two to six are contained the percentage weight of carbon, manganese, silicon, niobium, titanium and vanadium.

% V % Nb % Ti Steels Id. % C % Mn % Si 0.045 0.45 0.069 0.0056 0.002 0.080 2 0.038 0.300 0.009 0.005 0.0020.0020.002 3 0.082 0.480 0.045 0.036 0.002 0.014 0.023 0.013 0.003 4 0.071 0.758 5 0.0028 0.170 0.009 0.035 0.035 0.005 6 0.053 0.7840.010 0.026 0 0

Table 1. Chemical composition of steel.

From the industrial data 17 instances were defined, which can be consulted in [22]. Each instance defines the parameters of a different rolling problem. A rolling problem consists in determining the intermediate reductions needed to roll the slab steel and to obtain the final thickness in a 6-stand roll mill. Table 2 shows the parameters included in an instance: the data source, the number rolling stands (n), the instance name, the initial thickness (h_0) , the final thickness (h_f) , initial width (w), chemical composition (%C, %Mn, %Si, %Mo, %Nb, %Ti, %V), and for each rolling stand the roll diameter (D_i) , the roll speed (v_i) , the temperature (T_i) , the grain size (do_i) . Also the source of the data is indicated (Hylsa Monterrey or software HSMM of INTEG Process Group)), the motor power (P_i) and the inter-stand distance (l_i) are indicated.

Industrial Da	ta: Hylsa	n	= 6	Nan	Name: hyl001.txt		
$h_{\theta} = 48 \text{ mm}$		h	$_f = 3.8 \text{ mm}$. w=	991mm		
%C=0.053, %N	In=0.784,	%Si=0.01	7, %Mo=0,	%Ti = 0, %	6Nb = 0, %	V = 0	
Roll Pass No.	1	2	3	4	5	6	
D_i (mm)	752	764	758	492	456	474	
v_i (m/s)	0.81	1.43	2.21	3.38	4.57	5.54	
T_i (°C)	1010	987.64	964.25	942.7	927.32	908.27	
$d_{0i}\left(\mu\mathrm{m}\right)$	400	100	80	60	40	20	
$P_i(kW)$	7000	7000	7000	7000	7000	7000	
$l_i(\mathbf{m})$	3.5	3.5	3.5	3.5	3.5		

Table 2. Hot rolling scheduling problem instance.

Formulation of the optimization problem

Given an instance of the hot rolling scheduling problem, the goal is to determine the intermediate thicknesses h_1, \ldots, h_{n-1} to minimize the total rolling time:

$$t = \sum_{i=1}^{n} t_i$$

To calculate the total rolling time t, the process time in each stand is added, to calculate the total rolling time. The rolling time in each stand is calculated adding the contact time between the roll and the steel, and the time to take the steel from one stand to another, taking into account the roll radius R_i , roll peripheral speed v_i , inter-stand distance l_i , initial thickness h_i , and final thickness h_{i-1} (Fig. 3).

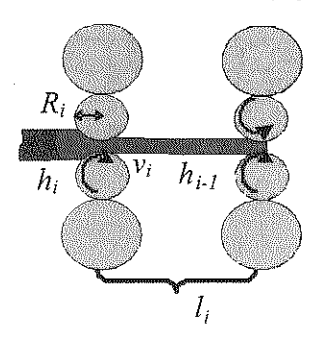


Fig. 3. Parameters to calculate the rolling time in a pass.

The rolling time in a stand can be calculated as follows:

$$t_i = \frac{\sqrt{\Delta h_i \cdot R_i} + l_i}{v_i} \tag{8}$$

where:

 R_i : roll radius in stand i. l_i : inter-stand distance

 v_i : roll speed in stand i. Δh_i : h_{i-1} - h_i

The problem includes the following two constraints:

1. In every rolling stand a reduction will be applied until the final thickness is obtained. Each intermediate thickness should be lower than the previous one:

$$h_0 > h_1 > h_2 > h_3 > h_4 > h_5 > h_f$$

To get the reduction in a rolling stand, a rolling power is applied. The rolling power should be lower than the motor power:

$$V_i < P_i$$
 for $i = 1 \dots 6$

6 Industrial rolling time calculation

For each kind of steel there is a rolling schedule given by the machine manufacturer. The rolling schedule proposes to the machine operator the reductions that must be applied to rolling the slab steel. These reductions are a suboptimal solution of the problem, but it is a good empirical solution. We use the instance parameters, the rolling schedule proposed by the manufacturer and the expression (8) to calculate the total industrial rolling time. Table 3 shows the reductions configuration for the steel specified in the Hylsa Monterrey instance and the rolling time calculated with expression (8) in each stand.

Table 3. Total industrial rolling time

Rolling stand No.	D _i mm	v _i m/s	I_i m		Stand exit ckness, mm	Rolling time,s
				h_0	48	
1	752	0.81	3.5	h_I	26	4.433
2	764	1.43	3.5	h_2	14.3	2.494
3	758	2.21	3.5	h_3	. 9.31	1.603
4	492	3.38	3.5	h_4	6.03	1.043
5	456	4.57	3.5	h_5	4.55	0.769
6	474	5.54		h_f	3.8	0.0024
			Total in	dustria	l rolling time:	10.3444

The total industrial rolling time will be the reference time to compare the rolling time obtained with the solution methods.

Experimental results

In this section the experimental results of the model evaluation are described. The experiments were carried out with Microsoft Windows Server 2003 for Small Business, dual Xeon CPU 3.06 GHZ, 3.87 GB RAM and the compiler C++.

To evaluate the quality of the proposed model, the rolling time obtained solving the modeled problem with a genetic algorithm (GA) and the industrial time calculated

using the rolling schedule proposed by the manufacturer were compared for each of the 17 considered instances. Each instance was solved 30 times to obtain the average results. The genetic algorithm uses SBX crossover, uniform mutation and population with feasible and unfeasible individuals and was configured using 40% of crossover, 50% of mutation, a population of 100 individuals and 100 generations.

The accumulated of the average execution time required for solving each instance is 42.62 cpu sec. The accumulated of the average execution time required for the GA to get the best solution is 23.62 cpu sec. While the average of the improvement percentage in the rolling time respect to the industrial time is 0.051%.

Table 4 shows the rolling schedule proposed by the manufacturer, and the rolling schedule generated by the GA for the Hylsa Monterrey instance. In both cases we can see the exit thicknesses and the rolling time in each stand.

	lable	าเม.					
		Manufacti	irer proposed	GA generated			
Roll pass		thickness mm)	Industrial rolling time (sec)	Exit thickness, (mm)		Rolling time, (sec)	
	h_0	48		h_0	48		
1	h_1	26	4.433	h_1	36.67	4.401	
2	h_2	14.3	2.494	h_2	22.52	2.498	
3	h_3	9.31	1.603	h ₃	13.57	1.610	
4	h_4	6.03	1.043	h_4	8.23	1.046	
5	h_5	4.55	0.769	h ₅	5.80	0.771	
6	6 $h_{\rm f}$ 3.8 0.0			h_{f}	3.8	0.0039	
	Total t	time :	10.3470	Total	Time:	10.3317	

Figure 4 shows the typical differences that were observed between the rolling schedules proposed by the manufacturer and the genetic rolling schedules generated for a given instance. In the graph, the rolling time and the thickness reductions for each one of the six stands are showed.

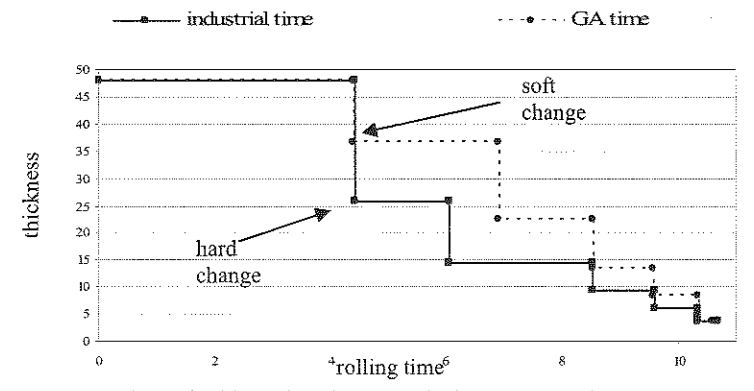


Fig. 4. Comparison of rolling schedule obtained with the GA vs the industrial schedule

As we can see the global rolling time obtained solving the modeled problem with a genetic algorithm is 0.051% better than the industrial time. Additionally the rolling schedule generated produces softer reductions than the rolling schedule proposed by the manufacturer. This characteristic of the solutions generated using the proposed model, diminishes the equipment damage risks.

8 Conclusions

In this work the problem of minimizing the hot rolling time was approached. Unlike the traditional approaches, the steel chemical composition is incorporated as a problem parameter allowing the automatically setup of the hot mill for different steels. To validate the approach a six-stand rolling mill is modeled as an optimization constrained problem. The mathematical model and the instances set were completely described. The used instances were built with realistic data of industrial schedules. The suboptimal industrial rolling time was used as the reference time to evaluate the solution methods performance. Also we present the results obtained using a solution method based on genetic algorithms. The global rolling time obtained solving the modeled problem with a genetic algorithm is 0.051% better than the global industrial time. Additionally the generated rolling schedule using the model diminishes the equipment damage risks because it produces softer reductions than the rolling schedule proposed by the manufacturer.

Currently we are developing new solution methods using different metaheuristics.

Acknowledgments. This work was economically supported by IPN, CONACYT and DGEST.

References

- G.E. Dieter et al. (2003) Chap 16-Rolling, Handbook of Workability and Process Design, ASM International, Materials Park, Ohio.
- L.Nolle, et al. (2002) Simulated Annealing and Genetic Algorithms Applied to finishing mill optimisation for hot rolling of wide steel strip International Journal of Knowledge-Based Intelligent Engineering Systems, 6 (2): 104-111,
- V.Oduguwa and A. Tiwari (2004). Sequential Process Optimisation Using Genetic Algorithms. Lecture Notes in Computer Science. Springer. Berlin, pp. 782-791,
- N. Chakraborti, and A. Kumar (2003) The Optimal Scheduling of a Reversing Strip mill: Studies using Multipopulation Genetic Algorithms and Differential evolution, Materials and Manufacturing processes, 18 (3): 433-445.
- N.Chakraborti et al. (2006). Optimizing Surface Profiles during Hot Rolling: A Genetic Algorithms Based Multi-objective Optimization, Practical Approaches to Multi-Objective Optimization, Comp. Mat. Sci., 37: 159-165,
- N.Chakraborti (2004). Genetic algorithms in materials design and processing, Int. Mat. Rev., 49 (3-4): 246-260,
- A. Gorni (1992). The Application of Neural Networks in the Modeling of Plate Rolling Process, JOM-e
- L. Nolle et al. (1999). Optimum Work Roll Profile Selection in the Hot Rolling of Wide Steel Strip using Computational Intelligence, Lect. Notes in Comp. Sci., 1625: 435.
- C. Pataro and H. Herman (1999). Direct determination of sequences of passes for the strip rolling by means of fuzzy logic rules. Proc. 2d. Conf. on Intell. Proc. and Manuf. of Mat., IPMM. pp. 549.

- 10 R. Shivpuri and S. Kini (1998). Application of Fuzzy Reasoning Techniques for Roll Pass Design Optimisation. Proc. 39th Mech. Work and Steel and Symp. on New Metal Form. Proc. pp. 755.
- 11 S. F. Medina and C. A. Hernández (1996). General Expression of the Zener-Hollomon Parameter as a Function of the Chemical Composition of Low Alloy and the Microalloyed Steels. Acta Metall. et Mater., 44 (1): 137-148.
- 12 S. F.Medina and C. A.Hernández (1996). The Influence of Chemical Composition on Peak Strain of Deformed Austenite in Low Alloy and Microalloyed Steels. Acta Metall. et Mater. 44(1): 149-154.
- 13 C. A. Hernández et al. (1996). Modelling Austenite Flow Curves in Low Alloy and Microalloyed Steels. Acta Metall. et Mater. 44 (1): 155-163.
- 14 S. F. Medina and C. A. Hernández (1996). Modelling of the Dynamic Recrystallization of Austenite in Low Alloy and Microalloyed Steels. Acta Metall. et Mater., 44(1): 165-171.
- 15 Z.Wusatowski (1969). Fundamentals of Rolling, Pergamon Press.
- 16 W.Roberts (1983). Hot Rolling of Steel, CRC.
- 17 C. A. Hernández and J. E. Mancilla (2003). Evolución de los precipitados en un acero microaleado al Nb fabricado por laminación directa. Informe técnico sobre estudios metalúrgicos y por MET en planchones de acero 7095. HYLSA Monterrey. Com. privada.
- 18 R. B. Sims (1954). The Calculation of Roll Forces and Torque in Hot Rolling Mill, Proc. AIME 168 (6): 191-200.
- 19 P. M.Cook and A. W.McCrum (1958). The Calculation of Load and Torque in Hot Flat Rolling, Reporte B.I.S.R.A., Londres.
- H. Ford and J. M. Alexander (1963). Simplified Hot-Rolling Calculations, J. Inst. Met. 92: 397-404.
- 21 HSMM Rel. 3.0. INTEG process group, inc., AISI/DOE Technology (2006).
- 22 F. K. Espriella (2008). Optimización mediante algoritmos genéticos: aplicación a la laminación en caliente. Master Thesis. Instituto Politécnico Nacional.

Biomedical Engineering

Analisys of 5 source separation algorithms on simulated EEG signals

Ricardo Salido-Ruiz², Rebeca Romo-Vázquez¹, Radu Ranta¹, Lorenzo Leija²

¹ Centre de Recherche en Automatique de Nancy (CRAN - UMR 7039), Nancy-University, CNRS ² CINVESTAV- IPN México D.F. radu.ranta@ensem.inpl-nancy.fr)

(Paper received on February 29, 2008, accepted on April 15, 2008)

Abstract. In this paper we evaluate the performance of 5 BSS algorithms (AMUSE, SOBI, SOBI-RO, SONS, JADE-TD) on simulated EEG signals. A first result evaluates the influence of the noise and signal characteristics (frequency, length, SNR) on the algorithms performance. A second objective is to introduce a new performance criterion, IEV which can be used to compare two matrices and is potentially useful on real signals. We validate this new index by comparing it with classic performance indices used in source separation.

1 Introduction

The electroencephalogram (EEG) is a medical examination based on brain's electric activity. The signal is recorded using electrodes placed on the scalp of the patient. One of the most common brain's diseases investigated through an EEG examination is the epilepsy. Epilepsy is a cerebral disease which is characterized by repeated crisis due to an excessive burst of synchronized neural activity. EEG signals are useful to detect this kind of anomalies as we mentioned before; however, these signals present several inconvenients:

- Recorded brain's signals are corrupted by artifacts (extra-cerebral signals) and noise, which are superimposed to the informative signals and make harder the interpretation for the physicians.
- Scalp EEG signals are by themselves a mixture between intra-cranial unknown sources and its mixing process is itself unknown.

A first step towards an easier interpretation for the physicians can be the development of a technique that allows the elimination of the artifacts and noise that the EEG signals present.

One current hypothesis is that these artifacts are independent from brain activity, either normal or pathologic. Under this hypothesis, a frequently used method is the blind source separation (BSS). The goal of BSS is to recover independent sources, given only sensor observations. This sensor observation is modeled as a linear mixture of independent source signals. The term blind indicates that both the source signals and the way the signals are mixed are unknown. Several algorithms for BSS were developed in the last 15 years [1, 2].

© E. V. Cuevas, M. A. Perez, D. Zaldivar, H. Sossa, R. Rojas (Eds.) Special Issue in Electronics and Biomedical Informatics, Computer Science and Informatics
Research in Computing Science 35, 2008, pp. 177-186



The main objective of this work is to test different source separation algorithms in order to examine their future use on real EEG signals. Besides classical performance criteria, in our opinion it is also necessary to asses the sensitivity of the algorithms to noise type and power, to the mixing model, as well as to the characteristics of the signal (frequency content, duration).

This communication is organized as follows. In the second section, we describe the source separation problem and its relation with EEG; in the third section we present the simulated EEG and noise test signals, and the evaluation criteria. The fourth section presents the obtained results and it is followed by a fifth section that concludes and presents the perspectives of this work.

2 Source Separation Problem

A method for solving the BSS problem it is to find a linear transformation of the measured sensor signals such that the resulting source signals are as statistically independent from each other as possible. The most widely used model considers N the number of unknown sources equal to the number of electrodes In this case the noisy mixture writes:

$$\mathbf{x}(k) = \mathbf{A}\mathbf{s}(k) + \mathbf{n}(k) \tag{1}$$

where \mathbf{x} is the vector of the mixed signals (sensors), $\mathbf{A} \in \mathbb{R}^{N \times N}$ is the unknown nonsingular mixing matrix, \mathbf{s} is the vector of independent source signals, \mathbf{n} is an additive vector noise, k being the time index after sampling.

The objective is to find a linear transformation ${\bf B}$ of the sensor signals ${\bf x}$ that makes the outputs as independent as possible:

$$y(k) = Bx(k) = BAs(k) + Bn(k)$$
(2)

where, y is the estimation of the sources and B is the separation matrix. The ideal separation is obtained when $\mathbf{B} = \mathbf{A}^{-1}$ and, consequently, y is a (noisy) estimate of s.

As it has been pointed out by different authors [1,2], obtaining the exact inverse of the **A** matrix is, in most of the cases, impossible. Therefore, source separation algorithms search a **B** matrix such as the product **BA** is a permuted diagonal and scaled matrix. Consequently, sources can be recovered up to their order (permutation) and their amplitude (scale).

Many different algorithms are available; these can be summarized by the following fundamental approaches, depending on the cost functions minimized to find the separation matrix **B**:

The most popular approach exploits as cost function some measure of signals statistical independence, non-gaussianity or sparseness. When original sources are assumed to be statistically independent (regardless of their temporal structure) the higher-order statistics (HOS) are essential (implicitly or explicitly) to solve the BSS problem. In such case, the method does not allow more than one Gaussian source [1–3].

- If sources have temporal structures, then each source has non-vanishing temporal correlation, and less restrictive conditions than statistical independence can be used, namely, second-order statistics (SOS) are often sufficient to estimate the mixing matrix and sources. As they exploit temporal correlations, SOS methods do not allow the separation of sources with identical power spectra shapes or i.i.d. (independent and identically distributed).

Most of BSS methods (HOS and SOS) include a SOS only pre-processing step: the spatial decorrelation or whitening. The conventional whitening exploits the equal-time correlation matrix of the data \mathbf{x} , which is often considered a necessary criterion, but not sufficient for the independence. The whitening of \mathbf{x} consists of the decorrelation and the normalization of its components. The idea is to find a matrix $\mathbf{W_b}$ known as whitening matrix, such as,

$$\bar{\mathbf{x}} = \mathbf{W_b} \mathbf{x} \tag{3}$$

with the covariance matrix of $\bar{\mathbf{x}}$ equal to the identity matrix: $\mathbf{R}_{\bar{\mathbf{x}}} = \mathbf{I}$. One can show that the whitening matrix \mathbf{W}_b can be written as:

$$\mathbf{W_b} = \Sigma \mathbf{V^T} \tag{4}$$

where Σ is a diagonal matrix and V an orthogonal matrix, obtained from the eigen decomposition of R_x , the covariance matrix of the data.

Independent estimates of the sources will be obtained from the whitening signals $\bar{\mathbf{x}}$ by a second transformation:

$$\mathbf{y} = \mathbf{J}\bar{\mathbf{x}} = \mathbf{J}\mathbf{W}_b\mathbf{x} \tag{5}$$

As the covariance matrix $\mathbf{R}_{\mathbf{y}}$ has to be also equal to the identity matrix (estimates are independents, so uncorelated), \mathbf{J} is necessarily an orthogonal matrix. The minimisation of the cost functions reminded earlier leads to this matrix.

Another whitening method is the robust whitening based on time-delayed correlation matrices. This method is used to minimize influence of the (white) noise in different algorithms (SOBI-RO, SONS, AMUSE).

Temporal, spatial and spatio-temporal decorrelations play important roles in EEG/MEG data analysis. Therefore, a lot of algorithms used in this domain are based only on second-order statistics (SOS) [5–8], although other authors prefer HOS algorithms [11–13].

The 5 algorithms compared in this work are:

- JADE-TD (HOS Joint Approximate Diagonalization of Eigen matrices with Time Delays), uses a combination of source separation algorithms of second order time structure (TDSEP) [14] and high order cumulant information (JADE) [15]. In principle, it is able to separate simultaneously timecorrelated and non-Gaussian signals [10].
- 2. SOBI (SOS Second Order Blind Identification), is an algorithm adapted for temporally correlated sources. It is based on the 'joint diagonalization' [5] of an arbitrary set of covariance matrices and relies only on second-order statistics of the received signals. It allows separation of Gaussian sources [9].

- 3. SOBI-RO (SOS Robust SOBI with Robust Orthogonalization), combines robust whitening (in the presence of temporally uncorrelated additive noise) and time-delayed decorrelation, as SOBI. It improves the classical SOBI method by integrating robust whitening instead of simple whitening [6].
- 4. AMUSE (SOS Algorithm for Multiple Unknown Source Extraction), is based on the EVD (eigenvalue decomposition) of a single time-delayed covariance matrix for prewhitened data. This algorithm also integrates a method for ordering automatically the estimated sources [7].
- 5. SONS (SOS Second Order Nonstationary Source Separation) algorithm exploits the nonstationarity and temporal structure of the sources. This method needs only multiple time-delayed correlation matrices of the observed data at several different time-windowed data frames to estimate the mixing matrix. This algorithm is not sensitive to additive white noise [8].

3 Method

The goal of our evaluation is to assess the performance for the 5 BSS algorithms described before. They were tested on different simulated signals, mixing matrices and noise vectors, also they were compared using several evaluation criteria.

3.1 Simulated Signals

In order to test the BSS algorithms it was necessary to create different signals that simulate the EEG's source signals. We propose four signals having different characteristics close to the real EEG and a fifth signal simulating the eye blinking artifact. Four test sets were created using these five signals:

- The first one figure 1(a), having 2048 samples/signal and frequencies ranging from 0.5 Hz to 26 Hz.
- A second set contained only the first half of the previous one (1024 samples), thus having lower frequencies (range 0.5 Hz - 10 Hz).
- A 3rd one contained the second half (1048 samples, mainly high frequencies).
- The last one was made duplicating the original set, having thus a 4096 samples signal and the same frequency range.

As we mentioned above the signals of each set were mixed using random mixing matrices (uniform distribution between -1 and 1). At the resulting mixture, two types of noises (Gaussian and Uniform) were added, with five different signals to noise ratios (0 dB, 5 dB, 10 dB, 15 dB and 20 dB).

Figure 1(b) presents an exemple of the simulated EEG (the noisy mixture of the 5 sources from figure 1(a)).

3.2 Evaluation Criteria

Index of Separability (IS) To validate the separation, the first criterion we have chosen is the index of separability IS [4]. The index is computed from the

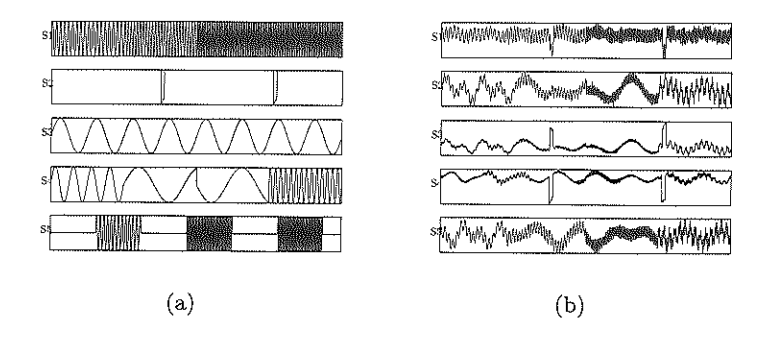


Fig. 1. Simulated EEG's: (a) original sources for a recording length of 8 seconds (sampling rate 256 Hz) resulting in signals of 2048 samples. Above (s1), a signal with 4 successive frequencies (9 Hz, 12 Hz, 14 Hz and 23 Hz), (s2) eyes artifact, (s3) a low frequency signal (1 Hz), (s4) a signal varying in frequency (2 Hz, 0.5 Hz, 7 Hz), (s5) three bursts of 10 Hz, 10 Hz and 26 Hz frequencies respectively; (b) noisy mixture.

 $N \times N$ transfer matrix **G=BA** between the original sources and the estimated ones. In order to obtain the IS it is necessary to take the absolute value of the elements of G and to normalize the rows g_i by dividing each element by the maximum absolute value of the row. The rows of the resulting matrix G' are:

$$\mathbf{g_i}' = \frac{|\mathbf{g_i}|}{\max|\mathbf{g_i}|} \tag{6}$$

The separability index is obtained from the new G' matrix:

$$IS = \frac{\sum_{j=1}^{N} \left(\sum_{j=1}^{N} \mathbf{G}'(i,j) - 1\right)}{N(N-1)}$$
 (7)

Correlation (CC) The second criterion is the correlation ρ between the simulated sources \mathbf{s}_i , i=1...N and the estimated independent components \mathbf{y}_i . To avoid taking into account small values of correlation and estimated sources correlated with more than one original source, correlation values smaller than 0.5 were discarded:

$$\rho_{ij} = \frac{\text{cov}(\mathbf{s}_i \mathbf{y}_j)}{\sigma_{\mathbf{s}_i} \sigma_{\mathbf{y}_j}} \qquad r_{ij} = \begin{cases} \rho_{ij} & \text{if } \rho_{ij} \ge 0.5\\ 0 & \text{if } \rho_{ij} < 0.5 \end{cases}$$
(8)

The retained estimated source \mathbf{y}_j for the source \mathbf{s}_i is the one for which the correlation is maximal $r_i = \max r_{ij}$. Finally, the CC criterion is defined as:

$$CC = \frac{1}{N} \sum_{i} r_i \tag{9}$$

Eigen Values Vector's Norm-1 Distance(IEV) Besides the previous evaluation criteria, we propose a new one base on the eigen values of the mixing and separation matrices. The basic idea is that, if the separation is successful, the mixing matrix and the inverse of the separation matrix must be similar (after reordering and normalization). The goal of the method is to evaluate this similarity. As seen previously (section 2), the BSS algorithms cannot find source estimates in the same order, with the same amplitudes and with the same signs as the original signals. Thus the inverse of the separation matrix, which is supposed to be equal to the mixing matrix has different values and the order of its rows may be changed. Therefore, before comparing two steps must be taken:

- 1. Normalization: first, the elements in ${\bf B}$ and in ${\bf A}^{-1}$ are taken in absolute values (to eliminate sign ambiguity). Next, each line is divided by his maximum value to normalize it to a maximum value of 1.
- 2. Permutation: the lines in matrix \mathbf{A}^{-1} are permuted, using the same method as for the correlation index.

In this way, we obtain $A_{\rm inp}$, the inverted, normalized and permuted version of A and B_n , the normalized version of B. To compare the previously obtained matrices, we chose to compute their eigen values. For each matrix, we construct a vector containing their eigen values and we compute the norm 1 distance between those two vectors:

$$IEV = \left| \sum_{i=1}^{N} \left(\lambda_{A_{inp}} - \lambda_{B_n} \right) \right| \tag{10}$$

where IEV is the newly obtained index, $\lambda_{A_{inp}}$ and λ_{B_n} are the eigen values of the described matrices.

So, if we have two equal matrices (mixing matrix = inverse of separation matrix) our index will be zero, indicating that the separation was performed at 100%. Generally speaking, a small value of IEV indicates good separation.

4 Results

The first aspect evaluated in this work is the behavior of the BSS algorithms using different noise vectors and mixing matrices. The second objective of our work is to analyse the tested algorithms according to their performances for all combination of signal and noise, as described previously. Finally, a third goal is to evaluate the accuracy of our new performance index IEV by comparing it with the two others.

In order to evaluate the influence of the random noise on the separation index, we created 10 simulated EEG (noisy mixtures of the original sources 8s) by using one mixing matrix and 10 noise vectors (Gaussian noise 15 dB). The results (mean value and standard deviation STD) are presented in figure 2(a).

As we can see in the figure 2(a), the standard deviation of the IS index is small and affects the methods almost in the same way. We conclude from this

simulation that the influence of the noise on the separation index is rather small (for a given SNR and probability law). Other simulations (not presented here), show that the IS values are much more influenced by the probability law of the noise and especially by the noise power (SNR).

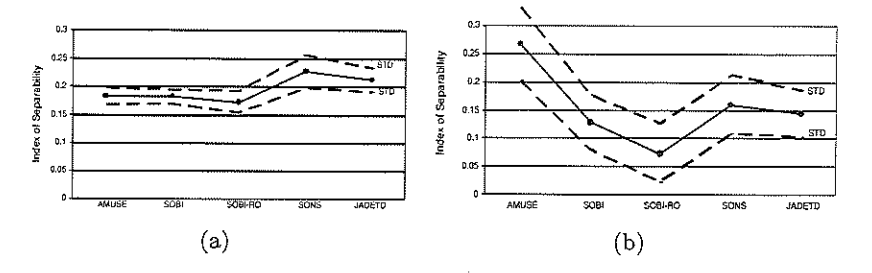


Fig. 2. Mean and STD for (a) one mixing matrix and 10 different noise vectors (b) 1000 different mixing matrices and noise vectors.

Concerning the influence of the mixing matrix on the index of separation (IS), we created 1000 simulated EEG (noisy mixtures of the original sources 8s) using the 1000 different mixing matrices and one noise vector for each one (Gaussian noise 15 dB). The results (mean value and standard deviation of the IS) are presented in figure 2(b). As we can see the relative standard deviation of the ISis larger than the one showed in figure 2(a). Our interpretation of this result is that, in order obtain a robust evaluation of the algorithms performances, it is necessary to test them by using an important number of mixing matrices, but it is not necessary to simulate an important number of noise vectors. A second conclusion is that SOBI-RO algorithm shows the best performances, at least for this signal and noise combination.

Therefore, for the following simulations, we only generated one noise vector for each particular situation (a given signal, a given mixing matrix, a given SNR and a given probability of the noise). We used the 4 signal sets previously presented, 1000 random mixing matrices, 5 signal to noise ratios (SNR = 0, 5, 10, 15, 20 dB) and 2 noise probability distributions, which leads us to 40000 simulations of noisy mixtures (10000 for each signal). We added also a no noise simulation, again using 1000 mixing matrices for each of the 4 signals (4000 simulations of no noise mixtures). The averaged results are presented in the next tables.

In table 1, we can see the behavior of the BSS algorithm, being evaluated for four evaluation criteria. The results obtained for each evaluation criterion are coherent with the Index of Separability (IS), and show that the best BSS algorithms are founded between SOBI and SOBI-RO.

Table 1. Results obtained for 4s-1 for the 5 algorithms.

1	AMUSE	SOBI	SOBIRC	SONS .	JADETD	AMUSE	SOBI S	SOBIRC	SONS .	JADETI
		W	ithout n	oise				with noi	se	
CC	0.97	0.99	0.99	0.88	0.95	0.56	0.68	0.65	0.57	0.64
IS	0.07	0.03	0.03	0.16	0.12	0.31	0.17	0.13	0.2	0.22
IEV	0.56	0.43	0.44	0.57	0.76	0.74	0.71	0.65	0.71	1.21

Table 2. Results obtained for 4s-2 for the 5 algorithms.

1	AMUSE	SOBL	SOBIRC	SONS.	JADETD	AMUSE		SOBIRC	SONS (JADET
		W	ithout n	oise	with noise					
CC	0.99	0.99	0.99	0.94	0.98	0.58	0.69	0.65	0.59	0.65
IS	0.04	0.02	0.03	0.12	0.05	0.3	0.16	0.11	0.19	0.2
IEV	0.63	0.4	0.41	0.49	0.71	0.74	0.67	0.61	0.66	1.16

In table 2, the results of the BSS algorithms seem to be improved. We can see it if we compare the values obtained in table 1 with the ones obtained in table 2. Both sets of signals have a 4s duration, but there is a big difference between their frequency content: 4s-1 has low frequency components, 4s-2 who presents mainly high frequencies.

Table 3. Results obtained for 8s for the 5 algorithms.

Î	AMUSE	SOBI	SOBIRC	SONS.	JADETD	AMUSE	SOBI	SOBIRC	SONS	JADET.		
	without noise						with noise					
CC	1	1	1	0.93	1	0.57	0.68	0.65	0.59	0.67		
IS	0.04	0.02	0.03	0.12	0.04	0.29	0.16	0.11	0.18	0.18		
ŒV	0.64	0.41	0.42	0.52	0.67	0.71	0.7	0.61	0.67	1.162		

In table 3 we can observe the results obtained for a larger length, and high and low frequency content signals. The results are even better than those presented for small length signals. We can see it by comparing the values obtained for the evaluation criteria. The hypothesis here is that a large amount of data (and also higher frequencies) facilitate the separation procedure for the BSS algorithms. Again we see that SOBI and SOBI-RO are the BSS algorithms with the best performance.

Another important observation (not shown in these tables which only present average values) is that between the behavior of these algorithms present small variations when the values are compared for uniform and Gaussian noises in each SNR level.

Table 4. Results obtained for 16s for the 5 algorithms.

-	AMUSE	SOBI S	SOBIRC	SONS .	JADETL	AMUSE	SOBI	SOBIRC	SONS	JADETD
		w	ithout n	oise				with noi	se	
CC	1.00	1.00	1.00	0.93	1.00	0.57	0.68	0.60	0.58	0.62
IS	0.04	0.02	0.03	0.12	0.04	0.29	0.16	0.10	0.18	0.17
IEV	0.64	0.40	0.41	0.54	0.70	0.72	0.68	0.57	0.69	1.16

The results shows different aspects of the behavior of the BSS algorithms. A first point is that for the sets of five simulated signals with short length (4 seconds) the evaluation criteria show worst performances for all the noise conditions and mixing matrices. The frequency content of the simulated signals played an important role in the performance of the BSS algorithms. Higher frequency signals are better separated. The set of simulated signals with the shortest duration and lower frequency content was the one with the worst performance for all performance criteria. The behavior of the BSS algorithms with respect to the type of the added noise was not so important. Very similar values were obtained for uniform and Gaussian noises. On the contrary, the noise level affected the separation performance for all signals. Almost all the algorithms struggle to obtain a good source separation when the signal to noise ratio is lower than 10 dB. Globally, all the results show that SOBI-RO and SOBI are the BSS algorithms which obtained the best scores in all the tested evaluation criteria the source separation performance. The IEV criterion indicate the same behaviour as the IS and CC indices.

5 Conclusion and Perspectives

As we mentioned above, the main objective of this work is to test different source separation algorithms in order to examine their future application on real EEG signals. Here we have presented a methodology that allows us to compare the BSS algorithms taking in account the nature of the EEG simulated signals. Namely, we simulated signals with different length, frequency, type and noise levels. Also, the important simulation number played an important role in our evaluation, because of the big and reliable data base which better support our conclusions.

Different interesting aspects of the behavior of the algorithms were presented here: the noise does not seem to play an important role in the performance of the separation except for its power. On the contrary the influence of the mixing matrix is much more important.

Some of the BSS algorithms presented considerable changes associated to the signal length, and to its frequency content. High frequency long signals are better separated than low frequency short ones. However, all the evaluation criteria show that SOBI-RO and SOBI algorithms are the best for the source separation on our simulated signals.

397

The new introduced criterion IEV allows us to compare directly two matrices and it aims to give a measure fo a kind of 'distance' between them: if its value es close to zero, the compared matrices are similar. Used on the (normalized) mixing marice and on the inverse of the normalized separation matrix, it gives similar indications as the other performance indices (IS and CC), which proves that IEV is a reliable performance criterion. Its main interest is its possible aplication on real signals.

References

- Te-Won Lee: 'Independent component Analysis Theory and Applications' Kluwer Academic Publisher. Boston, 1998.
- 2. A. Cichocki, Shun-ichi Amari 'Adaptative blind Signal and Image Processing Learning Algorithms and Applications' John Wiley and Sons, ltd, 2002.
- S. Choi, A. Cichocki, H. Park, S. Lee, 'Blind Source Separation and Independent Component Analysis: A Review' Neural Information Processing - Letters and Reviews, Vol. 6, no. 1, January 2005.
- 4. A. Cichocki, S. Amari, K. Siwek, T. Tanaka et al., ICALAB Toolboxes, http://www.bsp.brain.riken.jp/ICALAB.
- A. Belouchrani, K. Abed-Meraim, J.F. Cardoso, and E. Moulines, 'Second-order blind separation of temporally correlated source', Proc. Int. Conf. on Digital Sig. Proc., (Cyprus), pp. 346-351, 1993.
- A. Belouchrani, A. Cichocki, 'Robust whitening procedure in blind source separation contex' Electronics Letters, vol. 36, No. 24,pp. 2050-2053, 2000.
- L. Tong, V. Soon, Y. F. Huang, and R. Liu, 'Indeterminacy and identifiability of blind identification', IEEE Trans. CAS, vole. 38, pp. 499-509, March 1991.
- S. Choi and A. Cichocki, 'Blind separation of nonstationary sources in noisy mixtures', Electronics Letters, Vol. 36, pp. 848-849, April 2000.
- 9. A. Belouchrani, K. Abed-Meraim, J.F. Cardoso and E. Moulines, 'A blind source separation technique using second order statistics', IEEE Trans. on Signal Processing, vol. 45, No. 2, pp. 434-444, February 1997.
- K.-R. Mller, P. Philips, and A. Ziehe, 'JADEtd: Combining Higher-Order statistics and temporal information for blind source separation with noise', Proc. Int. Workshop on Independent Component Analysis and Blind Separation of Signals (ICA '99), Aussois, 1999.
- A. J. Bell and T. J. Sejnowski 'An information maximisation approach to blind separation and blind deconvolution', Neural Computation, 7, 6, 1129-1159, 1995.
- M. J. McKeown, S. Makeig, G. G. Brown, T. P. Jung, Kindermann, and T. J. Sejnowski, 'Analysis of fMRI by Blind Separation into Independent Spatial Components', Human Brain Mapping, 6(3):160-88 (1998).
- A. Hyvrinen and E. Oja, 'A Fast Fixed-Point Algorithm for Independent Component Analysis', Neural Computation, 9(7):1483-1492, 1997.
- A. Ziehe, K. R. Mller, ''TDSEP an efficient algorithm for blind separation using time structure', International Conference on Artificial Neural Networks, Sweden, 2 - 4 September 1998.
- 15. Jean-Franois Cardoso, Antoine Souloumiac, 'Jacobi Angles For Simultaneous Diagonalization', SIAM J. Matrix Anal. Appl. 17 (1), 161 164, 1996.

SISELS: a mediation system for giving access to Biology resources

Gabriela Montiel-Moreno^{1*}, José Luis Zechinelli-Martini¹, and Genoveva Vargas-Solar²

> Research Center of Information and Automation Technologies Universidad de las Américas, Puebla,
> Sta. Catarina Mártir s/n, 72820, San Andrés Cholula, México
> French National Council of Scientific Research Laboratory of Informatics of Grenoble
> 1081 rue de la Passerelle, BP 72, Saint Martin d'Hères, France

Contact: gabriela.montielmo, joseluis.zechinelli@udlap.mx, Genoveva.Vargas-Solar@imag.fr

(Paper received on February 29, 2008, accepted on April 15, 2008)

Abstract. This paper describes SISELS a mediation system that enables the configuration of virtual laboratories that support transparent access to biomedical data. The main objective of SISELS is to provide users with transparent access to distributed resources satisfying certain semantic requirements for contributing to the solution of a problem. Biomedical information is seen as distributed resources that can contribute to solve a biological problem. SISELS manages biological information using views that provide different perceptions of the same resources. A view represents the semantic requirements of a group of experts to study a specific problem. Given a problem expressed in terms of concepts, SISELS analyzes subscribed resources that provide related concepts and generates a view that represents an answer. Queries and their associated results are used to maintain a problem catalog. The problem catalog provides an easy access to frequent information and promotes information sharing and collaboration between researchers from different communities of the same knowledge domain. SISELS uses three ontologies defined in SHIQ(D) [4]. It implements them using OWL [11], and uses an inference service for mediating resources and managing generated knowledge.

1 Introduction

Medicine is a science that produces vast amounts of information, useful in the development of new treatments against diseases. This information is contained in different resources such as images, genome data, documents, and Web resources, which can be located in distributed geographic zones. This information can be manipulated in order to execute Bio-informatic processes. For this reason, medical area requires tools for integrating and manipulating existing biological information in order to generate new knowledge.

Nowadays, given a problem scientists have to manually analyze each resource with respect to the problem to verify its utility. This process is long and complex when the

© E. V. Cuevas, M. A. Perez, D. Zaldivar, H. Sossa, R. Rojas (Eds.) Special Issue in Electronics and Biomedical Informatics, Computer Science and Informatics
Research in Computing Science 35, 2008, pp. 187-198



number of resources increases. In some cases, scientists ignore resources useful to the problem because they are not defined explicitly in terms of the specified problem. In other cases, scientists from different communities explore the same problem from different perspectives and lack of a problem catalog to visualize different approaches.

A virtual laboratory provides transparent access to heterogeneous and distributed data providers and mechanisms to execute queries over resources according to concepts used in a specific knowledge domain. A virtual laboratory allows to share and manage great amounts of data in a coordinated and controlled way. Besides, it provides integrated views of resources (data, systems, documents) belonging to different organizations. These views are exploited by researchers in order to solve scientific problems.

In order to build a *virtual laboratory*, it is necessary to represent its knowledge that associates resources to concepts of a specific knowledge domain (e.g., Biology) [10]. From this knowledge, customized views of resources can be generated and adapted to the requirements of a group of experts. Retrieved information must be relevant and consistent with respect to a specific context of study.

This paper presents SISELS a knowledge based mediation system used to build virtual laboratories adapted to a knowledge domain (Biology). The rest of this article is organized as follows. Section 2 describes how to build a virtual laboratory. Section 3 describes metadata associated to a resource through the bio-resource ontology. Section 4 describes the mapping ontology that defines the semantic correspondence between concepts in Biology. Section 5 presents the view ontology used to store integrated views of information generated by SISELS. Section 6 describes our approach for generating views over resources based on semantics. Section 7 describes implementation issues concerning a prototype virtual laboratory. Section 8 describes related work and compares it with SISELS. Finally, Section 9 concludes the paper and discusses current results and future work.

2 Building a virtual laboratory

SISELS (Semantic Integration System for Explotation of biomedicaL resourceS) is a mediation system that enables the configuration of virtual laboratories to support transparent access to biomedical data (cf. Figure 1). In order to provide data according to given biological problems, SISELS uses the notion of view. A view expresses the relationship between a problem and resources that provide information about it. Both the problem and the resources are expressed under a normalized vocabulary shared by a set of experts (users). For example, a biologist studying cells from Basidiomycota fungi to determine a new treatment specifies his/her requirements with a set of concepts like: Cell, FungalCell, and Basidiocarp.

2.1 Resource

Resources are characterized in an structural and semantical way. In SISELS the semantical representation of a resource is defined by an ontology. An ontology is represented through concepts, attributes and properties within the biological area. Resources are represented in an homogeneous way through a single ontology that represents the knowledge domain of SISELS and classifies biological concepts.

2.2 Views

Information in SISELS is organized in views. A view represents the semantical requirements of a researcher and allows to have different perspectives from resources. A view is adapted according to a requirement expression. The requirement expression identifies those concepts used to access resources.

2.3 Problem

A problem is defined by concepts of the knowledge domain associated to resources that can be used for solving it. The problem catalog provides an easy access to frequent information and promotes information sharing and collaboration between researchers from different communities.

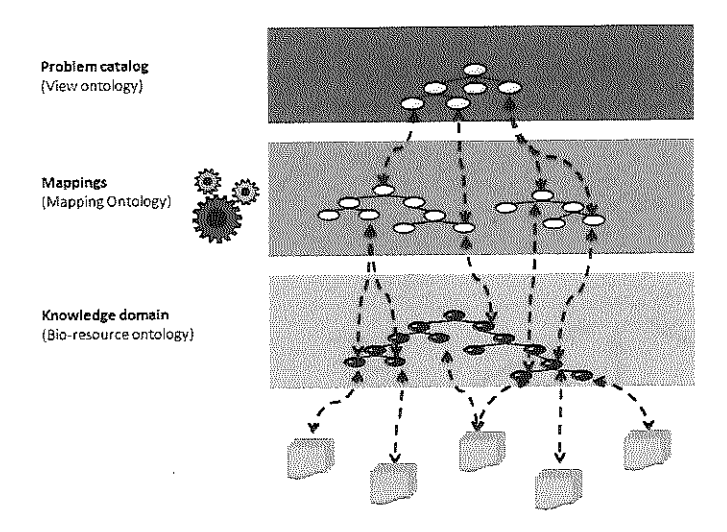


Fig. 1. SISELS general approach.

Integration approach in SISELS 2.2

The knowledge domain of SISELS is defined through the fusion of the ontologies describing the content of resources. The bio-resource ontology represents resources and associates them with biological concepts. The domain of SISELS is enriched when a new resource is subscribed to the system, when new knowledge is generated or when a biologist specifies his semantical requirements.

Researchers in the biological area specify their cases of study by using an ontology, composed by their own terms. When a biologist expresses a scientific problem in terms of biological concepts, she/he searches a set of resources that can contribute to solve a problem.

Given a problem expressed in terms of concepts of a knowledge domain, SISELS specifies the appropriate semantic mappings required to identify the resources satisfying the semantic defined by a researcher. We build the mapping ontology to represent the semantic correspondence between terms.

By using the defined mappings, SISELS analyzes subscribed resources that provide related concepts and generates a view that represents an answer.

SISELS uses knowledge representation models to achieve the semantic exploitation of biological resources. SISELS uses three ontologies based in the description logic $SHQ(\mathcal{D})$ [4] and implemented using OWL [11]: bio-resource, mapping and view. An ontology is composed by at least one class which represents a set of individuals sharing certain characteristics. A class is characterized by attributes that manage a data type (integer, string, and real) and has an extension defined by the concept of individual [2]. Normally, an ontology is composed also by one or more properties that define a binary relation between two concepts.

3 Bio-resources ontology

The bio-resources ontology models structural and semantic content of resources subscribed to SISELS (cf. Figure 2).

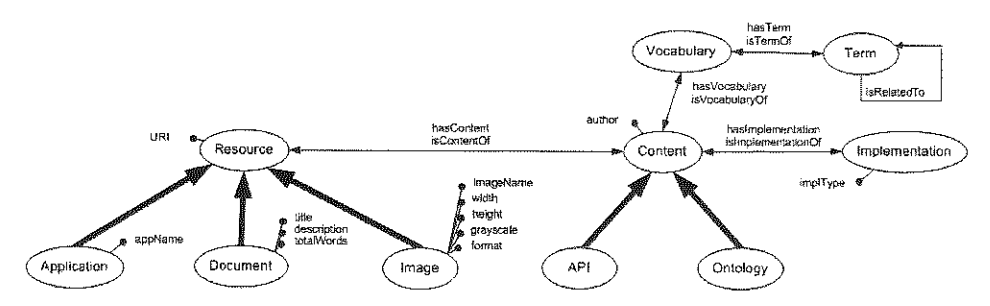


Fig. 2. Bio-resources ontology.

The main concept is Resource which is the general representation of a resource of the system. A resource is represented by an *URI* (*Universal Resource Identifier*) which is composed by a name and access protocol. In addition, a resource is characterized according to its type: Application, Document or Image. Associated to a resource, there is a Content that can be structured according to different models (e.g., an API or Ontology).

Formally, a resource is defined using SHIQ(D) in the following way:

Resource
$$\equiv \exists hasContent$$
.Content $\land = 1 URI(String)$

According to its format, a resource has associated metadata and characteristics describing its structure. For instance, the concept Document represents a specialization of a resource characterized by the attributes: title, description, totalWords. Once metadata

associated to a resource is defined, it is necessary to specify the nature of its content by the concept Content.

Information associated to a resource is managed as individuals under the ontology described. To illustrate, consider a resource denominated geneontology in PDF document format whose subject is genetics and that is related to a semantical content described in OWL format. This resource is represented as an individual geneontology of the concept PDF. The geneontology is related to contentgeneontology, which is an instance of Ontology, and with genetics which is an instance of Topic by using has-Content and has Topic properties.

4 Mapping ontology

The **mapping ontology** represents semantic correspondences, named mappings, between concepts of different sources and the bio-resources ontology (cf. Figure 3).

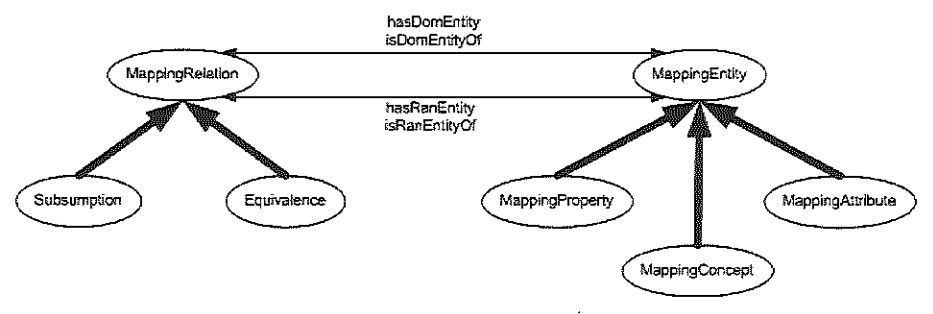


Fig. 3. Mapping ontology.

The main concept is MappingRelation which is classified in Equivalence and Subsumption. A MappingRelation is associated to the class MappingEntity by the properties hasDomEntity and hasRanEntity. A mapping is represented in $SHIQ(\mathcal{D})$ language as follows.

MappingRelation $\equiv \exists hasDomEntity.$ MappingEntity $\land hasRanEntity.$ MappingEntity

The mapping ontology is composed by instances of biological concepts, properties and attributes which own at least one semantic correspondence with another entity of a resource schema. SISELS allows to define three types of mappings as in [6]:

Equivalent mapping. Two concepts used by different resources are semantically equivalent i.e., ConceptA ≡ ConceptB, if an *equivalent mapping* is defined in the mapping ontology. For example, given the concept Cell, equivalent concepts in the bioresources are: Microorganism, Ectoplasm, Embryo, and Unit.

Sound mapping. A sound mapping establishes that individuals of a concept from the ontology A are a subset of individuals in a concept of the ontology B (ConceptA \subseteq

ConceptB). For example, given Fungi recovers all its existing specializations within the bio-resources ontology: Chytrids, Zygomycetes, Ascomycota, and Basidiomycota.

Complete mapping. A *complete mapping* states that a concept of resource A is a superset of a concept in resource B (ConceptA ⊇ ConceptB). For example, given the concept Arachnid, a supertype selection at second level, includes concepts which are its ancestors within the bio-resources ontology: Carnivorous, Arthropod, Chelicerata.

Queries are reformulated into subqueries for accessing information within different resources. In order to achieve this task, SISELS uses mappings between the bioresources ontology and concepts used by resources. Given a query defined as a domain ontology, SISELS proposes three types of selection of mappings: selection of equivalent concepts, selection of subtypes at n levels and selection of supertypes at n levels.

5 View ontology

The **view ontology** represents concepts related to a problem according to a knowledge domain. Each concept is associated to all resources which make reference to it (cf. Figure 5).



Fig. 4. View ontology.

A view is a set of concepts which define the semantics of a biological problem and is defined under SHIQ(D) language as follows.

```
Problem \equiv \exists isDefinedBy.Concept \land \exists isSolvedBy.Resource \land =1 title(String) \land =1 description(String)
```

The main concept in the view ontology is Problem which represents a biological problem. Each problem is associated with at least one Concept using the property isDefinedBy. A concept defines the semantics of the problem and must belong to the SISELS knowledge domain. Also, a Problem is associated to a set of instances of Resource for identifying those resources that provide content associated to the problem.

Generating views in SISELS 6

Given a query that defines the requirements of a biologist using a set of concepts, SISELS obtains an integrated view of resources. A view is specified as a query on the bio-resources ontology. Recall that the view represents the semantical requirements of a biologist.

Oueries are expressed in terms of SISELS domain. For example, consider a biologist who wants to study the behavior of the antimiotic agent Vinorelbine in the treatment of breast cancer. The biologist must specify to SISELS the semantic related to his problem through the definition of concepts like: Vinorelbine, Antimiotic_agent, Breast, and Cancer.

Views generation in SISELS is done in four phases: analysis, reformulation, assignment, and generation. The rest of this section focuses on the description of each phase.

6.1 Analysis

This task verifies if a query is well formed. A query is well formed if it is model of the ontology: its concepts are either a class, a property or an attribute; concepts belong to the SISELS domain, and if they verify the axioms and constraints associated to the bioresources ontology. This task executes a query by verifying whether each concept, representing the semantics of a problem, is defined as an instance by the bio-resources ontology.

6.2 Query rewriting

The objective of this phase is to prove whether a query can be rewritten with respect to the concepts representing resources content. Hence, a query is rewritten by expressing the concepts of the bio-resources ontology in terms of those used in the content of the resources. This is done by selecting equivalent concepts, supertypes or subtypes for each concept defined in the query over the mapping ontology using a reasoning service [21]. For example, consider the term: Cancer. In the rewriting phase, the biologist identifies that Cancer is a synonym of Malignant_tumor and a specialization of Tumor.

6.3 Resources filtering and assignment

From the lists of concepts retrieved by query rewriting, a biologist can filter the concepts that define his/her query domain so that SISELS looks for all resources that collaborate to the solution of a problem. Reselection allows users to access a larger amount of resources relevant to the solution of their problem.

Given a list of concepts defining the semantics of a query, a list of resources associated to these concepts must be generated (assignment process). The resource list is obtained by querying the bio-resources ontology. For example, suppose that we want to identify the resources described by the concept Vinorelbine. In first instance, it is necessary to recover the contents of type Ontology which are related to the concept through the property *isClassOf*. Then, it is necessary to find the resources related to each retrieved content by the property *isContentOf*. This way, we would recover a Breast Cancer web page and a Vinorelbine document.

Retrieved resources are described partially or totally by the concepts of the query. A biologist can filter the resources relevant to the solution of his/her problem.

6.4 Generation

After assignment, an integrated view with all the information required is generated. A view is defined as an instance of the view ontology and is described by the concepts of a query and their derivates (Section 5).

In our example, the system defines the problem over the breast cancer treatment breast_cancer_treatment as an instance of the concept Problem. The semantic of the problem is defined by expressing a relation between the problem and each query concept Vinorelbine, BreastCancer and MalignantTumor through the property *isDefined-By*. The solution of the problem is defined by expressing a relation between the problem and each relevant resource used by the biologist through the property *isSolvedBy*.

7 Implementation and experimental validation

In order to validate our approach we conducted an implementation of a Biology virtual laboratory oriented to biomedicine resources integration. Therefore we implemented mechanisms to characterize, manipulate, and enrich the knowledge located in heterogeneous resources. The objective was to help researchers in the detection of new knowledge and resources with content related to problems.

The prototype was implemented with the JAVA platform version 1.5.0, which offers libraries for implementation of graphical interfaces, generation of graphical trees and handling of data structures. Metadata ontologies were built using Protégé ontology editor that allows designing ontologies in OWL-DL language [11]. Query processing and knowledge inferences are achieved using a Racer inference engine which uses a set of mechanisms for querying, creating, and managing knowledge bases. Our ontologies are visualized using the JUNG framework.

7.1 Resource subscription

Our system allows to subscribe new resources into the system and to characterize them. By using a graphical interface, a user specifies the URI of the resource, information related to its format and the URL of the ontology representing its semantic. Given these data, the system creates a **bio-resource** as an instance of the class Resource in the bio-resources ontology and relates it to its semantical content. Content from a resource is represented through the extraction of concepts, properties and attributes defined in the ontology associated to a resource.

The prototype implements a set of schemas representing the content of different sources. The knowledge domain of the system is defined through existing bio-ontologies: Cell ontology, Amino-Acid ontology, Fungal anatomy ontology, and Clini-

cal ontology for breast cancer. The Cell ontology [13] is designed to identify an structured vocabulary to characterize different types of cells, and describe approximately 680 cell types related to Plantae, Fungi, Animal and Prokaryota. The Amino-acid ontology [12] represents the structure and properties of different types of amino-acids, around 50 concepts. The Fungal anatomy ontology [9] defines a controlled vocabulary to describe the anatomy of several fungi and other microorganisms and is composed by approximatively 100 concepts. Additionally, we built a Breast cancer ontology characterizing the existing types of cancer, their related symptoms, stages and their possible treatments.

7.2 **Explicit mapping constructor**

Our prototype provides a graphical interface to the users with two lists of concepts, attributes, and properties defined within the system. Based on these lists, a researcher can specify a set of semantic correspondences between two entities specifying their type (equivalence, subtype, supertype). The system generates each one of the specified mappings as instances of MappingRelation, whose domain and range are defined by the instances of the entities involved.

For example, a biologist can define the following mappings into the system: Vino $relbine@Source1 \equiv Navelbine@Source1, Cancers@Source1 \equiv MalignantTu$ mor@Source3, BreastCancer@Source3 \subseteq Cancers@Source1 and Cancers @Source1 ■ MalignantTumor@Source3.

7.3 Query processing

Our prototype provides the list of biological concepts stored in the laboratory as a hierarchical tree or a graph. From this list, the researcher selects the concepts representing the semantics of a biological problem and the type of search required (subclass, superclass, equivalence, predetermined). Consider a query Q defined by the concepts: Vinorelbine, Breast and Cancer and the presence of three resources defined by the following ontologies: Clinical ontology for breast cancer (Source1), Amino-Acid ontology (Source2) and Breast Cancer ontology (Source3).

The prototype uses SISELS to verify the consistency of the query and to recover the concepts related to the query based on existing mappings. By selecting or rejecting the retrieved concepts, the user can redefine his/her query. In our example, the query can be redefined by the concepts: Vinorelbine, Navelbine, BreastCancer and Malignant-Tumor. Then, the system generates a bidimensional list, where each element is composed by a biological concept and a set of resources. Our prototype counts with a virtual interface that allows biologists to filter the resources retrieved by the system and store his/her study case into the problem catalog. The problem catalog of our prototype is represented by an ontology implemented in the OWL language [11].

7.4 Experimental validation

We validate our virtual laboratory through the construction and evaluation of a set of queries composed by different number of concepts and requiring different kind of selection (equivalence and subtype). We analyze the efficiency of query processing in the prototype according to the execution time, the number of concepts retrieved after rewriting phase and the number of resources retrieved.

It is important to consider that the number of retrieved concepts after assignment phase depends strictly on the number of mappings defined in the system. For this reason, the queries used to evaluate the systems consider biological concepts defined as a generalization of one to twenty concepts. Our knowledge base was composed by 750 biological terms.

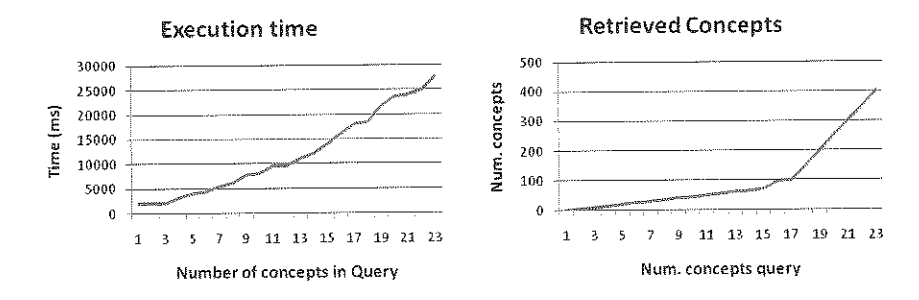


Fig. 5. Experimental results.

Figure 5a presents the execution time of query processing with respect to the analysis and rewriting phases for a set of queries defined by a set of one to twenty concepts. Figure 5b presents the number of retrieved concepts for the defined queries. The query processing execution time of in our system is reasonable when the system retrieves around 400 biological concepts. We use this result for estimating the execution time of queries over a bigger knowledge. It is of course influenced by the number of concepts in the query and the defined mappings among ontologies and it is polynomial. Finally, we consider that biologists must conduct a quantitative evaluation. We are currently working with Biology communities for validating SISELS.

8 Related Works

Centralized mediation systems like Carnot [8], SIMS [3], and TAMBIS [20] use a single ontology to model real world entities and properties. Other centralized systems like DWQ [7] and Picsel [16] use the hybrid ontology approach in order to achieve the resources integration and a conjunctive query model.

Mediation distributed systems like Observer [18] and Somewhere [1] manage multiple ontologies to integrate distributed resources. Peers are represented through an ontology which describes the content of a set of resources. Queries are expressed in terms of the ontology describing the node where it belongs and are executed locally in the

peer to retrieve data from its underlying resources. It is necessary to define the semantic correspondences between nodes for retrieving data and information stored in other nodes.

SISELS incorporates the exploitation and structural and semantical integration of resources through the use of a global schema. Inspired on description logics based knowledge representation, we express information associated to resources and queries using description logics.

9 Conclusions

SISELS is a mediation system that integrates resources (documents, applications and data bases). This system provides scientists transparent access to distributed information satisfying their requirements to study specific problems. As a result of structural and semantical characterization of resources, SISELS offers tools for classifying and semantically integrating resources to exploit biological information. SISELS maintains a knowledge representation of resources that describes their content structurally and semantically.

The knowledge domain in SISELS is defined by a set of biological concepts defined by experts and is enriched when a new resource is added, new knowledge is generated or a new problem is defined. Once the knowledge domain is defined, it is necessary to establish a relation between concepts through mappings. SISELS proposes techniques for query processing techniques bases on views. These views adapt to the requirements of a group of experts in order to study a Biology problem. Based on views, SISELS provides transparent access to biological resources and promotes information sharing between communities.

Future work relays on the definition of strategies and knowledge rules for view management and query processing by using inference mechanisms. This would reduce the computational cost related to the management of large amounts of data. We are currently defining techniques to prove the consistency of biological terms. This can be achieved through the construction of a knowledge base that contains a set of rules describing the principles of Biology. Finally, it is important to consider that reasoning is computational expensive especially when we deal with vast amounts of information. For this reason, it would be interesting to explore possible optimization strategies to reduce these computational costs.

Perspectives related to the implementation of our prototype include to stabilize and to validate the virtual laboratory with research groups in the biological area. It is necessary to formalize strategies for view management in order to satisfy in an optimal way the requirements of a group of experts and to define existing relations between different views. Consequently, we could use SISELS to define applications in other scientific areas like astronomy. We are currently collaborating in e-Grov project to give access to astronomical resources.

References

1. P. Adjiman, P. Chatalic, F. Goasdoué, M.C. Rousset and L.Simon (2004). Distributed reasoning in a peer-to-peer setting European Conference on Artifical Intelligence.

 Y. Arens, C.N. Hsu, C.A. Knoblock (1997). Query processing in the SIMS information mediator. Readings in Agents.

 F. Baader, D. McGuinness, D. Nardi, and P. Patel-Schneider (2003). The description logics handbook: Theory, implementation and applications, chapter An introduction to Description Logics. Cambridge University Press.

5. G. Bruno (2006). "ADEMS" a knowledge-based service for intelligent mediator configuration. PhD thesis, Institut National Polytechnique de Grenoble.

 D. Calvanese, G. De Giacomo, M. Lenzerini, D. Nardi and R. Rosati (1998). Information integration: Conceptual modeling and reasoning support Conference on Cooperative Information Systems.

 C. Collet, M.N. Huhns and W.M. Shen (1991). Resource integration using a large knowledge based in carnot, Building large knowledge based Computer IEEE, 24-12. Chs91

8. M. Constanzo (2005). Fungal anatomy ontology. Available at: http://www.yeastgenome.org/fungi/fungalanatomyontology/.

R. Davis, H. Shrobe, and P.Szolovits (1993). What is knowledge representation? AI Magazine, 14(1):17–33.

 L. Deborah and H.Frank (2004). OWL web ontology language overview. Available at: http://www.w3.org/TR/owl-features/.

 N. Drummond, G. Moulton, R. Stevens, and P. Lord (2005). Amino-acid ontology. http://www.co-ode.org/ontologies/amino-acid/2005/10/11/.

12. O. Hoffman. Cell ontology (2007). http://www.berkeleybop.org/ontologies/.

 T. Kirk, A.Y. Levy, Y. Sagiv, D. Srivastava (1995). The Information Manifold Information Gathering from Heterogeneous, Distributed Environments.

 D.B. Lenat and R.V. Guna (1990). Building large knowledge based systems Representation and Reasoning in the Cyc Project, Addison-Wesley, Reading, Massachusetts, United States.

 A.Y. Levy (2000). Queries using views: A Survey Technical Report: Computer Science Dept., Washington, Univ.

16. A.Y. Levy and M.C. Rousset (1998). Combining horn rules and description logics in carin, Artificial Intelligence 104-12.

 E. Mena, V. Kashyap, A.P. Sheth, A. Illarramendi (1996). OBSERVER: An approach for query processing in global information systems based on interoperation across pre-existing ontologies Conference on Cooperative Information Systems.mksi96

18. M.T. Ozsu and P. Valduriez (1999). Principles of distributed database systems. Prentice Hall, second edition.

 N. Paton, R. Stevens; P. Baker, C. Goble, S. Bechoofer, A. Brass (1999). Query processing in the Tambis bioinformatics source integration system SSDBM '99: Proceedings of the 11th International Conference on Scientific and Statistical Database Managment, IEEE Computer Society.

20. Racer Systems (2004). Racer reference manual version 1.7.19.

Fuzzy Gain Scheduling of PI Controller for an Anaerobic Digester

Albino Martínez-Sibaja¹, Rubén Posada-Goméz¹, Alejandro Alvarado-Lassman¹, Manuel Adam-Medina², Carlos M. Astorga-Zaragoza²

 Instituto Tecnológico de Orizaba, División de Estudios de Posgrado e Investigación, Av. Oriente 9 No. 852, Col. Emiliano Zapata, 94320 Orizaba, Veracruz, México.
 Centro Nacional de Investigación y Desarrollo Tecnológico, Depto de Ing. Electrónica, Interior Internado de Palmira s/n, 69490 Cuernavaca, Morelos, México Contact: albino@cenidet.edu.mx, astorga@cenidet.edu.mx

(Paper received on February 29, 2008, accepted on April 15, 2008)

Abstract. A cascaded controller for an anaerobic digester is presented. The upper-level controller is a Fuzzy Gain Scheduling of PI controller (FGS-PI) and the lower-level controller is a PI controller. The inner loop controller feeds the reactor pH back to the influent flow rate, and the outer loop controller measures the biogas flow rate and adjusts the pH set point. Simulation results of the proposed scheme show good performance during start-up operation of an anaerobic digester and also during rejection of disturbances. A comparison between FGS-PI controller and a Fuzzy Logic PI type controller is presented.

1 Introduction

The Anaerobic digestion processes are gaining an increasing interest in industrial waste treatments because of several advantages over other processes. The anaerobic digestion can reduce the influent Chemical Oxygen Demand (COD) producing valuable energy (a mixture of methane and carbon dioxide) and low sludge yield [1,4,9]. However, the interdependence of the different microbial groups involved in the degradation of organic matter may easily unstabilize the process and difficult the mathematical modeling of the anaerobic digestion [2,3,6,7].

In order to avoid the instability of anaerobic digestion processes, several techniques using monitoring and control has been used. The most widely used controller in industrial applications are PID-type controllers because of their simple structure and good performances in a wide range of operating conditions. But, these PID controllers can not always effectively control systems with strong nonlinearities. In recent years, fuzzy logic control (FLC) techniques have been applied to the control of anaerobic digesters [3,4,8,10]. However, the application of FLC has faced some disadvantages during hardware and software implementation due to its high computational burden. In order to overcome the disadvantages of PID controllers and FLC, a Fuzzy Gain Scheduling of PID controllers has been developed [13].

© E. V. Cuevas, M. A. Perez, D. Zaldivar, H. Sossa, R. Rojas (Eds.) Special Issue in Electronics and Biomedical Informatics, Computer Science and Informatics
Research in Computing Science 35, 2008, pp. 199-208



In this paper a cascaded control estrategy for an Upflow Anaerobic Sludge Blanket (UASB) digester is presented. The upper-level controller is a Fuzzy Gain Scheduling of PI controller (FGS-PI), and the lower-level controller is a PI controller. The goal is to achieve a good biogas production maintaining a stable process operation despite significant variations in the influent characteristics. The process and the control strategy has been simulated and tested in SIMULINK of MATLAB™.

2 Description of the process

Anaerobic digestion comprises basically two steps. In the first step, organic compounds are fermented into volatile fatty acids (VFA) and CO₂ by a group of acidogenic bacteria. In a second step, VFA are converted into CH₄ and CO₂ by a group of methanogenic bacteria. In order to design a cascaded controller for an UASB digester, a mathematical modeling of the process is necessary. The objective of the model is to simulate the process evolution and control the biogas production and pH.

In this paper, the control system was evaluated on a model of anaerobic digestion. Implementation depends on whether the liquid phase physico-chemical processes are implemented as kinetic rate equations. The mass balance for each state component in the liquid phase is as shown in Equation 1:

$$\frac{dS_{liq,i}}{dt} = \frac{q_{in}S_{in,i}}{V_{liq}} - \frac{S_{in,j}q_{out}}{V_{liq}} + \sum_{j=1-19} \rho_j V_{i,j}$$
 (1)

where the term $\sum_{j=i-19} \rho_j v_{i,j}$ is the sum of the kinetic rates for process j multiplied by $v_{i,j}$

[2]. The model was developed using SIMULINK of MATLABTM. The simulated equipment was a 1.4 liters UASB digester with regulated temperature at 35°C. Synthetic wastewater with variable substrate concentration from 10 to 20 gCOD/L, was assumed.

3 Control structure

The control system depicted in Fig. 1 is a cascaded control. The Upper-level controller is a Fuzzy Gain Scheduling of PI Controller (FGS-PI) and the Lower-level controller is a PI controller. The inner loop controller feeds the reactor pH back to the influent flow rate Qin. The outer loop controller measures the biogas flow rate Qgas and adjusts the pH setpoint.

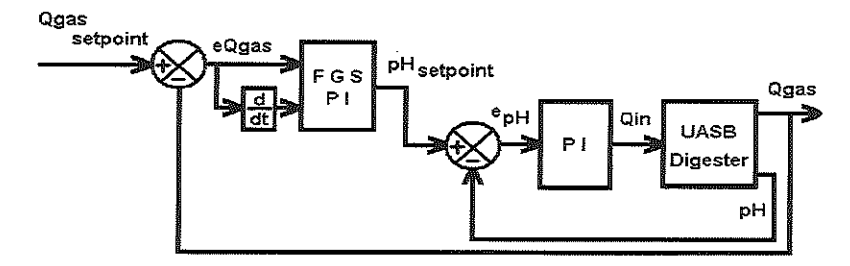


Fig. 1. Cascaded controller for an UASB digester. The upper level controller is a Fuzzy Gain Scheduling of PI contriler (FGS-PI), and the lower level controller is a PI controller.

3.1 Fuzzy Gain Scheduling of PI Controller (FGS-PI)

Fuzzy Gain Scheduling of PI Controller (FGS-PI) is a technique where PI controller parameters (kp and ki gains) are tuned during control of the system in a predefined way [13,14]. The structure of the control system is illustrated in Fig. 2. The fuzzy adapter adjusts the PI parameters to operating conditions, in this case based on the error and its first time derivative, during process control.

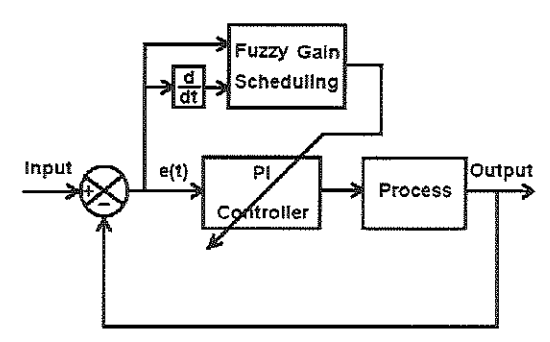


Fig. 2. Fuzzy Gain Scheduling of PI Controller.

3.2 Description of the Fuzzy Gain Scheduling of PI Controller

The parameters of the PI controller used in the direct chain, kp and ki, are normalized into the range between zero and one by using the following linear transformations [14]:

$$K'_{p} = (k_{p} - k_{p \, min}) / (k_{p \, max} - k_{p \, min})$$
 (2)

$$K'_{i} = (k_{i} - k_{i \min}) / (k_{i \max} - k_{i \min})$$
 (3)

The inputs of the fuzzy adapter are the error (e) and the first time derivative of the error (Δe), normalized using a predefined maximum error and a maximum first time derivative. The outputs are the normalized value of the proportional action (k'_p) and of the integral action (k'_i) . The parameters k'_p and k'_i are determined by a set of fuzzy rules of the form:

If
$$e$$
 is A_i and Δe is B_i then k'_p is C_i and k'_i is D_i (4)

where A_i , B_i , C_i and D_i are fuzzy sets on corresponding supporting sets. The membership functions for the inputs e and Δe are defined in the range [-1, 1], see figure 3(a), and for the outputs are defined in the range [0, 1], see figure 3(b). The fuzzy subsets of the input variables are defined as follows: NL: Negative Large, NM: Negative Medium, NS: Negative Small, Z: Zero, PS: Positive Small, PM: Positive Medium, PL: Positive Large. The fuzzy subsets of the output variables are defined as: L: Large, S: Small.

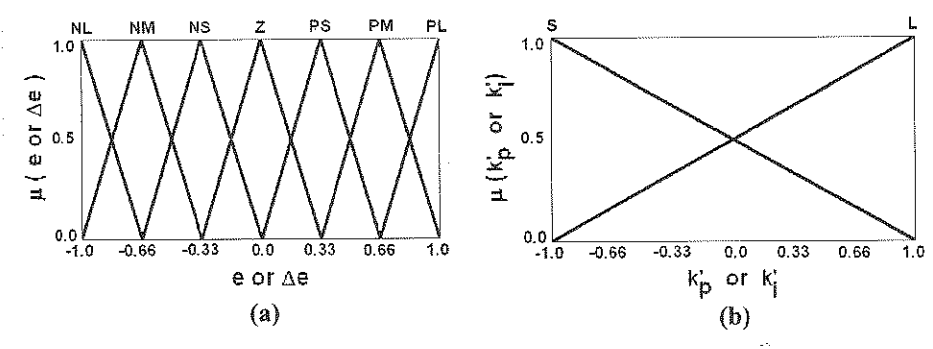


Fig. 3. (a) Membership functions for the inputs (e) and (Δe) . (b) Membership functions for the outputs k'_p and k'_i .

The fuzzy rules in (4) are extracted from operator's expertise. The tuning rules for k'_p and k'_1 are given in Tables 1 and 2 respectively.

							•	,
	e	NL	NM	NS	Z	PS	PM	PL
	Δe							
	NL	L	L	L	L	L	L	L
-	NM	S	L	L	L	L	L	S
	NS	S	S	L	L	L	S	S
	Z	S	S	S	L	S	S	S
	PS	S	S	L	L	L	S	S
	PM	S	L	L	L	L	L	S
	PL	I	L	L	L	L	L	L

Table 1. Fuzzy rules base for computing k_p .

By using the membership functions shown in Fig. 3, we satisfy the following condition:

$$\sum_{i=1}^{m} \mu_i = 1 \tag{5}$$

Table 2. Fuzzy rules base for computing k'_p .

$\setminus E$	NL	NM	NS	Z	PS	PM	PL
Δe							
NL	L	L	L	L	L	L	L
NM	L	S	S	S	S	S	L
NS	L	L	S	S	S	L	L
Z	L	L	L	S	L	L	L
PS	L	L	S	S	S	L	L
PM	L	S	S	S	S	S	L
PL	L	L	L	L	L	L	L

The defuzzification rule is chosen as:

$$k'_{p} = \sum_{i=1}^{m} \mu_{i} k'_{p,i} \tag{6}$$

$$k'_{i} = \sum_{i=1}^{m} \mu_{i} k'_{i,i} \tag{7}$$

where $k'_{p,i}$ is the value of k'_p corresponding to the grade μ_i for the i_{th} rule. $K'_{i,i}$ is similarly defined. Once the values of k'_p and k'_i are obtained, the new parameters of the PI controller are calculated by the following equations:

$$k_p = (k_{p \, max} - k_{p \, min}) k'_p + k_{p \, min}$$
 (8)

$$k_i = (k_{i max} - k_{i min})k'_i + k_{i min}$$
(9)

3.2 Description of the Fuzzy Logic PI type controller

The Fuzzy Logic PI type controller is essentially a low pass filter which attenuates high frequency signals, it is commonly used to design a robust controller for ensuring suppression of disturbances. In Fuzzy PI type controller (Fig. 4), which is the fuzzy equivalent of the conventional PI controller, its nonlinear mapping between the control rules and the fuzzy reasoning can be represented as a funcion of the error e and the first time derivative of the error Δe as follows:

$$\Delta u = FLC(e, \Delta e) \tag{10}$$

where Δu is the first time derivative of the output control action. Δu can be expressed approximately as follows:

$$\frac{\Delta u(t)}{S\Delta u} = \frac{\Delta e(t)}{S\Delta e} + \frac{e(t)}{Se} \tag{11}$$

where -Se<e(t)<Se, -S Δ e< Δ e(t)<S Δ e, -S Δ u< Δ u(t)<S Δ u or

$$u(t) = k_p e(t) + K_i [e(t)dt$$
 (12)

tegral action (k'_i) . The parameters k'_p and k'_i are determined by a set of fuzzy rules of the form:

If
$$e$$
 is A_i and Δe is B_i then k'_p is C_i and k'_i is D_i (4)

where A_i , B_i , C_i and D_i are fuzzy sets on corresponding supporting sets. The membership functions for the inputs e and Δe are defined in the range [-1, 1], see figure 3(a), and for the outputs are defined in the range [0, 1], see figure 3(b). The fuzzy subsets of the input variables are defined as follows: NL: Negative Large, NM: Negative Medium, NS: Negative Small, Z: Zero, PS: Positive Small, PM: Positive Medium, PL: Positive Large. The fuzzy subsets of the output variables are defined as: L: Large, S: Small.

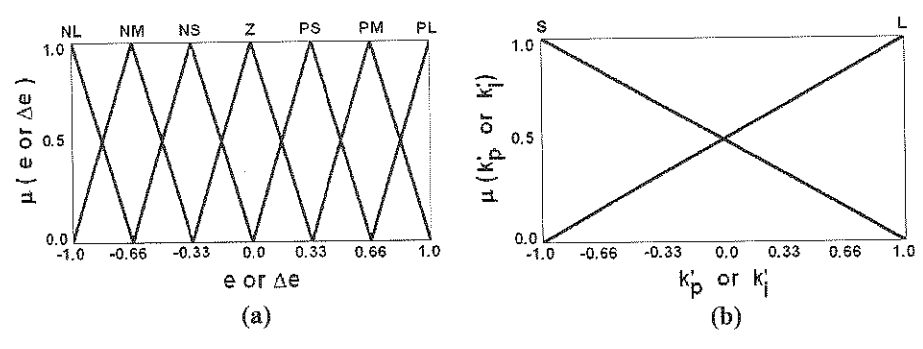


Fig. 3. (a) Membership functions for the inputs (e) and (Δe) . (b) Membership functions for the outputs k'_p and k'_i .

The fuzzy rules in (4) are extracted from operator's expertise. The tuning rules for k'_p and k'_i are given in Tables 1 and 2 respectively.

		•					
e	NL	NM	NS	Z	PS	PM	PL
Δe							
NL	L	L	L	L	L	L	L
NM	S	L	L	L	L	L	S
NS	S	S	L	L	L	S	S
Z	S	S	S	L	S	S	S
PS	S	S	L	L	L	S	S
PM	S	L	L	L	L	L	S
PL	L	L	L	L	L	L	L

Table 1. Fuzzy rules base for computing k'_{p} .

By using the membership functions shown in Fig. 3, we satisfy the following condition:

$$\sum_{i=1}^{m} \mu_i = 1 \tag{5}$$

The model and the experimentation allowed the rule table to be built up (Mamdani, 1975) [11]. The fuzzy rules are given in Table 3. In order to convert the fuzzy information into a numerical value to be applied to the process, the center of gravity method was used.

Table 3. Fuzzy rules base for computing Δu .

e Ae	NL	N	Z	P	PL
NL	NL	NM	NS	Z	PS
NM	NM	NS	Z	PS	PM
NS	NS	Z	PS	PM	PL

3.3 Description of the PI controller

The conventional PI controller for the proposed lower-level controller was designed with Ziegler-Nichols tuning formulas. In order to apply the Ziegler-Nichols tuning formulas based on frequency response [12], there are only two parameters which are necessary: the critical gain Kc, and the critical period Tc. To determine them, a delay is introduced in the control closed-loop, to force the system oscillates in a controlled limit cycle [5]. The tool box SIMULINK of MATLAB™ was used to obtain Kc and Tc. With those values, the proportional gain Kp and integral gain K_i were calculated.

4 Results

In order to test the ability of the developed control scheme to handle start-up condition, we apply the proposed scheme to the control of start-up operation of UASB digester. Fig. 7 shows a biogas flow rate comparison between the start-up period of the FGS-PI controller and FLC-PI controller, each one operating in the proposed cascaded controller of an UASB digester at constant influent substrate equal to 3 gCOD/L and Ogas setpoint = 1 Lgas/d. The settling time is 17 hours with the FGS-PI controller and 25 hours for the FLC-PI. For the same conditions, a comparison of the influent flow rate (i.e. the control action) between FGS-PI controller and FLC controller is presented in Fig. 8. When the influent flow rate (Qin) is increased at time=10.5h, for the control action of the FGS-PI controller, the pH decreases from 7 to 6.9 (Fig. 9), due to the increased Organic Load Rate (OLR) but, at time=15h, the pH increases up to 6.92 for the control action of the lower level controller. On the other hand, when the influent flow rate (Qin) is increased at time=13h (Fig. 8), for the control action of the FLC-PI controller, the pH decreases from 7 to 6.9, following the pH setpoint.

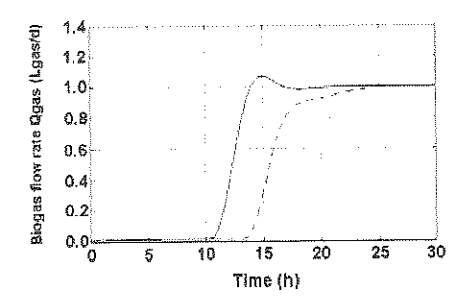


Fig. 7. Simulation of the biogas flow rate (Qgas) during a start-up procedure at constant influent substrate at 3 gCOD/L and Qgas_setpoint=1Lgas/d, with FGS-PI controller (solid line) or FLC-PI controller (dotted line), each one operating in the developed cascaded controller.

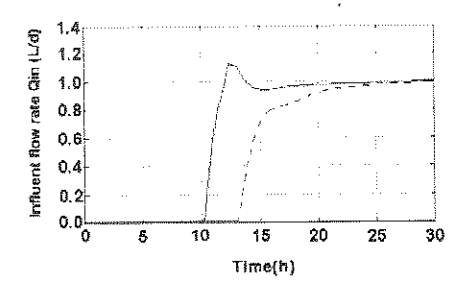


Fig. 8. Simulation of the influent flow rate (Qin) during a start-up procedure at constant influent substrate at 3 gCOD/L and Qgas_setpoint=1Lgas/d, with FGS-PI controller (solid line) or FLC-PI controller (dotted line), each one operating in the developed cascaded controller.

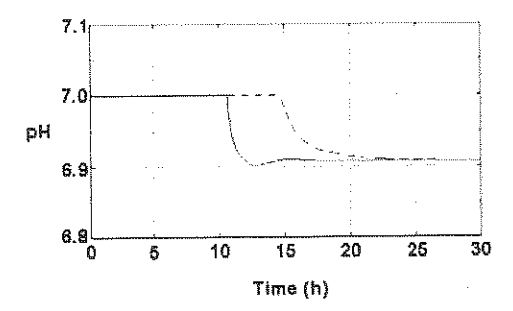


Fig. 9. Simulation of the behavior of pH during a start-up procedure at constant influent substrate at 3 gCOD/L and Qgas_setpoint=1Lgas/d, with FGS-PI controller (solid line) or FLC-PI controller (dotted line), each one operating in the developed cascaded controller.

In order to test the characteristics of the developed cascade controller, different disturbances are applied to the influent COD substrate concentration. The influent COD was increased by 33%, from 3 to 4 gCOD/L, at time=40h, with Qgas_setpoint = 1

Lgas/d. Fig. 10 shows a comparison of biogas flow rate between the FGS-PI controller and FLC-PI controller, at the same conditions. The FGS-PI controller rejects the disturbance more rapidly than the FLC-PI controller. To compare the performance of both controllers, the criterion of Integral Square Error (IAE), from 35 to 60 hours, was used. The obtained value when using the FGS-PI controller is IAE = 58950 versus 62280 when using the FLC-PI controller.

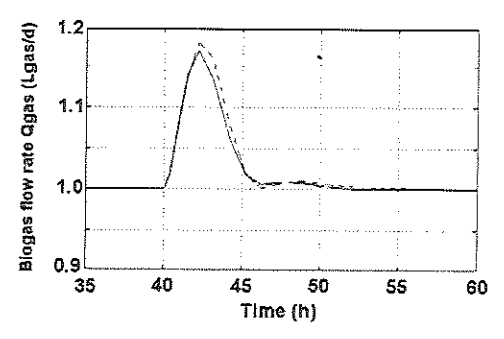


Fig. 10. Simulation of the biogas flow rate (Qgas) under influent COD variation from 3 gCOD/L to 4gCOD/L, at Qgas_setpoint=1Lgas/d, with FGS-PI controller (solid line) or FLC-PI controller (dotted line), each one operating in the developed cascaded controller.

4 Conclusion and directions for further research

A Fuzzy Gain Scheduling of PI (FGS-PI) controller operating in a cascaded controller was designed and simulated to operate an UASB digester. Good control performances were achieved during the start-up operations and during rejection of disturbances. The FGS-PI controller starts-up the process and rejects disturabances more rapidly than FLC-PI controller. A comparison between the developed FGS-PI controller and a Fuzzy Logic PI type (FLC-PI) controller was presented.

Through simulation we have shown the ability of the developed control scheme to handle start-up condition of an UASB digester at constant influent substrate equal to 3 gCOD/L and Qgas_setpoint = 1 Lgas/d (Fig. 7). The FGS-PI controller had a better performance than the FLC-PI controller, because the settling time using the FGS-PI controller was 17 hours against 25 hours using the FLC-PI controller. However, the fact that the influent flow rate (Qin) grow faster when using the FGS-PI controller (Fig. 8), at time 10 hours, causes the pH reaches a lower value compared with the FLC-PI controller (Fig. 9), at time 12.5 hours, due to increased of the organic load rate.

Moreover, we have shown the performance of FGS-PI controller versus FLC-PI controller (Fig. 10), under influent COD variation from 3 gCOD/L to 4gCOD/L, at Qgas_setpoint=1Lgas/d. We have compared the performance of both controllers using the criterion of integral absolute error (IAE), from 35 to 60 hours. The FGS-PI controller had a better performance than the FLC-PI controller, because its IAE=58950 was lower than the IAE=62280 for the other controller.

Nowadays, we are working on the physical verification of the simulations presented in this paper.

- J. Liu, G. Olsson, B. Mattiasson (2004). Control of an anaerobic reactor towards maximum biogas production, Water Science Technology, 50:189-198.
- D.J. Batstone, J. Keller, I. Angelidaki, S.V. Kalyuzhnyi, S.G. Pavlostathis, A. Rozzi, W.T.M. Sanders, H. Siegrist, V.A. Vavilin (2002). Anaerobic Digestion Model No. 1 (ADM1), IWA Task Group for Mathematical Modelling of Anaerobic Digestion Processes, IWA Publishing, London, UK.
- O. Bernard, M. Polit, Z. Hadj-Sadok, M. Pengov, D. Dochain, M. Estaben, P. Labat (2001). Advanced monitoring and control of anaerobic wastewater treatment plants: software sensors and controllers for an anaerobic digester, Water Science Technology, 30:21-29.
- 4. M. Estaben, J.P. Polit, J.P. Steyer (1997). Fuzzy control for an anaerobic digester, Control Engineering Practice, 5:1303-1310.
- C.C. Hang, A.P. Loh, V.U. Vasnani (1994). Relay feedback auto-tuning of cascade controllers. IEEE Transactions on Control Systems Technnology, 2:42-45.
- S.V. Kalyuznhyi (1997). Batch anaerobic digestion of glucosa and its mathematical modeling. Description, verification and application of model, Bioresource Technology, 59:249-258.
- S.V. Kalyuznhyi, V.I. Sklyar, M.A. Davlyatshina, S.N. Parshina, M.V. Simankova, N.A. Kostrikina, A.N. Nozhevnikova (1996). Organic removal and microbiological features of UASB reactor under various organic loading rates, Bioresource Technology, 55:47-54.
- S. Marsili-Libelli, A. Muller (1996). Adaptive fuzzy pattern recognition in the anaerobic digestion process, Pattern Recognition Letters, 17:651-659.
- R. Moletta, D. Verrier, G. Albagnac (1986). Dynamic modelling of anaerobic digestion, Water Research, 20:427-434.
- E. Murnleitner, T.M. Becker, A. Delgado (2002). State detection and control of overloads in the anaerobic wastewater treatment using fuzzy logic, Water Research, 36:201-211.
- 11. E. Mamdani (1975). An experiment in linguistic synthesis with a fuzzy logic controller, International Journal on Man Machine Studies, 7:1-13.
- 12. J.G. Ziegler, N.B. Nichols (1942). Optimum setting for automatic controller, Trans. ASME, 64:759-768.
- Z.Y. Zhao, M. Tomizuka, S. Isaka (1993). Fuzzy gain scheduling of PID controllers, IEEE Transactions on Systems, Man. and Cybernetics, 23(5).
- 14. A. Hazzab, A. Laoufi, I.K. Bousserhane, M. Rahli (2006). Real time implementation of fuzzy gain scheduling of PI controller for induction machine control, International Journal of Applied Engineering Research, 1:51-60.

Response of the gravito-inertial mechanoreceptors during a fall: a mathematical model

Vladimir Aleksandrov^{1,2}, Tamara Alexandrova^{1,2}, Rosario Vega³, Gregorio Castillo², Maribel Reyes², Yaneri Aguilar³, Aída Ortega³, Nelly Shulenina¹, and Enrique Soto³

Moscow State University, Leninskie Gory, 119991, Moscow, Russia vladimiralexandrov366@hotmail.com

²Facultad de Ciencias Físico Matemáticas, Universidad Autónoma de Puebla, Apartado Postal 1152, Puebla, Pue. C. P. 72000, México

maribelrr@gmail.com

Instituto de Fisiología, Universidad Autónoma de Puebla, Apartado Postal
406, Puebla, Pue. C. P. 72570, México,
esoto@siu.buap.mx

(Paper received on February 26, 2008, accepted on April 15, 2008)

Abstract. Various types of vestibular prosthesis prototypes have been developed as an aid for treatment of equilibrium disturbances. One of the primary tasks for improving these prosthetic devices is the development of output stimulating impulses that may resemble the natural response of the vestibular system. In this work, a mathematical model of the information output from the gravito-inertial mechanoreceptor of the vestibular apparatus is presented. For this, we have considered five compartments: mechano-electrical transduction, adaptation of transduction, hair-cell ionic current, synaptic transmission, and afferent neuron discharge. The numerical parameters of the model were obtained from experiments that were done in the inner ear of the rat. The results of the numerical analysis of the model showed that the mathematical modelling may be used to construct an encoder system for the artificial sensors (microaccelerometer) contributing to the development of a reliable vestibular prosthesis prototype.

1 Introduction

The vestibular system, as well as other sensory organs, is a complex structure in which optimization of incident energy to impinge and stimulate specific sensory cells takes place. In the vestibule, the semicircular canals and the otolithic organs allow the perception of the influence of gravity and of inertial forces produced by changes of the head position to provide information used to stabilize the gaze and the posture. Receptor hair cells of the vestibular system convert the energy of a mechanical stimulus and transmit information about it to the first afferent neurons and then to the central nervous system. The functional scheme of the vestibular mechanoreceptor is

© E. V. Cuevas, M. A. Perez, D. Zaldivar, H. Sossa, R. Rojas (Eds.) Special Issue in Electronics and Biomedical Informatics, Computer Science and Informatics
Research in Computing Science 35, 2008, pp. 209-218



In this work, we present a compartmental model of the vestibular mechanoreceptor in which we have considered five compartments: mechano-electrical transduction, adaptation of the transduction mechanism, hair cell ionic currents, synaptic transmission, and afferent neuron discharge. In relation to the control mechanism, we only considered the adaptation of the transducer mechanism. In this paper we consider the union of the mathematical models that were presented earlier as a gravito-inertial mechanoreceptor mathematical model.

2 Mathematical Model

Let us examine the extreme situation: initial stage of the uncontrolled fall of a man in the sagital plane (during 100 ms), when there is still a possibility of the vertical pose stabilization. As shown [2], the greatest reaction of hair cells to the mechanical stimulus, which leads to the fall, occurs for the cells situated along the axis of the sensitivity of the macula of sacculus, orthogonal at the local vertical line at the initial moment of the fall (Fig. 1).

The sacculus, just as the utriculus, is a multi-dimensional accelerometer that makes it possible to obtain information about the apparent acceleration of the otolith membrane from many directions of sensitivity. Only one of these directions interests us, as mentioned above. In connection with this, we will not consider the mathematical model of the dynamics of the whole otolith membrane on the plane that is parallel to the plane of the macula, and the response to this stimulus of many hair cells and primary afferent neurons, but only the dynamics along the axis of sensitivity that was determined above. Hair cells located along the considered axis of sensitivity (Fig. 1), in which the positive direction coincides with the direction of the forward fall (they are located before the striola – reversal line), and the hair cells in which the positive direction coincides with the direction of two hair cells with opposite polarity. We have designated the hair cell altogether with the primary afferent neuron as vestibular mechanoreceptor.

The term "gravito-inertial mechanoreceptor" for the stabilization of the vertical

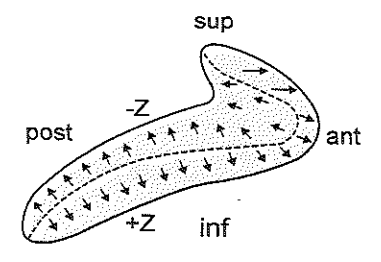


Fig. 1. Functional polarity of the sacculus hair cells. The striola is designated by the dotted line. Arrows represent the direction of maximal sensitivity for hair cells (Spoendlin H.H. In: Wolfson R.J.,ed. The vestibular system and its diseases. Philadelphia, 1966, University of Pennsylvania Press)

position will be used to name the set of the three mathematical models: the first of them describes the dynamics of the displacement (x_s) [3] of the otolith membrane along the axis of sensitivity that is being considered, and the other two models describe the response of the mechanoreceptors of the opposite directions sensitivity $(x=\pm x_s)$ of the otolith membrane (Fig. 2).

In sections 2.1 and 2.2 the basic model consisting of the "Current dynamics in hair cells" and "Afferent neuron dynamics" are presented. In section 2.3 these two blocks are connected by the "Synaptic transmission" block. Also described are the input of the "Mechanoelectrical transduction" and the "Transducer adaptation" to prolonged mechanical stimulus.

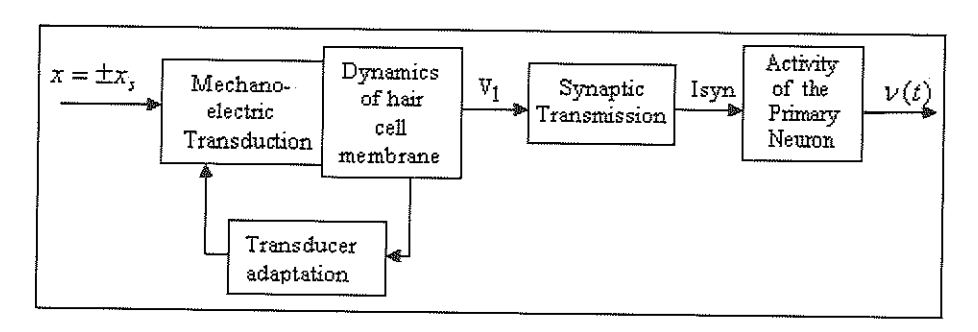


Fig. 2. Scheme of the vestibular mechanoreceptor compartments considered in the model.

2.1 Current dynamics in hair cells

The model is based on the Hodgkin-Huxley equations. This is a simplified model, assuming that the dynamics of a hair cell may be described using a single total ionic current I_T [1], where I_T is the sum of the principal currents of the hair cells. The model is summarized in (1).

$$\begin{split} C_{ml} \frac{dV_1}{dt} &= -I_{Tr} - I_T - I_{L1}, \quad I_T = g_T m^3 (h_1 + h_2) (V_1 - E_T), \quad I_{L1} = g_{L1} V_1, \\ & \tau_m (V_1) \frac{dm}{dt} = m_{ST} (V_1) - m, \\ & \tau_{h_1} (V_1) \frac{dh_1}{dt} = q_1 h_{ST} (V_1) - h_1, \end{split} \tag{1}$$

$$\tau_{h_2} (V_1) \frac{dh_2}{dt} = q_2 h_{ST} (V_1) - h_2, \end{split}$$

Here I_T is the total ionic current; m is the parameter that specifies the current activation process; h is the parameter that specifies the current inactivation process; g_T is the maximum conductance; I_L is the leakage current; and I_{com} is, under natural conditions, the current flowing into a hair cell through the transduction channels ($I_{com} = I_{T}$), or in the experiments, the command current. The inactivation parameter h has two constituents $(h=h_1+h_2)$ corresponding to the potassium channels with fast and slow inactivation time constants. Functional parameters are shown in table 1, where m_{\min} , h_{\min} , τ_{\min} , τ_{\max} , $V_{\rm ac}$, $V_{\rm r}$, $V_{\rm h}$, S_{ac} , S_r and S_h are coefficients of sigmoidal fitting curves that containing this functional parameters; k_{hl} , k_{h2} , b_{hl} , b_{h2} are coefficients of approximation for the fast and slow inactivation time constants.

Table 1. Functional parameters of the model used in (1)

Name	Functional Form	Name	Functional Form
Steady-state Activation	$m_{ST}(V_1) = m_{\min} + \frac{1 - m_{\min}}{1 + \exp\left(\frac{-(V_1 - V_{oc})}{S_{oc}}\right)}$	Fast Inactivation Time Constant	$\tau_{h1}(V_1) = k_{h1}V_1 + b_{h1}$
Activation Time Constant	$\tau_m(V_1) = \tau_{\min} + \frac{\tau_{\max} - \tau_{\min}}{1 + \exp\left(\frac{V_1 - V_r}{S_r}\right)}$	Slow Inactivation Time Consta	$\tau_{h2}(V_1) = k_{h2}V_1 + b_{h2}$ ni
Steady-state Inactivation	$h_{ST}\left(V_{1}\right) = h_{\min} + \frac{1 - h_{\min}}{1 + \exp\left(\frac{V_{1} - V_{h}}{S_{h}}\right)}$		

Parameter	Semicircular Canal	Parameter	Semicircular Canal	Parameter	Semicircular Canal
C_{ml}	11.26 <i>pF</i>	S_{τ}	15.68 mV	V_h	-9.82 mV
g _L	2.32 nS	\dot{V}_{ac}	$-25.36 \ mV$	S_h	$21.96 \ mV$
g _T	77.84 nS	S_{ac}	$15.06 \ mV$	h_{min}	0.73
E_{T}	$-79 \ mV$	m_{min}	0.37	r	3
I_{com}	0 pA	k_{hI}	0.82 ms/mV	q_I	1/2
τ_{max}	77.58 ms	k_{h2}	1.26 ms/mV	q_2	1/2
$ au_{min}$	6.55 ms	$b_{ m hl}$	55.86 ms		
V.	$-52.23 \ mV$	$b_{ m h2}$	282.38 ms		

The numerical parameters of the model were obtained from experimental voltageclamp recordings of the isolated hair cells from the semicircular canal of the rat [5,6] (Table 2).

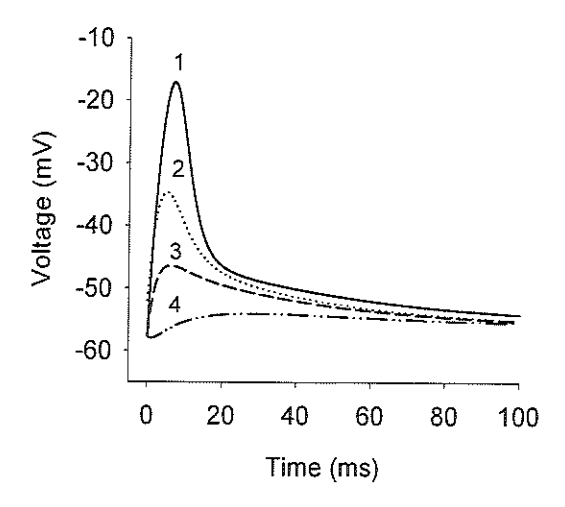


Fig. 3. Voltage response trajectories obtained for $I_{com} = 0$. These traces were obtained for different initial conditions taken for system (1): (1) $V_0 = -57.67 \text{ mV}$, m = 0.0041, $h_I = 0.9$, $h_2=0.1$; (2) $V_0=-52\ mV,\ m=0.240,\ h_1=0.8,\ h_2=0.2$; (3) $V_0=-57.67\ mV,\ m=0.340,\ h_1=0.8$ 0.8, $h_2 = 0.2$; (4) $V_0 = -57.67 \text{ mV}$, m = 0.440, $h_1 = 0.8$, $h_2 = 0.2$

In figure 3, there are the voltage response trajectories obtained for $I_{com}=0$. The model predicted a resting potential of -57 mV obtained with the values in table 1. The dynamics of the hair cell membrane potential, obtained with the use of the mathematical model shown in (1), qualitatively coincides with the results of the physiological experiments (Fig. 4).

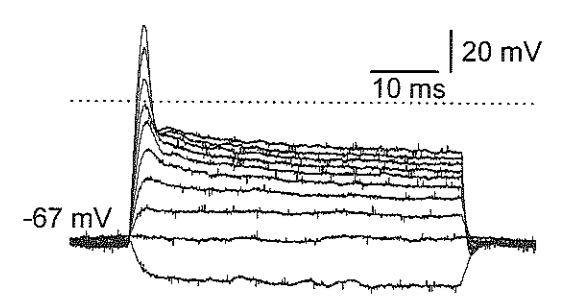


Fig. 4. Traces showing a typical voltage response of a hair cell obtained from the rat's semicircular canals subjected to current pulse injection (from -0.1 to 0.5 nA) (the dotted line shows the zero voltage)

2.2 Afferent neuron dynamics

In describing the activity of the primary afferent bipolar neuron, a Hodgkin-Huxley-type model was also used. The parameters were calculated using experimental results obtained from cultured vestibular afferent neurons of the rat [7,8]. The use of rat parameters in this model is the first modification with respect to the original Hodgkin-Huxley model. Other two modifications were about the time constants: an inactivation parameter for outward current " h_K " other is a modification in the mathematical model original of Hodgkin-Huxley where h+n=0.8, here we have next modification $h+n=C(V_2)$, $C(V_2)$ is an experimental results. The right part of this equality has a constant value for each V_2 . In addition, our model have a complex description for potassium current $I_K = g_K^{\max} n^4 h_K (V_2 - V_K)$. Based on these modifications and assuming that $\tau_m = 0$ and $\tau_{hk} = constant$ an intersection of two isoclines as an unstable point of repose was found. Therefore, a limit cycle and the correspondent auto-oscillations were also found.

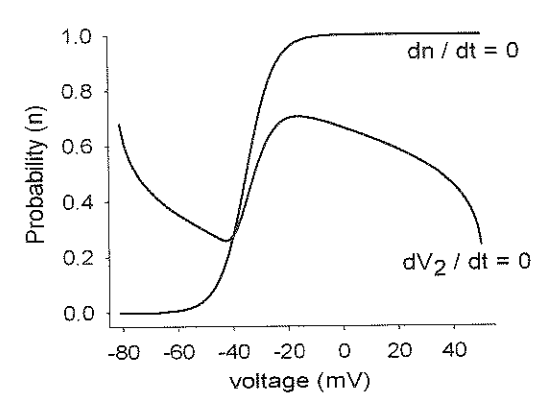


Fig. 5. Isoclines of the simplified and of the modified Hodgkin-Huxley model

The modified and simplified Hodgkin-Huxley model (see above) for the action potential generation takes the form as shown in [4].

$$C_{m2} \frac{dV_2}{dt} = I_{com}(V_1) - g_L^{\max}(V_2 - V_L) - g_{Na}^{\max} m_{\infty}^{-3}(V_2)(C(V_2) - n)(V_2 - V_{Na}) - g_K^{\max} n^4 h_k (V_2 - V_K)$$

$$\tau_n(V_2) \frac{dn}{dt} = n_{\infty}(V_2) - n$$

$$\tau_{hk}(V_2) \frac{dh_{-k}}{dt} = h_{k\infty}(V_2) - h_k(V_2)$$
(2)

The coefficients g_{No}^{\max} , g_{K}^{\max} , g_{L}^{\max} belong to confidence intervals in accordance with the experimental results. Table 4 present their values which correspond to the

greatest interval between two points (I_1, I_2) of the bifurcation of Hopf [9]. These points indicate the appearance and disappearance of the auto-oscillations.

Table 3. Parameters of the model for vestibular afferent neurons (2)

Activation stable state g_{Na} $m_{\infty}(V_2) = \frac{1}{1 + \exp\left(\frac{-(V_2 + 33.8)}{5.2}\right)}$	Inactivation stable state g_{Na} $h_{Na_{\infty}}(V_2) = \frac{1}{1 + \exp\left(\frac{V_2 + 60.5}{9.9}\right)}$
Activation stable state g_K $n_{\infty}(V_2) = \frac{1}{1 + \exp\left(\frac{-(V_2 + 35)}{5}\right)}$	Inactivation time constant g_{Na} $\tau_{hNo}(V_2) = \frac{1}{0.01 + \exp\left(\frac{79 + V_2}{-15}\right) + \exp\left(\frac{30 + V_2}{5}\right)} + 0.5$
Activation time constant g _K $\tau_n(V_2) = \frac{68}{\exp\left(\frac{25 + V_2}{-15}\right) + \exp\left(\frac{30 + V_2}{20}\right)}$	Inactivation stable state g _K $h_{K\infty}(V_2) = \frac{0.96408 - 0.7329}{1 + \exp\left(\frac{V_2 + 33.87968}{10.24986}\right)} + 0.7329$
	Inactivation time constant g _K $\tau_{h_K}(V_2) = \frac{1250}{\exp\left(\frac{15 + V_2}{-15}\right) + \exp\left(\frac{25 + V_2}{10}\right)} + 500$

Table 4. Numerical parameters of the model (2).

Constants	Units	Chosen Value	Constants	Units	Chosen Value
C_{m2}	μF/cm ²	1	g max g Na	mS/cm ²	2.3
V_{Na}	mV	52	${\mathcal G}_K^{\max}$	mS/cm ²	2.4
V_{K}	mV	-84	g max	mS/cm ²	0.03
V_{L}	mV	-63	I_{com}	μA/cm²	1 to 150

The amplitude of the auto-oscillations depends on the value of I_{com} (where I_{com} = - I_{syn}). The first point of bifurcation $I_I = 0.6 \,\mu\text{A/cm}^2$, the second point of bifurcation of Hopf $I_2 = 165.3 \,\mu\text{A/cm}^2$.

2.3 Synaptic transmission, mechano-electrical transduction and transducer adaptation

Data from experimental studies of synaptic transmission in the bullfrog inner ear [10] were used for the association of the blocks that describe the dynamics of ionic currents in the hair cell and in the primary afferent neuron (Fig 2). The curve shown in figure 6 shows the relationship between the voltage in the hair cell (V1 in model 1) and the synaptic current in the afferent neuron (I_{syn} equivalent to I_{com}). The maximum synaptic current was hypothesized to be equivalent to 40 μA/cm².

Let us add, to the chain of three blocks just described, an input block for the mechano-electrical transduction mechanism [1], and the mechanism of the hair cell

transducer adaptation to the prolonged mechanical stimuli. The mathematical model of these two mechanisms is represented in the form of equation (3).

The adaptation mechanism is given by [4]. Where s is the adaptation parameter; τ_{ad} is a time constant; k is a gain constant; I_{Tr} is the transduction current; I_{Tr0} is the transduction current in stationary state; p(x,s) is the probability of the opening of the canal; x is the displacement of a hair bundle.

$$\tau_{ad}\dot{s} + s = k(I_{Tr} - I_{Tro}); \quad I_{Tr} = g_{Tr}(x, s)(V_1 - E_{Tr}); \quad g_{Tr} = \overline{g}_{Tr}p(x, s);$$

$$g_{Tr} = 1.4nS; \quad \tau_{ad} = 100 \text{ ms}; \quad p(x, s) = \frac{1}{1 + Exp\left(-\frac{x + s - x_0}{s_1}\right)};$$

$$s_1 = 0.2 \text{ } \mu\text{m}; \quad k = 0.03; \quad I_{Tro} = -14.4 \text{ pA}; \quad x_0 = 0.3 \text{ } \mu\text{m}; \quad E_{Tr} = 0$$
(3)

Using this system, a mathematical model of the vestibular mechanoreceptor information output was obtained. It consists of equations (1), (2), (3), tables 1, 2, 3, 4 and the graph in Figure 6.

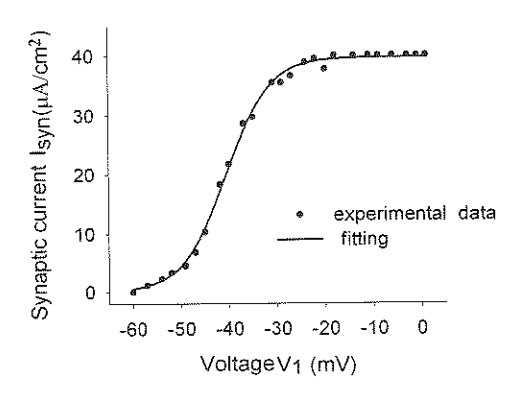


Fig. 6. Relationship between the membrane voltage in the hair cell and the synaptic current in the afferent neuron. Continuous line represent the best fit to the experimental data [10].

Numerical Results

After the association of all blocks of the model and the analysis of the dynamics of ion currents in the hair cell and in primary afferent neuron, the numerical parameters were selected on the basis of physiological experiments (tables 1, 2, 3 and 4). The results of the calculations for the initial stage of the fall are shown in Fig 7 (the inclination forward to 30 degrees-Figure 7A-). Development of membrane potential V_1 of hair cell as a result of the mechanism of adaptation acting against the background of the mechanical stimulus are shown in Figure 7 B. Finally we have a secondary information in the form of afferent impulses of the primary neuron with frequencies varying from 20 Hz to 40 Hz.

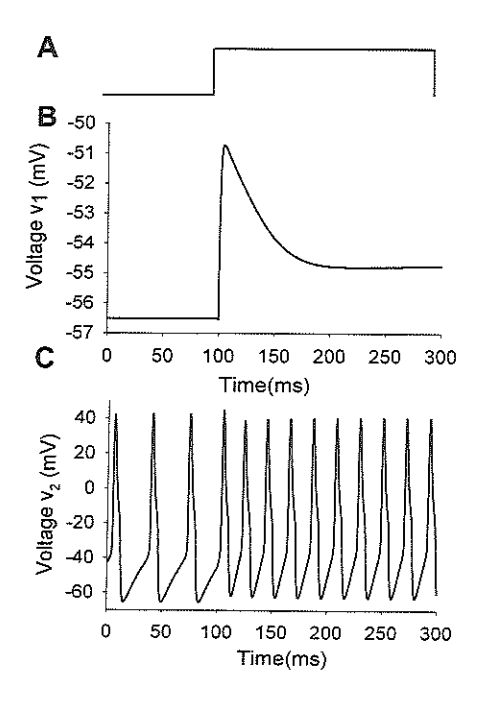


Fig. 7. The process of the information output from the vestibular mechanoreceptor. In A, mechanical stimulus displaces a hair cell bundle. Stimulus is absent during the first 100 ms (stationary situation of rest); in the course of the following 200 ms the hair bundle is displaced 1 µm. In B, the voltage response of the hair cell reflects the activation of the transducer adaptation mechanism. In C, the output of the model in the form of action potentials in the primary afferent neuron.

4 Conclusion

The numerical results indicate that the mathematical model of information processing in the gravito-inertial mechanoreceptor resembles the activity of the natural sensor as studied experimentally.

In the development of vestibular prosthetic devices a transfer function derived from the recordings in the monkey inner ear [11] has been used to convert the analog output of the device to a pulse train useful to stimulate the afferent nerve. We propose that the use of more realistic models based on the physiological knowledge and using parameters from animal experiments, will endow prosthetic devices with greater coding capabilities than those of devices using simpler transfer functions.

Our results demonstrate that the development of an integrated mathematical model of the function of vestibular endorgans is feasible and that it will resemble vestibular system coding capabilities.

It is concluded that the proposed mathematical model may be used to construct an encoder system for artificial sensors (eg: microaccelerometer and microgyroscope) contributing to the development of a reliable vestibular prosthesis prototype.

Acknowledgements

This work was performed with the support of UC-MEXUS-CONACyT grant from the University of California at Riverside project to ES; Russian state contract No 02.512.11.2161 for studies with the collaboration of foreign scientific institutions to VA: and VIEP-BUAP grant No. 0054 to VA.

References

- Alexandrov, V.V., Almanza, A., Kulikovskaya, N.V., Vega R., Alexandrova, T.B., Shulenina, N.E., Limón, A. and Soto, E.: A Mathematical Model of the Total Current Dynamics in Hair Cells. In Sadovnichii, V.A.(ed): Mathematical Modeling of Complex Information Processing Systems, Moscow State University, (2001) 26-41
- Alexandrov, V.V., Alexandrova, T.B., Astakhova, T.G. Kulikovskaya, N.V., Kurilov, V.I., Migunov, S.S., Shulenina, N.E., Soto, E., Vega, R.: A mathematical Model of the Response of Semicircular Canal and Otolith to Head Rotation under Gravity. J Gravitational Physiology 11(2)(2004) 25-26
- 3. Alexandrov, V.V., Alexandrova, T.B., Migunov, S.S.: The Mathematical Model of the Gravity-inertial Mechanoreceptor. Moscow University Mechanics Bulletin, No. 2, (2006) 59-64 (in passian)
- Alexandrov, V.V., Mikhaleva, E.Yu., Soto, E., García Tamayo, R.: Modification of Hodgkin-Huxley Mathematical Model for the Primary Neuron of Vestibular Apparatus. Moscow University Mechanics Bulletin, No. 5 (2006) 65-68 (in russian)
- Almanza, A., Vega, R. and Soto, E.: Calcium Current in Type I Hair Cells Isolated from the Semicircular Canal Crista Ampullaris of the Rat. Brain Research 994 (2003) 175-180
- Almanza, A., Vega, R., Naverrete, F. and Soto, E.: Nitric oxide modulation of L type Ca2+ current in sensory hair cells. J Neurophysiology 97 (2007) 1188-1195
- Soto, E., Limón, A., Ortega, A. and Vega, R.: Características Morfológicas y Electrofisiológicas de las Neuronas del Ganglio Vestibular en Cultivo. Gaceta Médica de México 138 (2002) 1-14
- Limón, A., Pérez, C., Vega, R. y Soto, E.: IK, Ca Current Density is Correlated with Soma Size in Vestibular Primary Afferent Neurons. J Neurophysiology 94 (2005) 3751-3761
- Troy, W.C.: The Bifurcation of Periodic Solutions in the Hodgkin-Huxley Equations. Quarterly of Applied Mathematics 36 (1978) 73-83
- 10. Keen, E.C. and Hudspeth, A.J.: Transfer Characteristic of the Hair Cell's Afferent Synapse. Proc. Natl. Acad. Sci. USA 103 (2006) 5437-5542
- Fernández, G. and Goldberg, J. Physiology of Peripheral Neurons Innervating Otolith Organs of the Squirrel Monkey. II. Directional Selectivity and Force-Response Relations. J Neurophysiology 29 (1976) 985-995.

Author Index Índice de autores

Aguilar Yaneri	209	Mancilla Juana	165
Alanis Alm	11	Martinez Albino	199
Aldape Mario	147	Medina Manuel	199
Aleksandrov V.	209	Montiel Gabriela	187
Aleksandrova T.	209	Muro Juan	3
Alvarado A.	199	Nuño Emmanuel	21
Alvarez Josue	107	Olmedo Jose	127
Astorga Carlos	199	Ortega Aida	209
Bader Maro	31	Ortega Susana	3
Basañez Luis	21	Palomo Leopoldo	21
Basil Hadithi	3	Parra Vicente	51
Block Marco	31	Pazos Rodolfo	137
Bravo Miguel	97	Perez Marco	41
Butron Alejandro	87	Posada Ruben	199
Camacho Oscar	147	Ramirez Marte	31
Castilla Gpe.	165	Ranta Radu	177
Castillo Gregorio	209	Raygoza Juan	3
Cedano Marco	107	Reyes Maribel	209
Chavolla Edgar	41	Riquelme Juan	3
Cruz Laura	137	Rodriguez A.	21
Cuevas Erik	31,41	Rojas Raul	31
De la Mora A.	41	Romo Rebeca	177
Delgado Jose	137	Salido Ricardo	177
Diez Hector	127	Sanchez Edgar	11
Dominguez Omar	51	Sepulveda G.	51
Espinosa G.	117	Shulenina Nelly	209
Espriella Karla	165	Solis Gualberto	63,157
Fraire Hector	137,165	Sossa Humberto	77
Galaviz G.	97	Soto Enrique	209
Giljum Manfred	63	Tapia Ernesto	31
Gonzalez Juan	137	Valle Daniela	157
Gunnarsson K.	31	Vargas Genoveva	187
Gurrola Marco	117	Vazquez Roberto	77
Harvey Richard	87	Vega Rosario	209
Hernandez Carlos	165	Yanez Cornelio	147
Hernandez Ivan	97	Zaldivar Daniel	31,41
Hernandez Jorge	107	Zechinelli Jose	187
Leija Lorenzo	177		
Loukianov A.	11		

Editorial Board of the Volume

Comité Editorial del volumen

Alejandra Santoyo

Alejandro Morales

Alma Alanis-Garcia

Antonio García

Basil M. Al-Hadithi

Carlos Lopez

Cuauhtémoc Aguilera

Didier WOLF

Dimitris Kalamatianos

Edgar N. Sanchez

Eduardo Ruiz

Efrén Aguilar

Enric Fossas

Ernesto Tapia

Felix Von Hundelshausen

Francisco Gómez

Freddy Lopez Villafuerte

Gustavo Sutter

Heriberto Zavala

Jagannathan Sarangapani

Jaime Alvarez

Jesus Palomino

Jochen Schiller

John Gray

José E. Rayas

Josúe Alvarez

Juan P. Garcia

Juan Raygoza

Juan Suardiaz

Luis Basañez

Mario Siller

Marco Block

Mark C. Readman

Marte Ortegon

Michael Himmelsbach

Michael Saliba

Mo Jamshidi

Nancy Arana-Daniel

Peter Cook

Peter Wellstead

Piotr Dudek

Radu Ranta

Raúl Rojas

Raúl Suárez

Richard Middleton

Rohan Munasinghe

Ronald Lasky

Susana H. González

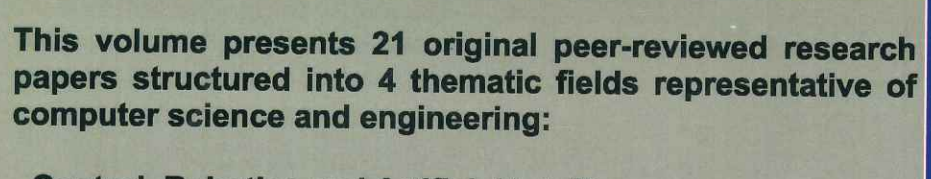
Susana Ortega

Valérie LOUIS-DORR

Zoltan Kutalik



Impreso en los Talleres Gráficos de la Dirección de Publicaciones del Instituto Politécnico Nacional Tresguerras 27, Centro Histórico, México, D.F. Mayo 2008. Printing 500 / Edición 500 ejemplares.



- Control, Robotics and Artificial Intelligence
- Signal and Image Processing
- Computer Science and Embedded Architecture
- Biomedical Engineering

The volume is of interest for computer science and engineering researchers and students, programmers and computer engineers, as well as general public interested in current research in computer science and engineering.

